Summer 8-15-2022

Modeling, Analysis, and Simulation to Reveal the Mechanisms of Ciliary Beating

Louis Woodhams
Washington University in St. Louis

WASHINGTON UNIVERSITY IN ST. LOUIS

McKelvey School of Engineering
Department of Mechanical Engineering & Materials Science

Dissertation Examination Committee:
Philip Bayly, Chair
Susan Dutcher
Guy Genin
Mark Meacham
David Peters

Modeling, Analysis, and Simulation to Reveal the Mechanisms of Ciliary Beating

by

Louis Woodhams

A dissertation presented to
the McKelvey School of Engineering
of Washington University in
partial fulfillment of the
requirements for the degree
of Doctor of Philosophy

August 2022
St. Louis, Missouri

Table of Contents

List of Figures

List of Tables

Acknowledgments

I would like to thank my advisor, Philip Bayly, for his advice and guidance, for finding interesting opportunities and projects for me, and for always finding time to talk about research and help when needed. I want to thank all the faculty who have helped to guide and advise me in my years at Washington University in St. Louis. These include Elliot Elson, Kenneth Pryse, Kenneth Jerina, Ruth Okamoto, and Mark Jakiela. I want to thank Guy Genin, Dave Peters, Mark Meacham, and Susan Dutcher for serving on my dissertation committee, advising me on research, and helping me navigate various academic processes. I want to thank Linda Buckingham for helping me collate my various roles at the university. I want to thank the members of the Pearson lab – Chad Pearson, Anthony Junker, and Adam Soh – for the fascinating collaborations. I would also like to acknowledge a few of the fantastic undergraduate researchers who helped push much of this work forward: Daniel Shen, Toby Utterback, and Alicia Gupte.

I would like to acknowledge funding from NSF grant no. CMMI-1633971 and the Children's Discovery Institute.

Finally, I would like to thank my Mom, my Dad, Hannah, Julian, Eric, Gloria, Ginny, and Lauren for their love and support.

Louis Woodhams

Washington University in St. Louis

August 2022

Dedicated to Suzanne.

ABSTRACT OF THE DISSERTATION

Modeling, Analysis, and Simulation to Reveal the Mechanisms of Ciliary Beating

by

Louis Woodhams

Doctor of Philosophy in Mechanical Engineering

Washington University in St. Louis, 2022

Professor Philip V. Bayly, Chair

Cilia are microscopic cellular appendages that help us breathe by clearing our airways, maintain the health of our central nervous system by circulating cerebrospinal fluid, and allow us to reproduce by transporting eggs and propelling sperm cells. Cilia even determine the asymmetry of our internal organs during embryonic development. However, the mechanisms underlying ciliary beating are not fully understood. Questions remain as to how arrays of the motor protein dynein generate the propulsive waveforms observed in cilia and how structural elements within the cilium and its connection to the cell deform during beating. In the current work, mathematical modeling, analysis, and simulation are applied to answering these questions in three related aims: (i) a mathematical model of ciliary beating driven by steady dynein forces solved by linear stability analysis of custom finite-element equations; (ii) a model of the basal body and cilium created in commercial finite-element software and solved using a geometrically-nonlinear time-domain solver; and (iii) a custom software tool written for automated tracing of ciliary imaging, and applied to the analysis of beating cilia. Through these aims, I estimated properties of the cilium and basal body, supported the plausibility of a model of ciliary beating, and gained insight into the motility of cilia on pancreatic beta cells.

Chapter 1: Introduction to the dissertation

1.1 Overview

Motile cilia are slender organelles, often described as ‘hair-like’ or ‘whip-like,’ that cells use to impel fluid or propel themselves through fluid. Arrays of cilia that protrude from the epithelial cells lining our airways beat in a coordinated motion to clear mucus that protects our lungs from pathogens and particulates [1]. Ependymal cells lining our brain ventricles circulate cerebrospinal fluid that clears waste and carries nutrients [2, 3]. Motile cilia are also important in our reproductive systems. Cilia within fallopian tubes are responsible for egg transport [4], and the tail of a sperm cell, often called a flagellum, is nearly identical to the cilia mentioned above in terms of its internal structure (the axoneme) [5, 6].

Small organisms propel themselves through fluid using cilia. *Tetrahymena thermophila* is a single-celled organism covered in an array of several hundred cilia that propel it through fluid [7]. The alga *Chlamydomonas reinhardtii* uses two cilia in a ‘breast stroke’ motion to pull itself through fluid [8], though in some cases it swims in reverse by using its cilia to push itself backwards in a symmetric beating motion often described as ‘flagellar’ [9]. Remarkably, the cilia used by these single-celled organisms are nearly identical to the motile cilia that occur in the human body. This fact illustrates how evolutionarily ancient these organelles are [10] and also makes *Chlamydomonas* and *Tetrahymena* ideal model organisms for the study of ciliary function and structure.

1.2 Motivation

Disorders of cilia, called ciliopathies, are implicated in a number of health problems and developmental defects. Primary ciliary dyskinesia (PCD) is a condition which affects the proper

function of motile cilia throughout the body. People affected by PCD experience chronic respiratory issues due to impaired mucociliary clearance, as well as issues with fertility [11]. In approximately half of all cases of PCD, a person's internal organs develop on the opposite side of the body from what is normal [12]. This condition, called *situs inversus totalis* (SI), arises because developmental asymmetry is established in the embryonic node by the swirling motion of nodal cilia [13]. The combination of respiratory symptoms and SI is known as Kartagener syndrome [14]. Cystic fibrosis (CF) is not a disorder of the cilia themselves, but it causes a decrease in mucociliary clearance by increasing the viscosity of the airway surface liquid (ASL) layer in which airway epithelial cilia beat [15]. While the study of ciliary mechanics is interesting from the perspective of pure science alone, a better understanding of how cilia beat and the effects of environmental parameters such as viscosity on ciliary beating could facilitate the development of treatments for ciliopathies and disorders affecting ciliary performance.

Researchers have taken a multi-faceted approach to studying the beating of cilia and eukaryotic flagella for decades, involving imaging, experiments, and modeling. Early applications of the electron microscope revealed similarities in the structure of cilia and flagella [16], and improvements in imaging technique have clarified the details of the complex internal structure now known as the axoneme [17-19]. Gibbons used extraction and reconstruction of axonemes in 1963 to determine that ATPase activity occurred in the 'arms on the outer fibers' [20]. We now know these arms to be the motor protein dynein. Interestingly, the necessity of distributed motors along the length of the axoneme had been predicted by Machin 5 years earlier through a mathematical model [21, 22]. Machin showed that mathematical models of beating driven by motion at the base of the flagellum did not create the type of shapes observed in flagella, but that such shapes could be created by modeling 'contractile elements' distributed along the flagellum.

This landmark paper put to rest one hypothesis and established the plausibility of another. Later experimental work showed that the beating of cilia and flagella is driven not by contractile elements, but by the relative sliding of the outer filaments of the axoneme [23]. These examples illustrate the complimentary nature of imaging, experiment, and mathematical modeling.

1.3 Current work

In the current work, I aim to better understand ciliary beating through modeling, analysis, and simulation of ciliary motion.

1.3.1 Modeling

A mathematical model is a simplified representation of a physical system in terms of mathematical equations [22, 24, 25]. The point of the model is to make predictions about the behavior of the system being modeled. Models must be consistent with the relevant physical and mechanical laws, but it is not possible to represent every minute detail of the system being modeled. Thus, the model is simplified to *include* those aspects of the physical system that are essential to predicting its behavior as accurately as desired but *exclude* information about the system that unnecessarily complicates the model or the solution of the model. For example, when we use modeling to predict the load that some structure can bear before failing (by some criterion), we make simplifying assumptions about the material properties, geometry, loading, and initial stress state within the structure. It is, of course, important to assess the impact that these assumptions make on our predictions.

Often a model is used to predict the behavior of a system with parameters that are known (with some degree of certainty). In that case the model is created, its solution is verified, and if the predictions are compared to the behavior of the real system, the model may be validated. In the

case of modeling cilia and associated structures, many of the parameters of the system are unknown. We only have estimates for a few parameters of the system and observations of the overall behavior. This is a kind of inverse problem where we are trying to determine the forces, structural properties, and nanoscale internal couplings in the axoneme that lead to the observed microscale (or nanoscale) behavior. While this type of *mathematical* modeling defies validation, it can rule out or establish the plausibility of a *conceptual* model (as Machin did in 1958). Whereas an experimentalist may ask if a hypothesis is testable, modeling gives us a way to determine whether the hypothesis is plausible or even possible.

1.3.2 Analysis

For experimental data to be useful, they must be put into a form that allows quantification, interpretation, and comparison for the purpose of gaining understanding of the system being studied and drawing conclusions. In the study of cilia, raw data are often in the form of image stacks (3D electron tomograms or confocal microscope stacks) or sequences of microscope images (videos). The first step in analyzing such data is often to create a coordinate system within the imaging data and assign coordinates to points along continuous structures such as individual filaments within the axoneme (electron tomograms) or whole cilia (bright-field microscopy). In the analysis of beating cilia, traces may be drawn (manually or using automated methods) frame-by-frame over hundreds of frames to determine the planar coordinates of the cilium as a function of time [26]. Here time means the relative position of an image in a sequence of images multiplied by the time delay between captured frames. Ciliary traces, in the form of arrays of coordinates locating points along the cilium at multiple times, may then need to smoothed or have the dimensionality of the data reduced through techniques such as polynomial regression, Fourier decomposition, or principal component analysis.

From these traces, we can calculate the frequency of beating as well as the kinematics of the cilium (e.g, position, angle, curvature, velocity) as a function of the distance along the cilium and the time. From the kinematics, we use fluid mechanics to calculate the dynamics (kinetics) of the system: forces the cilium applies to the surrounding fluid, the power output of the cilium, and the moment the basal attachment of the cilium must resist under beating.

By comparing the kinematic and dynamic quantities above, as well as qualitative observations of the traces, we can determine the effects of mutations and environmental parameters on the beating of cilia in model organisms [27-29]. We can also establish the plausibility of a mathematical model of ciliary beating by comparing the quantities solved for in the model with the quantities calculated from experimental data [21, 30, 31].

1.3.3 Simulation

For a mathematical model to be useful, we must be able to solve it. For some models, exact solutions are possible to obtain. However, multi-filament models of the axoneme give rise to coupled systems of nonlinear partial differential equations which are difficult or impossible to solve exactly. In these cases, we must use approximate methods, which are facilitated by modern computers.

One approach to solving such problems is to use a commercial finite-element (FE) or multiphysics software package. This approach allows the user to take advantage of one interface to define the model (geometry, material properties, body forces, boundary conditions, and multi-body couplings), discretize and solve the model, and extract data of interest from the solution.

In some cases, it may be advantageous or necessary to create a model, solve it, and analyze the results using a custom software implementation of the FE or other numerical method. In the

current work, the commercial FE software we were using did not permit efficient linear stability analysis of the multi-filament model of the axoneme we were studying. In this case the modeling and discretization were written “from scratch” in code to create a system of matrix equations. Built-in time-stepping and eigenvalue solvers were employed to solve the problem, and a combination of custom code and built-in visualization tools were used for analysis of the results.

1.4 Summary and aims

The goal of this dissertation is to improve our understanding of the underlying mechanisms of ciliary beating through mathematical modeling of the cilium and associated structures, analysis of images of beating cilia, and simulation of ciliary beating under various parameters and assumptions about the underlying forces and structures.

This dissertation has three specific aims:

1.4.1 Aim 1 – Efficient stability analysis of the axoneme through a custom multi-filament finite-element model

Though it has long been assumed that some mechanism of dynein regulation is necessary to create the oscillatory, base-to-tip propagating beating patterns observed in cilia, this mechanism has never been shown to be necessary or present in the axoneme. Recent work has demonstrated that oscillations may arise under steady dynein forces due to a dynamic instability similar to aeroelastic flutter [32, 33]. Here I model and efficiently predict ciliary beating behavior in a multi-filament model of the axoneme using custom-written FE software. This software captures the conventionally modeled effects of filament bending stiffness, the viscosity of the surrounding fluid, and the curvature inducing effects of the dynein motors, but it also captures elastic and viscous inter-filament couplings, and the geometric effects of the axial loading that can lead to buckling and unstable oscillations. The custom software allows for efficient eigenvalue-based

stability analysis of the mathematical model. This analysis is used to estimate properties of the axoneme and may be used to inform parameter selection for more computationally demanding time-domain analysis in commercially available finite element software.

1.4.2 Aim 2 – A finite-element model of the cilium and basal body to understand how forces are transmitted from the cilium to the cell

Basal bodies are microtubule-based structures that nucleate and anchor cilia in cells. Though they have been assumed to be relatively rigid structures, imaging data from the Pearson Lab have shown that basal bodies deform in phase with the beating of cilia in model organisms such as *Tetrahymena thermophila* [34]. Using computational modeling in commercial FE software, I reproduced important aspects of the bending behavior observed in imaging data using biologically plausible geometry, material parameters, and forces. This modeling work helps us to better understand the role that basal body components and accessory structures play in stabilizing the basal body against ciliary forces, understand the interactions between basal bodies in multi-ciliated organisms, and gain insight into the mechanisms of ciliary beating through this additional source of experimental and simulated data.

1.4.3 Aim 3 – A semi-automated software for the analysis of ciliary kinematics and dynamics

To understand the underlying mechanics of ciliary beating, we need to quantitatively analyze data from observations of cilia beating under various conditions. These data are used to understand the forces and kinematics involved in ciliary propulsion and are used to evaluate the plausibility of models of ciliary beating. Such data often come in the form of traces of ciliary shape from live image sequences obtained under the microscope [26]. This tracing process can be tedious and time-intensive if done by hand, motivating the need for an efficient software-

based approach to automatically trace cilia in sequences of images [35]. In this work I create such a software using a novel algorithm and apply it to the kinematic and kinetic analysis of motile and primary cilia and sperm flagella. Additionally, I apply waveform analysis and resistive force theory to study the effects of genetic mutations on the coordinated beating of *Tetrahymena thermophila* cilia [36].

Chapter 2 serves as an introduction to the study of ciliary beating.

Chapter 3 addresses Aim 1.

Chapter 4 addresses Aim 2.

Chapters 5 and 6 address Aim 3.

1.5 Statement of contributions

This dissertation describes research work done in the Bayly lab from May 2018 to July 2022. All work was advised by Professor Phil Bayly.

Chapter 2 is reproduced from Woodhams *et al.*, "Chapter 12: Physics and mechanics of ciliary beating," in *The Chlamydomonas Sourcebook, Volume 3: Cell Motility and Behavior,* S. Dutcher Ed., 3rd Ed. Elsevier 2022 (in press) [37]. Senior authors Phil Bayly and Kirsty Wan wrote the *Motivation and background* section. Phil Bayly wrote the initial draft of *Fundamental principles and concepts*. Louis Woodhams expanded *Fundamental principles and concepts* and wrote the section *Mechanics of waveform generation*. All authors contributed to editing and generation of figures.

Chapter 3 is reproduced from the article Woodhams L.G., Shen Y. and Bayly P.V. 2022, *Generation of ciliary beating by steady dynein activity: the effects of inter-filament coupling in*

multi-filament models, J. R. Soc. Interface [38]. Louis Woodhams was responsible for deriving equations, performing all the analysis, writing the first draft, creating all figures, investigation, and writing software. Phil Bayly contributed writing, revision, and leadership of the project.

Chapter 4 is reproduced from the submitted article Junker *et al., Basal bodies bend in response to ciliary forces*, (submitted to Current Biology) [34]. First author Anthony Junker was responsible for conceptualization, imaging, investigation, writing the first draft, revision, and creating figures. Co-first author Louis Woodhams was responsible for conceptualization, all mathematical modeling, writing the modeling methods and results, creating modeling figures, and contributing to the revision process.

Chapter 5 includes material reproduced from Cho *et al*., *Islet primary cilia motility controls insulin secretion* (in press – Science Advances) [39]. Louis Woodhams created software used for analysis and generation of figures, supervised early analysis conducted by undergraduate researcher Toby Utterback, and contributed to design of experiments. Chapter 5 also includes application of the software to sperm cell analysis. Tracing and analysis of sperm flagella was conducted by undergraduate researcher Alicia Gupte under the supervision of Louis Woodhams and Phil Bayly. This ongoing work was done in collaboration with the Celia Santi Lab and Juan Ferreira.

Chapter 6 includes material reproduced from Soh *et al.,* 2022, *Intracellular connections between basal bodies promote the coordinated behavior of motile cilia*, Mol. Biol. Cell [36]. First author Adam Soh is responsible for the bulk of this paper including experiments, manually tracing cilia, performing statistical analysis, and writing the first draft. Second author Louis Woodhams wrote

software for the dynamic analysis of ciliary traces, conducted statistical analysis, wrote results and methods related to that analysis, and contributed to the revision process.

Chapter 2: Mechanics of ciliary beating[1]

Louis G. Woodhams[1], Dario Cortese[2], Philip V. Bayly[1], Kirsty Y. Wan[2]
[1] Mechanical Engineering and Material Science, Washington University in St. Louis, MO, United States
[2] Living Systems Institute & Department of Mathematics, University of Exeter, Exeter, United Kingdom

2.1 Motivation and background

High-resolution cryo electron tomography (cryo-ET) has illustrated the structure of the *Chlamydomonas* cilium in exquisite detail, yet the mechanism of beating remains incompletely understood. In particular, the detailed explanation of how the forces produced by distributed dynein motor proteins generate propulsive, wavelike oscillations remains elusive. Moreover, it is not yet clear how cells are able to control and modulate these oscillations in real-time to change waveform or swimming direction in their response to behavioral cues. The question of generation and control of ciliary form is challenging in part because it lies at the interface of biology, physics, engineering, and mathematics. The following chapter focuses on illuminating this interface and summarizing the current state of knowledge with the goal of motivating continued interdisciplinary efforts in this field.

Ciliary oscillation has been investigated and progressively elucidated in a series of studies by biologists, biophysicists, and engineers. Pioneering theoretical work by Machin introduced the equations of slender beam bending, powered by waves of contractility. Machin's calculations demonstrated the existence of active force-generating components along the cilium to account for the capacity to sustain large amplitude oscillations, prior to experimental proof revealing these components to be dyneins [21]. His work was followed by Brokaw, who replaced local

[1] Material in this chapter is taken from [37] L. G. Woodhams, D. Cortese, P. V. Bayly, and K. Y. Wan, "Chapter 12: Physics and mechanics of ciliary beating," in *The Chlamydomonas Sourcebook*, vol. 3, S. Dutcher Ed., Third ed.: Elsevier, 2022 (in press). See section 1.5 *Statement of contributions*.

contractility with an active bending moment that is produced by shear force between sliding filaments [30]. Lubliner and Blum introduced the full 9+2 structure of the axoneme into the governing equations [40]. Hines and Blum followed the general approach of Brokaw, deriving a "single filament" model of ciliary waves that included properties (shear resistance) of the original composite structure [41].

The idea that dynein activity on different sides of the axoneme is switched on and off periodically, or modulated asymmetrically so that one side alternately bends the axoneme actively or is bent passively, has been pervasive since it was suggested by Satir [42]. The models of Brokaw as well as Hines and Blum demonstrated that feedback, in the form of modulation of dynein activity by curvature (including a time delay), sufficed to create wavelike oscillations in the axoneme. Although their simulations showed curvature feedback to be plausible, there was no evidence to directly support the assumption. Further models by Brokaw demonstrated sliding-control (regulation of dynein by interdoublet sliding) could also produce oscillations. Lindemann introduced the "geometric clutch" hypothesis, that spacing between doublets (or the induced tension on the dynein arms opposing separation) could regulate dynein [43]. Riedel-Kruse and colleagues promoted the plausibility of sliding-control [31], while other work has re-ignited interest in curvature control as a possible means of regulating dynein activity [44, 45]. In short, neither a precise biophysical mechanism of dynein regulation nor the general phenomenon of switching has been convincingly demonstrated to date.

Cryo-ET studies [6] showed that the distribution of dynein conformations appears to be different on different sides of the axoneme, in regions that correspond to principal and reverse bends. However, in cryo-ET it is not clear if the different conformations are the cause of, or a result of, bending. Recently, Bayly and co-authors [32] proposed that dynein regulation may not be

essential, and that a dynamic instability, like fluttering of a flag, can drive oscillations even while dynein activity is steady. This phenomenon has also been illustrated and extended in studies of single filaments under external axial loads [46, 47]. Later sections of this chapter (sections 2.2 and 2.3) will explore the basic mechanics and physical principles that underlie each of the current models of ciliary dynamics introduced above.

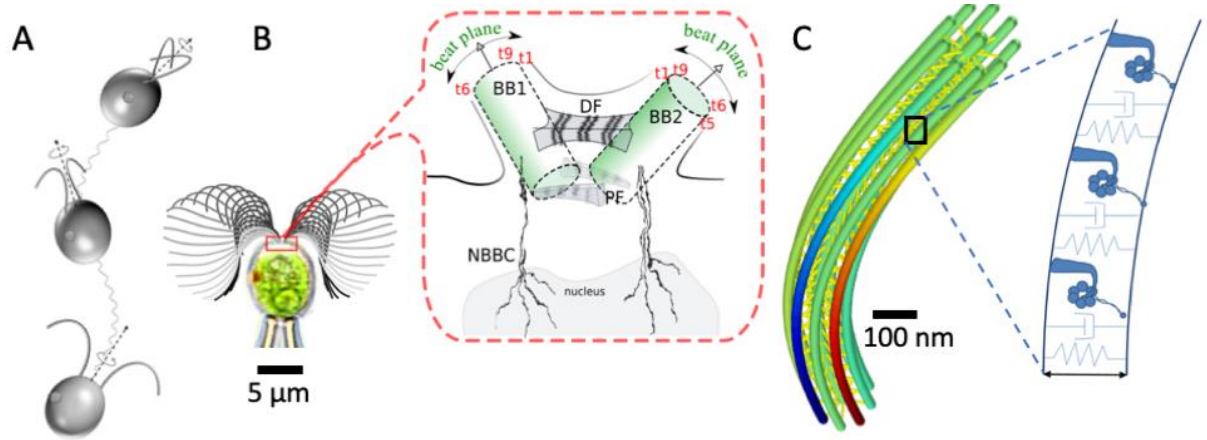

Figure 2.1: The multiscale physics and mechanics of ciliary beating in Chlamydomonas. (A) Motile cells swim along helical trajectories by actuating a pair of nearly identical cilia, which beat on slightly tilted planes. (B) The cilia, distinguished by their position relative to a unique eyespot, are coupled by cytoskeletal structures that promote synchronization, and relay signals during tactic behaviors. (C) The ciliary axoneme is a highly conserved structure comprising microtubule doublets and a central pair complex. The coordinated activity of dynein motors (inset) causes the structure to bend and produce propulsive waves.

2.2 Fundamental principles and concepts

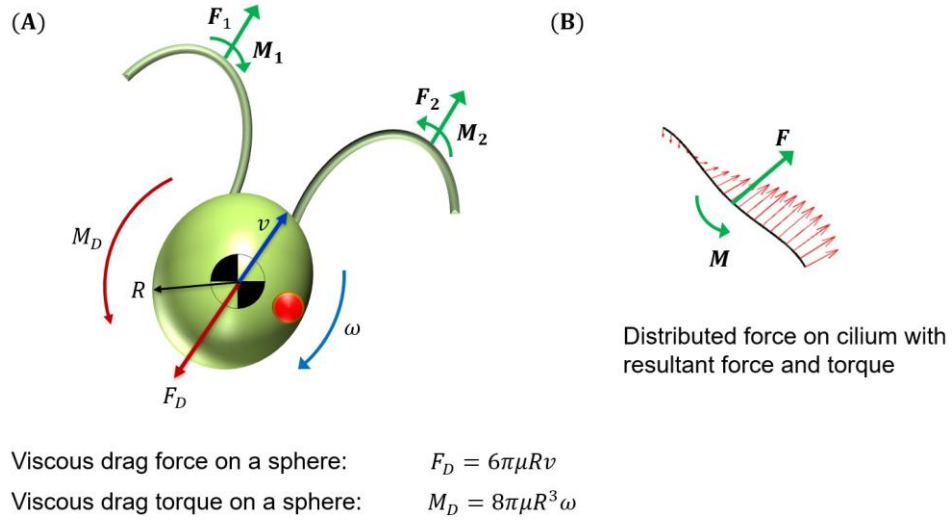

Figure 2.2: Viscous forces on a Chlamydomonas cell. (A) Equations of motion for a Chlamydomonas cell are derived by balancing viscous forces and torques on a cell body ($\boldsymbol{F}_D$, $\boldsymbol{M}_D$) and resultant forces and moments on the cilia ($\boldsymbol{F_1}, \boldsymbol{M}_1, \boldsymbol{F}_2, \boldsymbol{M}_2$). Here $\boldsymbol{v}$ is the velocity of the cell, $\boldsymbol{\omega}$ is the angular velocity, and R is an effective cell radius. (B) Resultant forces and torques on the cilium are calculated by integrating the local distributed viscous drag forces along the length of the cilium.

This section briefly summarizes the basic principles of physics and mechanics that underlie ciliary motion. Books by Howard [48], Boal [49], and Jacobs et al. [50] provide extensive and thorough treatments of cellular and cytoskeletal mechanics.

2.2.1 Useful Definitions

Vector: A physical quantity with both magnitude and direction, such as force or velocity (Fig. 2.2). Vectors can be compactly described in terms of their Cartesian components. We denote vectors by bold font; the same variable in regular font typically indicates the magnitude of that vector.

Kinematics: The motion of the cell body and the shape of the cilium, considered without regard for what creates the motion, comprise their *kinematics*. Kinematic variables include position, velocity, acceleration, angle, and curvature.

Kinetics: The causes and effects of forces and torques on ciliary beating and cell motion are described by physical *kinetics*. Kinetic variables include force, torque, work, and power.

2.2.2 Key physical quantities and units

Kinematics

Position: The location of a cell body or component is described with respect to a reference point in space, or on the body. Position can be written as a vector, $\boldsymbol{x}$.

Velocity: The rate of change of position. Velocity is a vector, $\boldsymbol{v} = \frac{\mathrm{d}\boldsymbol{x}}{\mathrm{d}t}$. Speed is the magnitude of velocity. Velocity of *Chlamydomonas* cells or cilia is typically expressed in units of μm/s.

Acceleration: The rate of change of velocity, $\boldsymbol{a} = \mathrm{d}\boldsymbol{v}/\mathrm{d}t$. In cell mechanics, acceleration is typically much less important than velocity because the force needed to overcome inertia (resistance to acceleration) in biological systems at cellular scales is much less than the force needed to overcome viscosity (resistance to velocity).

Angle: The difference in direction of two vectors, or between a vector and a reference axis. Angle can be expressed in degrees or radians (1 rad = $\frac{180}{\pi}$ degrees ≈ 57 degrees). The ciliary waveform is compactly described by the angle of the cilium as a function of distance from the base.

Curvature: Curvature, κ, of the cilium is the change in angle, ψ, with distance, s, along the cilium, $\kappa = \frac{\mathrm{d}\psi}{\mathrm{d}s}$. Appropriate physical units of curvature are rad/μm.

Kinetics

Force: An interaction that, if unopposed, causes a change in the velocity of a body. A body can have constant velocity if no forces act on it, or if forces are equally balanced, like propulsion and

drag. Force is generally expressed in units of Newtons (N): 1 N = 1 kg-m/s^2. In *Chlamydomonas*, forces are more usefully expressed in units of piconewtons (pN): 1 pN = 10^{-12} N.

Torque (or moment): The measure of how force changes the rotation of a body. Torque is produced by a component of force at a distance from an axis of rotation, in the direction of rotation. Units of torque are N-m; torques relevant to *Chlamydomonas* are better expressed in terms of pN-μm.

Work: Energy transferred to or from a body by the application of force as the body displaces. The unit of work is the joule (1 J = 1 N-m). In cell mechanics the units of attojoules are appropriate (1 aJ = 1 pN-μm).

Power: The rate at which work is done. The units of power are watts (1 W = 1 J/sec); power developed by cilia or cells can be expressed in attowatts (1 aW = 1 pN-μm/sec).

2.2.3 Physical principles

Newton's laws: The net force (the sum of all the force vectors) on a body equals the rate of change in its linear momentum. In a body with constant mass the net force equals the mass multiplied by the acceleration of the mass center. The net torque on a body equals the rate of change in its angular momentum. In cell mechanics, active forces and torques are required to balance forces of elastic and viscous resistance; the residual net force and torque needed to accelerate a cell or a cilium (i.e., inertial effects) are negligible at their respective length and time scales.

Energy balance: Energy is not created or destroyed, but can be transferred between parts of a system, or lost to its surroundings (dissipation).

2.2.4 Properties and interactions

Elasticity (stiffness)

Elastic components resist deformation, and store as potential energy the work done on them as they are deformed.

Flexural modulus (bending stiffness): Slender elements like beams bend in response to applied loads. The flexural modulus, EI, describes the elastic resistance to bending. In a uniform slender beam, energy of bending depends on the flexural modulus and the curvature, κ, of the beam-like element: $\frac{1}{2}\int_0^L EI\kappa^2 ds$. The bending moment required to produce the curvature is $M = EI\kappa$. The flexural modulus is a product of the Young's modulus, E (units N/m^2 or Pa), an intrinsic property of the material, and the area moment of inertia, I (units m^4), a property of the shape of the cross-section of the beam. Units of EI in cell mechanics are pN-μm^2 (1 pN-μm^2 = 10^{-24} N-m^2).

Persistence length: An alternative measure of bending stiffness, that describes the loss of correlation with length of a slender elastic element, due to thermal effects (Fig. 2.3) [51]. The persistence length is related to flexural modulus by Boltzmann's constant,k_B and temperature, T:

$L_p = \frac{EI}{k_B T}$

Axial stiffness: Elastic resistance to extension or compression is described as axial or "spring" stiffness. Radial spokes, nexin links, and doublets have axial stiffness. The simplest model assumes that force is a linear function of extension or compression: $f_k = k\Delta x$, where k is the stiffness (units of N/m, pN/μm or pN/nm) and Δx is the change in length. A slightly more sophisticated model is the tensile stress-strain relationship in a bar: $\frac{P}{A} = E\frac{\Delta L}{L}$, where stress is the

axial force P per unit cross-sectional area A and strain is the change in length normalized by the original length L. In this model the equivalent spring stiffness is $k = \frac{P}{\Delta L} = \frac{AE}{L}$.

Shear stiffness (elastic resistance to interdoublet sliding): Elastic resistance to sliding is commonly attributed to the stretching of links at an angle to the doublets. A simple, linear force-displacement relationship is sometimes assumed: $f_\tau = k_\tau u$, where k_τ is the shear stiffness and u is the relative axial displacement of the two doublets. These definitions are clear and precise for parallel, straight doublets, but in three-dimensional, curved doublets, the elastic forces that resist sliding are more complicated. In cilia, shear stiffness is given as stiffness (pN/μm) per unit length, with units pN/μm^2.

Dissipation

Viscosity: The resistance of a fluid to flow; specifically, the ratio of shear stress (force per unit area) to the rate of shear deformation (change in shape). Units of viscosity, μ, are Poise (1 Poise = 0.1 N-s/m^2=0.1 Pa-s) or centipoise (1 cP = 0.001 Pa-s = 0.001 pN-s/μm^2).

Drag: The force exerted by a viscous fluid on a moving body is the drag. The drag on a sphere of radius a can be determined when the inertia of the fluid can be neglected (at low Reynolds number): $f_D = 6\pi a^2 v$.

Resistive force coefficients: At low Reynolds numbers, the vector force per unit length on a cilium can be approximated by normal, $q_N = -c_N v_N$, and tangential, $q_T = -c_T v_T$, force components that are each proportional to normal, v_N, and tangential, v_T, velocity components. c_N and c_T are known as *resistive force coefficients*, and have units pN-s/μm^2

Friction and dissipation: Often elastic deformation (storing energy) is accompanied by dissipation. A common modeling strategy is to add a rate-dependent component (a "dashpot") to any elastic element (i.e., a spring). For example, axial force in a link with elasticity and dissipation could be modeled as: $f_k = k(\delta - \delta_0) + c\dot{\delta}$.

2.2.5 Active forces

Motor protein (dynein) behavior: Each dynein molecule uses hydrolysis of ATP to convert chemical energy into mechanical work, exerting a force as it 'steps' throughout each cycle. The molecular mechanism is described elsewhere [52, 53]. Here we summarize key mechanical features:

Dyneins exhibit force-velocity relationships characterized by decreasing force as velocity increases. The 'stall' force is the force developed at zero velocity, and the free-stepping speed is determined by the stepping rate at zero load. Different dynein classes exhibit different force-velocity relationships [29, 54-57].

Axonemal dyneins attach via their tail domain to the A-tubule (A-MT) and transiently by the microtubule binding domain (MTBD) at the end of the stalk to the B-MT[58]. Normal, forward stepping of the dynein motor moves it toward the minus end (proximal) of the B-MT[59], applying a tipward force on the B-MT. *In vitro* studies have shown that cytoplasmic dynein also can step 'backward' under an applied load in the opposite direction [60].

As the dyneins on the A-MT on doublet N exert a tipward force on the B-MT of doublet N+1, they also exert normal or 'transverse' forces between the doublets [61]. These normal forces tend to pull the doublets together or push them apart. Passive elements resist the dynein

forces, maintaining and modulating doublet separation. The result is a net bending moment (torque) [30, 41].

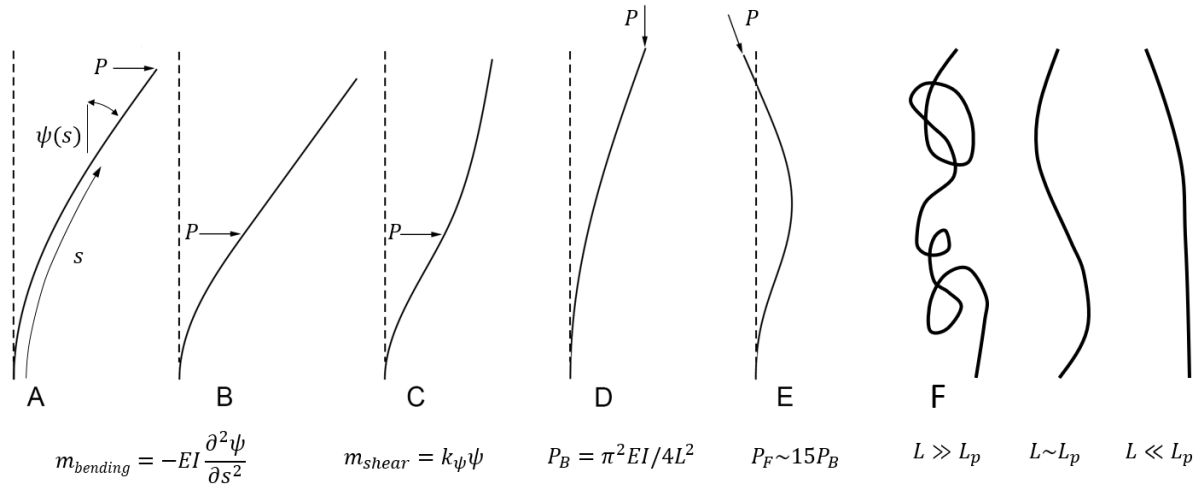

Figure 2.3: Beam bending. (A) A simple beam, fixed at its base (cantilevered), subjected to transverse tip load, P. The shape can be described by the tangent angle, ψ, which is a function of arc length, s. (B) A simple beam subjected to a transverse load at an intermediate distance along its length. The equation below states that the second derivative of ψ is proportional to the elastic bending moment per unit length. Because there is no moment distal to the applied load, there is no change in curvature from the point of application to the tip of the beam. (C) Internal elastic shear resistance, like that observed in axonemes, creates a counterbend distal to the applied load. The equation below the figure states that the elastic shear moment per unit length is proportional to ψ. (D) A compressive axial end load leads to Euler buckling when the load exceeds a critical value, P_B, given by the equation below the figure. (E) A 'follower' load tangent to the beam end leads to dynamic instability known as flutter when a critical load, roughly 15 times the buckling load in this case, is exceeded. (F) Persistence length is a measure of beam bending stiffness that describes the beam's conformational response to thermal excitation. Beams with length far exceeding the persistence length tend to be highly distorted by thermal effects, whereas beams with length smaller than the persistence length are less affected.

2.2.6 Basics of beams: bending, shear, buckling, and flutter

Slender filaments can be modeled as Euler-Bernoulli beams in which the curvature is proportional to the internal bending moment: $M = EI\kappa$. See [62, 63] for details. Several beam loading cases are shown in (Fig. 2.3). A simple beam fixed at its base with an applied transverse tip load, P, has an internal bending moment that diminishes in magnitude along its length: $M(s) = P(L - s) = EI\frac{\partial\psi}{\partial s}$. Note that we distinguish between the internal elastic bending

moment, $M(s)$, defined by standard beam conventions, and the (counterclockwise positive) applied moment per unit length, $m(s)$. Beam angle and small-deformation transverse displacement are obtained by successive integrations. A simple beam with an applied transverse point load shows no bending distal to the point of application as there is no bending moment in this region. In contrast, a beam composed of multiple filaments with shear resistance between those filaments exhibits a counter-bend [30, 64-66]. This counterbend is due to the applied moment from elastic shear, $m_{shear} = k_\psi \psi$. Deformations may be obtained by integrating the applied moment/unit length, $m_{applied} = -EI \frac{\partial^2 \psi}{\partial s^2}$, twice to obtain filament angle as a function of arc length.

Microtubules (MTs) are often treated as inextensible in mathematical models as axial deformations are insignificant compared to transverse deformations [67]. This has led many researchers to believe that axial loads could be safely ignored in models of ciliary beating. However, when beams are subjected to axially oriented loads, instabilities and large deformation geometric effects may emerge [61, 68-70]. Static instability (buckling) emerges when the transverse stiffness of a filament is effectively diminished by compressive axial loading until the undeformed conformation becomes unstable. Buckling loads for slender beams are given by Euler's critical load, shown in (Fig. 2.3D). To understand the critical buckling load, imagine adding small weights to the tip of a slender, flexible, *vertical* rod that is fixed at its base. For small weights, the rod will remain vertical. However, once the weight exceeds a critical value, the vertical position becomes unstable, and the rod will droop over to one side or another.

Dynamic instability (flutter) can emerge in cases where the orientation of a sufficiently large axial load remains tangential to the filament under deformation (Fig. 2.3E); this is called a

‘follower load’. Follower loads can add energy to a system by re-orienting their direction of application as the system deforms; growing oscillations can occur if this allows the forces to do positive work on the system each cycle. As a macro-example, flutter instability is responsible for the violent oscillations of a hose above a critical flow rate. This type of dynamic instability has been proposed as a mechanism for oscillations in cilia and biological filaments in recent years [32, 46, 47].

2.3 Mechanics of waveform generation

Chlamydomonas cilia exhibit two different kinds of propulsive waveform; they can use a forward, ‘breaststroke’ motion in which the cilia curve away from the longitudinal axis of the cell body, and a ‘reverse mode’ in which the mean curvature of each cilium, averaged over the beat, is close to zero (Fig. 2.4). In each of these beating modes, the movement of the cilium lies mostly within a plane, but there is a small out-of-plane component (Fig. 2.1). These beating patterns may be quantified by temporal and spatial characteristics including beat frequency and waveform curvature. See Table 2.1 for a summary of properties.

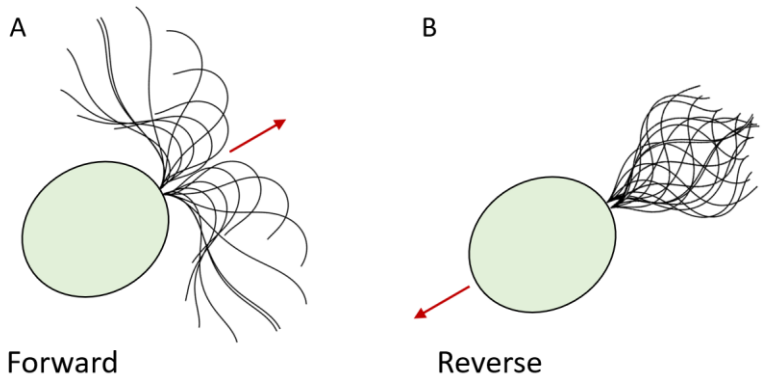

Figure 2.4: Chlamydomonas forward (A) and reverse (B) waveforms, over one beat cycle. Arrows show the direction of cell movement (contributed by M. Bottier).

2.3.1 Waveform characteristics

Table 2.1 - Properties of wild-type *Chlamydomonas* cells

Property	Estimated Value	References
Chlamydomonas swimming speed (average)	50-200 μm/s	[71-74]
Chlamydomonas swimming speed (peak instantaneous)	500-900 μm/s	[71, 73]
Beat frequency	50-70 Hz (breaststroke) 65-100 Hz (photoshock)	[29, 35, 75]
Rotational velocity (axial)	1-2Hz	[76]
Cell body diameter	7-10 μm	[8]
Cell body aspect ratio	0.66-0.94	[8]
Cilium length	10-14 μm	[29, 35]
Propulsive force / cilium (peak)	3-23 pN	[73, 77-79]
Average power / cilium	3.2-6.6 fW	[8, 71]

Beating frequency

Wild-type *Chlamydomonas* beat frequency is typically in the range of 50-70Hz for the forward, 'breast-stroke' mode, whereas beat frequency in the symmetric reverse mode is typically higher, in the range of 65-100Hz [26, 29, 35]. It should be noted that many of the studies of cilia motion in *Chlamydomonas* are conducted on uniciliate mutants such as *uni1* which, lacking a second cilium, tend to rotate in place rather than swim out of the field of view of the microscope.

Ciliary beating shape (kinematics)

Ciliary shape is conventionally described by the tangent angle of the cilium, ψ, relative to some axis, often the tangent to the cilium base as this is a convenient reference. Ciliary tangent angle is a function of arc length, *s*, and time, *t*. The *x* and *y* coordinates of the cilium can then be obtained by integrating the ciliary tangent angle over the length of the cilium as in (Fig. 2.5). It is often

convenient to represent local forces and velocities in terms of their components in the local tangent, $\boldsymbol{T}$, and normal, $\boldsymbol{N}$, directions.

A

$$x(s,t) = x(0,t) + \int_0^s \cos\big(\psi(\bar{s},t)\big)\, d\bar{s}$$

$$y(s,t) = y(0,t) + \int_0^s \sin\big(\psi(\bar{s},t)\big)\, d\bar{s}$$

$$\kappa(s,t) = \frac{\partial \psi(s,t)}{\partial s}$$

B

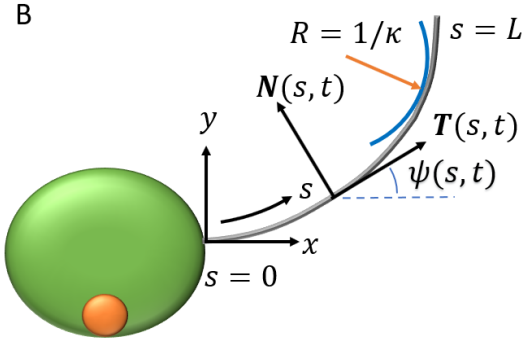

Figure 2.5: Kinematic equations of the Chlamydomonas cilium. (A) Parameters of the cilium shape depend on arc length, s, and time, t. Cartesian coordinates x and y are obtained by integrating the cosine and sine, respectively, of the tangent angle, ψ, along the arc length, s, of the cilium. Local curvature, κ, is the derivative of tangent angle with respect to arc length. (B) A Cartesian coordinate system is aligned to the base of a trans cilium. Arc length, s, is equal to zero at the base and L at the tip of the cilium. ψ is the angle between the local tangent vector, $\boldsymbol{T}$, and the x axis. The local normal vector, $\boldsymbol{N}$, is perpendicular to $\boldsymbol{T}$ and points in the direction of curvature. The radius, R, of an arc (blue line) with curvature equal to that of an arbitrary point along the cilium is represented by the orange arrow line. The radius of curvature, R, is inversely proportional to curvature, κ.

An important characteristic of ciliary shape is the curvature, κ. Curvature is the derivative of the tangent angle, ψ, with respect to the arc length, s, and is equal to the reciprocal of the radius of curvature, R (Fig. 2.5). Two opposite directions of planar curvature occur in the 'principal bend' and 'reverse bend'. In *Chlamydomonas*, the principal bend is the curvature responsible for the effective stroke and bends the cilium outward toward the 5-6 doublets. The reverse bend curves the cilium in the opposite direction, toward doublet 1 [18]. How these dynamically changing bends are created by the interaction of active and passive structural elements within the cilium is the fundamental question in ciliary mechanics.

Symmetry

Chlamydomonas cells typically swim in a ‘breast-stroke’ motion, where each cilium pulls the cell forward through its fluid environment with a waveform that is biased in curvature to the outside of the cell. In response to certain stimuli, such as bright light, *Chlamydomonas* cells undergo photoshock and enter a ‘reverse mode’ in which the cilia beat in a symmetric ciliary pattern to propel the cell backward. In this mode the average tangent angle of each cilium aligns roughly with the anterior-posterior axis of the cell [26].

Effects of mutations

Table 2.2: A few selected mutations and their effects

Mutant	Phenotype	Effect on beating	Phytozome Name/ Chlamydomonas Resource Center	References
uni1	Assembles primarily one cilium	Cell rotates in place	CC-1926	[80-83]
uni2-2	Assembles zero, one, or two cilia	50% of cells rotate in place	Cre09.g394695/ CC-4161	[82, 83]
uni3-1	Assembles zero, one, or two cilia	50% of cells rotate in place	Cre03.g187350/ CC-4179	[82]
oda2 *oda1*	Outer dynein arm deficient	Decreased beat frequency	Cre11.g476050/ CC-2231 Cre16.g666150/ CC-2229	[8, 28, 29, 84, 85]
ida1/pf9	I1/f Inner dynein arm deficient	Diminished waveform amplitude	Cre12.g484250/ CC-3904	
ida4	a, c, d, and DHC11 inner dynein arm deficient	Diminished waveform amplitude	Cre12.g494800 CC-2670	[86]
mbo1 *mbo2* *mbo3*	Lacks beak-like projections in doublets	Swims backwards only	CC-2376 Cre09.g41655 CC-2377 CC-2378	[9, 87]
pf1	Radial spokehead deficient	Reduced motility	Cre05.g242500 CC-1024	[88-91]
pf14	Radial spoke deficient;	Reduced motility	Cre06.g291700 CC-1032	[88-90, 92]
pf18	Central apparatus deficient	Paralyzed	CC-1036	[93]
agg1	Altered phototaxis	Negative phototaxis	Cre13.g590400/ CC-1328	[94, 95]
ptx1	Altered Phototaxis	Abnormal ciliary synchrony	CC-2894	[96-99]
vfl1 *vfl2* *vfl3* *asq1 asq2*	Lack of bicililate coordination and slow swimming	Abnormal ciliary synchrony	Cre08.g372900/ CC 1388 Cre11.g468450/ CC 2530 Cre06.g279900/ CC 1686 --- Cre09.g39488	[100-103].

Mutations in *Chlamydomonas* are crucial to our understanding of cilia biology, and for testing hypotheses about ciliary beating and cell behavior (Table 2.2). The uniciliate mutant *uni1* lacks a second cilium to balance the moment (torque) applied by its single, usually *trans*, cilium [81]. As a result, this mutant spins in place; this is ideal for microscope observation as the organism tends to remain within the field of view without the need for trapping or fixation by micropipettes. Recent studies of *Chlamydomonas* ciliary beating have made use of *uni1* as their 'wild-type' model organism, crossing this mutant with other mutants to observe the effects of those mutations.

Brokaw and Kamiya showed that *Chlamydomonas* mutants with impaired or missing outer dynein arms had a decreased beat frequency but waveforms similar to those of wild-type cells, whereas inner dynein arm deficiencies lead to subdued waveforms at close to wild-type frequencies [29]. The interactions of these defects with viscous media were explored in several studies [28, 57, 84]. The effect of select axonemal mutations are summarized in (Fig. 2.6).

Other mutants include strains that swim only in backward mode (*mbo*), that have reverse phototaxis (*agg1)*, and strains with cilia that lack the radial spoke structures (*pf14*). Detailed discussion of the effects of genetic mutations on the beating behavior of *Chlamydomonas* cells can be found in Chapters 4, 6, 8, and 17 of [37].

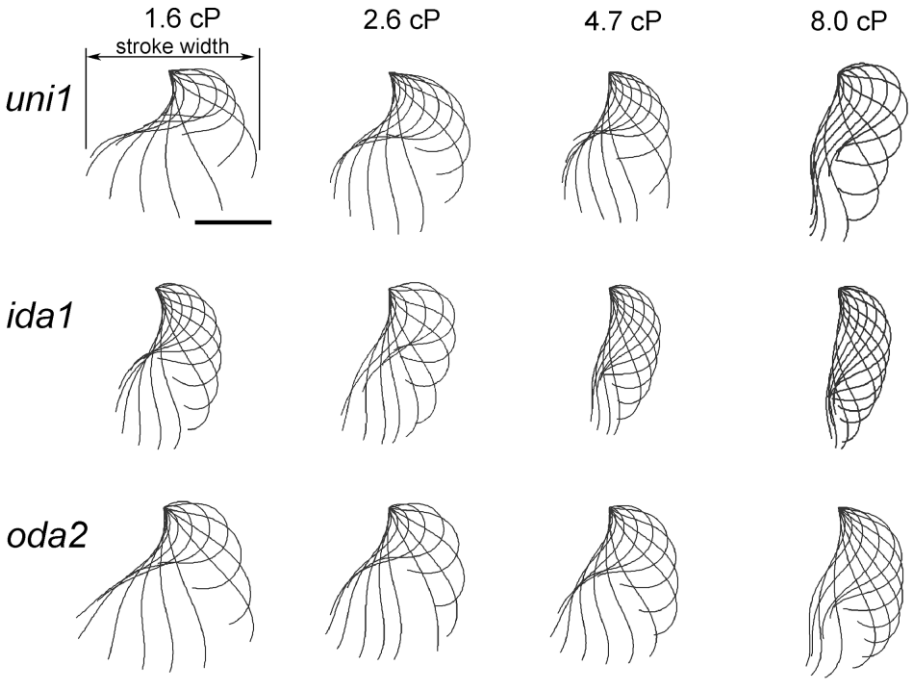

Figure 2.6: Each column shows results at a specific viscosity; each row corresponds to a specific mutant. Ciliary waveforms are shown at intervals of 1/12th period; scale bar 5 µm. Reproduced from [28] with permission.

Effects of viscosity

At the scale of *Chlamydomonas* cilia, the viscous resistance of the surrounding fluid medium is much greater than the forces needed to overcome inertia of the cell and surrounding fluid [104]. The reversibility of motion in viscous fluids means the waveform must be asymmetric about the axis normal to the direction of swimming: the *Chlamydomonas* cell would not swim forward if the power and recovery strokes were mirror images of each other, and would not swim backward (in photoshock) if the waveform did not propagate from base to tip [105, 106].

The Reynolds number is a dimensionless quantity that measures the relative influence of inertia to viscosity in a fluid system ($Re = \frac{\rho v D}{\mu}$), where ρ is the density of the fluid, v is a characteristic velocity, D is a characteristic dimension such as cilium diameter, and μ is the dynamic viscosity of the fluid. In cilia, the Reynolds number is usually in the range of 10^{-5} to 10^{-3} indicating the

dominance of viscous over inertial effects. This allows the modeling of viscous forces on the cilium by simple resistive force theory, in which force is linearly proportional to velocity (Fig. 2.7) [107, 108]. In large deformation models of ciliary beating, a different coefficient is given for resistance to motion tangent and normal to the ciliary axis. Resistance to cell body translation and rotation can be treated similarly using Stokes' Law (Fig. 2.2) [8].

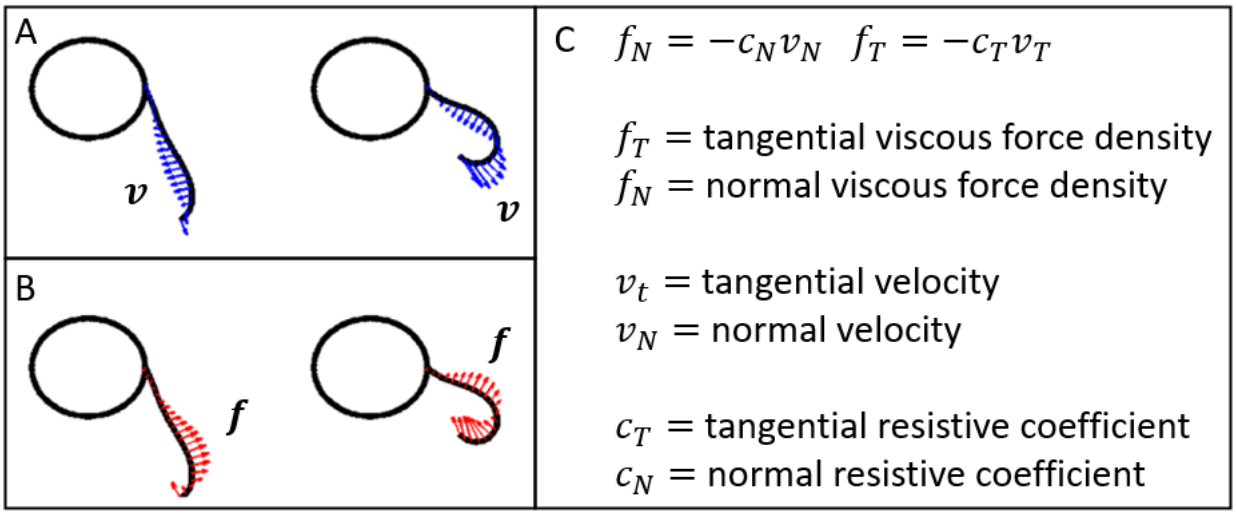

Figure 2.7: Resistive force theory applied to the cilium. (A) Local velocity vectors are shown along the length of the cilium. (B) Local force vectors are proportional in magnitude and opposite in sense to the velocity vectors above. (C) Normal and tangential components of viscous force, f_N and f_T, on the cilium are proportional in magnitude and opposite in direction to the velocity components, v_N and v_T. The proportionality constants, c_N and c_T, are often called resistive force coefficients. In cilia, the normal resistive force coefficient, c_N, is typically roughly twice the tangential coefficient, c_T.

Brokaw studied the effect of viscosity on spermatozoa waveforms and found that increasing viscosity uniformly decreased beat frequency and bend propagation velocity, and usually decreased waveform amplitude. Curvature of the waveforms either increased or remained constant with increased viscosity [27]. Yagi and coauthors as well as Wilson and coauthors studied effects of increased viscosity on *Chlamydomonas* waveforms [28, 57]. Yagi and coauthors found that swimming velocities greatly decreased for *Chlamydomonas* cells in higher

viscosity fluid and that this was especially true for the inner dynein arm deficient mutant *ida9*. The *ida9* mutant produced far less propulsive force than wild-type cells at higher viscosities. Wilson and coauthors found that wild-type and inner (*ida1*) and outer (*oda2*) dynein arm deficient mutant waveforms were affected differently by increasing viscosity. Beat frequencies decreased less in *ida1* than in wild type, while *oda2* mutants had consistently low beat frequencies at all viscosities. In contrast, high viscosity decreased the waveform amplitude of *ida1* more than in wild-type or *oda2* cells (Fig. 2.6).

Some cilia operate in fluids with more complex properties such as mucous. Using *Chlamydomonas* as a model system for ciliary beating in mucosal environments, Qin and coauthors explored the effects of non-Newtonian viscoelastic fluid properties on the beat dynamics. Here elastic properties are quantified by the Deborah number De=ωλ, where ω is beating frequency and λ is a characteristic fluid relaxation time. They found that while fluid elasticity increased beat frequency, it slowed cell swimming speed [109]. Viscoelastic effects are further explored using computer simulations in [110].

Another important dimensionless number is the *sperm number*, $Sp = L\left(\frac{\omega c_N}{EI}\right)^{\frac{1}{4}}$, which measures the relaxation timescale of the filament relative to a characteristic timescale such as beat period [70, 111-113]. Here L is the length of the cilium, ω is a characteristic beating frequency, c_N is the normal resistive force coefficient, and EI is the flexural rigidity. Small values of the sperm number indicate filaments that are rigid with respect to the fluid forces. The relaxation timescale is given by the relative contributions of hydrodynamic forces to elastic bending forces $c_N L^4/EI$.

2.3.2 Structure of the axoneme

The microtubule structure of cilia is called the axoneme [17, 18, 114, 115]. The outer structure comprises nine MT doublets arranged in a cylindrical array roughly 200nm in diameter. Looking distally from the base, these are numbered sequentially in a clockwise direction (Fig 2.8) with doublet microtubule (DMT) 1 of each cilium facing the other cilium. A pair of singlet MTs runs along the axial center of the axoneme surrounded by multiple appendages (see Chapter 7 of [116]). The outer doublets are circumferentially interconnected by nexin-dynein regulatory complexes (N-DRCs) (See Chapter 7 of [116]) and are connected to the central pair complex by radial spokes (see Chapter 6 of [116]). Motive force in the axoneme is provided by arrays of the motor protein dynein and associated proteins (Chapter 4 of [116]). Dyneins are arranged in arrays of inner and outer arms and create a one-way, axially oriented sliding force between adjacent MT doublets.

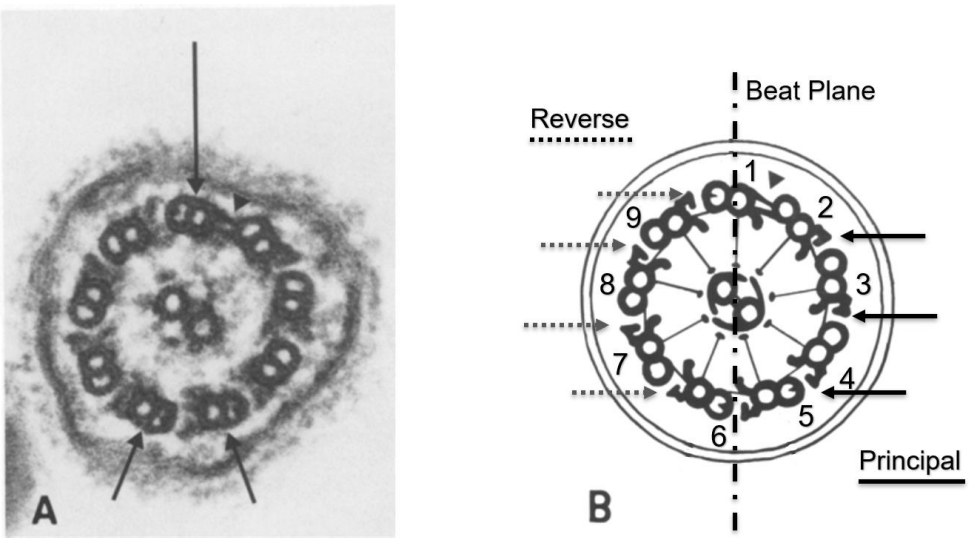

Figure 2.8: Model of bending by alternate-side dynein activation (switching). (A) Electron micrograph of a Chlamydomonas axoneme, showing structural heterogeneities. View is looking from proximal to distal. (B) Schematic showing switching model. In this model, dyneins associated with doublets 2,3,4 produce principal bending (toward doublets 5-6) and dyneins associated with doublets 6,7,8,9 produce reverse bending (toward doublet 1). Figure adapted from [18].

Although the axoneme has a high degree of 9-fold rotational symmetry, there are components that break this symmetry (see Chapter 10 of [116]). These include the central pair and its associated projections as well as the bridge between DMT 1 and 2 found in the *Chlamydomonas* axoneme [18]. These asymmetries may lead to a preferred bending direction in the axoneme and could explain why the *Chlamydomonas* cilium has a largely planar beat [5]. It has been shown recently however that there is a slight non-planar aspect to the beat pattern of the individual cilia, which underlies the organism's helical swimming trajectories [117]. While the basic structure of the axoneme is by now well understood, the physical or material properties of many axonemal components have proven difficult to measure.

Physical properties of the axoneme and its components

Some physical properties of the ciliary structures may be investigated experimentally, but many of the nanoscale structures present are too small to be investigated directly [64, 66, 90, 118-121]. Estimates of some physical properties that can be obtained experimentally are given in Table 2.3. Other values, such as the axial and bending stiffness of radial spokes, have been estimated from the shape and constituents of these nanoscale structures. Properties may also be estimated through inverse modeling, where parameter estimates are made and adjusted to bring the behavior of models of ciliary beating in line with observed behavior[38].

Table 2.3: Relevant physical parameters of the axoneme

Parameter	Estimated Value	Description	References
EI	200-1,000 pN-μm^2	Flexural Rigidity - axonemal resistance to bending due to stiffness of MT doublets	[64-66, 121]
k_T	1,000-2,500 pN/μm^2	Interdoublet Shear Stiffness - resistance to relative sliding of doublets	[66, 90, 122]
c_N	0.001-0.003 pN-s/μm^2	Resistive force coefficient in normal direction	[8]
p	200-1,000pN/μm	Applied dynein force per unit length along doublet	[123]
L	10-14 μm	Length of wild-type *Chlamydomonas* Cilium	[29, 35]
a	180-200 nm	Axoneme outer diameter	[115, 124]
μ	1 mPa-s	Dynamic viscosity of water at 20 ℃	

Active properties of the axoneme

Arrays of dynein motor proteins create a one-way sliding force between adjacent MT doublets to cause ciliary bending. As noted earlier, dynein arms attach to the A-MT of doublet N at one end by a stem structure and transiently attach to the B-MT of doublet N+1 by a tubulin binding domain at end of the dynein stalk. Dyneins then undergo an ATP-driven power stroke and release [52]. This creates the relative longitudinal force between adjacent doublets as well as an applied bending moment due to the distance between the points of application of the opposing forces. The exact mechanics of this motor protein mechanism are a topic of active research, and the binding of individual dyneins is thought to be stochastic [52, 125]. The net result force is probably smoothed by the high number of individual dyneins participating.

2.3.3 Review of models of ciliary beating

The central questions of ciliary beating mechanics revolve around whether there is an active mechanism by which dynein activity is regulated, and if so, what is it? A closely related question is, what are the spatiotemporal patterns of dynein activity during beating? In other words, are

dynein motors switched on and off during beating by some external signal, or do beating waveforms arise simply due to biophysical feedback, or even just mechanical instability in the system?

Much of the work aimed at uncovering the mechanism of ciliary beating has involved creating mathematical models to represent the theories of ciliary beating and assessing their ability to explain observed beating behavior in a manner consistent with physical principles. Any model of ciliary beating must also account for both asymmetric (forward) and symmetric (reverse) waveforms on the same structure (Fig. 2.4).

The conventional wisdom in ciliary mechanics is that in order to achieve bending, dyneins on one side of the axoneme must be active and, at the same time, dyneins on the other side of the axoneme must be passive, or at least less active [126]. A mechanism that would enforce this condition is called reciprocal inhibition [67]. It is often thought that without a net difference in dynein force on either side of the beating plane, dynein activity will lead to a rigor state in which the axoneme is locked in a static, twisted shape [6, 104]. However, some models have shown that concurrent activation need not lead to paralysis; symmetry-breaking instabilities (buckling or flutter) could, in principle, lead to oscillations under steady, balanced dynein loading [32, 38].

Single filament vs. multifilament models

Many mathematical models of ciliary beating reduce the axonemal system to a single filament, treating interactions between dyneins and doublets as an internally generated bending moment that creates curvature in the axoneme. Although multiple filaments may have been taken into account in development of the model, the equations of motion for a single filament are derived and solved [30, 31, 41].

Multiple filament models are more complex and allow the study of geometric interactions between multiple filaments as they dynamically deform. Equations of a 2-filament model are derived and analytical solutions proposed in [32]. Higher-complexity models typically must be solved using numerical solution methods, often implemented in commercial finite-element method software [32, 33, 38, 127].

Equations of motion

Conversion of dynein force to bending

To understand the conversion of dynein activity into curvature, we begin by looking at a reduced two-filament system. This could be viewed as a pair of doublets studied in isolation, but this has also been used as a reduced model of the axoneme [30, 31]. The combination of one-way dynein shear force between two doublets, an applied moment due to interdoublet spacing, passive resistance to interdoublet sliding at the basal attachment, and passive structures resisting interdoublet sliding and separation distributed along the length of filament couple lead to a curvature in the direction of the higher-numbered doublet to which the dynein attaches transiently (Fig. 2.9).

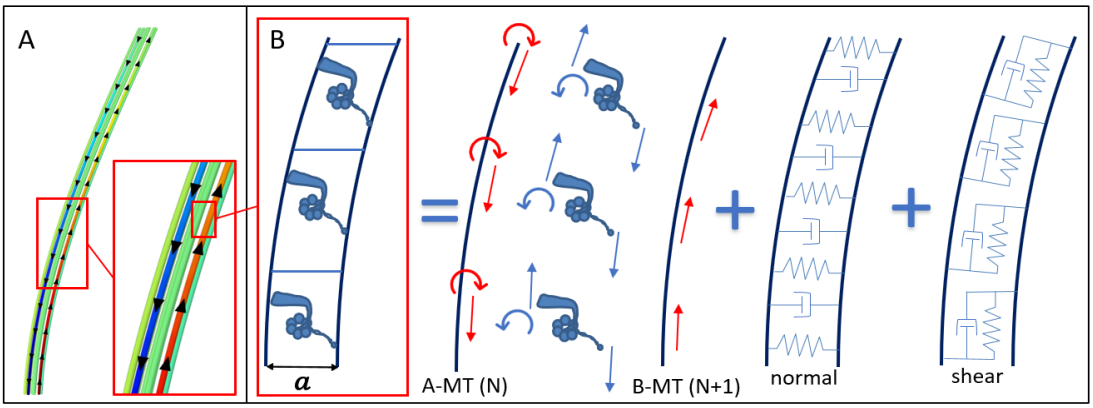

Figure 2.9: (A) Computational (finite-element) model of the 9+2 axoneme. Blue indicates compression, red indicates tension, and arrowheads indicate applied dynein force. Note that the tension and compression of loaded doublets is opposite in sign to what would be caused by passive bending of the structure. (B) Schematic model of a pair of doublets coupled by dynein motors and passive components, such as N-DRCs. Passive elements contribute normal and shear stiffness and damping. Dyneins contribute active shear and bending moments in addition to their passive contributions.

Brokaw showed that in such a model, internal resistance to double sliding (shear stiffness) led to curvature in one direction proximal to an applied shear load (dynein force) and an opposite counter-curvature distal to the applied shear force [30]. The total curvature at any point along the cilium is proportional to a balance of the accumulated bending moment due to internal dynein forces, velocity proportional viscous forces, and internal shear stiffness of structures such as N-DRCs. The spatial derivative of curvature is the balance of the distributed moment densities. For derivations of equations of motion see [30, 32, 41].

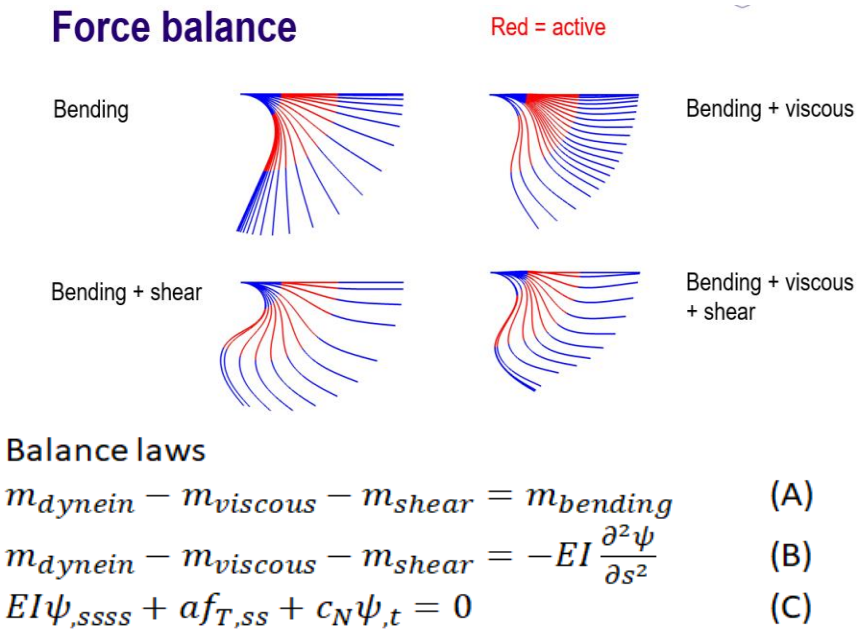

Figure 2.10: (A) General equation of equilibrium for a single filament expressed in terms of the distributed moment densities (torque per unit length); contributions of each term illustrated above. (B) Distributed moment density from elastic bending is proportional to spatial derivative of curvature. (C) Equation of motion for small deflections of a slender filament (flexural modulus EI) in viscous fluid (coefficient of normal resistance c_N), subject to distributed shear force (active and passive), f_T, acting across effective diameter a. Subscript terms after comma represent partial derivatives.

2.3.4 Leading models of cilia oscillation

Mathematical modeling of ciliary beating has been an active area of study since Machin [21], and no single model has gained consensus support. Models are based on the combination of fundamental physical principles with what is known about the geometry, biophysics, and mechanical properties of the cilium and its environment. Here, we summarize what we believe to be representative and relevant models. For other reviews and commentary on models of cilia beating see [67, 128].

Open loop (no feedback) models

Central pair as distributor

Omoto and Kung found that the central pair in the ciliate, *Paramecium*, rotates with respect to the outer doublets during beating [129]. This led to a hypothesis that the central pair acts as a rotational 'distributor' for a dynein regulation signal, where the radial spokes might convey activation signals from the central pair to the dynein motors. It should be noted that the *Chlamydomonas* central pair has also been shown to rotate during beating [130]. Smith and Sale found further evidence for the hypothesis that radial spokes convey activation information to dyneins in the *Chlamydomonas pf14* mutant that lacks radial spokes. While axonemes from this mutant normally showed lower MT sliding velocities than those of wild-type axonemes, sliding velocities could be increased using dynein from axonemes with intact spokes [54].

However, not all motile cilia have central pair microtubules that rotate [114]. In those that do, rotation of the twisted central pair can be explained as a response to, not a cause of, oscillatory bending [131, 132]. Additionally, Omoto and coauthors note that there are motile cilia that lack a central pair [133], which casts doubt on the central pair as distributor theory. They propose that there is a default behavior of dyneins that is modified by interactions between the central pair

and radial spokes to create a more complex beat shape. Smith and Yang proposed a mechano-chemical regulatory system that acts through the radial spokes [134].

Switched inhibition

Lin and Nicastro used cryo-ET with sub-tomogram averaging to determine activation states of dyneins in rapidly frozen sea urchin sperm cells [6]. They found alternate activation states of dyneins on either side of the cilium depending on the direction of curvature. In principal bend, they found conformations thought to be active in dyneins attached to the A-tubules of doublets 2, 3, and 4, and all other dyneins to be in an inactive pre-powerstroke configuration. In reverse bend, they found the active conformations in dyneins attached to the A-tubules of doublets 7, 8, and 9, with inactive configurations in all other dyneins. This study suggests that there is some mechanism for programmed activation or inactivation of dyneins, but what this mechanism might be is still unclear. Nicastro proposes a 'Switch-inhibition' model in which dynein activity states are actively regulated by an inhibitory signal. In this model, dyneins are active by default leading to 'rigor' state of the cilium. Ciliary beating occurs as an alternating principal-reverse inhibition signal propagates distally along the cilium.

Mechanical feedback mechanisms

An argument against the activation of dynein motors being dependent on a signal from the cell body out through the axoneme is the fact that demembranated isolated axonemes (in the absence of the cell body) beat in the presence of ATP [135]. This demonstrates that all the necessary components of ciliary beating are contained within the axoneme itself.

If dyneins have different activation states, the switch that activates, inactivates, or alters dynein function could be some physical feedback mechanism. A number of such feedback mechanisms

have been proposed including interdoublet sliding, interdoublet spacing, and axonemal curvature (Fig. 2.11A-C).

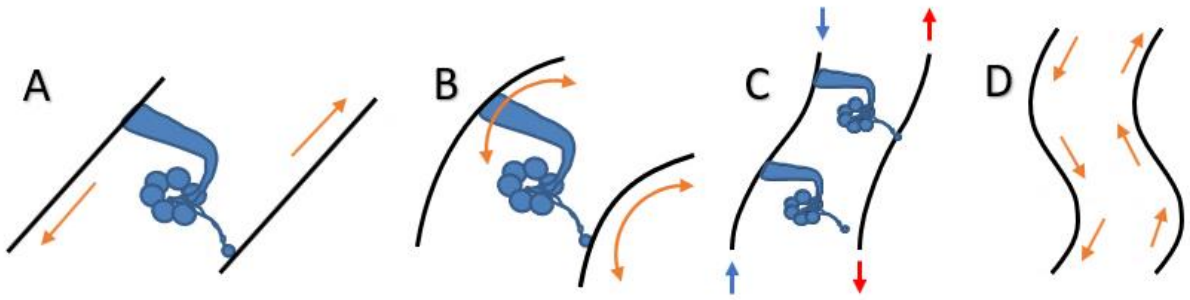

Figure 2.11: Models of mechanical feedback in the axoneme. (A) Sliding control is a hypothesized mechanism in which dynein activity is regulated by a rate or distance of interdoublet sliding. (B) Curvature control involves regulation of dynein activity by the curvature of the doublets to which dynein motors are attached. (C) The interdoublet spacing (geometric clutch) theory proposes that dyneins have greater binding affinity and therefore create more force when interdoublet separation is lower. Arrows indicate internal compressive and tensile forces in the filaments. (D) Dynamic instability is a phenomenon that can arise when steady loads remain tangential as filaments deform, leading to oscillations. Arrows indicate 'follower' forces due to dynein activity.

Sliding control

Different forms of feedback mechanisms based on interdoublet sliding have been proposed. In one version, dyneins actively create sliding force between adjacent doublets until sliding is slowed to a halt by elastic resistance to bending and sliding [136]. At this point dyneins that created this curvature are inactivated or overwhelmed and temporarily unable to bind and opposing dyneins activate to create curvature in the opposite direction. Physically, this can be justified by the hypothesis that dyneins bind more easily when sliding in their preferred direction leading to positive feedback of more bound dyneins and greater applied force until elastic bending resistance is insurmountable. Brokaw suggests that this behavior is similar to a relaxation oscillator [67]. Riedel-Kruse and coauthors explore sliding-control feedback using a complex proportionality constant between dynein force and sliding displacement called the

‘dynamic stiffness’ that allows for positive feedback proportional to sliding rates (negative damping) or sliding displacements (negative stiffness) [31].

Curvature control

The idea that ciliary beating may be driven by curvature feedback dates back to Machin, who proposed active contractile elements along the cilium that were controlled by local curvature [21]. Machin found that a time delay was necessary between curvature feedback and activation of contractile elements; in Machin’s model this delay would need to vary to allow for different beating frequencies. Brokaw extended curvature control to a sliding filament model consisting of two parallel, inextensible filaments, though the equations are reduced to those of a single equivalent filament. Brokaw found using the sliding filament model removed the necessity of a time delay in the feedback mechanism for small deformations but did require nonlinear feedback to produce acceptable waveforms at large deformations [30]. Later work by Brokaw adds a time delay to curvature control on the grounds that, “It is unlikely that any control mechanism for the active process can respond instantaneously to changes in curvature” [137]. Hines and Blum derived the equations of motion for a single-filament model with computational efficiency in mind. They found that a time delay, implemented by making the time derivative of dynein activity proportional to the curvature, was necessary for local bending moments to overcome elastic bending and shear resistance. This time delay was found to be the dominant parameter controlling beat frequency [41]. Recent papers have supported curvature control [138, 139].

Although feedback from curvature to dynein regulation has largely been a mathematical abstraction used in models, Cibert proposed a plausible biophysical mechanism for the idea [127]. When a filament bends, one side of that filament is compressed, and the other side is elongated. Because microtubule doublets are composed of discrete tubulin monomers, when the

doublets bend, the spacing between monomers will be reduced on the compression side and expanded on the elongated side. Cibert proposes that the difference in spatial frequency of these monomers in adjacent doublets may provide a physical mechanism for dynein regulation. Another possible biophysical mechanism for curvature control is the coupling of bending to torsion in the axoneme [138].

Interdoublet spacing or transverse force

Lindemann proposed a mechanism of dynein regulation based on interdoublet spacing. This is often referred to as the 'geometric clutch' hypothesis [43]. The model starts with the assumption that there are active dyneins between doublets 2-3-4 and 7-8-9. The idea is that dyneins may be more likely to bind to the adjacent doublet when the space separating the doublets is below a threshold. The spacing between doublets is modulated by the transverse force or 't-force' between the doublets. Lindemann proposed two sources of t-force: a 'global' component (Fig. 2.11C) due to longitudinal forces on curved filaments (equal to the longitudinal force times the curvature), and a 'local' component due to tension on interdoublet links (a function of local shear displacement). Because the sign of the global t-force will vary with the direction of filament curvature as well as the sense of the longitudinal forces applied to the filament by the dyneins, dynein activity will tend to alternate across the beat plane based on curvature. Computer simulations were able to produce convincing beat patterns based on this model and asymmetric beating was created by setting different binding thresholds on the two sides of the cilium.

Models of the geometric clutch hypothesis have been implemented as numerical simulations of discrete systems of springs and rigid links [43, 56, 124]. Bayly and Wilson derived a set of partial differential equations (PDE) from a continuum model of a simplified axoneme [140]. These PDEs allow for eigenvalue stability analysis of the system and provide insight into aspects

of the model such as spatially dependent dynein behavior and base-to-tip (anterograde) propagation of waves.

Viscoelastic instability

Another theory of the origin of ciliary beating has been proposed in recent years based on dynamic instability without dynein regulation. If dynein forces act tangentially to the doublets, then as the doublets are reoriented under axonemal deformations the direction of the dynein force is reoriented as well. This reorienting force is often called a ‘follower load’ and has been known to lead to oscillations by what is known as ‘dynamic instability’ or ‘flutter’ which is similar to the static instability known as ‘buckling’ [68, 69].

Gadêlha and coauthors investigated the role that geometric nonlinearity could play in ciliary beating and showed that nonlinear instabilities can have important effects on models of ciliary beating, leading to symmetry breaking in waveform and trajectory. Since the model assumed a prescribed symmetric spatiotemporal distribution of dynein force, this study did not investigate instability as a cause of oscillation, but rather as an important contributor to waveform behavior [70].

Bayly and Dutcher first investigated a purely mechanical dynamic instability as a primary cause of oscillation [32]. They showed that steady dynein forces can lead to oscillatory behavior in a two-filament model of ciliary beating. Stability analysis and simulation of the partial differential equations of motion of the two coupled filaments revealed unstable oscillatory solutions that generate propulsive waves. Propulsive waveforms were also found in time-domain simulations of a six-doublet finite-element model. This model is appealing in that it does not require active feedback or dynein regulation in order to produce beating. The model was further explored by

Hu and Bayly in ‘6+1’ and ‘9+1’ systems with additional nonlinearities such as sliding of radial spokes at the central pair attachment [33]. Similar single-filament models explored in [46, 47] also exhibit spontaneous wavelike oscillations under follower loads, although these loads do not represent internal forces that could be produced by dynein activity.

Work by Woodhams, Shen, and Bayly [38] using custom finite-element code has confirmed the emergence of waves from dynamic instability in multi-filament systems with internal, steady dynein activity. This recent work has demonstrated the importance of coupling between the filaments which is physically provided by passive elements such as radial spokes and N-DRCs.

Chapter 3: Generation of ciliary beating by steady dynein activity: the effects of inter-filament coupling in multi-filament models[1]

Louis G Woodhams[1], Yenan Shen[2], Philip V Bayly[1]

[1] Mechanical Engineering & Materials Science, Washington University in St. Louis, St. Louis, MO
[2] Mechanical & Aerospace Engineering, Princeton University, Princeton, NJ

Abstract

The structure of the axoneme in motile cilia and flagella is emerging with increasing detail from high resolution imaging, but the mechanism by which the axoneme creates oscillatory, propulsive motion remains mysterious. It has recently been proposed that this motion may be caused by a dynamic "flutter" instability that can occur under steady dynein loading, and not by switching or modulation of dynein motor activity (as commonly assumed). In the current work, we have built an improved multi-filament mathematical model of the axoneme and implemented it as a system of discrete equations using the finite-element method. The eigenvalues and eigenvectors of this model predict the emergence of oscillatory, wavelike solutions in the absence of dynein regulation, and specify the associated frequencies and waveforms of beating. Time-domain simulations with this model illustrate the behavior predicted by the system's eigenvalues. This model and analysis allow us to efficiently explore the potential effects of difficult-to-measure biophysical parameters, such as elasticity of radial spokes and inter-doublet links, on the ciliary waveform. These results support the idea that dynamic instability without dynamic dynein regulation is a plausible and robust mechanism for generating ciliary beating.

[1] This chapter is reproduced in its entirety from the publication of the same name [38] L. G. Woodhams, Y. Shen, and P. V. Bayly, "Generation of ciliary beating by steady dynein activity: the effects of inter-filament coupling in multi-filament models," *J. R. Soc. Interface*, no. 19, 06/07//2022 2022, Art no. 20220264, doi: https://doi.org/10.1098/rsif.2022.0264.. See section 1.5 *Statement of contributions*.

3.1. Introduction

Cilia are slender organelles that cells use to move fluid or propel themselves. Motile cilia clear mucus from our airways, circulate cerebrospinal fluid in our brain ventricles and play important roles in reproduction and embryonic development. Cilia are highly conserved from single-cell ciliates to humans. Ciliary motion is driven by an active, microtubule-based cytoskeletal structure known as the 9+2 axoneme (Fig. 1). The axoneme is approximately 200nm in diameter and consists of nine outer microtubule doublets (MTDs) arranged in a cylindrical array surrounding two inner microtubule singlets in the central pair complex (CPC) [18, 124]. The CPC is connected to the MTDs by radial spokes (RSs), and adjacent MTDs are circumferentially interconnected by nexin-dynein regulatory complexes (NDRCs). Though the basic structure of the axoneme has been known for decades, details of its intricate architecture are still emerging [6, 19, 141, 142].

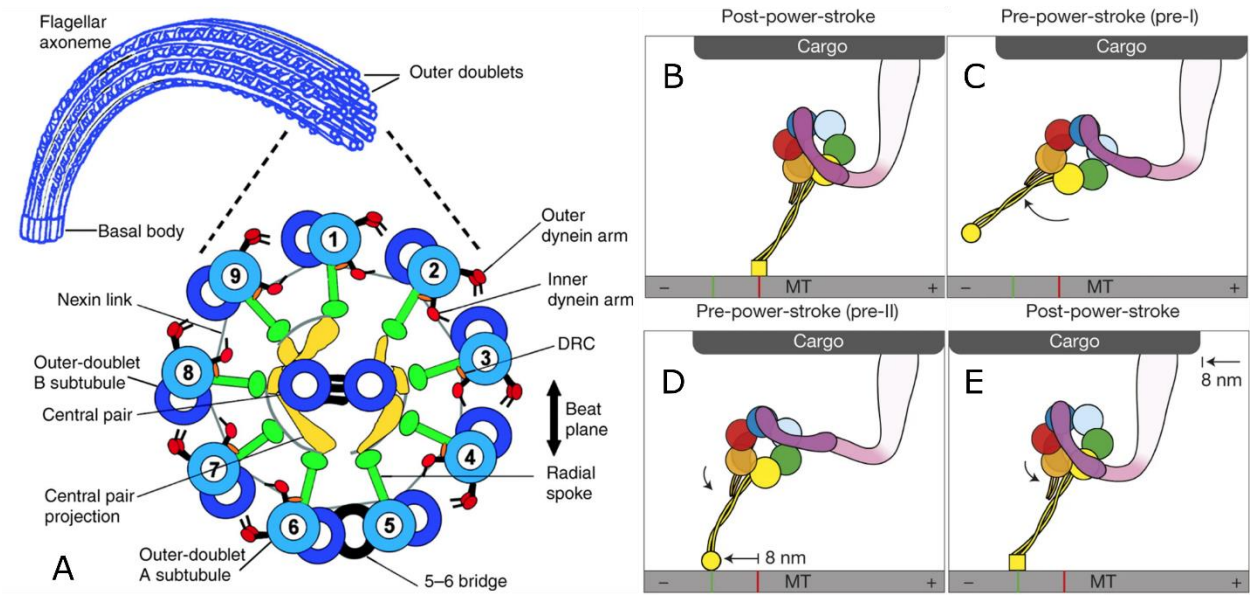

Figure 3.1: (A) Structure of the axoneme. Reproduced from [128]. (B-E) Model of individual dynein arm and interaction with microtubule (MT) reproduced from [143]. Upon binding an ATP molecule, the microtubule binding domain (MTBD) releases and the dynein reconfigures, moving the MTBD toward the minus end of the MT (B-C). Hydrolysis of ATP causes a rebinding of the MTBD to the MT and "power-stroke" reconfiguration of the dynein that pulls the cargo (the A subtubule of the adjacent MTD in the case of axonemal dynein) toward the minus end of the bound MT (D-E). DRC: Dynein Regulatory Complex.

Ciliary beating is driven by the motor protein dynein. Dynein is arranged in arrays of inner and outer arms permanently attached by tail (stem) structures to the A subtubules of the outer MTDs. At the opposite end of each dynein arm is a stalk that terminates in a microtubule binding domain (MTBD) that intermittently attaches to the B subtubule of the adjacent MTD. Dyneins create a one-way sliding force between adjacent MTDs through a cycle of binding, power-stroke, release, and reconfiguration using energy from the hydrolysis of ATP [52, 144]. This one-way sliding force has been shown and measured experimentally [123, 145-148].

Most research on waveform generation has been guided by the assumption that oscillatory motion requires periodic modulation of dynein activity, so that dynein arms on each side of the axoneme alternately produce bending in the corresponding direction [67]. There are multiple

competing theories of dynein regulation. Several theories propose that dynein activity is regulated locally by feedback, either from inter-doublet sliding [31, 136], axoneme curvature [30, 45], or axoneme twist [44]. Some possible biophysical mechanisms have been proposed for such feedback [61, 127], but to date, none have been clearly established. Other studies have postulated regulation of dyneins through a mechanically or chemically distributed signal [6, 133].

Although the assumption of dynein switching or regulation is intuitive, it may not be necessary. Steady forces or fluid flows produce oscillations in many mechanical systems, such as flags or aircraft wings, by a mechanism known as dynamic instability or "flutter" [149]. Dynamic instability occurs when a system departs from equilibrium by way of oscillations of increasing amplitude. In the case of filaments under steady axially oriented loading, the dynamic instability arises as the deflection of the initially perturbed filament reorients the local tangent vector and therefore re-orients the direction of axial load. This phenomenon is well known for the case of a "follower" end load ("Beck's Column") and has also been studied in filaments with distributed follower loads (Fig. 2) [46, 47, 68, 69]. The phenomenon in which an oscillatory system becomes unstable and a periodic solution emerges as a control parameter is varied is called a "Hopf bifurcation" [150].

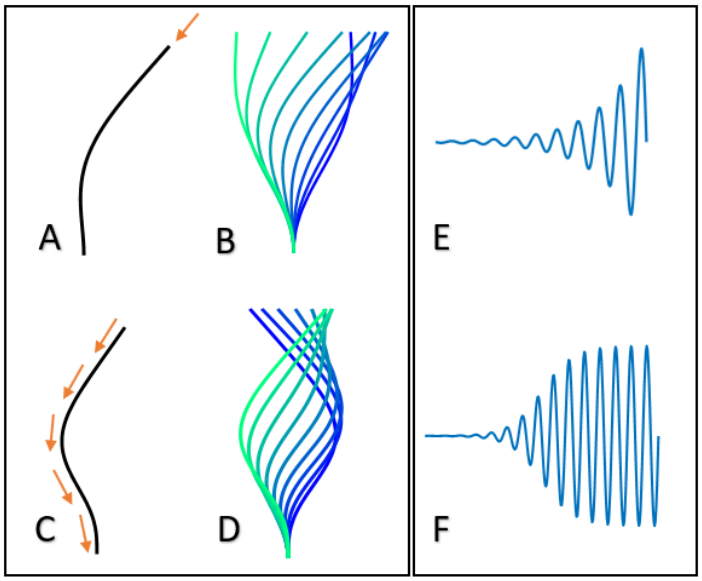

Figure 3.2: (A) A single filament with a follower tip load (Beck's column) provides an example of flutter. (B) Oscillation shapes of the filament under tip load through one half cycle (from blue to green in time). (C) A single filament with a distributed follower load loosely approximates the distribution of dynein along the MTD, but lacks internal force and moment balance. (D) Oscillation shapes of a filament under distributed follower load through one half cycle (from blue to green in time). (E) The eigenvalues of either system, linearized about the straight equilibrium, predict exponentially growing oscillations (flutter) when the applied load is larger than a critical load. This panel shows transverse tip displacement for an unstable oscillation. (F) Tip displacement prediction from a time-domain simulation that includes geometric nonlinearities. Nonlinearities typically limit growth, leading to finite oscillations (limit cycles).

Previous studies have suggested that steady (unregulated) dynein forces can lead to oscillatory, cilia-like beating in models of the axoneme through dynamic instability [32, 33, 47]. In the current work, we develop an improved model and a corresponding system of discrete equations, which can be analyzed to efficiently explore the effects of various biophysical parameters on predicted beating behavior.

This study advances earlier work in three ways: (i) The current model enforces the exact balance of internal dynein forces. The equations in prior models [32, 33] included the approximation that opposing dynein forces between two doublets act parallel to each doublet. While this is approximately true, when doublets are not perfectly parallel, internal forces do not balance

exactly. In the current model, the opposing forces on each active doublet pair are aligned in the direction of their average tangent vector, enforcing balance. (ii) The current model is implemented using a custom finite-element approach to obtain discretized equations governing the motion of multiple coupled doublets. These equations can be analyzed efficiently by finding eigensolutions that identify and characterize oscillatory behavior. (iii) The current model includes a model of dynein arm kinematics that predicts changes to the force and moment produced by the dynein motor under variation of the inter-doublet spacing.

In any mathematical model, the choice of parameters is important. In general, a model is more useful if its predictions are not sensitive to parameter values, i.e. the existence of a certain behavior does not depend sensitively on the precise value of an unknown parameter. The ability of a model to predict trends in behavior in response to changes in parameter is also important. A useful model will predict trends in simulated behavior that resemble trends in observed behavior under analogous parameter variations. The complexity of the axoneme leads to a large set of parameters, and its spatial scale (on the order of nanometers) makes it difficult to determine those parameters. While some parameters may be measured experimentally, others may only be estimated from the size, shape and composition of substructures, and some parameters are not known at all. In this situation, models can be used to estimate plausible values for un-measured or currently unmeasurable parameters.

The custom finite-element implementation of the current model allows us to efficiently explore this large parameter space to find ranges of parameter values that generate propulsive, oscillatory waveforms. It further allows us to investigate the effects of model parameters on behavior. In particular, the aggregate elastic and dissipative properties of the components that couple doublets to each other, either directly or through the central apparatus, such as the RSs and NDRCs, are

difficult to characterize. In this study we investigate the role of these inter-doublet coupling elements in determining the existence and properties of oscillatory waveforms produced by steady, unregulated dynein activity.

3.2. Methods

3.2.1 Modeling the axoneme

Microtubules within the axoneme are modeled as Euler-Bernoulli beams subject to inter-doublet dynein forces, inter-doublet viscoelastic coupling, and viscous resistance due to the fluid in which the cilium is beating. The boundary conditions on each beam represent attachment at the basal body. The system was first reduced to a single beam with a baseward oriented follower load (Fig. 3.2C) to study the behavior of a single filament under steady dynein-like loading.

A system of two coupled beams in two dimensions (Fig. 3.3B) was then used to study how the coupling of two doublets affects the dynein force required to cause the system to oscillate, as well as the beating shape and frequency. In this system the dynein forces are modeled as equal and opposite forces on the two beams, and a distributed moment is imposed due to the distance (the length of the dynein arm) between the opposing forces. Distributed springs and viscous dampers couple the two beams.

A system of four coupled beams in three dimensions (Fig. 3.3C) was created to model axoneme behavior more accurately. This system essentially couples two of the previously-described two-doublet systems so they act in opposition; its 3D structure allows out-of-plane beating. The four-filament system is the least complex system in which the bending moments of opposing MTD pairs oppose each other. Finally, the model was extended to include six outer MTDs coupled to a

central filament representing the CPC (Fig. 3.3D). While still a simplification, this seven-filament system replicates the approximately circular symmetry and behavior of the axoneme.

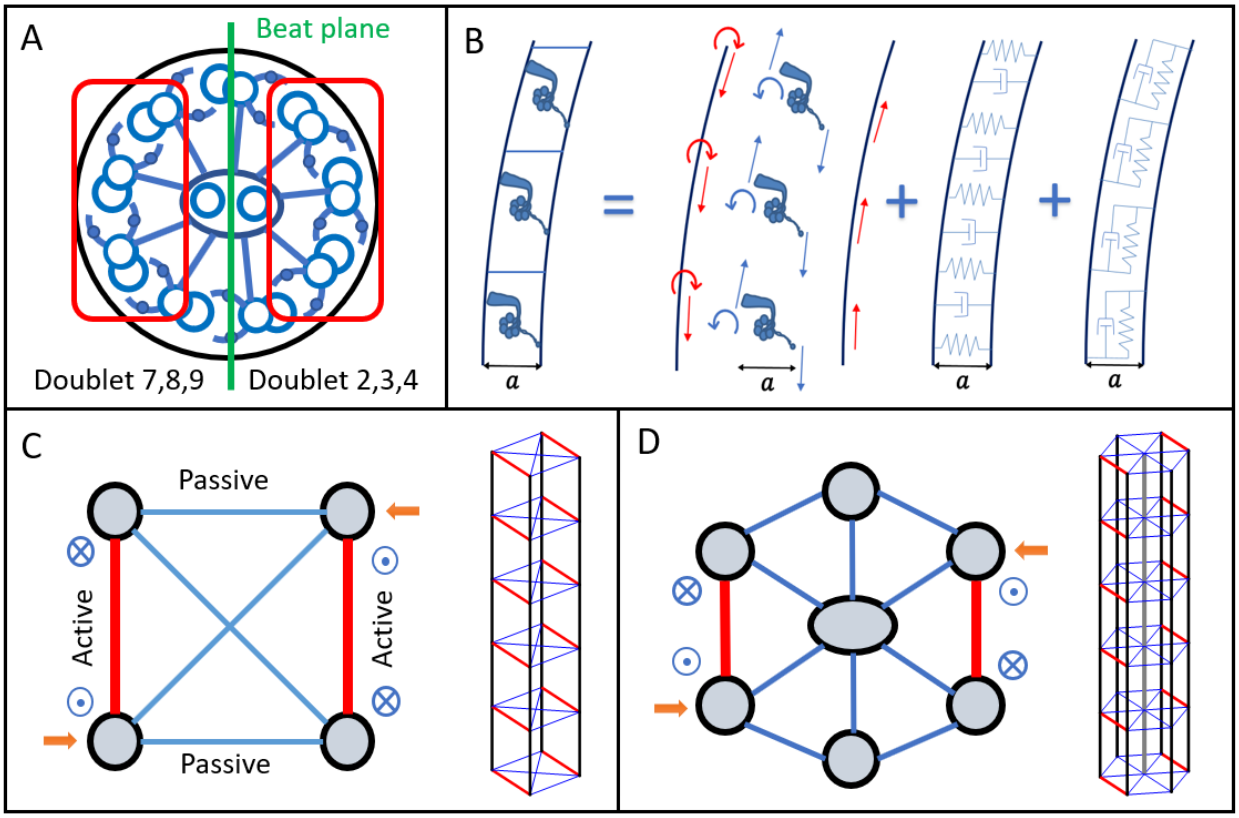

Figure 3.3: Mathematical models of the axoneme. (A) Conceptual model: dyneins between MTDs 2, 3, and 4 are placed in one "active" group and dyneins between MTDs 7, 8, and 9 are placed in another "active" group on the opposite side of the beat plane. The two groups are treated as having 180° rotational symmetry about the central axis. (B) The two-doublet system is modeled as a pair of beams with tangential follower loads, moments, and elastic and viscous damping. See Supplemental Material for details. (C). Combining two two-doublet systems creates the simple four-doublet representation. Baseward and tipward forces are represented as dotted and crossed circles, respectively. Orange arrows represent applied moments. (D) Adding additional doublets and a beam representing the CPC leads to a more accurate seven-beam model of the axoneme.

3.2.2 Rotational symmetry of the axoneme

The axoneme has several features that may cause it to bend preferentially in the plane that passes through MTD 1 and between MTDs 5-6. One is the CPC, which rotates in some species, but not in others [129]. Others are permanent cross-bridges between MTDs 1-2 in *Chlamydomonas* cilia

[18], and between MTDs 5-6 in other species [151]. In sperm flagella, a central partition lies between MTDs 3-8 [5, 152]. To model these effects, the bending stiffness of the axoneme was doubled in the out-of-plane direction. To model the effects of inactive dynein cross bridges, the normal elastic stiffness between "inactive doublet pairs" was increased by a factor of 10 relative to the stiffness between "active doublet pairs."

3.2.3 Modeling the applied dynein force and moment

Because dynein motors are distributed along the axoneme, the force of a linear array of dyneins applied to a single MTD is modeled as a distributed force approximately tangent to the longitudinal axis of the MTD (Fig. 3.2C). This "distributed follower load" model [69] leads to oscillatory beating, but physically it is incomplete as it does not maintain a balance of forces within the axoneme. Therefore, in multi-doublet models, dynein forces are modeled on pairs of MTDs, where the dynein forces applied to one doublet are equal and opposite to the dynein forces applied to the adjacent doublet. These forces are oriented along the average tangent vector of the two doublets. Basing the dynein force orientation on the average tangent angle rather than orienting dynein forces directly along the tangent vector of each doublets ensures a balance of internal forces (a key improvement on the model of [32]). Additionally, there must be a distributed bending moment applied to one or both doublets to account for the moment created by the dynein force couple (Fig. 3.3B).

Dynein force or moment will depend on inter-doublet spacing

In the simplest model of dynein as a steady-force mechanical motor, the shear force created between adjacent doublets is constant, as is the moment created by the application of forces separated by the inter-doublet spacing. However, the axoneme is a dynamic system in which the spacing between adjacent doublets varies as the cilium deforms. There are several possible ways

to model the relationship between the dynein force and moment as the inter-doublet separation varies.

Under *case A*, the axial component of the force produced by the dyneins is constant and in the linearized model, the moment is exactly proportional to the inter-doublet distance $a = a_0 + \delta a$:

$$m = m_0 \left(1 + \frac{\delta a}{a_0}\right) \tag{3.1}$$

Here $m_0 = p_0 a_0$ (the moment due to the steady dynein force, p_0, and undeformed inter-doublet spacing, a_0). This case in which the moment is directly proportional to the inter-doublet spacing will be referred to as having a *moment gain* of 1.

Under *case B*, the dyneins are assumed to produce a constant moment (*moment gain equal to* 0), so the axial force is inversely proportional to the inter-doublet distance: $p = \frac{m_0}{a_0 + \delta a}$. When this is linearized using a first-order Taylor series expansion, the equation for the force becomes: $p = \frac{m_0}{a_0}\left(1 - \frac{\delta a}{a_0}\right)$.

A third case, *case C*, is one in which the moment produced by dynein increases less than proportionally with increasing inter-doublet separation (*moment gain less than 1*). The dynein moment may even decrease with inter-doublet spacing (*moment gain less than 0*). This behavior occurs in the kinematic model of the dynein motor shown in Fig. 3.4. In this model, the stem of the dynein is treated as a rigid arm and the stalk is treated as a flexible fiber in tension, so the dynein arm acts like a mechanical "winch" [153, 154]. A geometric analysis and linearization of this model leads to equations for the variation of moment and axial force with respect to variation in inter-doublet spacing.

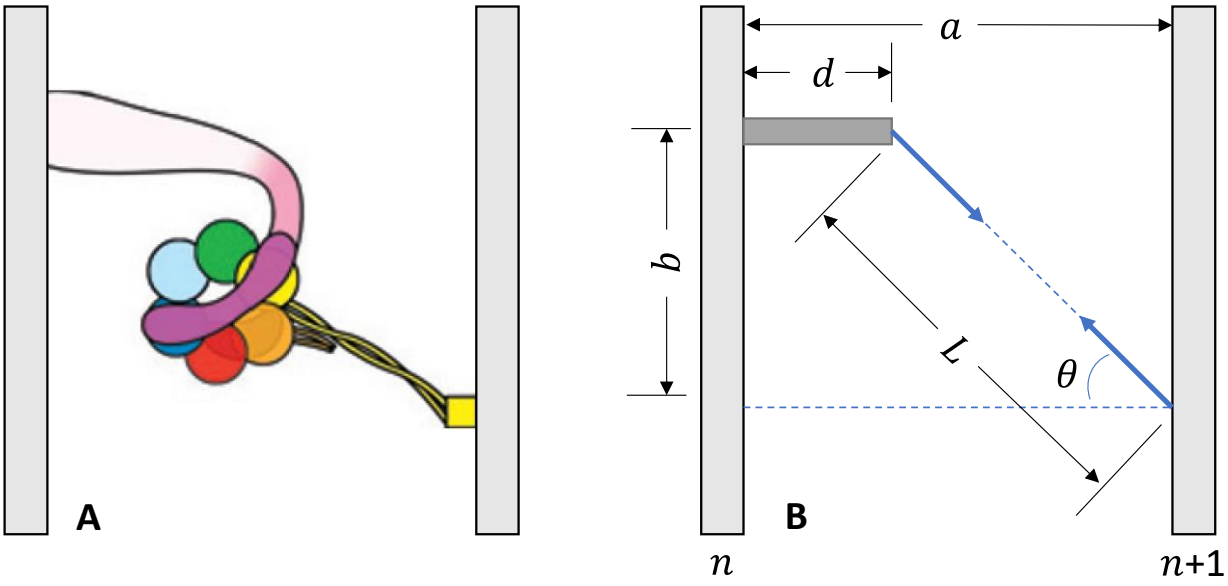

Figure 3.4: (A) Dynein schematic diagram adapted from [143]. (B) Model of dynein kinematics. The inter-doublet spacing is a, the dynein stem length is d, the distance from the stem to the binding domain is L, and the distance between the fixed attachment at MTD n and the transient attachment at MTD n+1 is b. The dynein force is modeled as a tensile force along the stalk, which is treated as a flexible fiber.

If the length of the stalk is assumed constant and the longitudinal attachment length, b, is allowed to vary with the inter-doublet spacing, $a = a_0 + \delta a$, the equations become:

$$m = m_0 \left(1 + \left(1 - \frac{a_0(a_0 - d)}{b^2}\right)\frac{\delta a}{a_0}\right) \tag{3.2}$$

The difference between Eq. 3.2 for the dynein winch model and Eq. 3.1 for the steady dynein force model is the moment gain term $\left(1 - \frac{a_0(a_0-d)}{b^2}\right)$ in front of the inter-doublet distance variation. This value is less than unity, and for plausible estimates of this dynein geometry, the moment gain is negative, indicating the moment decreases as the inter-doublet spacing increases. Moment gain is incorporated into an additional matrix term in the equation of motion (see Appendix A - *Dynein kinematics and moment gain*).

3.2.4 What are the parameters that affect ciliary beating?

As any model increases in complexity, the number of model parameters grows as well. Estimates are available for some mechanical properties of the axoneme, such as the flexural rigidity of MTDs [65, 66, 120]. However, other properties, such as stiffness and damping of individual NDRCs and RSs, are not easily measured; this leaves the corresponding parameters undetermined within a large, physically plausible range (Table 3.1). The efficient exploration of this undetermined parameter space – exploring the effects of parameter combinations on the overall behavior of the model system – is the focus of this work. By identifying which parameter combinations give rise to cilia-like oscillation, we can efficiently obtain estimates of physical properties that would lead to beating under steady dynein loading.

Table 3.1: Estimated values of some axoneme parameters.

Parameter	**Estimated Value**	**Description**	**references**
L	5.6 – 200 μm	Length of cilia of various organisms and gametes	[29, 35, 104]
D	180 – 200 nm	Axoneme outer diameter	[115, 124]
EI	200 – 1,000 pN-μm^2	Flexural rigidity of axoneme	[64, 66, 121]
k_L	1,000 – 2,500 pN/μm^2	N-DRC normal stiffness	[90, 122]
k_S	10^6 – 2.5×10^6 pN/μm^2	RS axial stiffness	estimated
k_T	1,000 – 2,500 pN/μm^2	Shear stiffness of axoneme	[66]
p	20 – 1,000 pN/μm	Applied dynein force	[123, 145]
c_N	0.001 – 0.003 pN-s/μm^2	Resistive force coefficient	[8, 107]
c_L	τ / 200	Link damping	estimated
k_θ	90×10^6 pN-μm/rad	Tangent angle Coupling	estimated

3.2.5 Overview of derivation of finite-element equations of motion

The mathematical model used in this study is based on the finite-element method. For a single beam element, displacements are represented as a sum of *basis* or *shape* functions ϕ_i which are functions of longitudinal position x. The *nodal displacements* or *generalized coordinates,* q_i, are functions of time, t:

$$y(x,t) = \sum_i \phi_i(x) q_i(t) \tag{3.3}$$

Using small-angle assumptions and Euler-Bernoulli beam theory, equations were derived for the kinetic and potential energy of the beam in terms of the generalized coordinates. Using Eq. 3 to represent the state of the continuous system by a finite number of these coordinates, Lagrange's equations (Eq. 3.4) were employed to derive the discretized equations of motion.

$$\frac{d}{dt}\left(\frac{\partial T}{\partial \dot{q}_i}\right) - \frac{\partial T}{\partial q_i} + \frac{\partial V}{\partial q_i} = Q_i^{nc} \tag{3.4}$$

The resulting equations take the form (using Einstein notation):

$$\ddot{q}_j \int_0^L \bar{m}\phi_i\phi_j dx + \dot{q}_j \int_0^L c_n \phi_i \phi_j dx + q_j \int_0^L EI\phi_i'' \phi_j'' dx + q_j \int_0^L N(x)\phi_i'\phi_j' dx$$

$$= q_j \int_0^L -p\phi_i\phi_j' \, dx \tag{3.5}$$

Here $\bar{m}$ is mass per unit length (kg/m), c_n is a distributed resistive force coefficient ($\frac{\mathrm{Ns}}{\mathrm{m}^2}$), EI is the flexural rigidity (Nm^2), $N(x)$ is the internal axial tension (N), and p is the distributed follower load ($\frac{\mathrm{N}}{\mathrm{m}}$). Derivatives with respect to t are denoted with an overdot, and derivatives with respect to x are denoted with a prime. The first and third terms of Eq. 3.5 represent the consistent mass and stiffness matrices. The fourth term is a "geometric stiffness matrix" that describes the effects of loading on the effective stiffness of the beam (filament). The viscous damping matrix

(second term) and non-conservative follower load matrix (right hand term) are derived from the virtual work of these non-conservative forces under variation of the generalized coordinates.

Finite-element matrices (4 x 4) for individual elements were created by analytically evaluating the terms in Eq. 3.5 with cubic Hermite interpolating polynomials for shape functions, and these element-level matrices were combined to create filament-level matrices. System-level matrices for multi-filament systems were created by combining filament-level matrices in block matrices.

Additional system-level matrices were derived to model viscoelastic coupling between filaments and follower loading on active MTD pairs based on the average tangent angle (to ensure internal force balance). Coupling block matrices are created as the Kronecker product of a truss matrix representing the filament links and the filament-level coupling matrices.

The final system may be written compactly as:

$$\boldsymbol{M\ddot{q} + C\dot{q} + (K + K_G - P)q = 0} \tag{3.6}$$

$\boldsymbol{M}$ is the system-level consistent mass matrix (a diagonal block matrix of beam-level mass matrices). **C** is the damping matrix which captures the effects of external fluid damping (mass-proportional), internal beam damping (stiffness-proportional), and damping in the beam coupling. $\boldsymbol{K}$ is the global stiffness matrix which captures both the flexural rigidity of the individual beams and the beam coupling stiffness. $\boldsymbol{K_G}$ is the system-level geometric stiffness matrix. **P** is the system-level geometric loading matrix, which due to the non-conservative follower load is non-symmetric. This loading matrix represents the ability of non-conservative forces to add energy to the system and leads to the possibility of dynamic instability without dynein regulation.

Non-dimensionalization of the system

The system above can be written in dimensionless form using appropriate definitions of characteristic length, time, and force (Table 3.2); this reduces the complexity of the matrix equations and avoids ill-conditioning. The system in Eq. 5 is first nondimensionalized using a characteristic length, L, and a characteristic force, $f_c = \frac{EI}{L^2}$. Using parameter estimates for typical cilia [32] the coefficient of the dimensionless mass matrix is on the order of 10^{-7}, hence inertial terms are neglected. The characteristic time is chosen to be $\tau = \frac{c_N L^4}{EI}$, so that the period of the system will generally scale with c_N.

$$\left(\frac{\bar{m}L^4}{\tau^2 EI}\right)\widetilde{\boldsymbol{M}}\ddot{\boldsymbol{q}} + \left(\frac{c_n L^4}{\tau EI}\right)\widetilde{\boldsymbol{C}}\dot{\boldsymbol{q}} + \left(\widetilde{\boldsymbol{K}} + \widetilde{\boldsymbol{K}}_{\boldsymbol{G}} - \widetilde{\boldsymbol{P}}\right)\boldsymbol{q} = \boldsymbol{0} \tag{3.7}$$

$$\widetilde{\boldsymbol{C}}\dot{\boldsymbol{q}} + \left(\widetilde{\boldsymbol{K}} + \widetilde{\boldsymbol{K}}_{\boldsymbol{G}} - \widetilde{\boldsymbol{P}}\right)\boldsymbol{q} = \boldsymbol{0} \tag{3.8}$$

System behavior is described in terms of dimensionless parameters, such as the dimensionless dynein force $\bar{p} = \frac{pL^3}{EI}$, and distributed link stiffness nondimensionalized as $\bar{k} = \frac{kL^4}{EI}$. Table 3.2 lists example values of these dimensionless parameters.

Table 3.2: Example dimensionless model parameters

Dimensional	Dimensionless	Description
L = 12 μm	~	Characteristic length
EI = 73 pN-μm^2	~	Flexural rigidity per filament
c_N = 0.003 pN-s/μm^2	~	Resistive force coefficient
$\tau = 0.8554$ s	~	Characteristic time $c_N L^4/EI$
p = 25 pN/μm	$\bar{p} = 600$	$\bar{p} = \frac{pL^3}{EI}$
k_s = 3.5×10^3 pN-μm^2	$\bar{k}_s = 10^6$	$\bar{k}_s = \frac{k_s L^4}{EI}$

3.2.6 Eigenvalue-based stability analysis of linearized finite-element model

The analysis is based on finding the eigenvalues and eigenvectors of the finite-element matrices of the system, linearized about an equilibrium position (linear stability analysis). The construction of the finite-element matrices and subsequent eigenvalue analysis are computationally inexpensive and can be easily parallelized. This allows rapid generation of solutions over a wide range of parameter combinations to obtain a quantitative portrait of system behavior over the defined parameter space.

Once the finite-element matrices have been assembled, the eigenvalues and eigenvectors of the system are found numerically using the MATLAB solver *eig() [155]*. The real part of each eigenvalue tells us the rate of growth (positive real part) or decay (negative real part) of the corresponding mode shape. The imaginary part of the eigenvalue tells us the frequency of oscillation (if it is nonzero). Eigenvalues with a positive real part and a nonzero imaginary part are said to be dynamically unstable. Dynamically unstable modes exhibit growing oscillations when perturbed from equilibrium. In most physical systems, such growing oscillations are limited in amplitude by nonlinearities in the system and settle into limit cycles.

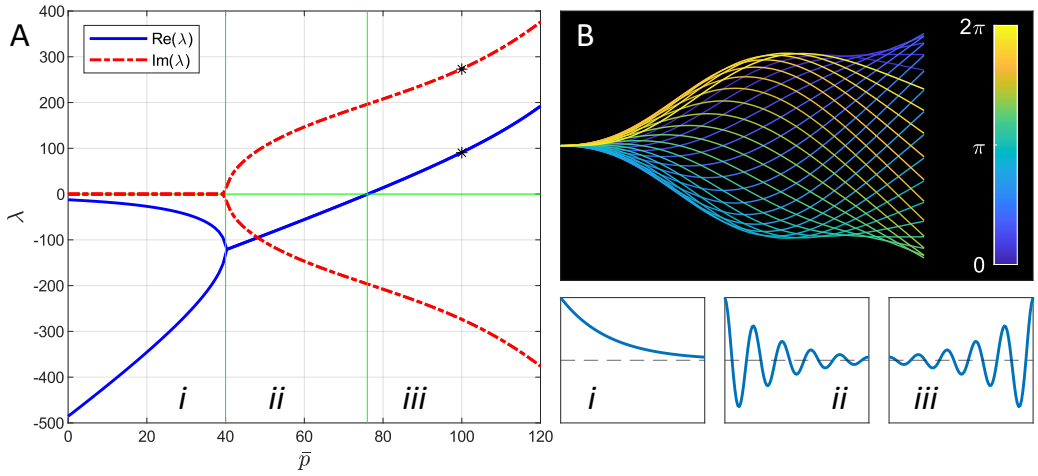

Figure 3.5: Eigenvalue analysis for the example of a single filament with distributed follower load. (A) Eigenvalues, λ, are calculated as a function of nondimensional distributed force $\bar{p}$ and separated into real and imaginary parts. Negative real parts indicate the mode is stable (i, ii). Positive real parts indicate the mode is unstable (iii). Nonzero imaginary parts (ii, iii) indicate frequency of oscillation (nondimensional in this example). (B) The complex mode shape at $\bar{p} = 100$ (corresponding to the eigenvalue denoted by asterisks in panel (A)) visualized through one beat cycle.

Each eigenvalue has a corresponding eigenvector which determines the waveform. If the eigenvalue/eigenvector pair is complex, the angles of the complex values of the eigenvector indicate the phase delay as a function of axial position and determine propagation of the ciliary waveform. These "mode shapes" may be visualized to compare their shape and propagation to those observed in cilia. The eigenmode with the largest positive real eigenvalue part is the most unstable (will grow the fastest) and will dominate the system behavior. We focus on this single eigenvalue for each parameter combination, although other unstable modes may participate.

3.2.7 Time domain simulations

Representative predictions from stability analysis were confirmed by time-domain simulation. A cubic nonlinearity was added to the linking stiffness as a simplified representation of the multiple physical nonlinearities that might limit the beating amplitude and create limit cycle behavior. The system was solved using the MATLAB *ode15s()* solver for stiff systems.

3.3 Results

3.3.1 Overview of multi-filament system behavior

Analysis of system eigenvalues reveals regions of stability in parameter space, as well as regions of dynamic instability and, in some cases, static instability (buckling- or divergence). For regions showing dynamic instability, visualization of the eigenvectors shows cilia-like beating shapes. The effect of system parameters on frequency and instability is described in detail below.

Overview of frequency and stability behavior - eigenvalues

System behavior is summarized by contour plots of output characteristics, such as dominant frequency, as input parameters are systematically varied. Frequency maps for 4- and 7-filament systems are shown in Fig. 3.6, as functions of non-dimensional dynein force and spoke stiffness. Nondimensional frequency is dimensionalized by the characteristic time in Table 3.2.

The 4- and 7-filament systems share key behaviors. With all other parameters held constant, below a critical value of $\bar{p}$, the system is stable and non-oscillatory as evidenced by the zero frequency and negative maximal real eigenvalue part (to the left of the red “critical value” line). Oscillations emerge when the frequency (imaginary eigenvalue part) becomes nonzero. As the critical value is exceeded, the system becomes unstable, exhibiting a Hopf bifurcation and the emergence of oscillations. As $\bar{p}$ increases further, frequency initially increases as well, but the relation is generally nonlinear and non-monotonic. In some cases, if $\bar{p}$ is increased further still, the oscillation frequency eventually vanishes, and the system becomes statically unstable (divergent).

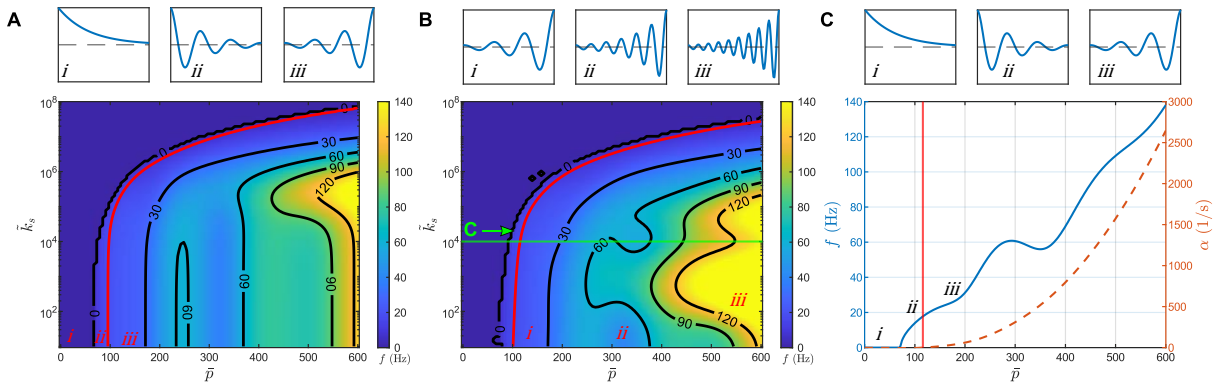

Figure 3.6: Effect of nondimensional spoke stiffness, $\bar{k}_s$, and nondimensional dynein force, $\bar{p}$, on stability and frequency for 4- and 7-filament systems. Color indicates frequency of the dominant (least stable) mode. (A) Stability/frequency plot for the 4-doublet system. The red line indicates the stability border. Points to the left of the red line (lower $\bar{p}$) are stable, and points to the right of it (higher $\bar{p}$) are unstable. (B) Stability/frequency plot for the 7-filament system. Values along the horizontal green line at $\bar{k}_s = 10^4$ are shown in the next panel. (C) Frequency and growth rate (not shown in color maps (A,B)) for points along the horizontal green line from previous panel. The vertical red line indicates the critical value of $\bar{p}$ for instability (Hopf bifurcation). Growth rate increases monotonically with increasing $\bar{p}$.

Overview of spatial behavior – eigenvector mode shapes

Example mode shapes of 1-beam system under a distributed follower load, as well as 2-, 4-, and 7-filament systems are shown in Fig. 3.7. All systems produce oscillatory waveforms, although only the 4- and 7-filament systems are consistent with internal loading (balanced opposing dynein force pairs *and* moments). In Fig. 3.7A-D, the mode shapes shown are calculated at the same $\bar{p}$. In the 1-beam case (Fig. 3.7A), the filament experiences an unopposed baseward compressive force; the system oscillates at 347Hz. In the 2-filament case, forces are balanced, but there is an omitted unbalanced moment (the mode shape is shown without the static bend that would be imposed by the unbalanced moment). In the 4- and 7-filament cases, moments are balanced by those in the opposing dynein-coupled pairs of MTDs. These systems both beat at ~50 Hz. In Fig. 3.7E-H, all parameters are kept constant other than $\bar{p}$. As $\bar{p}$ is increased, the temporal frequency increases and the spatial wavelength decreases.

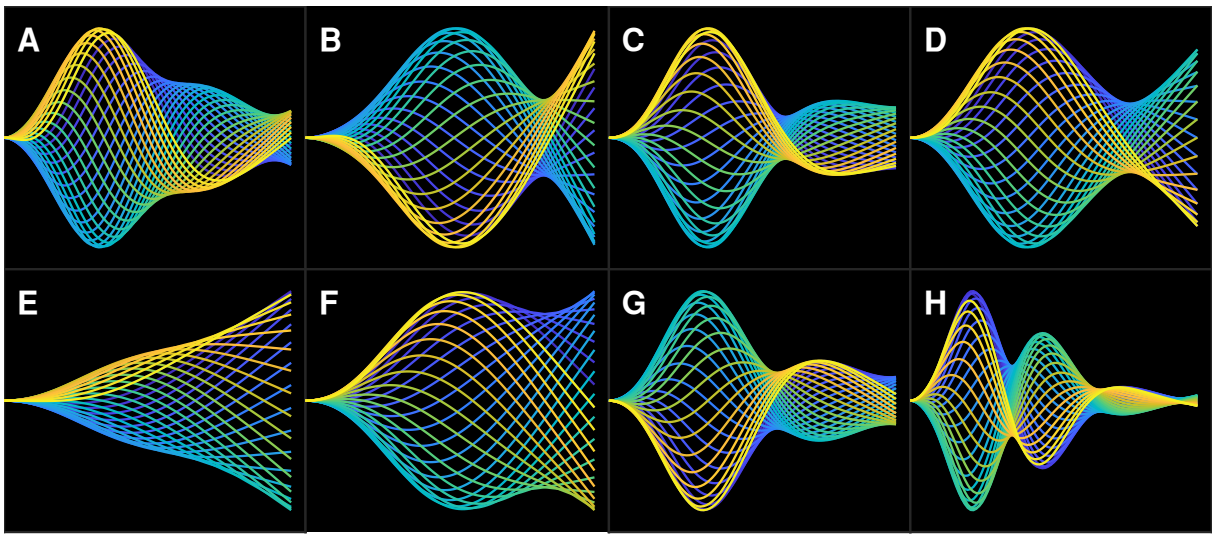

Figure 3.7: (A-D) Comparison of mode shapes from 1-, 2-, 4-, and 7-filament systems at $\bar{p} = 300$. For multi-filament systems, $\bar{k}_s = 10^6, \bar{k}_L = 10^3, \bar{c}_L = \frac{1}{200}$. (A) 1-filament (347 Hz). (B) 2-filaments (83 Hz). (C) 4-filaments (49 Hz). (D)7-filaments (51 Hz). (E-H) Effect of increasing steady dynein force on mode shapes of 7-filament system. Points in parameter space for (E-F) are labeled in Fig. 8D. (E) $\bar{p} = 150$ (17 Hz). (F) $\bar{p} = 200$ (22 Hz). (G) $\bar{p} = 400$ (66 Hz). (H) $\bar{p} = 800$ (245 Hz). Animations for (E-F) are shown in Supplemental Movies S1-S2 [38].

3.3.2 Effect of inter-doublet stiffness

RSs and NDRCs create elastic resistance to changes in inter-filament spacing. To reduce the parameter space, the ratio of RS stiffness to NDRC stiffness was studied at three markedly different values: $1{:}\,1, 10^3{:}\,1, 10^6{:}\,1$. RSs are larger structures than NDRCs and therefore thought to be stiffer [142, 156]. Increasing the inter-doublet stiffness had a stabilizing effect on the system at all ratios and in all ranges of stiffness values (Fig. 3.8). At high RS:NDRC ratios oscillation is dominated by circumferential motion of outer MTDs relative to the CPC.

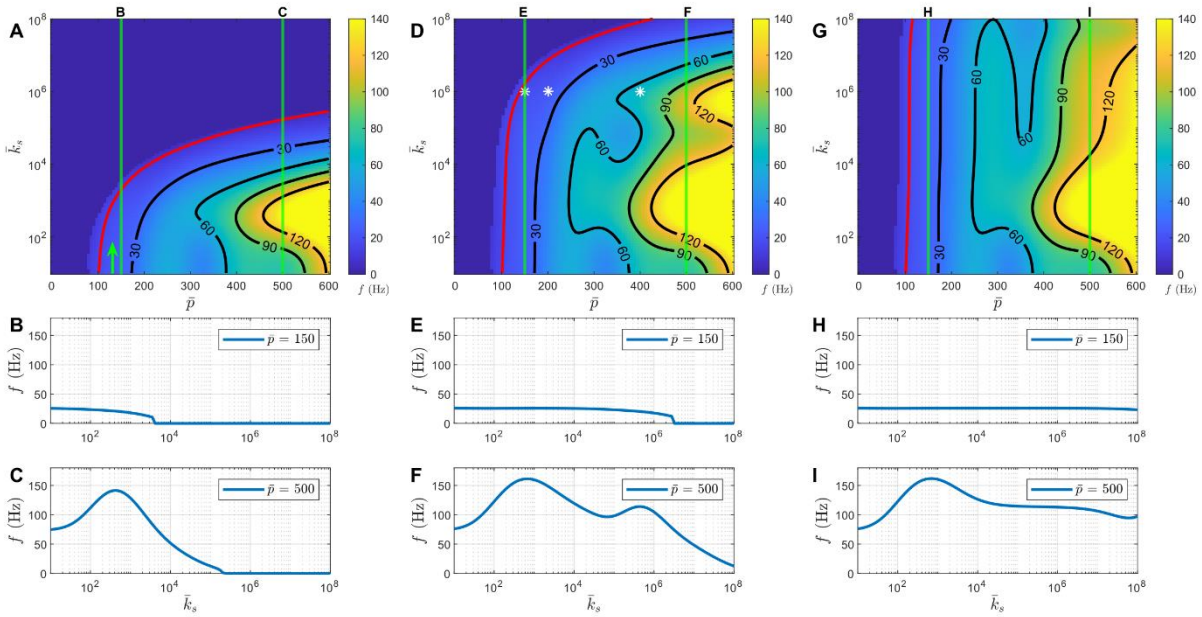

Figure 3.8: Effect of nondimensional inter-filament RS stiffness, $\bar{k}_s$, and nondimensional dynein force, $\bar{p}$, on frequency. Plots of frequencies along the vertical green lines at $\bar{p} = 150$ and $\bar{p} = 600$ are shown below. (A) RS:NDRC (spoke:link) stiffness ratio 1:1. (B) Plot of frequency vs $\bar{k}_s$ at $\bar{p} = 150$. (C) Plot of frequency vs $\bar{k}_s$ at $\bar{p} = 500$. (D) RS:NDRC stiffness ratio 10^3:1. White asterisks indicate points in parameter space with mode shapes shown in Fig. 7E-G. (E) Plot of frequency vs $\bar{k}_s$ at $\bar{p} = 150$. (F) Plot of frequency vs $\bar{k}_s$ at $\bar{p} = 500$. (G) RS:NDRC stiffness ratio 10^6:1. (H) Plot of frequency vs $\bar{k}_s$ at $\bar{p} = 150$. (I) Plot of frequency vs $\bar{k}_s$ at $\bar{p} = 500$

3.3.3 Effect of inter-filament damping

In addition to elastic coupling between filaments, internal viscous coupling is provided by cytoplasm and rate-dependent resistance of NDRC and RS structures. Though difficult to measure, these viscous properties may affect the stability and frequency of the system. Physically, internal damping can modulate the frequency and stability of the system.

At RS:NDRC ratio $k_s/k_L = 10^3$, and $\bar{k}_s = 10^3$, different behavior is observed again in the relationship of frequency to link damping, $\bar{c}_L$, at different ranges of $\bar{p}$ (Fig. 3.9). At lower values of $\bar{p}$ (150), $\bar{c}_L$ has little effect on the frequency, though frequency eventually decreases slightly as $\bar{c}_L$ becomes very large. At larger values of $\bar{p}$ (500), $\bar{c}_L$has a strong nonlinear, non-monotonic effect on of the system. Increasing $\bar{c}_L$ from 10^{-4} initially drives the frequency up. In the higher

range of spoke stiffness ($\bar{k}_s$ = 10^6), increasing $\bar{c}_L$ tends to strongly decrease the frequency of the system.

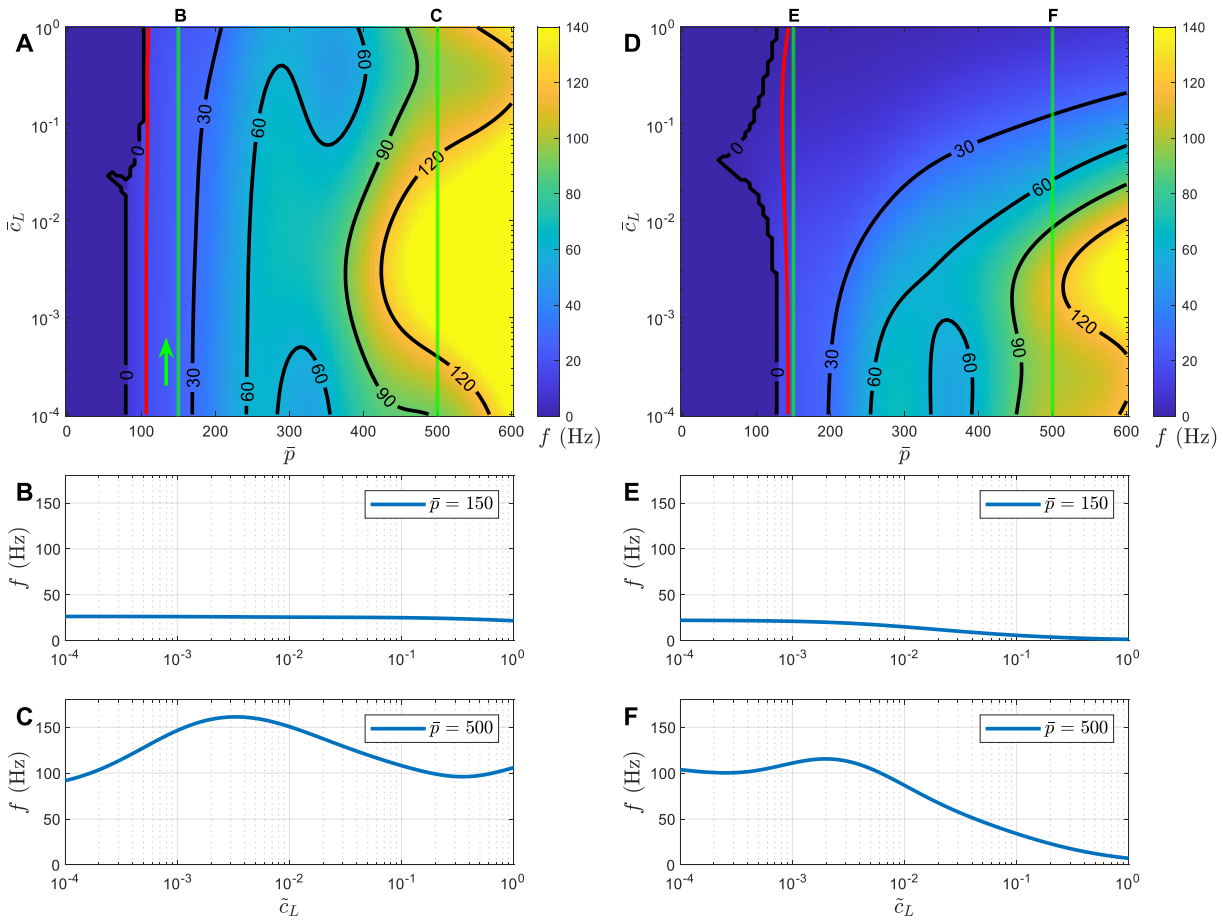

Figure 3.9: Effect of nondimensional link damping, $\bar{c}_L$, and nondimensional dynein force, $\bar{p}$, on frequency. Colormap indicates frequency. RS:NDRC ratio k_s/k_L = 10^3. Red line indicates stability boundary. Plots of frequencies along the vertical green lines at $\bar{p} = 150$ and $\bar{p} = 600$ are broken out below. (A) Stability plot for $\bar{k}_s$ = 10^3. (B) Plot of frequency vs $\bar{c}_L$ at $\bar{p} = 150$. (C) Plot of frequency vs $\bar{c}_L$ at $\bar{p} = 500$. (D) Stability plot for $\bar{k}_s$ = 10^6. (E) Plot of frequency vs $\bar{c}_L$ at $\bar{p} = 150$. (F) Plot of frequency vs $\bar{c}_L$ at $\bar{p} = 500$.

The effect of $\bar{c}_L$ on stability is more straightforward in this regime as increasing damping monotonically increased stability (lowered the positive real part of the eigenvalue) at all values of $\bar{p}$ for which the system was unstable.

3.3.4 Effect of dynein moment gain

Increasing the dynein moment gain, γ (the effect of doublet separation on active bending moment), lowers the critical value of $\bar{p}$ for instability (Fig. 3.10) and generally speeds growth of oscillations. However, the effect of moment gain on frequency is more pronounced. Decreasing moment gain from zero (so that active bending moment decreases with doublet spacing) increases frequency sharply, and higher values of $\bar{p}$ increase the steepness of that slope. Likewise, raising moment gain from zero decreases frequency until it vanishes. To the right of the neutral stability isoline, this zero-frequency contour represents the border between oscillations and divergence (static instability). An animation of the dominant mode shape with $\bar{p} = 400, \gamma = -2$ is shown in Supplemental Movie S3 [38].

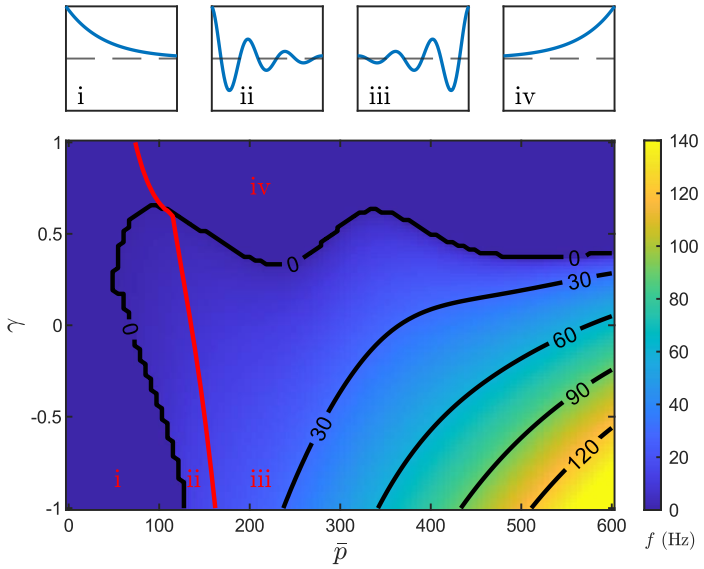

Figure 3.10: Effect of moment gain, γ, and nondimensional dynein force, $\bar{p}$, on frequency. $\bar{k}_s$ = 10^6, RS:NDRC ratio k_s/k_L= 10^3, $\bar{c}_L$ = 1/20. The stability boundary is lowered by increasing the value of the moment gain as indicated by the red contour indicating the largest real eigenvalue part is zero. To the left of this line the axoneme is stable; to the right of this line the system is dynamically unstable (flutter) or divergent (buckling-type behavior).

3.3.5 Propagation velocity and wavelength of the dominant mode

Propulsive beating patterns of cilia and flagella have a base-to-tip propagation direction [107]. The propagation rate is quantified in the current model by calculating the average gradient of the phase of the dominant complex eigenmode. The sign of this gradient gives the direction of propagation, and its magnitude provides propagation rate. The axial distance associated with a 2π difference in the phase is the spatial wavelength of the mode.

All parameter combinations that led to oscillations also led to anterograde (base-to-tip) beating propagation. For the parameter values analyzed in Fig. 3.11, the wavelength of the mode shape varies between 6.4-50um, and propagation velocity ranges from 50-1350 um/s. These values overlap with values found in [26, 157, 158], where investigators obtained wavelengths of 10-20μm in *Chlamydomonas* cilia and 20-30μm in sperm flagella. The values of wavelength and frequency from these prior measurements correspond to a propagation velocity range of 500-1200μm/s.

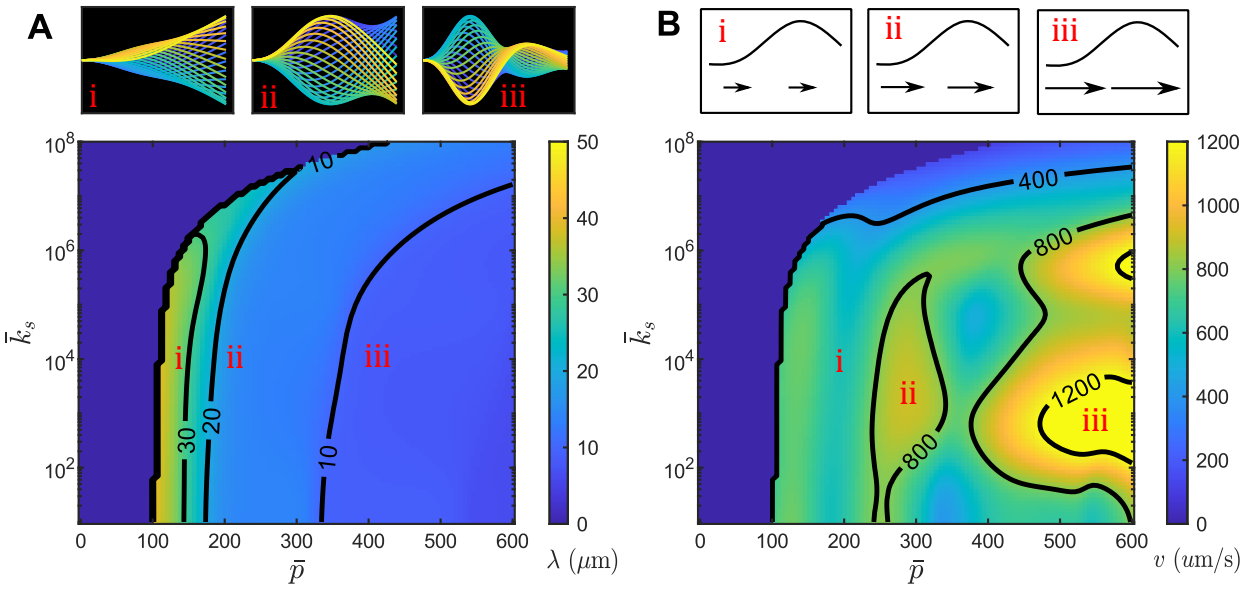

Figure 3.11: (A) Wavelength, λ, as a function of nondimensional spoke stiffness, $\bar{k}_s$, and nondimensional dynein force, $\bar{p}$. Mode shapes for points i, ii, and iii shown above. (B) Propagation velocity is calculated from the product of the wavelength and the beat frequency at each point in the parameter space

3.3.6 Out-of-plane beating

While many cilia beat predominantly in a plane, other cilia, such as nodal cilia, have waveforms that are highly nonplanar [13, 159]. The dominant mode shapes obtained from the eigenvectors of the current model are predominantly planar, though they tend to lie in planes at a slight angle from the plane dividing the two active halves of the model (Fig. 3.12). These modes typically exhibit a small out-of-plane component, with less than 5% of the amplitude of the in-plane component (Fig. 3.12). At values of $\bar{p}$ studied in this work, additional mode shapes become unstable and may contribute to the waveform. An example of such an out-of-plane mode shape is shown in *Additional results* section 3.6.2 (Fig. 3.14). Additionally, the axoneme undergoes torsion (rotation of the osculating plane) and twisting about its axis during beating [160]. These behaviors are illustrated in *Additional results* section 3.6.4 (Fig. 3.16).

3.3.7 Comparison with time-domain simulations

Time-domain simulations generate solutions by iteratively marching forward in time, updating the state of the model at discrete, consecutive time points. Simulations performed with parameter values near the stability boundary confirm that beating occurs as predicted by dominant eigenvalues and eigenvectors (Fig. 3.12). A small perturbation is applied to initiate departure from the straight equilibrium configuration. As predicted by the eigenvalue analysis, simulations in unstable regions of the parameter space exhibit growing oscillations (as determined from visualizations of the time-domain beating shapes and time-series plots of the tip displacements (Fig. 3.12D,E).

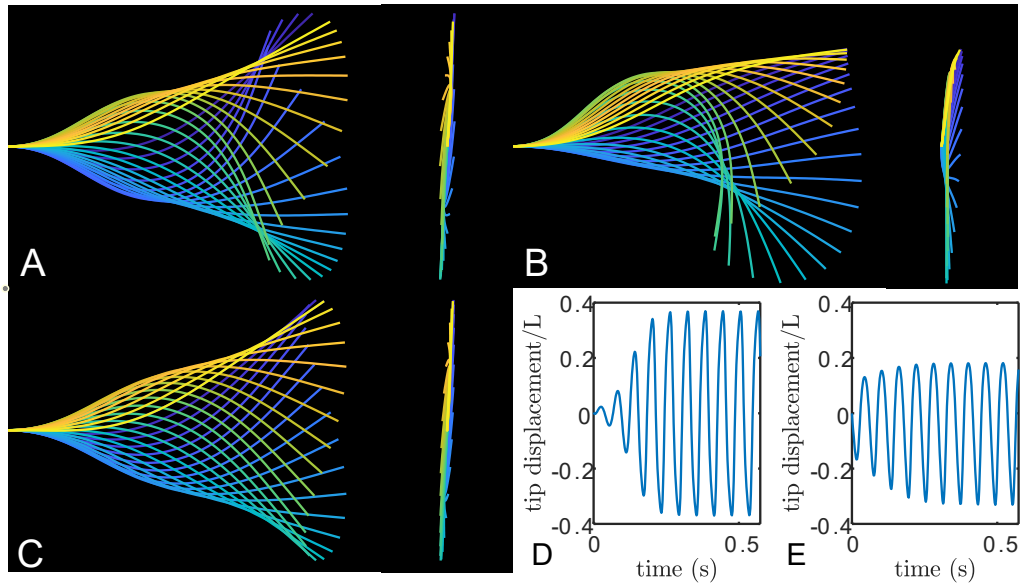

Figure 3.12: Comparison of behavior predicted by time-domain simulation and eigenanalysis with parameter values $\bar{k}_s = 10^6, RS{:}\,NDRC = 10^3, \bar{p} = 150, \bar{c}_N = \frac{1}{200}$. (A) Waveform predicted by time-domain simulation. (B) Non-symmetric beat shapes predicted by time-domain simulation of oscillation superimposed on a curved configuration produced by an imbalanced moment. Animation shown in Supplemental Movie S4. (C) Waveform predicted from the unstable eigenmode. (D-E) Time series of non-dimensional tip displacement corresponding to waveforms in panels (A,B).

Asymmetric beat shapes

It has been proposed that asymmetric beat shapes in multiciliate cells and organisms may arise from the superposition of a symmetric beat and an asymmetric curvature [45, 157]. In the current steady dynein force model of ciliary beating, asymmetric curvature could be caused by an imbalance in dynein forces on opposite sides of the beat plane, or alternatively, by an initial static (buckling) instability. Our eigenvalue analysis, which is based on a model linearized about the straight equilibrium, cannot capture the effects of large initial deformation due to either mechanism. This phenomenon can be seen in time-domain simulations, however. Adding a constant distributed moment to the steady dynein forces along the entire flagellum leads to the asymmetric beat patterns shown in Fig. 3.12B (Supplementary Movie S4)[38], which qualitatively resemble the waveforms observed in cilia of mammalian airways or

Chlamydomonas algae. This simulation produces a waveform with wavelength 17μm, frequency 17Hz, and dynamic amplitude 0.71 rad. The static curvature was -0.044 $\frac{\text{rad}}{\mu\text{m}}$, as measured by the approach of Geyer et al. [157] with a 12μm cilium length and a moment imbalance corresponding to dynein force on one side of the axoneme approximately 5 times the force on the other side. While the results here are not intended to replicate any of the cases shown in [157], they are comparable to values observed for mutant (mbo2; curvature -0.04±0.01 $\frac{\text{rad}}{\mu\text{m}}$ and frequency 28±7Hz) and WT (curvature -0.24±0.02 and frequency 68±3Hz) axoneme waveforms in that study.

3.4 Discussion

Analysis of finite-element models of the ciliary axoneme, each consisting of coupled filaments under steady, unregulated dynein loading, reveal different types of behavior including wavelike oscillations. In all examples shown, there exists a boundary between stability and dynamic instability of the straight equilibrium shape. This boundary is strongly affected by dynein force, length and flexural rigidity of the axoneme, but is also affected by parameters such as inter-doublet elastic and viscous resistance, and the kinematics of dynein motors. While the oscillation frequency is not uniquely defined by the non-dimensional loading parameter $\bar{p}$, values corresponding to a distributed dynein force of ~20-40 (pN/μm) gave realistic frequencies with reasonable estimates of other system parameters.

Increasing RS and NDRC stiffness tends to increase stability and generally decreases oscillation frequency near the stability boundary, but the relationship between stiffness and frequency is nonlinear and non-monotonic. If the NDRCs are made much less stiff than the RSs (by a factor of 10^6), the system remains unstable for higher values of RS stiffness, as shown by the stability

boundaries in Fig. 3.9. While radial motion of outer filaments becomes constrained at high RS stiffness, circumferential motion of filaments remains relatively unrestricted.

Inter-doublet damping provides a potential mechanism for the control of ciliary beat frequency. Near the stability boundary, adding damping to inter-filament links surprisingly increases instability in some ranges of parameter values. At larger values, inter-filament damping stabilizes the system. Likewise, near the stability boundary inter-filament damping lowers the beat frequency, but at higher values of $\bar{p}$ the dependance is nonlinear and non-monotonic. This non-monotonic behavior is difficult to explain, but may be related to the emergence and interaction of different unstable modes as parameters are varied (see section 3.6.3 in *Additional Results*).

Beat propagation is anterograde (base-to-tip; Fig. 3.11B) in all cases analyzed here. This is likely due to the boundary conditions: motion is constrained at the base of the axoneme and free at the tip. While this behavior is consistent with most observations of ciliary beating, retrograde propagation has been reported under some conditions [161]. It is possible that changes to the boundary conditions and inter-filament coupling (i.e., adding compliance to the base and constraining relative motion of filaments at the tip) might lead to retrograde propagation. If and how this occurs could be a topic of future work.

The current model of dynein arm kinematics reveals the potential influence of a parameter we denote as “moment gain”. Positive values of the moment gain decrease frequency, increase instability, and can lead to divergence as a dominant mode of instability. Negative values of moment gain increase frequency, and slightly stabilize the system. Both positive and negative values of moment gain can be obtained using plausible dimensions in the dynein model. Small changes in baseline dynein geometry lead to qualitative differences in behavior, providing a

plausible mechanism to vary the beating of cilia and flagella. Mutations (*sup-pf-1*) affecting the dynein stalk can restore motility to central-pair deficient cilia and affect beating frequency [162]. Axonemes lacking spokes or central pair likely have different passive properties and dynein kinematics from wild type axonemes, and it is plausible that suppressor mutations like *sup-pf-1* compensate for these differences. The behavior of paralyzed mutants and their suppressors clearly merits future investigation. Negative moment gain has similar effects to the "geometric clutch" described by Lindemann, although without actual modulation of dynein activity [43, 163].

The possibility of divergent (buckling-like) behavior deserves attention. In this small-deformation model, divergence (monotonic growth without oscillation) may seem inconsistent with cilia behavior. However, eigenvalue analysis cannot predict the behavior of the fully nonlinear system. An axoneme that initially diverges from its straight equilibrium configuration may reach a new curved equilibrium, and undergo a secondary dynamic instability leading to limit cycle oscillation about that curved shape. This can only be studied in a model that rigorously accounts for large-deformations and is thus deferred to future work.

Future work should include exploration of asymmetric beating patterns and non-planar beating. In the current steady dynein force model, asymmetry may arise from sustained imbalance between dynein activity on opposite sides of the axoneme. Time-domain simulations in the current model exhibit asymmetric beating similar to the asymmetric beating patterns of cilia in airway epithelia or *Chlamydomonas* algae. The controllability of this asymmetry offers a possible explanation for the presence or absence of static curvature in waveforms observed by Geyer et al. [157].

The current model also exhibits non-planar beating. All eigenmodes had some non-planar component, and some unstable modes were highly nonplanar, consistent with the helical motion of nodal cilia [13]. Complete exploration of this behavior will require nonlinear models, but such models can be guided by the current results. Finally, all parameters have been assumed constant along the axoneme. Future studies might explore the effects of longitudinal variations.

This study confirms the general predictions of an earlier study that suggested steady dynein force can lead to wavelike oscillations in axonemes [32]. The current study addresses a key limitation of the previous model, in which dynein forces on opposing doublets did not exactly balance if doublets did not remain parallel. We note that even though the current model predicts that steady dynein activity is sufficient to drive ciliary oscillation, it does not rule out alternative mechanisms. Nevertheless, the current work strongly supports an important role for axial loading of doublets in ciliary beating.

3.5 Conclusion

This study confirms that steady dynein forces without active dynein regulation can lead to oscillatory beating in mathematical models of the axoneme with biologically plausible physical parameters. Predicted waveforms resemble those observed in cilia in terms of their physical shape, frequency, and direction of propagation. Eigenanalysis of discrete finite element models provides an efficient way to identify parameters that lead to cilia-like beating and to assess the effects of those parameters.

Future directions include stability analysis of more realistic axoneme models, as well as extending the current models to capture larger deformations and more complicated behavior of dynein and passive structural components.

Data accessibility

The code is available via Zenodo: https://doi.org/10.5281/zenodo.6762933.

Derivations are presented in Appendix A.

Additional results are provided in Section 3.6.

Authors'contributions

L.G.W.: conceptualization, investigation, methodology, software, writing—original draft; Y.S.: investigation; P.V.B.: conceptualization, funding acquisition, methodology, project administration, supervision, writing—review and editing.

Funding

The work was supported by NSF grant no. CMMI-1633971and the Children's Discovery Institute

3.6 Additional results

3.6.1 Assumptions about stiffness between active pairs

In the manuscript, all results are based on the assumption that the passive elastic coupling between 'non-active' MTD pairs is ten times as stiff as the elastic coupling between active pairs, due to the assumed resistance of inactive dynein arms. However, this assumption is not necessary to produce oscillations by dynamic instability. In Fig. 3.13A, unstable oscillatory modes are shown over a wide range of spoke stiffness and dynein force values for the case where elastic stiffness is equal among all doublet couples. Representative mode shapes at high RS stiffness values ($k_s = 10^6$ pN/μm^2) and the effect of moment gain on the mode shapes are shown in Fig. 3.13B-E.

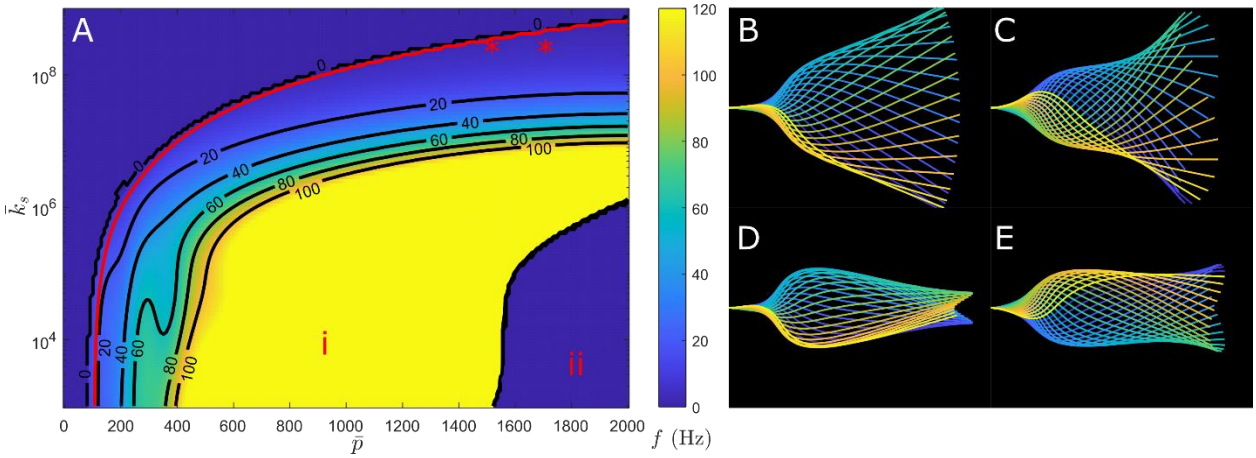

Figure 3.13: (A) Oscillation frequency as a function of nondimensional dynein force $\bar{p}$ and nondimensional spoke stiffness $\bar{k}_s$. RS:NDRC stiffness ratio 10^3, link damping, $\bar{c}\_L = 1/200$. Here the coupling stiffness between each doublet pair is equal whether the pair is active or passive. The central yellow region (i) is a region of high frequency (>100Hz) oscillation. The blue region in the lower right (ii) denotes parameter combinations that lead to divergence. The two asterisks indicate the parameters for the mode shapes in (B-E). (B) Dominant mode shape at $\bar{p} = 1500$ (p=63pN/μm), $\bar{k}_S = 3 \times 10^8 (k_s = 10^6 pN/(\mu m^2))$, geometric moment, γ=0, $f = 2.7Hz$. (C) Mode shape with all parameters equal to those of (B), but with $\gamma = -2$. $f = 11.7Hz$. (D) Dominant mode shape at $\bar{p} = 1700$, $\gamma = 0$. $f = 3.4Hz$. (E) Mode shape with all parameters equal to those of (D), but with $\gamma = -2$. $f = 14.6\ Hz$.

3.6.2 3D Shapes

Though planar oscillations have been the primary focus of the current work, 3-dimensional helical waveforms emerge when asymmetries such as the increased bending stiffness about the axis running between doublets 1 and 5-6, and the increased elastic coupling between inactive MTD pairs are removed. This is shown in Fig. 3.14 both in the most unstable mode and also in a higher but still unstable mode.

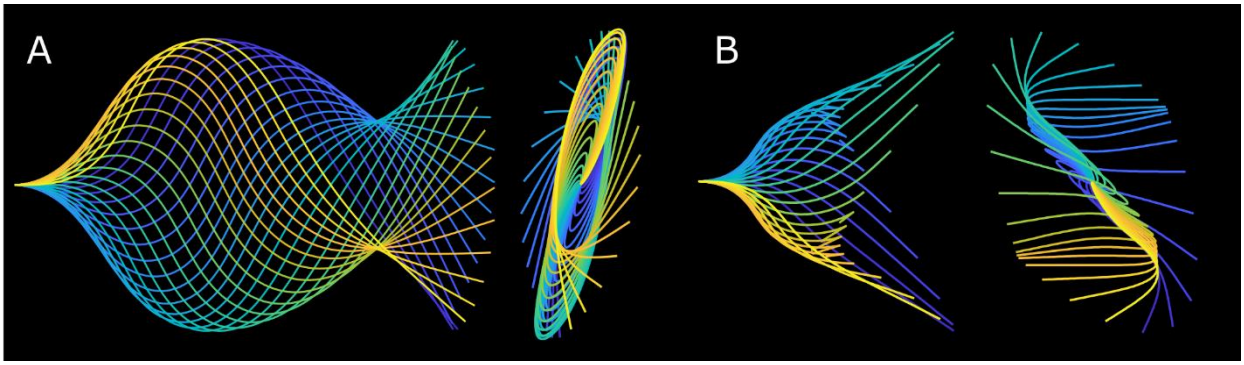

Figure 3.14: Mode shapes with equal stiffness in x and y directions and equal elastic coupling between all doublet pairs. $\bar{p} = 350, \bar{k} = 10^6, RS: NDRC = 10^3, \gamma = -2, \bar{c}_L = \frac{1}{200}$. (A) Mode 1 (mode with most positive real eigenvalue part). $f = 108Hz$ (B) Mode 5. $f = 20Hz$.

3.6.3 Emergence of unstable modes and frequency changes under parameter variations

As control parameters such as $\bar{p}$ are varied, additional unstable modes emerge as the real parts of the eigenvalues become positive (Fig. 3.15A,B). Nonmonotonic behavior of the modal frequencies with respect to $\bar{p}$ is clearly seen in Fig. 3.15B. As additional unstable modes emerge and existing unstable modes become more unstable, the interactions of these modes affect how dynein motors add energy to the system, and how internal and external viscous resistances dissipate energy from the system. Though it is difficult to explain specific frequency changes, this type of behavior is common to variation of several system parameters such as link stiffness (Fig. 3.8) and damping (Fig. 3.9) that affect the coupling between interdoublet motion and axoneme bending.

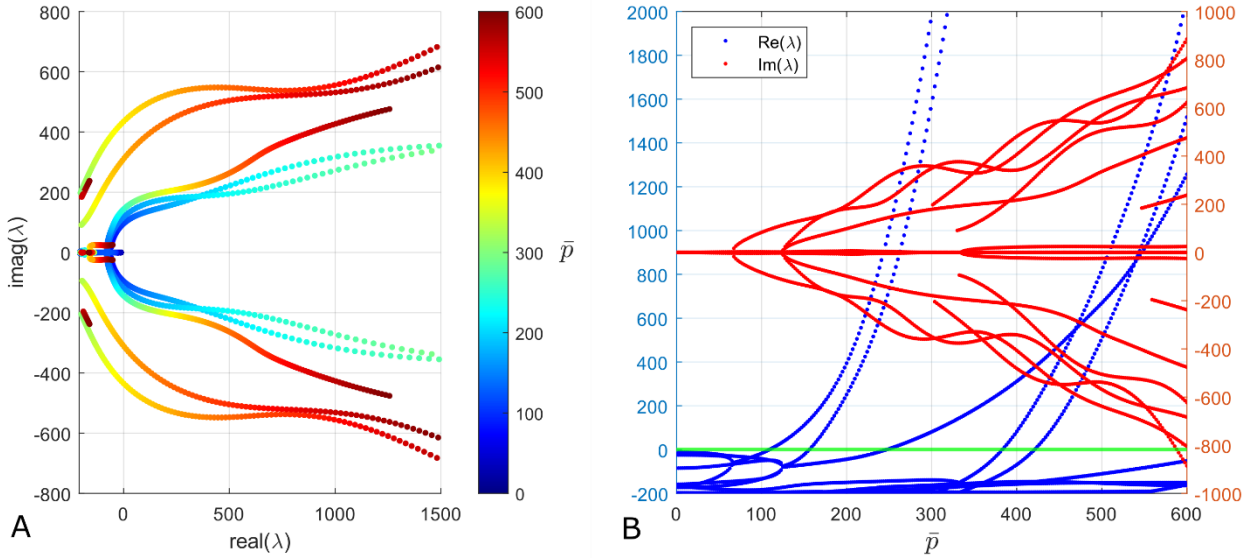

Figure 3.15: As the control parameter $\bar{p}$ is increased, additional unstable modes emerge in the 7-filament system. $\bar{k} = 10^4, RS{:}\,NDRC = 10^3, \bar{c}_L = 1/200, \gamma = 0$. The eigenvalues of the 16 modes with the largest real part are shown here. (A) Plot of the imaginary vs real components of the eigenvalues as $\bar{p}$ is varied. Eigenvalues become unstable as they cross to the right of the $real(\lambda) = 0$ line. (B) Real eigenvalue parts are shown in blue with values on the left axis, imaginary parts are shown in red with labels on the right axis. Modes become unstable as the real part of the eigenvalue becomes positive.

3.6.4 Axonemal twist and torsion during beating

As cilia beat, it has been observed that the axoneme undergoes twisting about its axis [44]. The torsion, or rate of change of the osculating plane [164], was measure in [160]. Plots of axonemal twist rate from the 7-filament model were obtained by averaging the change of angle in the transverse plane of each outer filament with respect to the reference configuration. The derivative of this angle with respect to arc length is the twist rate (Fig. 3.16). Symmetric beat shapes obtained by modal analysis are observed to have a pattern of twist and torsion that repeats with twice the frequency of bending (which has two mirror-image subintervals) (Fig. 3.16A,B,C). *Asymmetric* beating in time-domain simulations has a pattern of twist and torsion with the same period as the beat stroke in the time domain study shown (Fig. 3.16D,E,F). These results invite comparison to the results of Mojiri et al. [160], although a thorough analysis of this behavior is beyond to scope of the current work and will be a subject of future investigation.

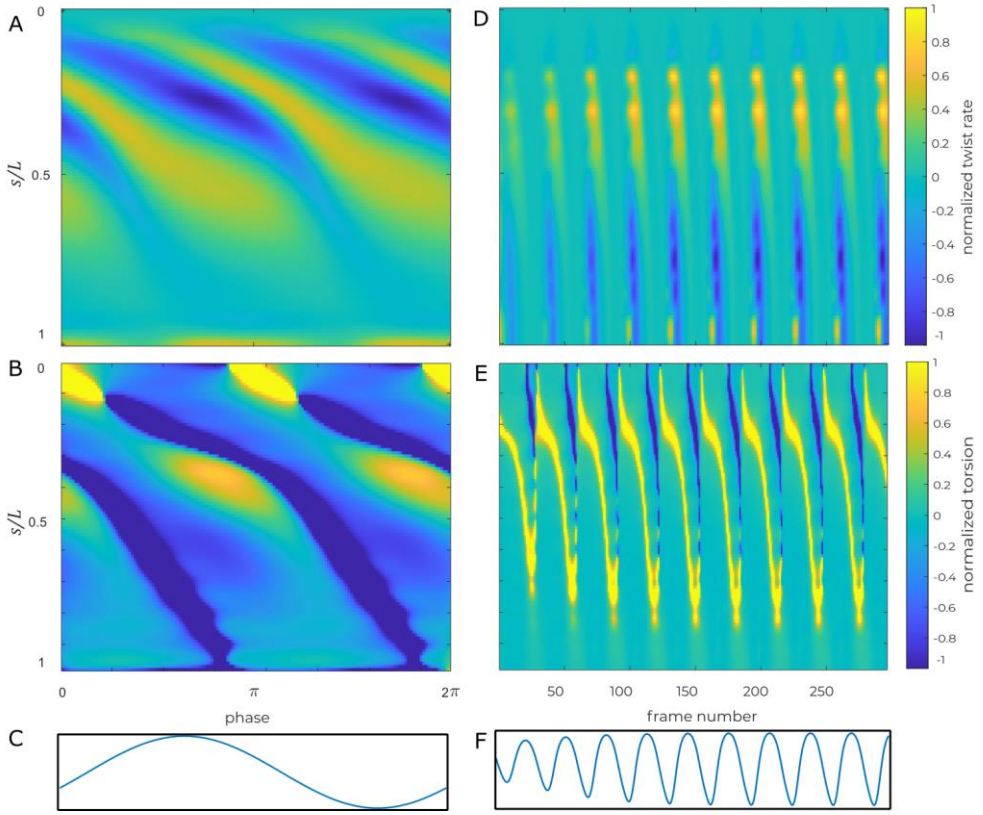

Figure 3.16: Axonemal twist rate and torsion of the ciliary shape in the 7-filament model. As filaments deform under beating, the cross sections undergo an average rotation. The change in this rotation with respect to axial position is the twist rate. Only the relative values are meaningful in these small deformation studies, hence the values are normalized by the maximum absolute value. Positive values indicate a 'right-handed' twist or torsion (like a screw thread), and negative values indicate 'left-handed' twist or torsion. Torsion indicates the rate of change of the osculating plane with respect to the axial distance. (A) Normalized twist rate as a function of normalized axial position ($\frac{s}{L}$; 0 at the base, 1 at the tip) from eigenvalue analysis. $\bar{p} = 250, \bar{k} = 10^6, RS: NDRC = 10^3, \bar{c}_L = \frac{1}{200}$. (B) Normalized torsion as a function of normalized axial position for the same study as (A). (C) Plot of tip displacement as a reference for (A,B). (D) Normalized twist rate from the time-domain simulation with unbalanced moment shown in Fig. 12B. (E) Normalized torsion for the study shown in (D). (F) Plot of tip displacement as a reference for (D,E).

3.6.5 Videos of mode shapes

Animations are available online at https://doi.org/10.6084/m9.figshare.c.6060227.v4 [38]

Animations are of the 7-filament system with parameters $\bar{k}_S = 10^6, \bar{k}_L = 10^3, \bar{c}_L = \frac{1}{200}$. All animations have been plotted by integrating the predicted tangent angle $\theta(s,t)$ (the mean of the tangent angles of the 7 individual filaments) along the cilium to obtain Cartesian coordinates according to $x(s,t) = \int_0^s \cos\theta(\zeta,t)\,d\zeta$, $y(s,t) = \int_0^s \sin\theta(\zeta,t)\,d\zeta$. This allows for a length preserving visualization of the small deformation predictions.

Movie S1. Oscillations of least stable mode at $\bar{p} = 150$ (Fig. 7E)

Movie S2. Oscillations of least stable mode at $\bar{p} = 200$ (Fig. 7F)

Movie S3. Oscillations of least stable mode at $\bar{p} = 400$ with moment gain $\gamma = -2$.

Movie S4. Time domain simulation of beating with moment imbalance (Fig. 3.12B)

Chapter 4: Basal bodies bend in response to ciliary forces[1]

Anthony D. Junker[1,&], Louis G. Woodhams[2,&], Adam W. J. Soh[1], Eileen T. O'Toole[3], Philip V. Bayly[2], Chad G. Pearson[1]
[1] Department of Cell and Developmental Biology, University of Colorado Anschutz Medical Campus, Aurora, CO
[2] Department of Mechanical Engineering and Material Science, Washington University in St. Louis, St. Louis, MO
[3] Department of Molecular, Cellular and Developmental Biology, University of Colorado, Boulder, CO
[&] These authors contributed equally to this work.

Abstract

Motile cilia beat in a coordinated fashion with neighboring cilia to generate fluid flow. Ciliary beating is produced by dynein microtubule (MT) motors that slide doublet MTs within the ciliary axoneme relative to each other to produce asymmetric ciliary bending patterns. *Tetrahymena thermophila* cilia undergo an asymmetric ciliary waveform consisting of a power stroke that generates a propulsive force and a recovery stroke that returns the cilium back to the start of this cycle. Cilia are anchored to the cell cortex by basal bodies (BBs) that are directly coupled to the ciliary doublet MTs. While forces from doublet MT sliding are transmitted to the cell via BBs, the transmission of ciliary forces through BBs is not well understood. Using a combination of genetics, live cell microscopy, EM tomography, and computational modeling, we find that, consistent with ciliary forces imposing directly on BBs, bending patterns in BB triplet MTs are responsive to the ciliary beating pattern. BB bending varies as environmental conditions change the ciliary waveform. The dominant site of BB bending is where striated fibers (SF) attach to BB triplet MTs. Mutants with short SFs that fail to make connections to adjacent BBs exhibit abnormal BB bending patterns supporting a model in which SFs couple ciliary forces between

[1] This chapter is reproduced in its entirety from the article of the same name [34]A. D. Junker, L. G. Woodhams, A. W. J. Soh, E. T. O'Tool, P. V. Bayly, and C. G. Pearson, "Basal bodies bend in response to ciliary forces," *Current Biology*, 2022 (in review). See section 1.5 *Statement of contributions*.

BBs. Finally, loss of the BB stability protein, Poc1, that helps link BB triplet MTs prevents the normal distributed BB bending patterns. Collectively, BBs experience ciliary forces and manage the mechanical coupling of these forces to their surrounding architecture in the cell.

4.1 Introduction

Ciliary beating is utilized by microorganisms and epithelia to move fluid for cell motility and the clearance and circulation of biological fluids [165, 166]. Motile cilia comprise axoneme scaffolds of nine doublet (A-B) microtubules (MTs) radially arranged around a central pair of singlet MTs. Doublet MTs slide and bend by the coordinated activities of axonemal dynein motors, nexin links, and radial spokes [167]. Concerted axonemal bending promotes an asymmetric waveform that drives directed fluid flow and exerts asymmetric mechanical forces to the cell.

Computer models of ciliary and flagellar beating indicate that the ciliary forces needed to bend axonemes dominate over viscous drag forces generated by cilium-fluid interactions [168, 169]. Thus, the major forces acting upon cilia are created by the activities of cilia themselves. *Axonemal* dynein microtubule motors are anchored to A-tubules of the ciliary doublet MTs and the motor domain extends to the B-tubules of adjacent doublet MTs. Dynein activation slides doublet MTs relative to each other [31, 146, 147, 158, 170]. Doublet MT sliding is resisted by nexin links that connect adjacent doublet MTs, thereby promoting axonemal bending. Through concerted dynein activity and interconnection between the doublet MTs, axonemes produce asymmetric and cyclical bending patterns during ciliary beating. The cyclic axonemal trajectory consists of a power stroke, which generates directed fluid flow, and a recovery stroke, which resets the cycle back to the beginning. Several models propose that the asymmetric ciliary waveform is established by asymmetric dynein activation, which spatially and temporally

regulate doublet MT sliding along the axoneme [6, 31, 61, 171-173]. Each model uses dynein-based doublet MT sliding of 25-100 nm to create and propagate ciliary waveforms [31, 171, 173, 174]. The sliding control model hypothesizes that the mechanical properties of the axoneme base can modulate the forces that are transmitted along the axoneme [31, 173, 174]. Flagellar doublet sliding at the axoneme base, so called basal sliding, imposes mechanical forces on the outer dense fibers associated with the axoneme MTs and the connecting piece [173, 175]. The sperm base is predicted to resist doublet MT sliding for propagating axonemal bends [176]. Resistance to basal sliding through variance in asymmetric elastic compliance and deformation of the connecting piece or basal region modulates flagellar beating [5, 31, 171, 173, 175, 177]. Less is understood about how basal sliding forces in cilia at the cell cortex impacts the canonical basal body (BB) structure. It is suggested that the BB at the ciliary base may experience and resist ciliary forces [173, 178]. How axonemal forces are transmitted, resisted, and regulated at the ciliary base remains poorly understood.

Cilia are anchored to promote the transmission of axonemal forces to the cell for both cell motility and epithelial fluid flow. Motile cilia are nucleated, positioned, and anchored to the cell cortex by BBs. BBs comprise nine triplet MTs (A-B-C) where the A-B tubules of BBs are continuous with the axoneme's A-B tubules. The cartwheel (CW) at the BB proximal end comprises a central hub and spokes that connect to the proximal end of the BB triplet MTs. The CW is important for new BB assembly. Moreover, Bld10, a protein that establishes CW-triplet MT connections is required to stabilize BBs against ciliary forces [179, 180]. The nine BB triplet MTs are linked to each other by connections with neighboring triplet MTs (A-C linkers and the helical inner scaffold) [181-183]. Poc1 is a helical inner scaffold protein and loss of Poc1 disrupts A-C linker positioning and spacing [181-183]. Loss of Poc1 also causes ciliary beating-

dependent BB instability and the asymmetric disassembly of specific triplet MTs relative to the axis of the ciliary power stroke [181, 184]. This suggests that the asymmetric forces produced by beating cilia are resisted by BBs. Consistent with this, both BB proteins and MT post-translation modifications that stabilize BBs localize asymmetrically to BBs relative to the direction of the power stroke [180, 185, 186]. BBs are considered structurally rigid because of the many linkages within the BB ultrastructure (triplet MTs, CW, helical inner scaffold, A-C linkers), the presence of stabilizing MT post-translation modifications, and the lack of ciliary dynein [7, 187]. However, sperm that lack conserved BBs structures (CWs and A-C linkers), deform at the connecting piece, and produce sperm head translocations during flagellar beating [124, 173, 188]. This is consistent with axonemal basal sliding force transmission to the sperm head [171, 173, 188, 189]. While BBs are responsive and stabilized against ciliary forces and suggested to deform [178], it is still unclear how asymmetric forces from cilia are transmitted to BBs and how the conserved BB structures respond to ciliary forces.

Cilia and BBs are attached to the surrounding cortical cytoskeleton and plasma membrane by BB-appendage structures [3, 190-197]. These structures help establish and maintain the positioning of BBs and motile cilia. Moreover, BB-appendage structures and the surrounding cytoskeletal network resist the ciliary forces and / or shear forces from ciliary beating and fluid movement [3, 195, 198, 199]. *T. thermophila* BBs possess three BB-appendage structures – two MT bundles facing the cell posterior and right (when viewed from above) of the BB, and one striated fiber (SF) facing the cell anterior [200]. While all BB-appendages appear to be important for BB organization, SFs elongate in response to elevated ciliary forces and gain attachments to the cell cortical cytoskeleton [191, 201]. This was suggested to further anchor BBs to resist the elevated ciliary forces. Moreover, mammalian and *C. elegans* rootlet structures, analogous to

Tetrahymena SFs, are required for ciliary base stability [202, 203]. When the *Tetrahymena* SF length is reduced, BBs and cilia disorganize in a ciliary force-dependent manner [191, 201, 204]. SFs maintain BB organization by contacting anteriorly positioned BBs and the cortical cytoskeleton [191]. Interconnections between neighboring BBs through their SFs are thought to regulate ciliary beating through intracellular coupling [191, 205]. Thus, SFs are responsive to forces from cilia. The inherent asymmetries within *T. thermophila* ciliary units (cilium, BB, and BB-appendages) and the asymmetry of their beat stroke would suggest they establish mechanisms for transmitting and resisting asymmetric mechanical forces from cilia to the BB and cell cortex.

Cilia, BBs, and BB-appendages experience mechanical forces produced by motile cilia. We show that the triplet MTs of BBs bend coincident with cilia bending during the beat stroke. BB bending is focused to the triplet MTs adjacent to the SF connection. Environmental temperature alters BB bending patterns coincident with changes to the ciliary waveform and SF connectivity to neighboring BBs and the cell cortex. BB bending is no longer focused on the SF connection when SF length and inter-BB connections are reduced. Furthermore, the BB stability protein, Poc1, helps propagate normal bending patterns through the BB. This suggests that BBs physically transmit forces from beating cilia into the cell and that the structural properties of BBs and BB-appendages chaperone force transmission.

4.2 Results

4.2.1 Basal bodies bend during ciliary beating

Axonemal doublet MTs are continuous with the A-B MTs of BBs, providing a direct link between ciliary sliding forces and BBs (Appendix C: Fig. C1A; [178]). To test whether forces produced by axonemal dynein sliding affect the canonical BB architecture, swimming *T. thermophila* cells were fixed using high pressure freezing and freeze substitution (HPF-FS) to catch beating cilia and BBs in their dynamic states. Thin section EM images and 3D EM tomography of BBs were visualized relative to cilia at different positions in their beat stroke. Both methods show BB triplet MTs bend in response to ciliary beating while unciliated BBs do not bend (Figs. 4.1 and C1B; [200, 206]). The BB MTs' bend is concave relative to the cell anterior at the beginning of the power stroke (negative curvature) and convex at the end of the power stroke (positive curvature). At the midpoint of the ciliary power stroke, when doublet MTs are not displaced relative to their neighbors, BBs are straighter. Consistent with BB bending as a direct response to ciliary beating, the magnitude of BB bending corresponds with that of the bending cilium (Fig. 4.1B). The primary site of BB bending is near the junction connecting BBs to the SF (Fig. 4.1C). SFs are oriented towards the cell's anterior, opposite to the direction of the ciliary power stroke. Thus, BB bending is asymmetric and maximal at the site of BB connection to the SF that anchors BBs to neighboring BBs and to the cell cortex. SFs may therefore transmit the asymmetric forces produced by cilia into the cell cortex.

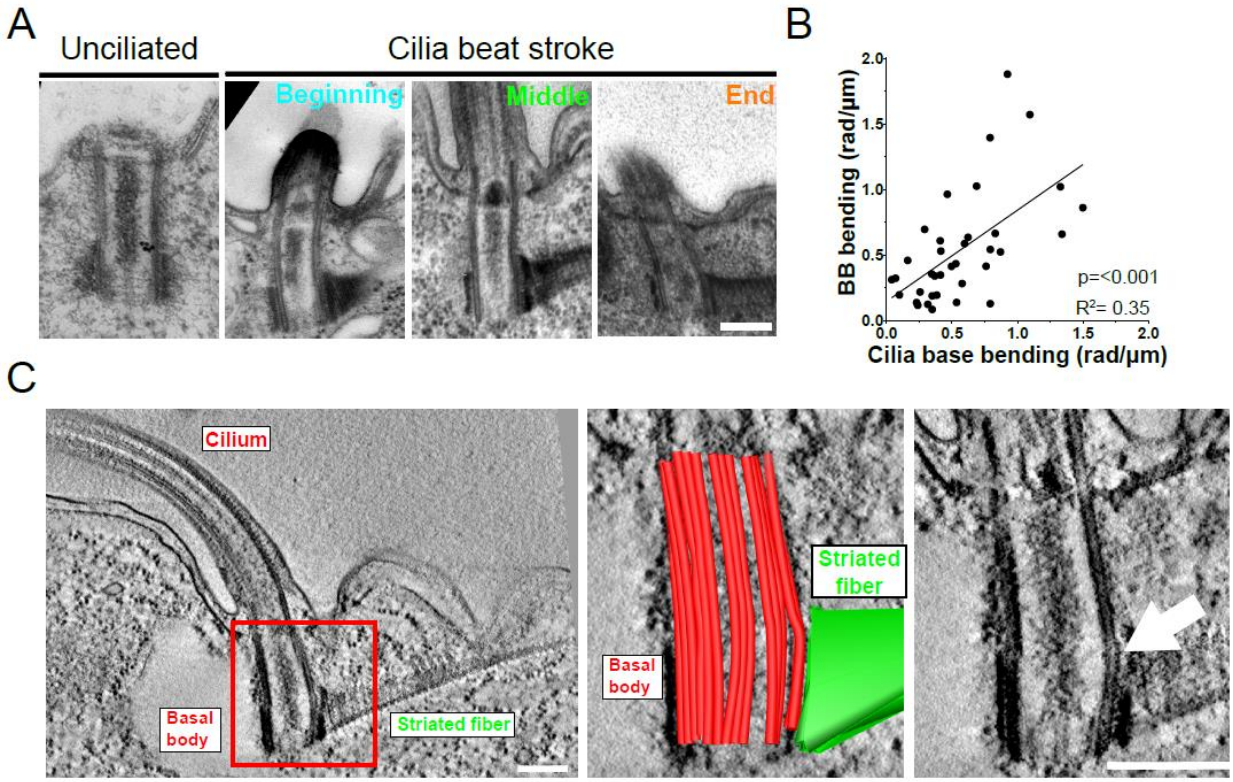

Figure 4.1: **Basal bodies bend consistent with ciliary bending.** (A) Thin (80 nm) section EM images of T. thermophila BBs show triplet MT bending. Unciliated BB triplet MTs are straight. Conversely, in ciliated BBs the bending in the BB's triplet MTs corresponds to the direction of the ciliary bending. Scale bar, 200 nm. n=37 BBs. (B) Increased cilia bending correlates with increased BB bending (p=0.013, R^2=0.16). Measurements were taken from thin section EM images. BB bending (y-axis) is defined as the average angle formed by three points (BB proximal and distal ends and the BB mid-point) of BB MT walls. Cilia bending (x-axis) is defined as the angle formed by three points (the cilium proximal end, 750 nm up the cilium, and a central point in between; Fig. S1E). Data are represented as dots on an x-y plot. n=37 BBs. (C) Representative image of a bent BB and cilium at the end of the power stroke acquired by 3D EM tomography. Left image displays cilium, BB, and SF. Middle image is a single slice view of a model overlay of the BB triplet MTs (red) and SF (green) constructed using 3D modeling. Right image displays a single slice view without the model. White arrow denotes a bending triplet MT. Scale bar, 200 nm.

4.2.2 Patterns of isolated triplet MT curvature relative to cilia position in the beat stroke

The ciliary beat stroke of *T. thermophila* consists of a power stroke moving in the anterior to posterior direction and then a counterclockwise recovery stroke in which the cilium travels parallel to the cell surface in preparation for the next power stroke (viewed from above the cell; [207]). The power stroke produces directed fluid movement for motility. The bending of BBs

relative to the ciliary power stroke at 37°C was analyzed to test when, during the ciliary power stroke, forces are transmitted to specific triplet MTs within BBs. BB curvature was quantified relative to the cilium's position. EM sections of tomograms were scanned to identify ciliated BBs in the medial region of unobstructed cells. For each condition, 50-100 BBs were screened in 10-20 cells. Only BBs in the beginning, middle or end of the power stroke were analyzed. Where tomograms were acquired, BB triplet MTs were modeled in 3-dimensions, and their maximum curvature was quantified (Figs. 4.2 and C2). BB bending differs in amplitude and location depending on the cilium's position in the power stroke. At the power stroke beginning (0-60°), BBs bend in the same direction as their cilium (Figs. 4.2A and C2). The bending is negative (concave curvature relative to cell's anterior-posterior axes) within the triplet MTs and is greatest (max=3.6 rad/μm) at triplet MTs 5 and 6. Triplet MTs 5-6 connect to the SF and the observed bending in these triplet MTs occurs just above the SF attachment. In the middle of the power stroke (61-120°), when the cilium is relatively straight, BBs display less curvature. The curvature is positive (convex curvature relative to the cell's anterior-posterior axes) and distributed around the medial region of the triplet MTs. At the end of the power stroke (121-180°), the cilium is pointed towards the cell's posterior and the BB bends in the same direction. The positive bending is again focused on the anterior triplet MTs 5-6 (max=2.5 rad/μm) adjacent to the SF. At the beginning of the recovery stroke or end of the power stroke, BBs bending is focused on anterior triplet MT 6 (max=3.3 rad/μm). Thus, the individual BB triplet MTs bend with distinct patterns relative to the ciliary position in the power stroke. This bending pattern is focused asymmetrically to triplet MTs 5 and 6 that attach to the SF.

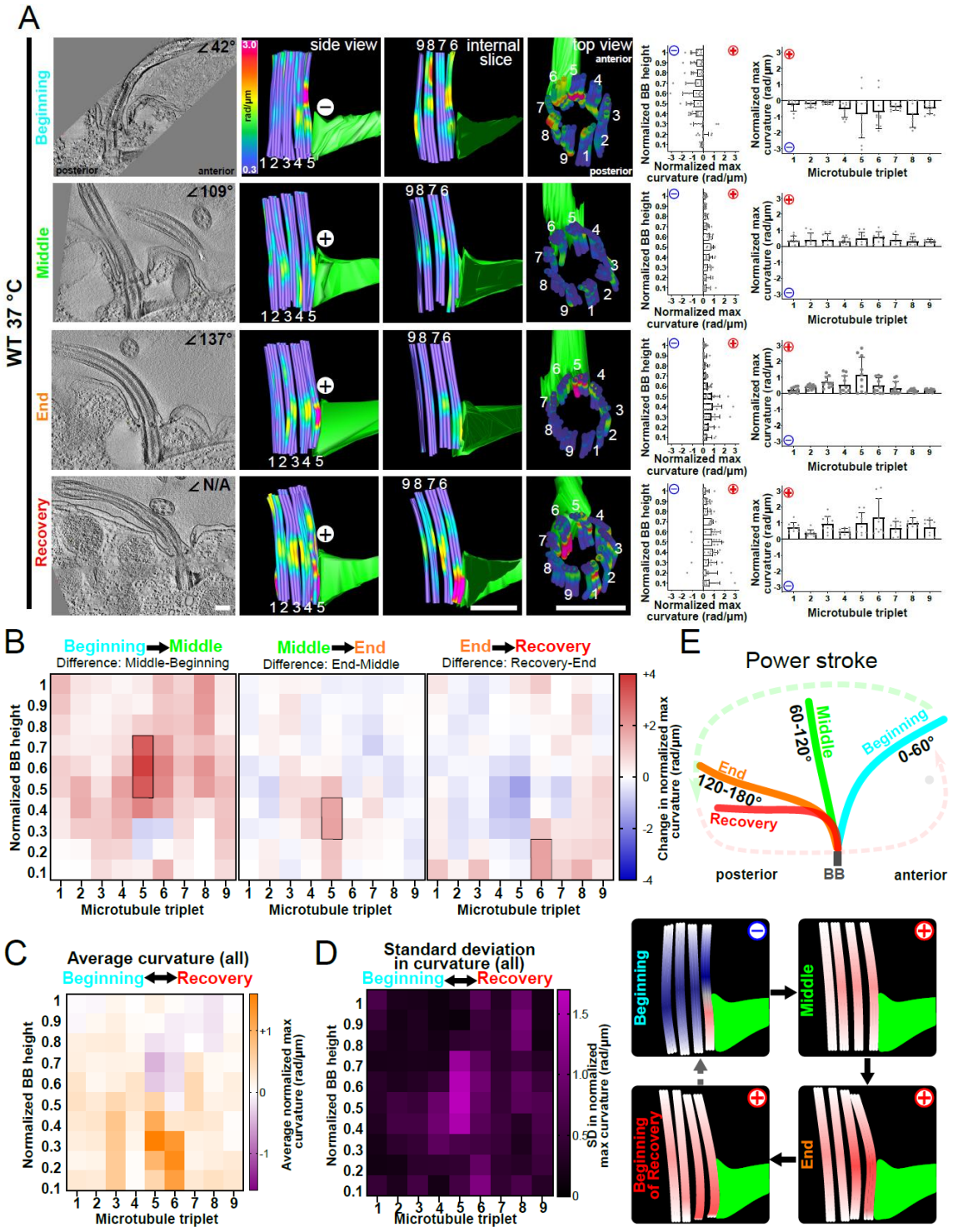

Figure 4.2: **Basal body bending is consistent with its ciliary position in the beat stroke.** (A) BBs display different bending patterns at distinct positions in the beat stroke. Left panels are 8.6 nm max-projected images of EM tomograms. Scale bar, 200 nm. The three middle panels are model views (side view, internal slice view, and top view) of BB triplet MTs from the corresponding BBs in the EM tomogram. Colors indicate curvature of the modeled triplet MTs where "cold" colors (purple-blue) indicate low curvature and "warm" colors indicate high curvature (red-magenta) (range= 0.3 to 3 rad/µm). Right two panels show graphs of the BB proximal to distal axis (left) and normalized maximum BB curvature for each triplet MT (right). The maximum value for each bin (1/10th the length

of the BB) along the BB proximal-distal axis is normalized by subtracting the lowest maximum value of all bins in each BB. The graph represents the means and standard deviations of these normalized maximum values for each proximal to distal bin (left) or each triplet MT (right). n=8 tomograms, 5 BBs analyzed. (B) BB bending depending on the cilium's position along the power stroke. The left heatmap quantifies the change in bending between the beginning and middle of the power stroke. BB bending becomes more positive in the middle of triplet MT 5 (indicated by black boxes: p=>0.05, >75% greatest difference from other bins). The middle heatmap quantifies the change in BB bending between the beginning-middle and middle-end phases of the power stroke. BB bending changes are most prominent at the base of triplet MT 5 where bending becomes more positive (p=>0.05, >75% greatest difference from other bins). The right heatmap indicates the changes in BB bending between the end of the power stroke and the beginning of the recovery stroke. Prominent BB bending is observed at the base of triplet MTs 6-8 where bending becomes more positive (indicated by black boxes; p=>0.05; >75% greatest difference from other bins). The blue and red colors indicate the negative and positive direction of curvature relative to the cell's anterior-posterior axis and the axis of the ciliary power stroke (range= -4 to +4 rad/μm). (C) Average BB bending is greatest at triplet MTs 5-6. Heatmap indicates the average of normalized maximum curvature values from the four BBs in Fig. 2A. Purple indicates negative bending and orange indicates positive bending (range= -1.5 to +1.5 rad/μm). The presence of the greatest positive and negative bending in triplet MTs 5-6 indicates that these triplet MTs experience the greatest structural deformations during the ciliary beat stroke. (D) The greatest standard deviation to BB bending occurs in the middle and at the base of triplet MTs 4-6. Heatmap indicates the standard deviation in the normalized maximum curvature values from the four BBs in Fig. 2A. Black indicates low standard deviation and magenta indicates high standard deviation (range= 0 to 1.5 rad/μm). The presence of the greatest standard deviation in bending at triplet MTs 5-6 indicates that these triplet MTs experience the greatest structural deformations during these events of the ciliary beat stroke. (E) Schematic models represent cilia and BBs through the power stroke (Beginning, Middle, and End) and the onset of the recovery stroke.

To understand the dynamic BB changes, BB bending during the ciliary power stroke was quantified and differences were visualized as heatmaps depicting each triplet MT along the BB axis. Each model analyzed for this dynamic distribution of bending is based on a single BB. Between the beginning and middle of the power stroke, the primary curvature change is in the middle-anterior region of the BB that switches from a negative bending direction to a positive one (Figs. 4.2A-B and C2). Between the middle and end of the power stroke the positive curvature moves downward to the proximal end of triplet MT 5. Between the end of the power stroke and the beginning of the recovery stroke, the positive curvature shifts to triplet MTs 6-8. When BB bending patterns from all four BBs shown in Fig. 4.2A are combined and averaged for each bin, the greatest curvature occurs in the medial (negative curvature) and basal (positive curvature) regions of triplet MTs 5-6 (Fig. 4.2C). The standard deviation of the described maximum curvature indicates which regions of the BB undergo the greatest changes during the

ciliary beat stroke. The greatest standard deviation occurs in the medial and proximal regions of triplet MTs 4-6 (Fig.4.2D). These regions therefore undergo the most physical deformation in triplet MT bending. We posit that these regions must be stabilized to maintain the structural integrity of BBs. Overall, this supports a model for BBs experiencing and absorbing mechanical forces through triplet MT bending (Fig. 4.2E). Furthermore, prominent BB bending is adjacent to the SF (triplet MTs 5-6) and the transverse MTs (triplet MT 4), supporting a model in which SFs and the transverse MTs also experience ciliary forces from BBs and transmit them to neighboring BBs and the cell cortex.

4.2.3 Computer simulation of BB bending in response to ciliary beating

We next tested whether the BB bending patterns observed in our 3D EM tomography studies would be recapitulated in a computational model of ciliary beating that includes the BB. A computational (finite-element) model of the cilium, BB, SF, BB-appendage MTs, and cell cortex was generated in the commercial simulation software COMSOL Multiphysics (COMSOL Multiphysics® v. 5.6. www.comsol.com. COMSOL AB, Stockholm, Sweden.) using the Beam interface within the Structural Mechanics module (Figs. 4.3A and C3). All MT filaments including axonemal doublet MTs and BB triplet MTs are modeled as slender (Euler-Bernoulli) beams. The central pair MTs are modeled as a single beam with a preferential bending direction. Viscous drag is applied using resistive force coefficients [8, 107]. This model uses asymmetric activation of dynein on one side of the axoneme (doublet MTs 5-9) to model the power stroke. Radial spokes in this model are flexible enough to allow sliding between doublets and central pair, but do not support sliding at their attachment points. To avoid undesired structural nonlinearities and ensure convergence of the simulation, relative sliding between adjacent doublet MTs was limited by reducing the maximum distributed dynein force to 125 pN/μm;

deformations were scaled to account for effects of larger forces (see Methods). This analysis predicts a maximum sliding amplitude at the tip between doublet MTs 6 and 7 of 151 nm (Table 3). At the base of the cilium, maximum sliding amplitudes of ~25 nm occurred between doublet MTs 2 and 3. While a rigorous comparison of these sliding amplitudes to experimental data is beyond the scope of the current work, these results show that inter-filament sliding occurs in the model at amplitudes comparable to experimental measures. Further computational model details are provided in the Methods.

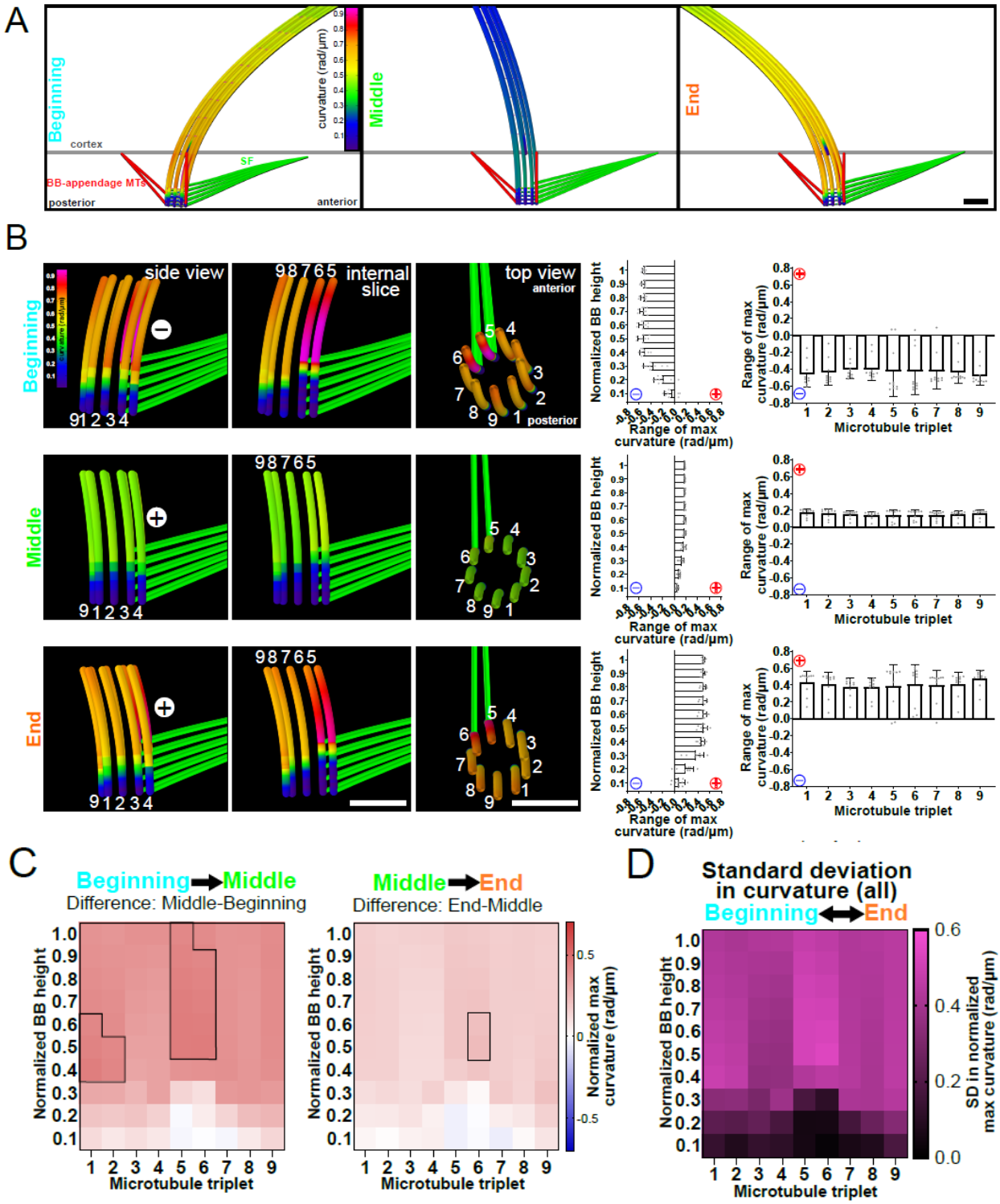

Figure 4.3: **Computer model of BB bending relative to ciliary bending.** (A) Computational model depicting the cilium, BB, SF, and BB-appendage MTs at the beginning, middle, and end of the power stroke. The model was used to determine the parameters required to simulate BB bending in Fig. 3B-C. Scale bar, 200 nm. (B) Computational modeling can replicate the BB bending profiles that are observed in the EM tomograms. Focused bending occurs at triplet MTs 5-6. The three left panels are model views (side view, internal slice, and top view) of BB triplet MTs from computational models. Colors indicate curvature of the modeled triplet MTs where cold colors (purple-blue)

indicate low curvature and warm colors indicate high curvature (red-magenta) (range = 0 to 0.95 rad/μm). Right two panels are graphs showing BB curvature for the BB proximal to distal axis (left) or for each triplet MT (right). Scale bar, 200 nm. (C) BB bending direction changes with ciliary position in the power stroke. The left heatmap quantifies the curvature difference in BB bending between the beginning-middle and middle-end phases of the ciliary beat stroke. BB bending becomes more positive in the middle of triplet MTs 1-2 and middle/top of 5-6 (indicated by black boxes: >75% greatest difference from other bins). The right heatmap quantifies the difference in BB bending between middle and end of ciliary beat stroke. BB bending becomes more positive in the middle of triplet MT 6 (indicated by black boxes: >75% highest difference from other bins). The blue and red colors indicate the direction of curvature relative to the cell's anterior-posterior axis (axis of the ciliary power stroke). Blue and red indicate negative or positive bending (range= -0.6 to +0.6 rad/μm). (D) The largest standard deviation to BB curvature occurs at triplet MTs 5-6. The heatmap indicates the standard deviation in the maximum curvature values from computer modeled BBs at the beginning, middle and end of the power stroke. Black indicates low standard deviation while magenta indicates high standard deviation (range= 0 to 0.6 rad/μm). The presence of the highest standard deviation in bending at triplet MTs 5-6 indicates that these triplet MTs experience the greatest structural deformations during the power stroke.

The BB is anchored to the cell cortex by several attachments: (1) the distal end of the BB is linked to the cortex, (2) post ciliary MTs link the proximal end of BB triplet MT 9 to the cell cortex, (3) transverse MTs link the proximal end of BB triplet MT 4 to the cell cortex, and (4) the SF links triplet MTs 5 and 6 to the cell cortex. All of these structures are required for BB anchorage to resist ciliary forces (Movies 1-8). Detachment of the SF from the cell cortex in the model led to a 6-fold increase in BB front-to-back rocking (periodic rotation in the direction of the predicted cell anterior-posterior axis) and an 11-fold increase in side-to-side rocking, as well as an average 25% reduction to maximum BB bending in triplet MTs 5 and 6 (Table C4). However, removal of the SF attachment places additional burden on the remaining accessory structures and the triplet MTs they are attached to. Maximum bending in triplet MT 4 increased by 30% and maximum bending in triplet MT 9 increased by 85%. Detachment of the post-ciliary MTs at the cell cortex led to a complex rocking motion with a 3-fold increase in BB front-to-back rocking and a 5-fold increase in side-to-side rocking, as well as an average 10% increase in maximum bending in triplet MTs 5 and 6. Detachment of the transverse MTs at the cell cortex led to no significant increase in the amplitude of front-to-back rocking, but a 6-fold increase in side-to-side rocking. Maximum curvature in triplet MT 9 increased 18% at the end of the cycle.

In all cases, removing one of the three BB anchoring structures led to increased bending and twisting in the remaining two. These three structures are analogous to a three-legged stool, as the loss of any one component leads to increases in rocking about the axis defined by the remaining two cortical attachments. Baseline rocking measurements in the computational model (measured at the BB base) show maximum amplitude of 6.8 degrees of front-to-back rocking and 6 degrees of side-to-side rocking. This equates to a predicted displacement of 59 nm. All rocking data are given as the angle swept by a vector tangent to the proximal end of the BB. Experimental rocking data are difficult to obtain due to the lack of a consistent reference against which to measure BB angles.

Consistent with the experimental results in Fig. 4.2, the BB bends coincident with the cilium's position in the beat cycle (Fig. 4.3A-B; Movies 1-2). At the beginning of the power stroke the BB bends negatively, in the middle it is relatively straight, and at the end bending is positive (Fig. 4.3B). At both the beginning and the end of the power stroke the bending is focused to the medial region of triplet MTs 5-6, adjacent to the SF (Fig. C3). The predominant differences between the beginning, middle, and end of the power strokes are also focused on triplet MTs 5-6 (Fig. 4.3C). This is evident by the highest standard deviation of BB curvature at triplet MTs 5-6 (Fig. 4.3D). The BB bending direction and the focus of bending to triplet MTs 5-6 is consistent with the experimental EM tomography data (Fig. 4.2). The principal difference between BBs in the computational model compared to experimental EM tomograms is in the degree to which BB bending is focused at triplet MTs 5-6 at the BB-SF interface. BB bending at triplet MTs 5-6 in the EM tomograms is elevated and less distributed across the other triplet MTs when compared to the computational model (Figs. 4.2 and 4.3). This suggests that additional BB structural elements and/or events may be required in the model. For example, the SF may exert additional

forces to the BB absent from this model or the helical inner scaffold, missing from this model, may be important to create the deformed shape (see below). Differences may also result from the limited bending amplitudes the current computational model can achieve. Despite these differences, the computational simulation supports our hypothesis that axoneme sliding forces can produce the bending patterns in BBs found in our EM tomography. Moreover, this bending is focused to the site of connection between BB triplet MTs 5 and 6 and the SF.

4.2.4 Environmental temperature reverses the direction of BB bending

Ciliary forces can be reduced by decreasing the environmental temperature of culture conditions that also reduce cell motility rates [201, 208]. To test whether altered ciliary forces change BB bending, we reduced the cellular growth temperature from 37°C to 30°C. Surprisingly, BBs at 30°C have a greater maximum curvature across triplet MTs when compared to 37°C (2.8-fold increase; Fig. 4.4A-B). Moreover, the direction of BB curvature at the end of the power stroke is reversed at 30°C (negative) compared to 37°C (positive). At 30°C, BB bending is focused to the medial region of the BB as opposed to the proximal end at 37°C (Fig. 4.4A-B). The greater overall BB bending at 30°C is accompanied by a distribution of the bending to triplet MTs around the entire BB (Figs. 4.4A-B, C2A, and C4A). However, focused bending on triplet MTs 5-6 still occurs just above the BB's attachment to the SF (Fig. 4.4A). These results remain consistent across multiple BBs at different phases of the ciliary beat stroke (Figs. 4.4A, C2, and C4). Thus, the distribution and the directionality of BB curvature changes when ciliary forces are reduced with decreased temperature and asymmetric forces are more equally distributed across triplet MTs.

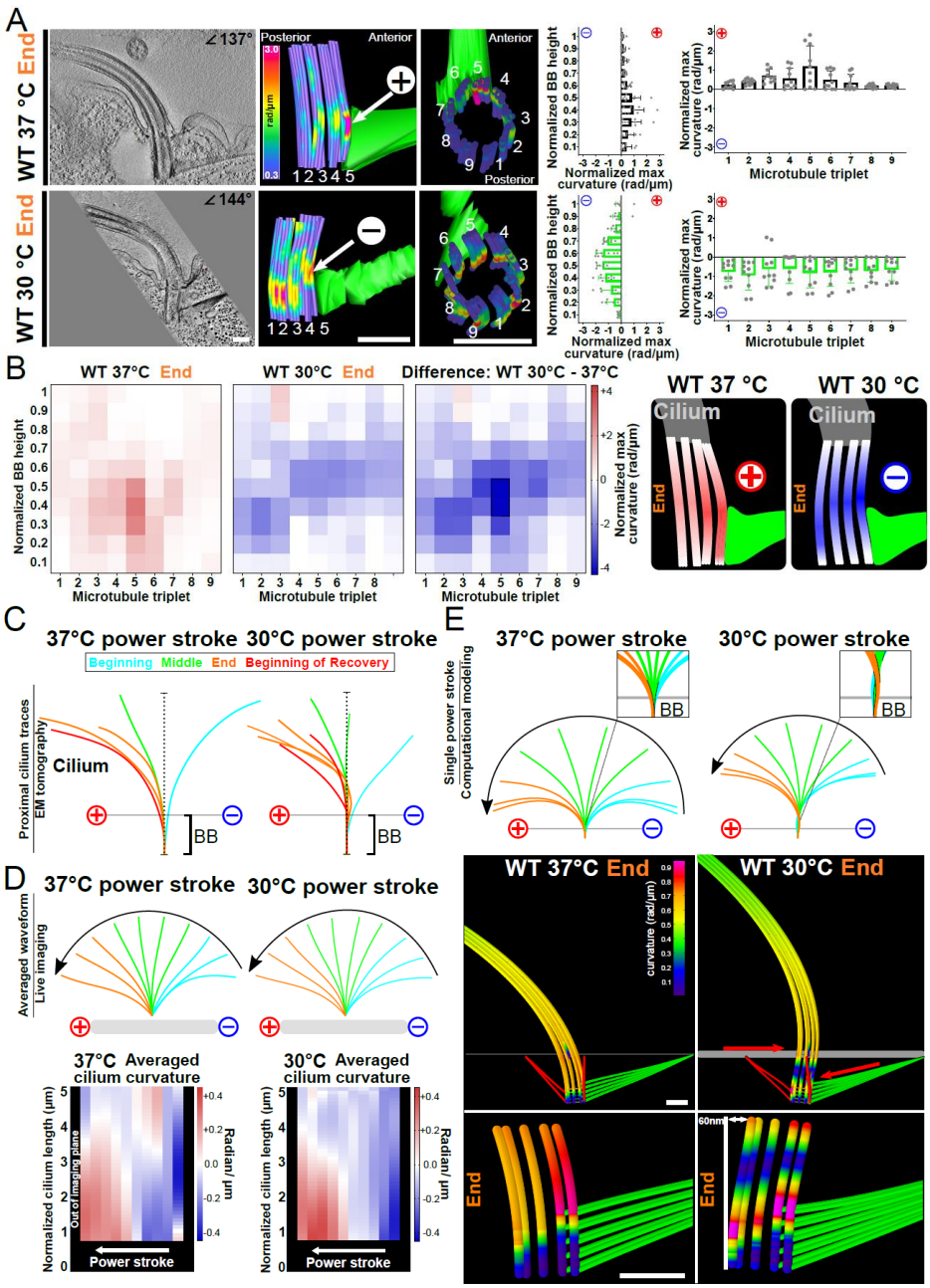

Figure 4.4: **Changes in temperature impact BB bending patterns and ciliary waveform.** (A) The direction of BB bending at the end of the power stroke changes at 30°C. Left panels are 8.6 nm max-projected images of EM tomograms. Scale bar, 200 nm. The two middle panels are model views (side view and top view) of BB triplet MTs from corresponding BBs in EM tomogram. White arrows indicate regions with high curvature. Colors indicate curvature of the modeled triplet MTs where cold colors (purple-blue) indicate low curvature and warm colors indicate high curvature (red-magenta) (range= 0.3 to 3 rad/µm). Right two panels are graphs showing BB curvature for the BB proximal to distal axis (left) or for each triplet MT (right). The maximum value for each bin ($1/10^{th}$ the length of the BB) along the BB proximal-distal axis is normalized by subtracting the lowest maximum value of all bins in each BB. The graph represents the means and standard deviations of these normalized maximum values for each proximal to distal bin (left graph) or for each triplet MT (right graph) n= 15 tomograms, 9 BBs analyzed. (B) Heatmaps show the difference in curvature directionality and location when comparing 37°C and 30°C BBs at the end of the power stroke. The left heatmap shows 37°C BB curvature. The middle heatmap shows 30°C BB curvature. The right heatmap, quantifies the difference between triplet MT bending between 37°C and 30°C. The

greatest difference between 37°C and 30°C BB curvature is in the medial region of the BB at triplet MTs 2-5 and 7 (indicated by black boxes: p=>0.05, >75% highest difference from other bins). The blue and red colors indicate the direction of curvature relative to the cell's anterior-posterior axis (axis of the ciliary power stroke). Blue indicates negative bending which is towards the cell anterior. Red indicates positive bending which is towards the cell posterior (range= -3.3 to +3.3 rad/μm). Schematic model on the right represents differences at the end of the ciliary power stroke between 37°C and 30°C. (C) Cilia at 30°C compared to 37°C display more curvature at the proximal region of the cilium at the end of the power stroke. The curvature of cilia in EM tomograms is represented by traces along the anterior wall of the BB and cilium. Colors indicate the relative position of the cilium in the power stroke, beginning (cyan), middle (green), end (orange), and beginning of the recovery stroke (red). Traces include the BB and approximately the proximal 1 μm of the cilium depending on their orientation within the tomogram. (D) Cilia at 30°C display more curvature than cilia at 37°C throughout the power stroke. Average ciliary curvature is displayed as colored lines. Colors indicate the relative position of the cilium in the beginning (cyan), middle (green), and end (orange) of the power stroke. Heatmaps of cilia curvature show that 30°C cilia curvature is greatest in the proximal regions of cilia at the beginning and end of the power stroke. The blue and red colors indicate the direction of cilium curvature relative to the cell's anterior-posterior axis (axis of the ciliary power stroke). Blue indicates negative bending which is towards the cell anterior. Red indicates positive bending which is towards the cell posterior (range= -0.5 to +0.5 rad/μm). (E) Computer simulated BB bending can recapitulate negative bending and ciliary waveform through the addition of a posteriorly-oriented force on the SF attachment and an anteriorly-oriented force on the cortex attachment resulting in a 60 nm relative displacement along the anterior-posterior axis. This model mimics forces from coupled BBs, both anterior and posterior, and from forces transmitted through the SF from neighboring cilia. The resulting shear and rotation of the BB reorient the cilium at its base with respect to the 37°C model (hence the clockwise rotation of the 30°C cilium in the figure).

Because BB bending was increased and in the opposite direction when ciliary forces were reduced by lowering the temperature, we asked whether the ciliary waveform was different between these conditions. Using live cell differential interference contrast (DIC) microscopy at high frame rates, we visualized ciliary beating of immobilized *T. thermophila* cells at different environmental temperatures. Immobilization of *T. thermophila* cells was performed via a magnetism-based approach [36]. Consistent with an elevated *T. thermophila* swim speed at higher temperatures, the cilium beat frequency (CBF) at 37°C was elevated by approximately 10% as compared to 30°C. Quantification of cilia curvature revealed that the ciliary waveform changes when *T. thermophila* cells are cultured at 30°C compared to 37°C (Fig. 4.4C-D). At 30°C, the magnitude of cilia bending increases. The increased bending is most prominent at the proximal end of the cilium (closest to the BB) at the beginning and end of the power stroke. Therefore, bending patterns of BBs and their cilia are altered based on the cell's environmental response to temperature.

That BB bending and cilia waveform change when temperatures are lowered was unexpected. To gain insight into how this may occur, computational models were utilized to determine the conditions that recapitulate similar BB bending patterns. The WT power stroke at 30°C exhibits a greater degree of 'counterbend' (a reversal of the ciliary curvature at the distal end of the cilium) as compared to the 37°C power stroke (Fig. 4.4C-D). To test whether the cause of the ciliary counterbend could also be responsible for the reversal of curvature in the BB at 30°C, we created counterbend in the cilium by two different methods. The dynein activation model relies on asymmetric activation of dynein on one side of the axoneme. First, the dynein activation model was altered by replacing the longitudinally uniform, temporally varying activation pattern with a sinusoidal spatial activation pattern (with an amplitude 250 pN/μm and wavelength 7.5 nm) that propagates distally to create the beat stroke. While this change did create a counterbend in the cilium, it did not reverse the bending of the BB. Second, an increased shear stiffness was applied at the distal end of the cilium by stiffening the distal array of radial spokes to the stiffness of the doublets. This created a counterbend in the cilium and reduced the overall beating amplitude but did not reverse bending in the BB. None of the tested manipulations of the axoneme produced BB bending consistent with the negative BB bending observed at the end of the power stroke in our experimental results. This suggests that the changes to the ciliary waveform are not responsible for the changes to the BB bending pattern that we observe at 30°C. SFs are shorter and have fewer cortical cytoskeleton attachments when cells are grown at 30°C compared to 37°C [191, 201]. The mechanical and structural properties of SFs therefore change at lower temperatures. We hypothesized that force transmission (from neighboring BBs) through the SF onto the BB could produce the bending patterns observed in the EM tomography. To test this in the computational model, a translational force was exerted on the distal end of the SF such

that it would transmit into the BB (Fig. 4.4E and Movies 9-10). This represents the force created by the SF connection to the pcMTs of the anterior BB and its surrounding cell cortex [191, 206]. A force in the opposite direction was applied to the BB distal end attached to the cell cortex, representing force transmitted from the posterior BB SF to the pcMTs. Adjacent *Tetrahymena* cilia in the cell medial region beat with a temporal delay, whereby the posteriorly positioned cilium is approximately 3 msec ahead in its beat cycle [36]. To account for this temporal delay, the applied forces were coordinated with the ciliary beat cycle. Thus, the force that is exerted by the anterior BB is a function of its cilium's position during the power stroke, which is 3 msec behind in its beat cycle relative to its posterior cilium neighbor. The combination of these forces resulted in a 60 nm relative translation of the distal end of the BB to the proximal end during the power stroke (Fig. 4.4E). A force amplitude of 900 pN (estimated 3600 pN at large deformation) was required to create the BB counterbend that has a comparable magnitude to those observed in EM tomography results. This magnitude is comparable to the total shear force produced between two adjacent doublet MTs if all the dynein arms generate ~2 pN each.

Indeed, imposing this change to the SF forces produced a negative bending pattern of the BB similar to that observed by EM tomography (Fig. 4.4E). Furthermore, forces transmitted from SFs into BBs created a counterbend at the ciliary base suggesting it is possible for intracellular SF forces to alter ciliary power strokes by BB bending and force transmission to the cilium (Fig. 4.4E). This suggests a model in which changes to BB bending upon environmental temperature change occurs through altered force transmission by SFs. While much remains to be understood about these forces, they may be responsible for propagating mechanical coupling of neighboring BBs and impacting the ciliary waveform. These results highlight the importance of SFs in promoting cilia and BB dynamics.

4.2.5 SFs focus BB bending to triplet MTs 5 and 6

BB bending concentrates at the site of connection between BBs and SFs suggesting that SFs are a focal point where ciliary forces are imposed upon BBs. To test if SFs are responsible for focused BB bending through their attachments to neighboring BBs, we quantified BB bending in a *T. thermophila* genetic mutant with short SFs that lose connections with neighboring BBs (*disA-1*; [191, 201, 204]). BB bending was compared between WT and *disA-1* cells at 30°C with cilia at matching positions at the end of the power stroke. Unlike WT BBs, *disA-1* BBs had increased levels of triplet MT curvature in both positive and negative directions within the same BB (Fig. 4.5). This bending or buckling is distributed throughout BBs without focused bending at triplet MTs 5-6, as observed in WT BBs (Figs. 4.5 and C5). BB bending is observed at other triplet MTs (e.g., triplet MT 4) that are not connected to SFs but are linked to the transverse MTs (Figs. 4.5B and C5A-B). Additionally, WT BBs at 30°C bend primarily in the BB's medial region while *disA-1* BBs bend throughout the BB length (Fig. 4.5A-B). Thus, SF length or connectivity to neighboring BBs and the cell cortex is important for focused bending of the medial region of BB triplet MTs 5-6 that normally connect to SFs.

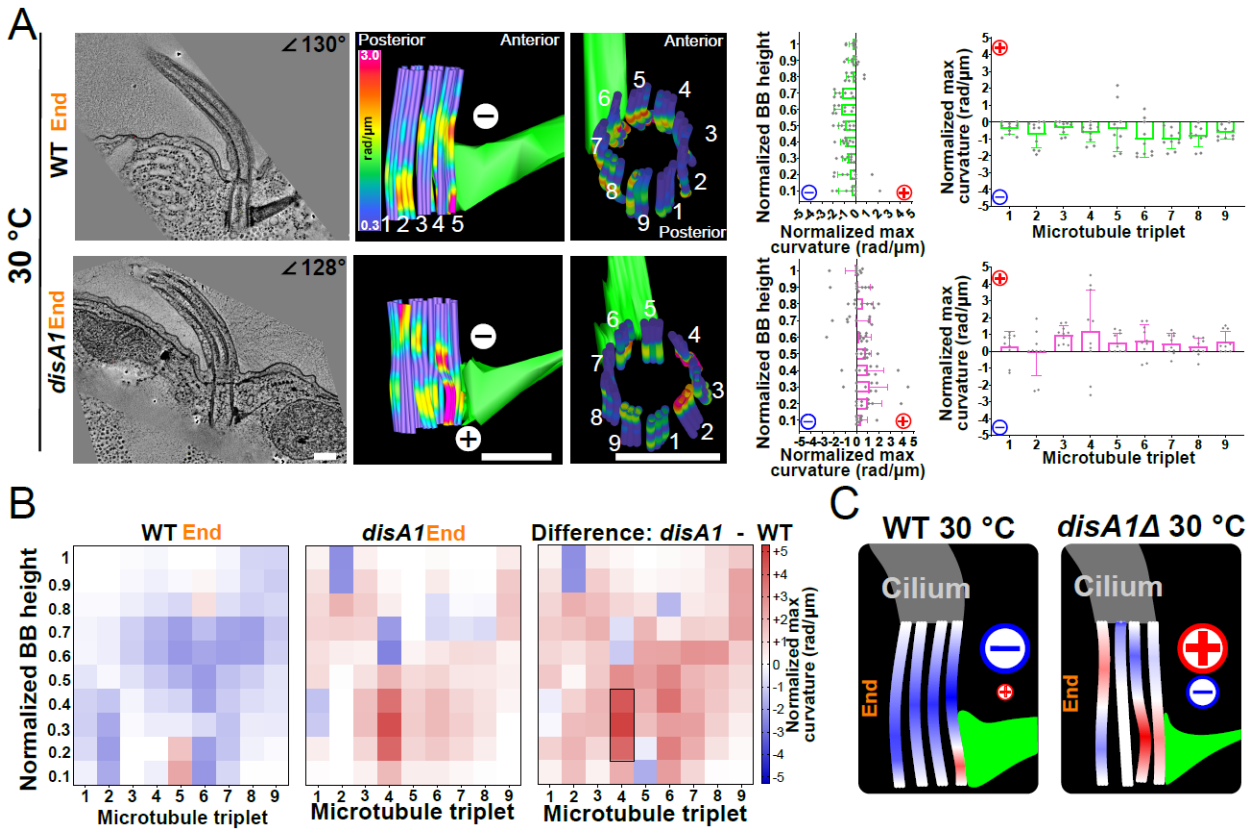

Figure 4.5: **SFs focus bending to specific BB regions.** (A) The direction and locations of BB bending at the end of the power stroke change in disA-1 mutants have short SFs and reduced connections to neighboring BBs and the cell cortex. Left panels are 8.6 nm max-projected images of EM tomograms at 30°C. Scale bar, 200 nm. The two middle panels are model views (side view and top view) of BB triplet MTs from corresponding BBs in EM tomogram. Colors indicate curvature of the modeled triplet MTs where cold colors (purple-blue) indicate low curvature and warm colors indicate high curvature (red-magenta) (range= 0.3 to 3 rad/µm). Right two panels are graphs showing BB curvature for the BB proximal to distal axis (left) or for each triplet MT (right). The maximum value for each bin (1/10th the length of the BB) along the BB proximal-distal axis is normalized by subtracting the lowest maximum value of all bins in each BB. The graph represents the means and standard deviations of these normalized maximum values for each proximal to distal bin (left graph) or each triplet MT (right graph). n=7 tomograms, 3 BBs analyzed. (B) SF connections are important for consistent negative bending that is focused at triplet MTs 5-6. The left heatmap shows 30°C WT BB curvature. The middle heatmap show 30°C disA-1 BB curvature. The right heatmap quantifies the difference between triplet MT bending between WT and disA-1 BB curvature. The greatest difference between WT and disA-1 BB curvature is in the elevated positive bending in triplet MT 4 (indicated by black boxes: p=>0.05, >75% highest difference from other bins). The blue and red colors indicate the direction of curvature relative to the cell's anterior-posterior axis (axis of the ciliary power stroke). Blue indicates negative bending which is towards the cell anterior. Red indicates positive bending which is towards the cell posterior (range= -5.3 to +5.3 rad/µm). (C) SF connections are important for negative BB curvature and focused bending at triplet MTs 5-6. Schematic model shows disA-1 BBs have both positive and negative curvature with positive curvature predominating across the BB compared to WT.

A major difference between WT and *disA-1* BB bending at 30°C is that *disA-1* BB bending is mostly positive while WT BB bending is mostly negative (Fig.4.5B). This demonstrates

experimentally that SFs at 30°C promote negative bending in BBs at the end of the power stroke as *disA-1* mutant cell SFs are disconnected from neighboring BBs and the cell cortex and should therefore weaken force transmission to BBs. The lack of negative bending in *disA-1* BBs is consistent with our computational simulation that reproduced negative bending in WT BBs by the addition of forces transmitted through SFs (Fig. 4.4E). We hypothesize that SF linkages to the anterior BB allows for physical coupling between neighboring BBs that regulate BB bending and ciliary beating. Importantly, BBs in *disA-1* cells do not display WT 37°C BB bending patterns as focal bending at the medial-proximal regions of triplet MTs 5-6 were not observed. Moreover, when the SF is detached in the computer simulations, we observe a similar result. The mean curvature over the entire BB at the end of the beat stroke is similar between the two models (approximately 0.4 rad/μm). However, the maximum curvature in triplet MTs 5-6 in the baseline model is 0.92 rad/μm but exhibits a 20% reduction in the detached SF model (0.74 rad/μm). Removal of the SF led to an increase in curvature in triplet MT 9 from 0.73 in the baseline model to 1.28 rad/μm in the detached SF model. Triplet MT 9 attaches to the pcMTs that link to the cell cortex and this suggests that a balance between anchorage structures is important for BB bending. This indicates that SF length and connectivity to neighboring BBs and/or the cell cortex is important for transmission of ciliary forces through triplet MTs 5-6. We predict that this asymmetric force transmission towards the regions of the BB that face the cell anterior is utilized for directed cell motility.

4.2.6 Poc1 is required for dissipating forces in BB bending to neighboring triplet MTs

BB triplet MTs are laterally interconnected by structures including the A-C linkers and the helical inner scaffold [181-183]. The Poc1 protein resides at the BB helical inner scaffold and is enriched at the proximal region of BBs [180, 181, 183, 184]. When Poc1 is lost, A-C linker spacing is disrupted, most commonly triplet MTs 1-2 facing the cell posterior disassemble, and BB instability increases with increasing ciliary force [180, 181, 184]. To test whether BB triplet MT interconnectivity is important for normal BB bending, we quantified triplet MT bending in WT and *poc1Δ* BBs at 30°C. In contrast to WT BBs, *poc1Δ* BBs exhibit isolated regions of both positive and negative triplet MT bending within the same BB, particularly on triplet MT 5 (Figs. 4.6A and C6). Curvature in WT BBs at 30°C is distributed across multiple triplet MTs. Importantly, this was not observed in *poc1Δ* BBs (Figs. 4.6A and C6). *poc1Δ* BB bending is specifically enriched at triplet MT 5 which exhibits a higher degree of curvature in both the positive and negative directions (Fig.4.6A-B). The bending is not propagated to neighboring triplet MTs. In addition, the overall direction of *poc1Δ* BB bending is positive as compared to the negative bending in WT BBs at 30°C (Fig. 4.6B). In the *poc1Δ*, negative bending is limited to triplet MT 5 and is absent in neighboring triplets. This suggests that forces from SFs are received by triplet MT 5 but are not effectively dissipated to neighboring triplet MTs in *poc1Δ* cells. These data support a model where Poc1, by promoting linkage between neighboring triplet MTs, is important for the distribution of forces between triplet MTs (Fig. 4.6C; [182]).

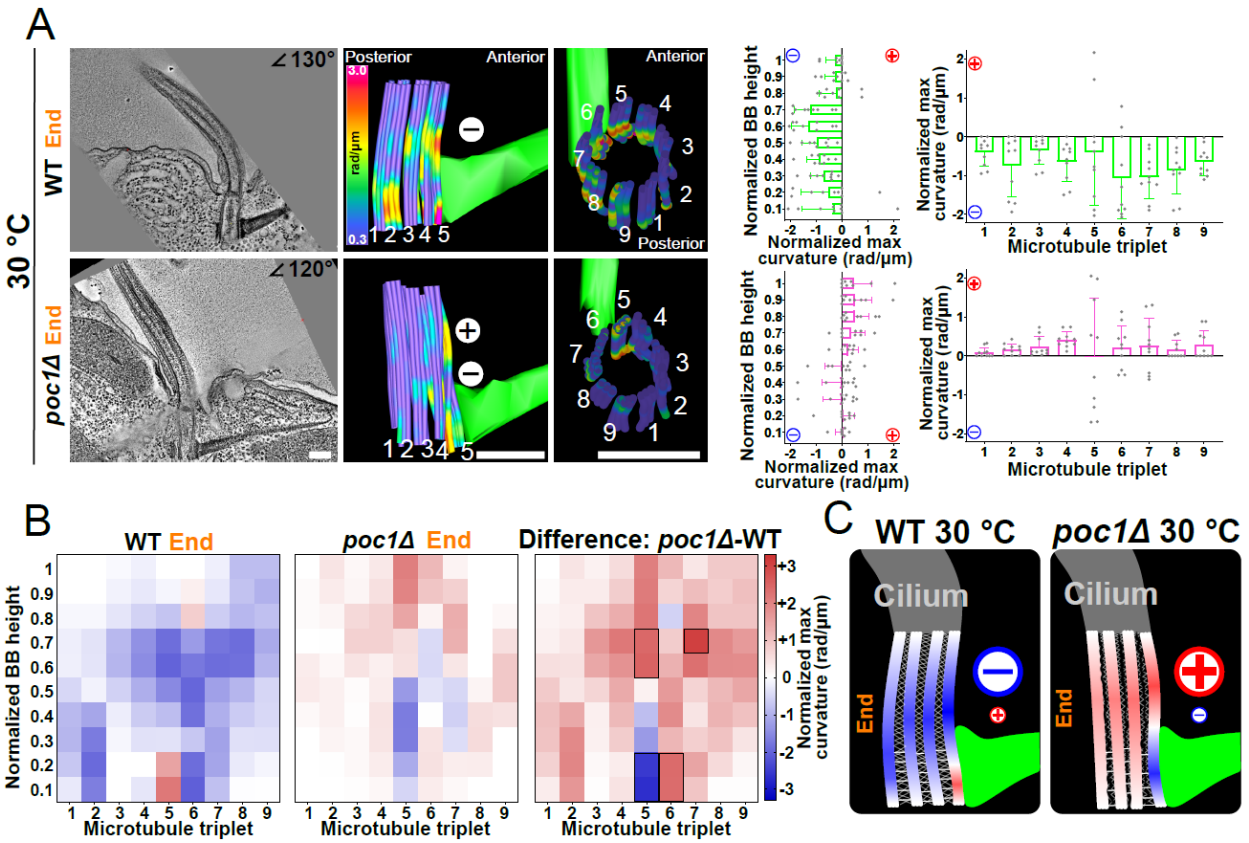

Figure 4.6: **Poc1 distributes coordinated BB bending.** (A) The direction and location of BB bending at the end of the power stroke change in poc1Δ at 30°C. Left panels are 8.6 nm max-projected images of EM tomograms at 30°C. The two middle panels on the left are model views (side view and top view) of BB triplet MTs from corresponding BBs in EM tomogram. Colors indicate curvature of the modeled triplet MTs where cold colors (purple-blue) indicate low curvature and warm colors indicate high curvature (red-magenta) (range= 0.3 to 3 rad/µm). Right two panels are graphs showing BB curvature for the BB proximal to distal axis (left) or for each triplet MT (right). Each maximum value for a proximal-distal bin (1/10th the length of the BB) is normalized through the subtraction of the smallest maximum value in each BB. The graph represents the means and standard deviations of these normalized maximum values for each triplet MT or proximal distal bin. Scale bars, 200 µm. n=12 tomograms, 3 BBs analyzed. (B) poc1Δ BBs show both positive and negative bending focused on triplet MT 5. The heatmap on the left shows BB curvature in 30°C WT BBs. The heatmap in the middle shows BB curvature in 30°C poc1Δ BBs. The right heatmap quantifies the difference between WT and poc1Δ BBs. The greatest difference between WT and poc1Δ BBs are in triplet MTs 5-7 which display curvature in opposing directions (indicated by black boxes: p=>0.05, >75% highest difference from other bins). The blue and red colors indicate the direction of curvature relative to the cell's anterior-posterior axis (axis of the ciliary power stroke). Blue indicates negative bending which is towards the cell anterior. Red indicates positive bending which is towards the cell posterior (range= -3.3 to +3.3 rad/µm). (C) Inner scaffold and A-C linker integrity is important for distributing negative curvature. Schematic model shows poc1Δ BBs have high positive and negative curvature on triplet MT 5 which is not effectively propagated across the BB compared to WT.

poc1Δ BBs can also exhibit highly variable curvature in triplet MTs 1, 7, 8, and 9 (Fig. C6C-E). This region of high variability corresponds to the triplet MTs that face the cell posterior and specifically disassemble when experiencing ciliary forces in *poc1Δ* cells (Fig. C6F; [181]). We suggest that the elevated and variable curvature in these triplet MTs contributes to BB instability

in *poc1Δ* cells. This elevated and variable triplet MT curvature may be due to defective transmission of ciliary forces between triplet MTs resulting in local focal bending events that cannot be redistributed to neighboring triplet MTs. Further studies are required to identify the key events that produce BB instability in *poc1Δ* cells. Our studies suggest that most bending occurs at triplet MT 5 and may be stabilized by SF attachment. Conversely, variable bending in posterior facing triplet MTs 1, 2, 8, and 9 may precipitate in their instability, breakage, and loss. These MTs were found to disassemble before complete loss of the BB [181]. To further capture these disassembly events, we performed thin section EM of chemically fixed *poc1Δ* cells at high temperatures to escalate BB disassembly. As found previously, we observed weak triplet MT breakage near the middle of the BB but this appears to be a transient event that is difficult to capture in our fixed cell EM analyses (Fig.C6F-H; [184]). Further studies of high-resolution defects associated with *poc1Δ* BBs are necessary. In summary, triplet MT interconnectivity contributed by the helical inner scaffold and/or the A-C linkers produce consistent and distributed BB bending patterns and likely act to distribute forces from both cilia and SFs (Fig. 4.6C).

4.2.7 Improved simulation using triplet MT connections and SF forces

To simulate the effect of Poc1 loss on BBs, the stiffness of the A-C linkers in the model was reduced by an order of magnitude. This led to an increase in BB rocking concentrated in the front-to-back direction (Table 4), an increase in the maximum curvature in triplet MTs connected to external structures (triplet MTs 4, 5, 6, and 9), and a relative decrease in the maximum curvature of triplet MTs not connected to external structures (Table 4). Interestingly, the average interdoublet shearing at the transition zone increased by ~20% when the A-C linker stiffness was reduced in the model, indicating an increase in BB shearing.

Because Poc1 also localizes to the helical inner scaffold, we next included a predicted helical inner scaffold into the model [209]. The overall dimensions of the modeled helical inner scaffold (155 nm diameter and extending 150-450 nm from the base of the BB) were based on the structure obtained for *Paramecium tetraurelia* BBs [209]. The helical inner scaffold was parameterized by assigning it an elastic modulus of ~1 GPa and varying the diameter of the beams from 2-16 nm. At small diameters (2 nm), the helical inner scaffold had a minimal effect on the overall BB bending, but as the diameters were increased, overall BB bending decreased. Thus, the helical inner scaffold has a stabilizing effect on BBs.

We hypothesized that the helical inner scaffold may account for some of the observed differences between the EM tomography and the computer model, including the concentration of the medial bend at the end of the power stroke that was observed in the EM tomography (Fig. 4.2A). In contrast, the computer model exhibited a more evenly distributed bend (Fig. 4.3B). Indeed, in the model at low to moderate helical inner scaffold stiffness, the helical inner scaffold suppresses curvature in the distal region of triplet MTs 5-6, while having a minimal impact on the curvature of those triplets adjacent to the SF (Fig. C3D). However, we were not able to completely recreate the medial to distal diminishing average curvature observed in the EM tomography. A possible explanation for these differences is material nonlinearities not accounted for in the model. Regions of elevated curvature adjacent to the SF in triplet MTs 5-6 in the model may lead to increased nonlinear local bending (‘kinking’) that more closely resembles the EM tomography.

Though the 37°C model captures many aspects of the deformations observed by EM tomography, as noted above, differences remain (Fig. C3A). Significantly, the average BB curvature at 37°C decreases from the medial to the distal region thereby concentrating medial

curvature at the end of the power stroke (Fig. 4.2A). In the model, the average curvature remains nearly constant. In our initial model (Fig. 4.3), the SF at 37°C is longer and attaches to the cell cortex, causing it to be a stationary structure, whereas the shorter SF at 30°C is detached from the cell cortex and is therefore able to transmit motion and force between the adjacent BBs that the SF couples. However, to determine if SF pushing and/or pulling forces could be responsible for differences between the model and the data, we modulated the phase and magnitude of the periodic force applied to the SF attachment point. If the SF force transmission is reversed in phase from the 30°C model – pulling on the BB during the power stroke and pushing on the BB during the recovery stroke – it magnifies the curvature of the medial region of the BB (with a 2-fold increase in triplet MTs 5-6; Fig. C3D). The overall effect of this is that the average curvature is elevated in the medial region. However, the distal curvatures are not as low as those observed in the EM tomography.

To attempt to reduce distal curvatures in the model, the reverse SF force was applied to the model including the helical inner scaffold. Though adding the helical inner scaffold did reduce curvature in the distal region, it did not reduce the average curvature in that region to below the levels of curvature in the proximal region, as observed in the EM tomography (Fig. 4.2A). The helical inner scaffold in this case has the additional effect of transmitting the elevated curvature adjacent to the SF in triplet MTs 5-6 to triplet MTs 7-8, which was not observed in the EM tomography. Thus, additional modeling parameters are required to resolve the bending observed in the EM tomography.

4.3 Discussion

We illustrate how BBs receive and transmit mechanical forces imposed by beating cilia (Graphical Abstract). Previously, BBs were thought to be rigid and stable structures. We show

BB structural deformations via triplet MT bending that correspond with ciliary beating. Temperature-dependent changes to the BB bending pattern are coincident with alterations to ciliary waveform. SFs are critical for focusing BB bending to sites of connection between BBs and SFs. This is consistent with a physical model where forces from asymmetric ciliary beating are transmitted to the cell by SFs. Moreover, these forces likely promote BB dynamics allowing force transmission to neighboring BBs, helping to coordinate ciliary beating. Finally, the structural integrity of the helical inner scaffold and / or A-C linkers are important for ciliary force distribution and generalized BB bending patterns. Coordinating these activities facilitate rapid cilia dependent hydrodynamic flow that responds to environmental conditions.

4.3.1 Flagellar and ciliary basal deformation

Pioneering studies in mammalian and urchin sperm set the stage for how basal sliding forces are propagated to the base of the axoneme. In the case of sperm flagella, doublet microtubules link to the connecting piece at the base of the cilium via outer dense fibers. Sliding forces then impose both compressive and tensile forces upon the connecting piece thereby creating deformations and changes to the position of the sperm head. Moreover, changes to resistance to these sliding forces by the basal domain are proposed to impact flagellar beating by controlling switching in beating direction and changes to the waveform. A more rigid base was proposed to anchor cilia and produce a more rigid waveform. Thus, basal sliding forces are both imposed upon the base of the flagellum and tune flagellar activities. A key question is whether and how the connecting piece at the flagellum and the BB at the cilium share similar activities in limited basal sliding and controlling ciliary beating [31, 173, 178].

Our studies show that BBs experience basal sliding forces that causes bending to the triplet microtubules. In contrast to changes in the sperm head position and forward motility found in

sperm flagella, ciliary beating imposes mechanical bending at triplet MTs experiencing compression. This bending requires attachments to SFs that, along with post-ciliary MTs and transverse MTs, anchor BBs and cilia to each other and to the cell cortex. Changes to SF anchorage and movement may be responsible for changes to the ciliary waveform. This is consistent with intracellular coupling found for *Chlamydomonas* flagella [205, 210]. Moreover, linkages within the BBs appear to further support resistance to basal sliding forces. As predicted by Vernon and Woolley [173], loss of linkages impact the coupling between triplet microtubules and this disrupts both the stability of BBs as they resist basal sliding forces. We now know that these linkages may be in the form of A-C linkers and/or the helical inner scaffold [181, 209, 211]. Ultimately, our studies suggest that dynamic impact and resistance of ciliary forces on BBs support the models that basal resistance and deformation impact dynein motor coordination required for ciliary and flagellar beating. Further studies are required to dissect the precise interplay between BB and ciliary dynamics, but this is the first model to show discrete and quantifiable differences in BB morphology as a function of ciliary beating.

4.3.2 Conservation of BB triplet MT bending

Motile cilia are present across all eukaryotic lineages [212-214]. Force transmission from motile cilia to BBs is likely be conserved. We hypothesize that organisms with similar cilia and BB-appendages to *T. thermophila* also exhibit analogous BB bending patterns. Upon reinspection of published EM images, we find BB bending in *T. thermophila* to be apparent in previous publications (Figs. 4.1 and C1; [200, 206]). Triplet MT bending is also observed across several subphyla or classes of ciliate BBs [215, 216]. Additionally, BB triplet MTs of algae, such as *Chlamydomonas*, bend [217]. The bending of vertebrate multiciliary arrays is less evident, possibly because of rotational triplet MT bending [218].

While BB and BB-appendage structures of vertebrate multi-ciliary arrays have differences from single-celled organisms, we suspect that BB curvature will similarly be focused at junctions between BBs and BB-appendage structures. For example, BB bending may focus on connection sites between BB triplet MTs and the basal foot that nucleates the MTs for BB orientation and interconnection. BB rootlets may also serve as a hinge point in BB bending. In mice, rootlets in multiciliated epithelia are striated fibers at the base of BBs that may distribute or restrict BB bending to the proximal ends of BBs as found in *T. thermophila*. In *Xenopus*, striated rootlets extend from the BB base and fan out to contact actin filaments from posterior BB neighbors [194]. Moreover, mammalian and *C. elegans* rootlet structures are required for ciliary base stability [202, 203]. Thus, the position, orientation, and interactions of BB-appendage structures at the cell cortex may influence the transmission of forces to and from neighboring cilia. We suspect that the BB bending patterns will differ between organisms based on the structures of the BBs, the BB-appendages, and the waveforms of the cilia. Importantly, we predict that the focused site of triplet MT bending will occur on the BB side that is opposite to the direction of fluid flow as that is the site of sliding compression when ciliary are at the end of their power stroke. For flagella that have relatively symmetric waveforms and conserved BB structures, connecting piece deformations or BB bending is expected to similarly occur in the plane of the ciliary beat stroke most prominently near BB-appendages [188, 219, 220]. Thus, BBs and their associated structures adapt to the ciliary waveform and environment in which they beat to maximize effective cell motility and fluid flow.

4.3.3 Plasticity of ciliary waveform and SFs to environmental change

BB bending and ciliary waveform adjust with an environmental change to temperature [36, 221-223]. Elevated temperature increases ciliary beat frequency [224, 225]. Both BB bending

patterns and ciliary bending waveforms are different when comparing cells at 37°C and 30°C [36]. While the bending pattern of 37°C BBs can nearly be computationally modelled utilizing the forces of the ciliary bend alone, the inverse bending observed in 30°C BBs could not be recapitulated by changing the cilia bending waveform itself (Fig. 4.4C-D). SFs decrease in length at lower temperatures suggesting that BBs are less stably anchored to neighboring BBs or to the cell cortex [191, 201]. Using computer modeling, we show that pushing forces imposed on BBs by SFs can reverse the direction of BB bending (Fig. 4.4E). The negative bending in these BBs also propagates to the cilium. The cilium bending increases at the end of the power stroke, particularly at its proximal or basal region, and this is consistent with the bending changes observed in live imaging of beating cilia (Fig. 4.4C-D; [36]). This suggests that changes in force transmission by SFs can regulate the ciliary waveform. Therefore, changes to ciliary waveform and associated changes to fluid flow and cell motility might be produced through changing intracellular force transmission through SFs and BBs.

T. thermophila disA-1 and *poc1Δ* mutants provide further insight into how force transmission through BBs and SFs can impact the ciliary waveform. Neither of these mutants have known ciliary defects yet they both display altered ciliary waveforms compared to control cilia (our unpublished data). Thus, while 37°C BB bending can be explained using ciliary force transmission through BBs to the junction with SFs, our findings with WT at 30°C, *disA-1*, and *poc1Δ* BBs all support a model where changes in force transmission from SFs and neighboring BBs can explain changes to bending patterns of both BBs and cilia. This is consistent with computer models proposing that the mechanical properties of BBs and coupling between BBs can regulate ciliary waveform [5, 31, 171, 226]. In the context of temperature changes, this

indicates that changes to force transmission through BBs and SFs could provide a mechanism for ciliary waveform modulation.

4.3.4 SFs connect BBs and ciliary units

The differences between BB bending at 30°C, 37°C, and in *disA-1* mutants can be explained through changes in length and connectivity of SFs to neighboring BBs and the cell cortex and the consequent changes in force transmission between these structures. This begs the question as to how forces from SFs are generated and transmitted back onto their BBs and cilia. SFs point anteriorly and contact the posterior facing post-ciliary MT bundle from the anterior BB, and also contact the nearby cortical cytoskeleton (Graphical Abstract; [191]). Thus, forces from anterior BBs and cilia could be transmitted to neighboring BBs through the physical connections between post-ciliary MT bundles and SFs. These physical connections are hypothesized to provide a means of intracellular physical coupling to regulate the synchronicity between beating cilia. We propose that changes to BB bending, and ciliary waveform are achieved though force transmission from adjacent ciliary units through post-ciliary MT bundles and SFs. At 30°C, SFs shorten and lose connections with the cortical cytoskeleton adjacent to the anterior BBs. If this connection of SFs to the cortical cytoskeleton acts to ground ciliary forces, then loss of this secondary connection could increase force transmission between post-ciliary MTs and SFs of adjacent BBs and cilia. We suggest that this creates a route for the increased transmission of ciliary forces between adjacent ciliary units. Increasing the forces transmitted between the two ciliary units could explain the increase in overall BB bending and the directional inversion in the BB bend when comparing BBs at 37°C to those at 30°C. Thus, force transmission between ciliary units is modulated by the length and connectivity of SFs (and possibly post-ciliary MTs). In turn, this impacts BB bending patterns. This intracellular coupling between adjacent BBs and

cilia might also provide a means for regulating ciliary beating and metachronal synchronicity. Further studies are required to capture the precise dynamics for how pushing and pulling forces may be produced between neighboring BBs using SFs and how this might be controlled. In summary, we propose that cells modulate ciliary waveforms (e.g. in response to changes to environmental temperature) by altering BB bending by tuning the relative transmission of force from the cilium to the neighboring BBs, through changes to BB-appendages, in particular the SF.

4.4 Conclusions

This study demonstrates that BBs bend in response to forces from beating cilia. Asymmetric forces from beating cilia are transmitted into the cell through BB bending and focused on the BB triplet MTs that connect to SFs. Both cilia waveform and BB bending are responsive to temperature changes and these differences can be explained by SF force transmission altering BB bending patterns. Both the length and connectivity of SFs and the doublet MT interconnections are important for normal BB bending patterns. Together, we propose a model where cilia, BBs, and BB-appendages interact through the transmission of mechanical forces for ciliary beating and directed fluid flow.

Acknowledgements

Funding: ADJ, AWJS and CGP were supported by NIH/NHLBI # F31HL1474495 and NIH/NIGMS # R01GM099820 and R35GM140813. LGW and PVB were supported by NSF Grant CMMI-1633971. The authors would like to thank Courtney Ozello for EM imaging, Alex Stemm-Wolf for feedback on the manuscript, and the Pearson lab for insightful discussions. Thank you to Garry Morgan, David Mastronarde, Janet Meehl, and Mark Winey for EM tomography samples and IMOD training. Electron tomography was performed in the Boulder Electron Microscopy Services at the University of Colorado, Boulder.

Author contributions

Conceptualization: A.J., L.W., A.S., P.B., & C.P.
Methodology: A.J., L.W., A.S. & E.O.
Software: A.J., L.W., A.S. & E.O.
Validation: A.J., L.W., A.S. & E.O.
Formal analysis: A.J., L.W., A.S. & E.O.
Investigation: A.J., L.W., & A.S.
Resources A.J., L.W., A.S., E.O., P.B., & C.P.
Data Curation: A.J., L.W., A.S., E.O., P.B., & C.P.
Writing – Original draft Preparation: A.J., L.W., P.B., & C.P.
Writing- Review & Editing: A.S. & E.O.
Visualization: A.J., L.W. & A.S
Supervision: P.B. & C.P.
Project Administration: P.B. & C.P.
Funding Acquisition: P.B. & C.P.

Declaration of Interests

The authors have no competing interests to declare.

Resource availability

Lead contact
Further information and requests for resources and reagents used in this study should be directed to and will be fulfilled by the lead contact, Chad Pearson (CHAD.PEARSON@CUANSCHUTZ.EDU).
Materials availability
This study did not generate any new unique reagents.
Data and Code Availability
All data reported in this paper will be shared by the lead contact upon request.
This study does not report original code.
Any additional information required to reanalyze the data reported in this paper is available from the lead contact upon request.

4.5 Method details

4.5.1 Experimental model and subject details

Tetrahymena thermophila wild type B2086, SB1969 and their derived mutant strains *disA1-1* and *poc1Δ* were used in experiments for this study. Each strain is verified as *T. thermophila* through successful conjugation/mating events with known *T. thermophila* strains and genome sequencing[227]. The sex of *each Tetrahymena thermophila* strain were not accounted for because *T. thermophila* has 7 mating types (sexes). All experiments were performed in accordance with governmental and institutional guidelines.

4.5.2 *Tetrahymena* strains and culture

Tetrahymena thermophila cells B2086, SB1969, *disA-1, and poc1Δ* were obtained from the *Tetrahymena* Stock Center (tetrahymena.vet.cornell.edu/index). *T. thermophila* strains were cultured in 2% SPP media (2% protease peptone, 0.1% yeast extract, 0.2% glucose, and 0.003% Fe-EDTA) at 30°C unless otherwise indicated. Cells collected for analysis were grown to mid-log phase (approximately 3×10^5 cells/mL). Cell counts were determined using a Coulter Counter Z1 (Beckman Coulter). The forces from ciliary beating were manipulated by altering temperature [201]. For temperature shift experiments, cells were transferred into fresh SPP media and incubated for 24 hours at specified temperatures.

4.5.3 Electron microscopy and tomography

Cells were prepared for electron microscopy and tomography as previously described [181, 228]. Cells were gently spun in 2% SPP that contains 15% dextran (molecular weight 9000–11,000; Sigma-Aldrich) and 5% BSA. Cells were concentrated and transferred to a sample holder and high-pressure frozen using a Wohlwend Compact 02 high pressure freezer (Technotrade

International). After low-temperature freeze substitution in 0.25% glutaraldehyde and 0.1% uranyl acetate in acetone, cells were slowly infiltrated with Lowicryl HM20 resin. Serial thick (250–300 nm) sections were cut using a Leica UCT ultramicrotome. The serial sections were collected on Formvar-coated copper slot grids and poststained with 2% aqueous uranyl acetate for four min followed by Reynold's lead citrate for three minutes.

Dual-axis tilt series (−60 to +60°) of *Tetrahymena* cells were collected on a Tecnai F30 intermediate voltage electron microscope (ThermoFisher). Images were acquired using the SerialEM acquisition program with a Gatan CCD camera at 1.2 nm or 1.5 nm / pixel [229]. Serial section tomograms of *Tetrahymena* cortical structures were generated using the IMOD software package [228, 230]. Eight tomograms were reconstructed and modeled using the IMOD software package (bio3d.colorado.edu/imod/).

4.5.4 3D tomographic modeling and quantification

Three dimensional (3D) models of BBs were generated using the IMOD software package [228, 230, 231]. Using tomograms from tilt series, BBs were oriented in 3D space to obtain top-down views (looking down the cylinder of the BB). BB MTs were modeled as open contours in 5-slice max-projected z-stacks by picking 5-6 points along each of the MTs. MTs were identified as hollow, circular electron densities with diameters of approximately 25nm. In the event that the exact MT location was difficult to discern, crescent-shaped electron densities and relative location were used to define the MT location. The relative MT locations were informed by the known conserved triplet MT structure. No events deviating from the conserved structure were observed except in poc1 mutant BBs when triplet MTs were occasionally missing (Fig. C6F-G). IMOD drawing tool's Smooth Contours function was used to smoothen modeled MTs by adding 10x~ intermediate points (50~60 total points). The smooth tensile fraction was 0.5 pixels and

smooth point distance was 5 pixels, points were added in equal distribution regardless of Z-step and originally selected contour points were locked in place before smoothening. These points were then manually confirmed to be within the boundaries of the MTs in the tomograms. After smoothing modeled MTs, the curvature was quantified using the imodcurvature function. Imodcurvature calculates curvature based on circle-fitting to surrounding points over a length of 110 pixels (63 nm). For points near the end of the contour, the fit is to half of that length on the side away from the end and to whatever length is available on the side toward the end. This calculation was performed serially for every point with two flanking points. The curvature values calculated by imodcurvature are also directly applied as a heatmap on the modeled MTs in IMOD. BB curvature is binned as a 10 x 9 array, whereby curvature values along the length of a BB were split into 10 bins and the 9 triplet MTs were split into 9 bins, prior to averaging. The dynamic range of curvatures in all models are 0.3 rad/µm (dark purple) to 3 rad/µm (magenta). The maximum curvature values used in all quantifications were obtained by taking the maximum values from normalized bins equal to $1/10^{th}$ the length of the MT for each MT in the BB. Normalization was conducted by subtracting the average lowest maximum values from each triplet MT in the BB. Triplet averages (nine triplet MTs) of these maximum values where then calculated for each corresponding bin in each triplet MT. Averaging based on triplet MTs is consistent with visual representations of MTs in IMOD and curvature does not change based on MT identity (A, B, C tubule: data not shown). BB curvature values were represented as 10 x 9 heatmap arrays (10 bins long, 9 triplet MTs wide). 3D models of SFs were made in IMOD from side views of BBs. SFs were projected longitudinally and modeled as closed contours every 3 z-slices to generate a meshed model.

These EM tomogram modeling methods were analyzed for reproducibility through independent modeling. The same BB (Fig. 4.2) was independently modeled by authors A. Junker and A. Soh (Fig. C1F). The curvature amount and pattern was consistent between both independent models where most curvature found near the base-middle of triplet MTs 5 and 6. The only statistically significant difference ($p=<0.05$) was in triplet MT 1. This difference is located at a region of low curvature and does not impact the overall pattern of curvature found in the BB.

4.5.5 Computational modeling

The computational (finite-element) model of the cilium, BB, and BB-appendage structures was created in COMSOL Multiphysics using the Beam interface within the Structural Mechanics module (COMSOL Multiphysics® v. 5.6. www.comsol.com. COMSOL AB, Stockholm, Sweden). All MT filaments including axonemal doublet MTs and BB triplet MTs were modeled as slender (Euler-Bernoulli) beams. The central pair MTs were modeled as a single beam with an increased area moment of inertia about the non-power stroke transverse bending axis (to model the effect of two coupled MT singlets). All beam connections are modeled as fixed. Viscous drag was applied to the central pair using resistive force coefficients [8, 107].

Radial spokes (RSs) were modeled using beam elements: 30 circular arrays of 9 radially oriented beams were linearly patterned along the length of the model of the axoneme. Each beam represents the effects of multiple RSs as the actual number of RSs in the axoneme is much greater than the number of spokes in the model. Estimates for RS shear and normal stiffness were used to calculate flexural and axial rigidity for these beams. Spoke connections were modeled as fixed joints at the central and outer filaments. Though the spoke connections themselves do not slide, compliance of the spokes allows relative sliding of the axial filaments.

NDRC linkers were modeled using *extrusion coupling* operators within COMSOL, which make it possible to model inter-doublet stiffness as an applied-force function of relative displacement. The effect of this modeling is a continuous elastic connection between adjacent doublets that creates normal stiffness, but not shear stiffness at small deformations.

In the BB, AC linkers and the proximal cartwheel structure were modeled using a longitudinally oriented linear pattern of representative beams. BB accessory structures such as the SF, PCMT, and TMT were modeled as beams. Axial and flexural rigidity for these elements was calculated based on estimates of the physical properties of these structures. The helical inner structure was modeled as an array of nonagons with vertices located on a 155 nm circle. This array was patterned along the BB axis 150 nm to 450 nm from the base of the BB. Vertices of each nonagon were connected along the BB axis and to the neighboring MT triplets by beam elements. As with other structures represented in this model, the individual beam elements represent the overall effect of the biological structures and are not intended to be an accurate geometric reproduction. All inter-beam end connections were modeled as fixed joints. Connections between the modeled structure and structures external to the model, such as the cellular cortex and other BBs, were modeled using the *spring foundation* constraint. This allows elastic connections (with translational and rotational spring constants) to fixed points representing other cellular structures. In cases where those external structures were modeled as being in motion, the foundation attachment point was given a time-dependent prescribed displacement. Forces applied to the SF tip and cortical attachments were applied in this way. Beam elements in COMSOL use cubic shape functions for displacements. Large deformations in beam structures are obtained through a combination of element-level deformations as well as rigid body translations and rotations of linear beam elements. The beam mesh was therefore

refined along the BB triplet MTs to ensure deformations of individual elements were small. Mesh refinement studies were used to confirm convergence of curvature values in the BB triplet MTs in test studies. Meshing of radial spokes was restricted to one element per spoke to reduce undesirable behavior such as buckling of spokes, which will prevent convergence of the solution. Dynein forces were modeled as distributed axial forces that remain tangentially applied to doublets under time-dependent deformation (*follower loads*). Every base-ward force on one doublet must be balanced by a tip-ward force on the adjacent incrementally numbered doublet. This ensures that the net internal forces are balanced. Additionally, a distributed moment must be applied to counteract the force pair and keep internally produced moments in balance [66, 168, 232]. For simplicity of modeling, dynein force was prescribed using a 'switching' model in which dynein arrays on either side of the beat plane are alternately activated to produce the power and recovery strokes [147, 233]. In most cases, this was simply applied using sinusoidal function of time where dynein motors on the power stroke side of the axoneme activate in proportion to the positive regions of the sin wave and dynein motors on the recovery stroke side activate in proportion to the negative regions of the sin wave. In some specific studies, a prescribed spatiotemporally propagating activation pattern was used to drive the system. Time-dependent studies were solved using backward differentiation formula (BDF) time stepping with a relative error tolerance of 10^{-3}. Fully coupled nonlinear equations were solved using Newton's method with automatic damping. Geometrically nonlinear effects were included in the solution. Inertial effects were considered negligible and not included in the solution. This model of the axoneme (like all models) has limitations. Radial spokes likely slide along the central pair, and NDRC links may slide along doublets, but sliding at joints is challenging to simulate, and are not included in the current finite-element model. Instead, deformations of

spokes and links are limited by keeping dynein forces low, maintaining deformations in a regime where radial spoke beams and NDRC couplings do not become taut. Triplet MT stiffnesses were kept the same as doublet stiffnesses to increase curvature at lower dynein forces. For visualization and direct comparison with EM data, deformations and extracted curvature values were amplified fourfold.

A key objective was to accurately model how dynein forces drive ciliary beating; however, some compromises were necessary to limit the complexity of the model. First, dynein activation was prescribed along the length of the cilium, without modeling any specific theory of ciliary beat generation (of which none are yet generally accepted). Second, at large deformations, approximations in the model become increasingly inaccurate. For example, the moments associated with dynein forces acting across the axoneme diameter are oriented about an axis perpendicular to the dominant plane of beating, and do not reorient with out-of-plane deformation of the axoneme. This leads to internal moment imbalances at large deformations. Additionally, at the discretization level (mesh size) used to generate model results, internal moments from interdoublet links (modeled by “extrusion coupling” in the finite element model) do not balance. This effect approximately doubles the applied moment at maximum dynein load, which increases the bending of the cilium for a given level of dynein activity. Increasing the mesh resolution resolves the moment imbalance but prevents the model from converging. Finally, applied dynein forces are tangent to individual filaments, which leads to an applied force imbalance when loaded filaments become non-parallel (a maximum imbalance of 1.8 pN was calculated, which is a fraction of a percent relative to a total inter-doublet force of 700pN). Despite these imperfections of the model, it recapitulates many aspects of observed BB deformation and serves as a useful tool for gaining insight into the physical BB-cilium system

and understanding the role individual components (SF, AC-linkers, pcMT, tMT) serve in stabilizing the BB against forces transmitted from the cilium.

Inter-filament Sliding in Computational Model

Interdoublet sliding between doublets n and n+1 was evaluated by first calculating the position vector, $\boldsymbol{\delta}(s)$, from a point on doublet MT n to a point the same distance, s, along the length of doublet MT n+1, then projecting that position vector onto the tangent vector, $\mathbf{t}(s)$, of doublet n using the dot product: $\Delta(s)=\boldsymbol{\delta}(s)\cdot\mathbf{t}(s)$. As noted above, sliding between filaments (doublets and central pair) is permitted by elastic compliance of spokes and links; sliding at attachment points was not modeled. To avoid undesired structural nonlinearities that prevent convergence of the simulation, relative sliding between adjacent doublet MTs was limited by keeping the maximum distributed dynein force low: <125 pN/μm. Realistic model behavior, expected to be obtained at fourfold higher dynein forces, was obtained by scaling deformations by a factor of four. Maximum sliding amplitude at the tip of the small-deformation model was 38 nm between doublet MTs 6 and 7. To obtain the predicted sliding at deformations comparable to those observed, this amplitude was multiplied by four to obtain the predicted maximum relative sliding amplitude of 151 nm between MTs 6 and 7 (Table C3).

Computational Model Parameters

An additional challenge of the computer simulation is the estimation of the physical properties of the nanoscale structures present in the cilium and accessory structures. In cases where experimentally obtained estimates of properties were available, they were used in the model either as fixed estimates or plausible ranges. These included axoneme flexural rigidity, dynein force, NDRC stiffness, resistive force coefficients for a cilium in water, as well as parameters such as beat frequency and posterior-anterior phase lag (Table C3, Fig. C3).

Where experimental estimates of parameter values were not available, ballpark estimates were made based on the size, shape, and estimated material properties of structures. Simulation parameter sweeps were run to determine sensitivity of the model to the parameters and to bring the overall model behavior in-line with observed behavior. Initially, this parameter estimation and refinement was run on a 2D version of the model for rapid iteration before building the more complex 3D model.

4.5.6 Live cell imaging of cilia beating

Using a magnetism-based strategy, *T. thermophila* cells were immobilized and their cilia were imaged via fast timelapse DIC microscopy [36]. Briefly, cells were fed with iron particles (Sigma-Aldrich) that were suspended in SPP media. Next, cells were immobilized inside microfluidics chambers using bar magnets that are positioned along the chamber. All experiments were performed at the respective temperatures (30°C and 37°C) using a microscope stage incubator (Pathology Devices). Imaging was performed using an inverted widefield microscope (Ti Eclipse; Nikon). A 60X Plan Apochromat (NA 1.4) objective lens (Nikon) was used. 2D movies were acquired using a scientific complementary metal-oxide semiconductor camera (Zyla; Andor Technology) at approximately 650 frames per second.

Cilia waveform and curvature analyses were focused on the cilium power stroke axis using a previously described approach [78]. Briefly, consecutive movie frames of cilia were manually traced and fitted with a 2^{nd} order polynomial line function. Due to reduced contrast at the cilium base, analysis was performed on the distal 4.5 μm of all tracked cilia. Curvature along the cilium length was quantified. Curvature extrapolation was applied for both ends of all traced cilia. To ensure that the curvature of each cilium is uniformly weighted, each cilium was tracked for 6

beat cycles. Cilia waveform and curvature were obtained by averaging across nine cilia. All cilia were aligned along the same axis based on the relative of the anterior BB's position.

4.5.7 Data representation and graphing

Red-Blue heatmaps indicate differences in BB bending between different parts of the ciliary power stroke. The location, level, and direction of the normalized average in maximum curvature is determined by the axis and colors. The location of bending is indicated by the axis, y-axis indicates relative proximal distal height on BBs broken into 10 bins (normalized BB height, one bin= $1/10^{th}$ the height of a BB), x-axis indicates the triplet (1-9). The colors blue and red indicate the direction of curvature relative to the cell's anterior-posterior axis (axis of the ciliary power stroke). Blue indicates negative bending = bending towards the cell anterior, red indicates positive bending = bending towards the cell posterior. Colored lines and bars on all dot plots indicate the mean and standard deviation, respectively (Fig. C2 and C4-C6). Dots represent individual measurements; light grey lines indicate the location of zero.

4.5.8 Quantification and Statistical Analyses

All experimental data sets represent a minimum of three BB regions or triplet MTs. Comparisons between genotypes or conditions only include analyses from completely modeled BB with cilia in the same part of the beat stroke (beginning, middle, end, recovery) with no visible damage (Table 1). Statistical tests were run in Prism8 (GraphPad Software). Shapiro-Wilk normality test was performed to assess for normal distribution Normally distributed continuous data sets were analyzed using unpaired, two-tailed Student's t-test. Non-normally distributed datasets were analyzed using the Mann-Whitney test. F-tests were used to determine variance. This includes heatmaps of BB bending in which the normalized maximum values of each triplet in each

proximal-distal bin were compared between 2 BBs. All p values are numerically presented. Analyses between curvature values in proximal-distal, or lateral (triplet MTs) axes (Fig. C2 and C4-C6) were compared against other triplet MTs of the same BB. One-way ANOVA analyses were performed on normally distributed data. Wilcoxon Rank Sum Tests were performed to obtain p-values on non-normally distributed data. All p-values are numerically presented. Statistical significance in the variances between triplet MTs was tested using Bartlett's test. Power statistics was performed to ensure ample sample size for the comparison between cilium curvature obtained from live imaging. 5% margin of error and 95% confidence level were applied. Colored lines and bars on all dot plots indicate the mean and standard deviation, respectively.

Chapter 5: Semi-automated software for the analysis of ciliary kinematics[1]

This chapter describes the automated ciliary tracing and cell body tracking software packages I wrote for this project, as well as several of their applications.

5.1 Autotrace: ciliary tracing software

5.1.1 Motivation

Waveform analysis is important to studying how drugs, genetic mutations, and environmental conditions affect ciliary and flagellar beating. It is also used to study the underlying mechanisms that drive and regulate this beating. The analysis of ciliary beating typically involves tracing hundreds or thousands of still images from microscope videos of beating cilia [8, 26, 28, 29, 35]. This is a time-consuming and tedious process. Automatic tracing software has been developed by others [31, 35, 234, 235], but such software may perform poorly (fail to track the cilium accurately) on a given set of images due to noise, lack of contrast, or mismatch between image properties and the conditions the software was developed for. I therefore decided to develop a custom automatic tracing algorithm that was robust to noise and would work in a variety of imaging conditions, such as a dark subject against a bright background or vice-versa.

[1] This chapter contains figures from and describes work done for [39] J. H. L. Cho, Z.A.; Zhu, L; Muegge, B.D.; Roseman, H.F.; Lee, E.Y.; Utterback, T.; Woodhams, L.G., Bayly, P.V.; Hughes, J.W., "Islet primary cilia motility controls insulin secretion," *Science Advances*, 2022 (in press).. See section 1.5 *Statement of contributions*.

5.1.2 Autotrace algorithm

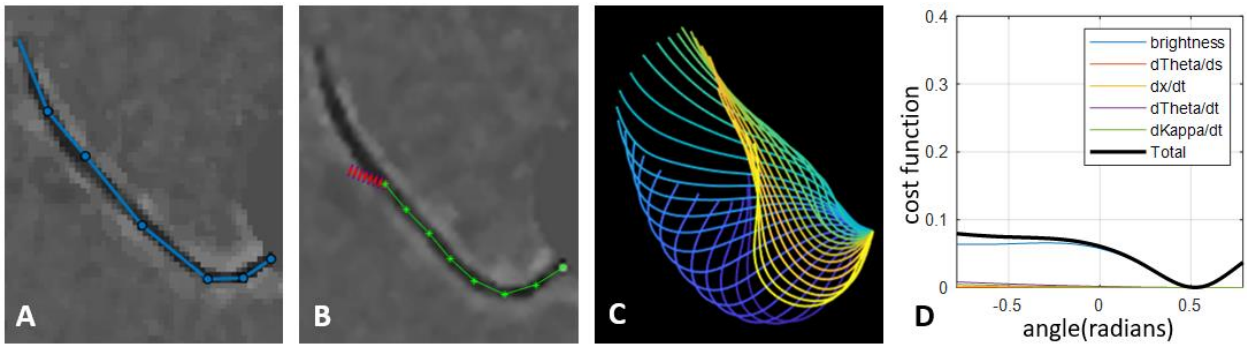

Figure 5.1: Autotrace algorithm. (A) An initial rough trace is obtained by selecting points along the cilium. (B) The algorithm proceeds along the cilium segment-by-segment, sweeping a grid of probes to find the optimal angle along which to proceed. (C) When all traces are complete, the waveform is interpolated and visualized. (D) The optimal angle is computed by an exhaustive sweep of the probe array. The angle chosen is the one that minimizes a linear combination of the weighted pixel intensity under the probe array as well as several penalty terms used to improve robustness in cases of noise, poor contrast, and poor focus.

Using the first image of a time series, the user manually traces the cilium to obtain the cilium length, L, as well as the initial coordinates (x_0, y_0) and angle, θ_0, of the cilium base (Fig. 5.1A). The program then automatically traces the path of the cilium in successive frames, using the following algorithm (Fig. 5.1B):

1. The length of the cilium is divided into n segments. For the first segment, a rectangular array of points with a width approximately equal to the diameter of the cilium and a length of one segment $(\frac{L}{n})$ is created. Every point in the array is given a numerical weight based on a gaussian distribution in the width of the array, with constant values along the length.

2. An array of angles is created centered at an initial estimate of the angle and spanning an allowable sweep range. The array is rotated through the range of angles with one end pivoting about the base point. At each angle, the weighted average (the 'brightness cost')

of the interpolated pixel intensities at all points in the array is calculated and stored temporarily.

3. The angle that minimizes the brightness cost is selected as the current angle. In the case of a bright cilium against a dark background, the brightness cost is the weighted average in (2) multiplied by negative one.

4. The next point along the cilium is located using the angle from (3), the current base coordinate, and the segment length.

5. The process is repeated from step (2) from each successively selected point along the cilium.

When all n+1 points along the cilium have been located, the program proceeds to the next image in the sequence until all traces are calculated (Fig. 5.1C). The program requires that any translation of the base of the cilium be removed [35]. The stabilization of body motion is addressed by the body tracking software in section 5.2.

To improve the robustness of the angle selection, terms are applied to penalize 'curvature' (change in angle from point to point along the length), translational velocity (change in position from previous frame), rotational velocity (change in angle from previous frame), and rate of change in curvature (change in approximate curvature from last frame) (Fig. 5.1D). These penalty terms are important in cases where lack of contrast, debris in the image, or the interaction of multiple cilia in the image may cause the global minimum of the brightness cost to occur at an angle other than along the cilium. In such cases, the penalty terms add cost to angles that are

unlikely to follow the cilium trace (because the angle bends sharply or would cause an unusually large change in translation, rotation, or curvature from the previous frame).

Note that the algorithm above describes an 'exhaustive sweep' of angles to minimize the cost. This was determined to be more robust than using more sophisticated optimization routines, such as *fminbnd()* in Matlab, which may converge to local minima.

5.1.3 Post-processing, dimensionality reduction, and kinematic analysis

Quantities of interest including period, periodicity, curvature, and amplitude are calculated by postprocessing raw angle data obtained by autotrace.

Period/frequency: Oscillation period is estimated from the nonzero time delay that maximizes the autocorrelation of the (interpolated) angle data; this delay is found at all points along the cilium and averaged to obtain a single estimate of the period. The frequency is the inverse of the period.

Periodicity: The mean of the maximum autocorrelation value described above at each point is used as a measure of periodicity, or how similar the beats are to each other.

Angle: For each frame (index *j*), a fourth-order polynomial is fit to the angle data and used to reconstruct the tangent angle as a continuous function of the arclength, s:

$$\theta(s, t_j) = c_4(t_j)s^4 + c_3(t_j)s^3 + c_2(t_j)s^2 + c_1(t_j)s + c_0(t_j) \tag{5.1}$$

Curvature: Curvature values are obtained as the first derivative of the tangent angle, $\theta(s, t_j)$, with respect to arclength:

$$\kappa(s, t_j) = 4c_4(t_j)s^3 + 3c_3(t_j)s^2 + 2c_2(t_j)s + c_1(t_j) \tag{5.2}$$

Wavelength: Wavelength is calculated as twice the distance between adjacent local minimum and maximum curvature values detected using the peak finding function *findpeaks()*. This value is calculated for all time points where both peaks exist and is then averaged to give a single quantity.

Propagation velocity: Propagation velocity is calculated as the time rate of change of the location (distance along the cilium or arc length) of the peak magnitude curvature value. This value is calculated following several peaks over time and then averaged to obtain a single quantity.

Amplitude: Amplitude of motion is quantified by taking the standard deviation of all angle data within the middle 80% of the length of the cilium, excluding the base and the tip, which are prone to fitting errors.

Position: The shape of the cilium, as represented by x and y positions along the cilium length, is reconstructed by numerically integrating the cosine and sine, respectively, of the tangent angle, θ, evaluated at discrete distances (index i) along the length of the cilium:

$$x(s_i, t_j) = x_0 + \int_0^{s_i} \cos\theta(\zeta, t_j)\, d\zeta \approx x_{ij} = x_0 + \sum_{k=1}^{i} \cos(\theta_{ij})\Delta s \tag{5.3a}$$

$$y(s_i, t_j) = y_0 + \int_0^{s_i} \sin\theta(\zeta, t_j)\, d\zeta \approx y_{ij} = y_0 + \sum_{k=1}^{i} \sin(\theta_{ij})\Delta s \tag{5.3b}$$

Velocity: Velocity components in the x and y directions are obtained through numerical differentiation (using central differences) of (Eq. 5.3a,b) with respect to time.

$$v_x(s_i, t_j) = \frac{\partial}{\partial t}\left(x(s_i, t)\right)|_{t=t_j} \approx v_{x_{ij}} = \frac{x(s_i, t_{j+1}) - x(s_i, t_{j-1})}{t_{j+1} - t_{j-1}} \tag{5.4a}$$

$$v_y(s_i, t_j) = \frac{\partial}{\partial t}\left(y(s_i, t)\right)|_{t=t_j} \approx v_{y_{ij}} = \frac{y(s_i, t_{j+1}) - y(s_i, t_{j-1})}{t_{j+1} - t_{j-1}} \tag{5.4b}$$

Some computations are more easily carried out using local tangent, $\boldsymbol{T}$, and normal, $\boldsymbol{N}$, direction vectors. Here only the continuous versions of the equations are shown for simplicity:

$$\boldsymbol{T}(s, t) = [\cos\theta(s, t), \sin\theta(s, t)] \tag{5.5a}$$

$$\boldsymbol{N}(s, t) = [-\sin\theta(s, t), \cos\theta(s, t)] \tag{5.5b}$$

Forces: We use the direction vectors (Eq. 5.5a,b) and velocity components (Eq. 5.4a,b) to obtain external viscous forces per unit length in the tangent/normal coordinate system using resistive force theory with respective tangent and normal resistive force coefficients c_T and c_N[8, 107]:

$$f_T = -c_T v_T = -c_T\left(v_x \cos\theta + v_y \sin\theta\right) \tag{5.6a}$$

$$f_N = -c_N v_N = -c_N\left(-v_x \sin\theta + v_y \cos\theta\right) \tag{5.6b}$$

These are then converted back to cartesian coordinates:

$$f_x = f_T \cos\theta - f_N \sin\theta \tag{5.7a}$$

$$f_y = f_T \sin\theta + f_N \cos\theta \tag{5.7b}$$

Torque: Torque about the cilium base is calculated by numerically integrating the cross product of cilium position relative to the cilium base with the applied viscous force along the length of the cilium.

$$\tau(t_j) = \int_0^L \boldsymbol{r} \times \boldsymbol{f} ds \; = \int_0^L \left[\left(x(s,t_j) - x_0 \right) f_y(s,t_j) - \left(y(s,t_j) - y_0 \right) f_x(s,t_j) \right] ds$$

$$\approx \sum_{k=1}^{n} \left[\left(x_{kj} - x_0 \right) f_{y_{kj}} - \left(y_{kj} - y_0 \right) f_{x_{kj}} \right] \Delta s \tag{5.8}$$

Power: Power dissipated by the cilium is calculated by integrating the dot product of the applied force with the local velocity along the length of the cilium.

$$P(t_j) = \int_0^L \boldsymbol{f} \cdot \boldsymbol{v} \, ds \approx -\sum_{k=1}^{n} \left[c_T f_{T_{kj}}^2 + c_N f_{N_{kj}}^2 \right] \tag{5.9}$$

5.2 Autotrack: body tracking software

5.2.1 Motivation

The Autotrace software described previously requires that the base of the cilium is stationary within the coordinate system of the image sequence. Typically, this requirement will not be satisfied for swimming cells, so the cell body must be stabilized before performing ciliary analysis. Furthermore, tracking the trajectory of microswimmers is useful in determining the effects of environmental conditions and mutations on ciliary coordination and effectiveness [117, 236-238], and potentially for future projects involving characterizing acoustofluidic traps and multi-cell interaction [74, 239]. For these reasons, I developed a custom cell body tracking algorithm. It should be noted that an algorithm had been developed for cell body stabilization as part of a previous project [35]. That software was based on a completely different fast Fourier transform (FFT)-based algorithm that was not effective in stabilizing motion of some videos (sperm cell bodies). The current software was written to improve performance in those cases, though the challenges presented in those cases (the sperm head changes appearance as it rotates due to directional illumination) affect the performance of the current software as well.

5.2.2 Autotrack algorithm

The Autotrack body tracking software optimizes a three-degree-of-freedom (DOF) rigid-body transformation (rotation and translation) of a region of interest (ROI) in the first frame (which we will call the *template*) to a region in every subsequent frame (we will call subsequent frames *images*). In computer vision, such a transformation is an instance of the more general category of *warping functions*, which may include linear and nonlinear deformations [240]. The current rigid body transformation will be denoted $\boldsymbol{w}(\boldsymbol{x},\boldsymbol{p})$, where $\boldsymbol{w}$ is a vector of transformed coordinates, $\boldsymbol{x}$

are the original coordinates, and $\boldsymbol{p} = [p_1, p_2, p_3]^T$ is a vector of the parameters of the warp (translation in x, translation in y, angle of rotation).

$$\boldsymbol{w}(\boldsymbol{x}, \boldsymbol{p}) = \begin{bmatrix} w_1 \\ w_2 \\ 1 \end{bmatrix} = \begin{bmatrix} \cos(p_3) & -\sin(p_3) & p_1 \\ \sin(p_3) & \cos(p_3) & p_2 \\ 0 & 0 & 1 \end{bmatrix} \begin{bmatrix} x_1 \\ x_2 \\ 1 \end{bmatrix} \tag{5.10}$$

The objective function used to optimize the warp parameters at each image can be chosen to be the sum of the squares of the differences between pixel values in the template ROI and the pixel values interpolated at the transformed coordinates in the image:

$$error = \sum_{i=1}^{N} \left(I\big(\boldsymbol{w}(\boldsymbol{x}_i, \boldsymbol{p})\big) - T(\boldsymbol{x}_i) \right)^2 \tag{5.11}$$

Here $I\big(\boldsymbol{w}(\boldsymbol{x}_i, \boldsymbol{p})\big)$ is the (scalar) pixel intensity in the *image* interpolated at the transformation, $\boldsymbol{w}$, of coordinate $\boldsymbol{x_i}$ using the parameters in $\boldsymbol{p}$, $T(\boldsymbol{x_i})$ is the pixel intensity in the *template* evaluated at coordinate $\boldsymbol{x_i}$, and *N* is the number of pixels in the ROI. Parameters in $\boldsymbol{p}$ are optimized for each frame subsequent to the first using *fminsearch()* in Matlab. As an alternative to the objective function in Eq. 5.11 above, the negative of the correlation between the two regions (the array of pixels in the ROI of the *template* and the array of pixels evaluated at transformed coordinates in the *image*) was tried as an objective function. This was determined to work similarly and have no significant impact on number of iterations required for convergence or the accuracy of the results.

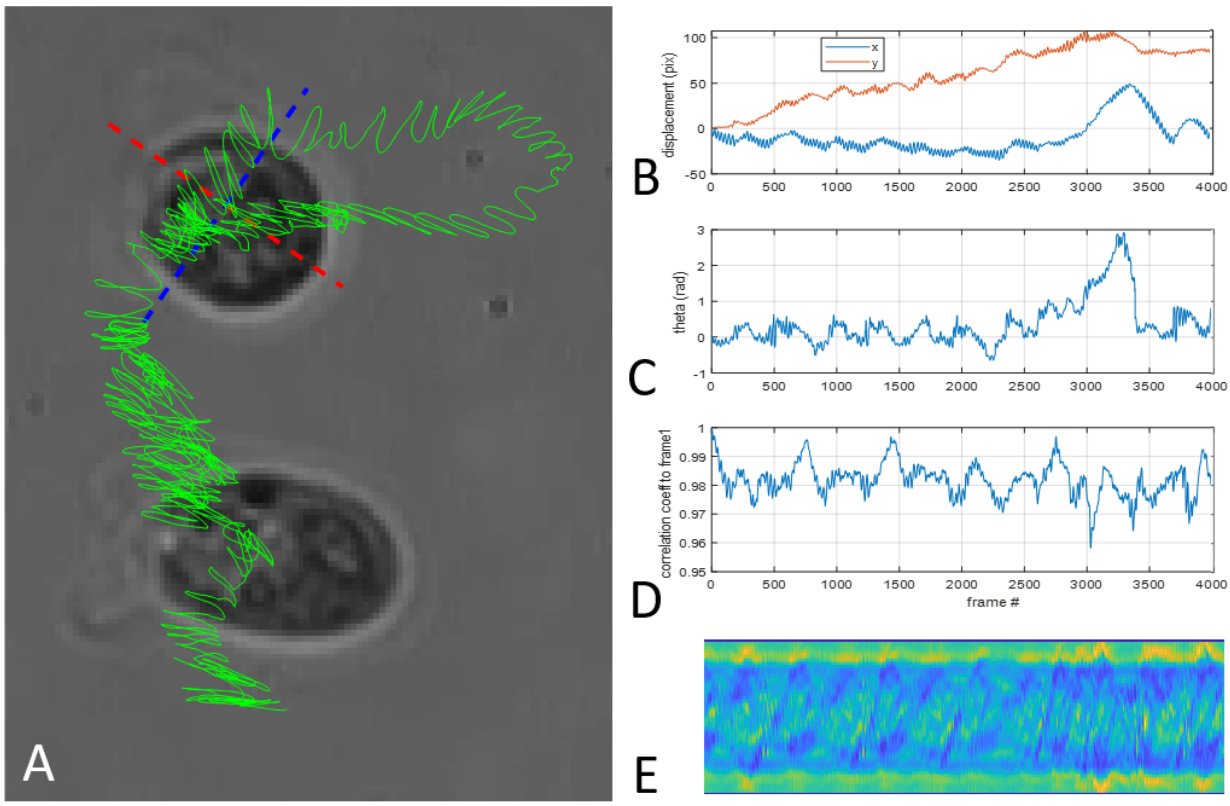

Figure 5.2: Body tracking software applied to one of two Chlamydomonas cells in an acoustic trap. Video courtesy of Mingyang Cui and Mark Meacham. Initial analysis by Advaith Narayan. (A) Crosshairs indicate orientation and location on the object being tracked. The green line indicates the path of the crosshair center over time. Here the cell being tracked has moved from the bottom of the frame to the top during the recording. (B) x and y displacement in pixels as a function of frame number. (C) Angle of rotation, θ, of the object being tracked. (D) The correlation coefficient is used here as the quantity to be maximized. Larger variation of the maximum correlation over time is likely due to rotation of the cell about its anterior-posterior axis. Higher frequency ripples observed in all quantities are caused by the beating of the cilia. (E) Kymograph of a stabilized column of pixels transverse to the anterior-posterior (AP) axis of the cell body intersecting the eye spot. Rotational motion of the body about its AP axis is apparent here as a corkscrew pattern of the darker eyespot. At approximately frame 3000, the cell body rotates so that the AP axis is perpendicular to the plane of view.

5.3 Applications

The autotrace software has reduced the time-consuming task of manual image tracing to an automated process that can process hundreds of frames in a few seconds. Several projects have used this software spanning the Bayly, Hughes, and Santi Labs at Washington University in St. Louis. Two of these projects are described below.

5.3.1 Motility of primary cilia on pancreatic beta cells

This section describes the methods and results of the publication *Islet primary cilia motility controls insulin secretion* [39]. Discussion here is limited to those parts of the study that used the methods of the current chapter. Additional details of the imaging and analysis methods, including Autotrace, are given in another paper, currently in review [241].

Motivation

Cilia described so far in this dissertation have been *motile* cilia, which typically contain a "9+2" axoneme (9 outer microtubule doublets and 2 central microtubule singlets) and are known to have motility driven by arrays of dynein arms. By contrast, primary cilia are sensory organelles, typically with a "9+0" axoneme [242], which are generally thought to be immotile. However, researchers in the Hughes Lab observed that cilia on pancreatic beta cells exhibited time-dependent deformation under laser-scanning and spinning-disk confocal microscopy. Pancreatic beta cells are cells in the pancreatic islets that are responsible for insulin production in response to detected glucose concentrations. Disfunction of beta cells and beta cell cilia are implicated in type-1 and type-2 diabetes [243, 244].

The Hughes Lab reached out to the Bayly Lab to collaborate on analyzing the observed ciliary motions and determining whether the motions were caused by forces internal to the cilium (i.e., dynein motors), forces within the cell body (i.e., actin-myosin interactions in the cell cortex), or forces external to the cell (i.e., hydrodynamic forces due to cell motions).

Methods

The autotrace software described previously was applied to the analysis of primary cilia on pancreatic beta cells. First, 3D image stacks obtained by confocal microscopy were reduced to 2D images using a mean projection along the z-axis (Fig. 5.3B). Imaging angles were chosen that

maximized the in-plane (x-y) motion of each cilium analyzed. From the automatically generated trace sequences of each cilium analyzed, the following quantities of interest were calculated for quantitative comparison under different experimental conditions: amplitude, frequency, maximum curvature, and periodicity. Calculation of these quantities is described in section 5.1.3.

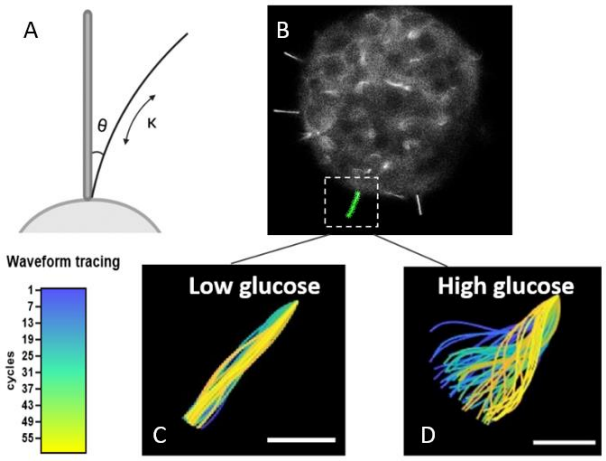

Figure 5.3: Tracing of pancreatic beta cell cilia. Reproduced from [39]. (A) Image illustrating the quantities of angle, θ, and curvature, κ. (B) Box shows a pancreatic beta cell cilium with points along its length traced using the autotrace software. (C) Representative automatically generated traces color coded according to order under low glucose conditions. Scale bar 5μm. (D) Representative traces under high glucose conditions. Scale bar 5μm.

Results

Several of the important results from this paper are summarized here. I will limit discussion to results obtained using the autotrace software, as those are relevant to this dissertation.

Firstly, motility of pancreatic beta cell cilia is significantly affected by glucose concentration (Fig. 5.4). Raising the glucose concentration from 1 mM to 11mM led to a statistically significant increase in amplitude, decrease in frequency, and increase in the maximum curvature observed. This result does not tell us the exact mechanism of motility in these primary cilia, but the dependence on glucose concentrations suggests that it is an active process.

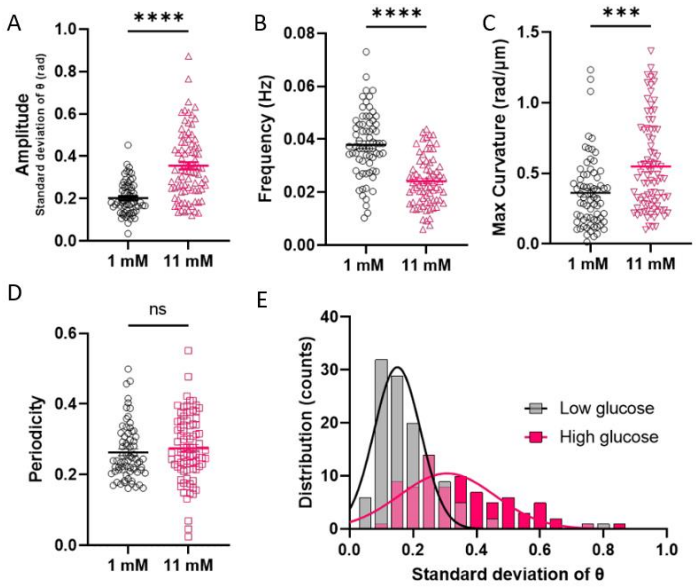

Figure 5.4 Analysis of quantities of interest at low (1mM) and high (11mM) glucose conditions. Reproduced from [39]. (A) Amplitude is increased at high glucose conditions. Bars show mean+/-SEM. (B) Frequency is decreased at high glucose conditions. (C) Maximum curvature in the cilium is increased at high glucose conditions. (D)Glucose concentration did not have a significant effect on periodicity of motion. (E) Histogram of amplitude (std(θ)) at high and low glucose conditions. n=80 per condition, ***p<0.001, ****p<0.0001

Secondly, the amplitude of beta cell ciliary motion was measured under several conditions to determine the source of the motility (Fig. 5.5). To further test whether ciliary motion was driven by an active internal process, the effect of exogenous ATP concentration in cilia without glucose stimulation was measured. The addition of 10 μM ATP increased amplitude by ~60% (Fig. 5.5B). Depletion of ATP by Antimycin A and 2-deoxy-D-glucose reduced ciliary motion. These findings suggest that motion is driven by an ATP dependent process such as actin-myosin or tubulin-dynein binding.

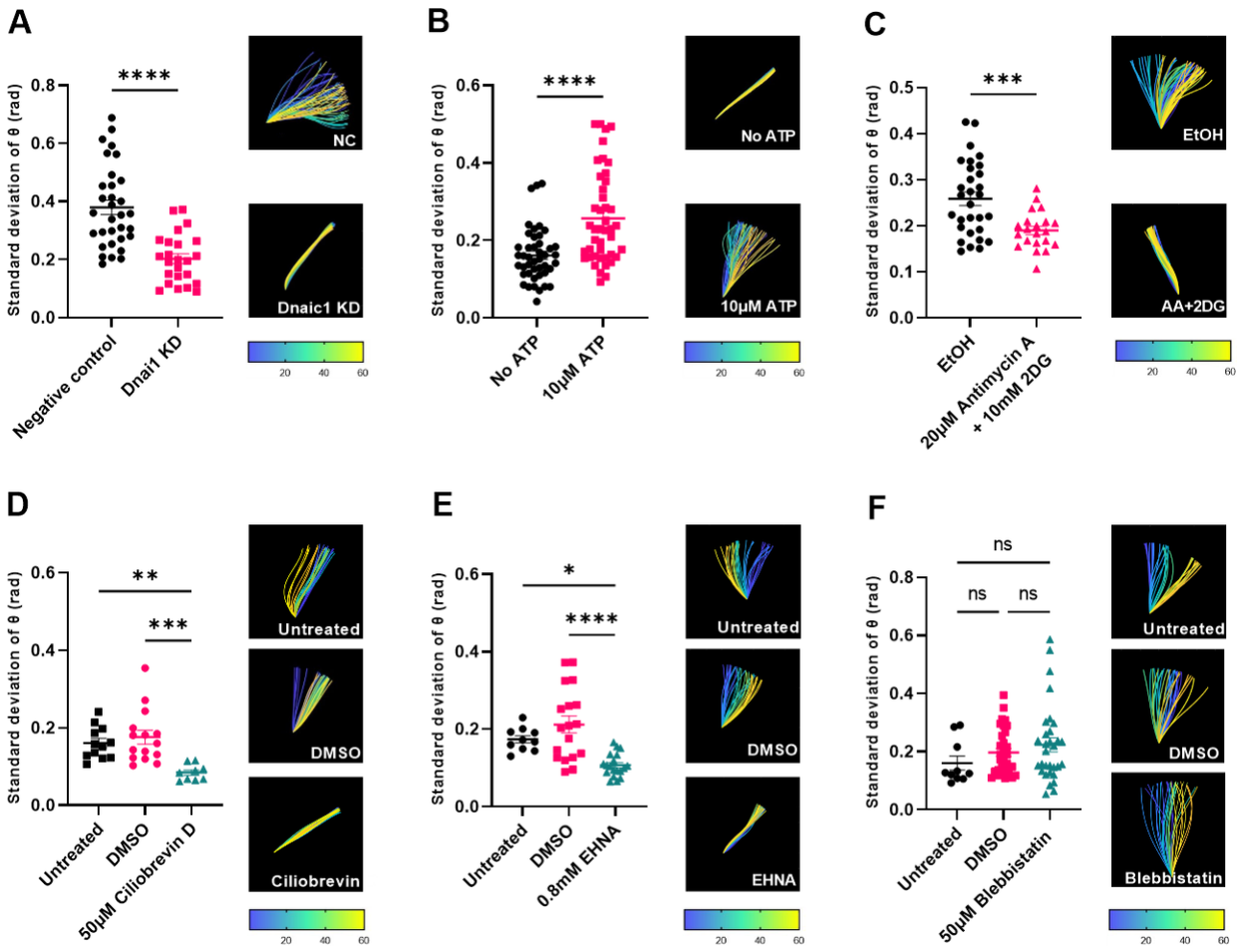

Figure 5.5: Response of beta cell cilia motion amplitude to various treatments. Reproduced from [39]. (A)Targeted dynein knockdown reduces motion amplitude. (B) ATP supplementation without glucose increases amplitude. (C) ATP depletion using antimycin A and 2-deoxy-D-glucose (2DG) inhibits cilia movement. (D) Dynein chemical inhibition by ciliobrevin D blocks cilia movement. DMSO-treated islet cilia exhibited unperturbed motility; untreated islet cilia are shown as an additional control. (E) EHNA inhibits cilia movement compared to DMSO-treated and untreated cilia. (F) The actin-myosin inhibitor blebbistatin does not significantly affect ciliary beat amplitude. *p<0.05, **p<0.01, ***p<0.001, ****p<0.0001; n = 10-50 traces per condition, pooled from three or more independent experiments.

Thirdly, it had already been determined through fluorescent labeling that the motor protein dynein was present in beta cell cilia. To determine if dynein is responsible for the observed motility, several experiments were conducted to study motion of cilia with diminished dynein presence or impaired dynein function. Targeted dynein knockout caused a decrease in amplitude (Fig. 5.5A). The AAA+ ATPase motor inhibitor ciliobrevin D also decreased amplitude, as did

the dynein inhibitor EHNA (Figs. 5.5D,E). To rule out actin-myosin interactions in the cell cortex as a cause of motion, the myosin inhibitor blebbistatin was introduced at a concentration of 50 μM and found to not have a significant effect on beating amplitude.

Discussion

Taken together, these results suggest that beta cell primary cilia are motile sensory organelles, driven by the motor protein dynein. This result contradicts the commonly held belief that these organelles are immotile.

5.3.2 Quantifying sperm capacitation

Work on quantification of sperm capacitation is ongoing and results presented here should be considered preliminary. Undergraduate researcher Alicia Gupte deserves credit for her excellent analyses of hundreds of video files and presentations of her findings on this work.

Motivation

When sperm cells enter the female reproductive tract, they undergo a physiological process called *capacitation* [245]. This process is essential to allowing the sperm cell to fertilize the egg and is associated with an increase in motility. Dr. Celia Santi's Lab studies sperm cell capacitation and reached out to the Bayly Lab to collaborate on characterizing the effects of capacitation on sperm motility through video analysis. If capacitated and non-capacitated sperm can be efficiently distinguished using video analysis, this could be an effective diagnostic in determining causes of infertility.

Methods

Videos of beating sperm cells were given to the Bayly lab that were labeled as ‘condition A’ and ‘condition B’. These were later revealed to be non-capacitating and capacitating conditions, respectively, though not all sperm cells incubated under capacitating conditions will undergo capacitation [246]. Traces of sperm flagella were generated using the Autotrace software (Fig. 5.6A,B). Because the videos were captured at low frame rates relative to the frequency of beating (20-60Hz framerate, ~10Hz beat frequency), Isomap was used to re-order temporally ordered traces according to their position in the beat cycle (Fig. 5.6C) [35, 247]. This effectively condenses many cycles with few frames per cycle into one ‘super cycle’ with many frames. This super cycle is spatially smoothed using a 4^{th}-order polynomial regression on each trace, and then temporally smoothed by applying a truncated FFT reconstruction of each polynomial term as a function of time. Analysis of the ‘super cycle’ improved estimates of velocities as well as estimates of kinetic quantities that are calculated from the velocities.

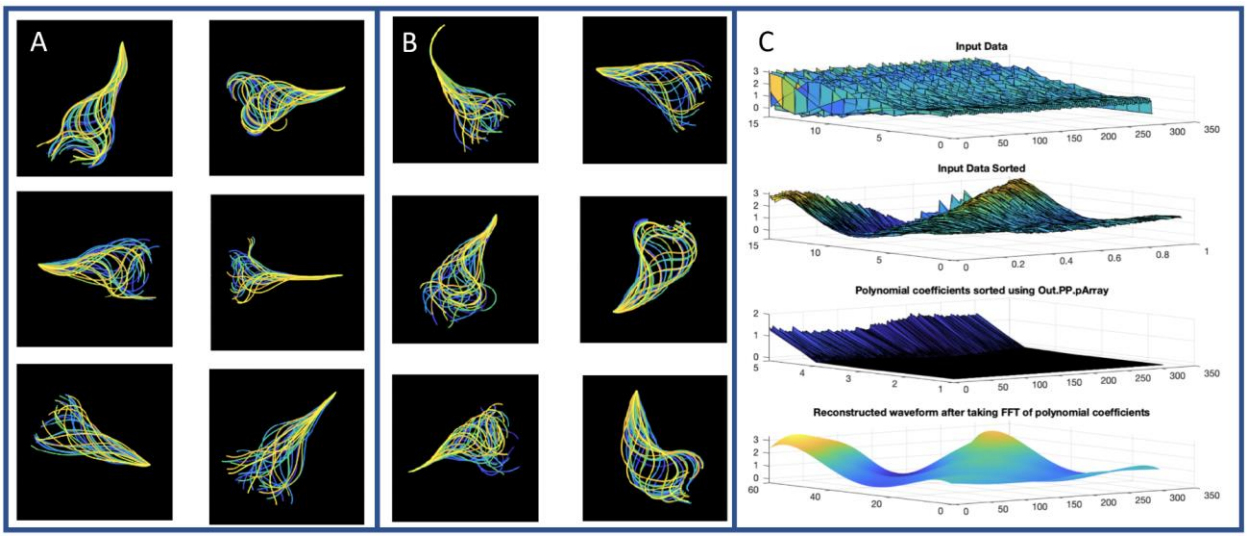

Figure 5.6: Traces of beating sperm cells and Isomap sorting. Analysis conducted by Alicia Gupte. (A) Sperm cells incubated under non-capacitating conditions. (B) Sperm cells incubated under capacitating conditions. (C) Input data are initially unsorted. Isomap software was used to sort the traces according to an estimate of their position in the cycle. 4^{th}-order polynomial coefficients are fit for each trace. A smoothed waveform is reconstructed using a truncated FFT of the time-series of polynomial coefficients.

Results

This is an ongoing project and any results presented here are preliminary.

Tracing and analysis of sperm cells using the methods described in this work has produced statistically significant results for some quantities of interest comparing groups of sperm cells thought to be in a quiescent state and those that were thought to contain hyperactivated sperm cells. One way to hyperactivate sperm cells is through the use of the drug thimerosal [248]. The results of a comparison of cells incubated under non-capacitating conditions and cells incubated under the same conditions with the addition of thimerosal is shown in Fig. 5.7. Using the methods described in this chapter, hyperactivated sperm show a decreased beat frequency, but an increased beat amplitude. Wavelength and maximum curvature are increased in hyperactivated sperm.

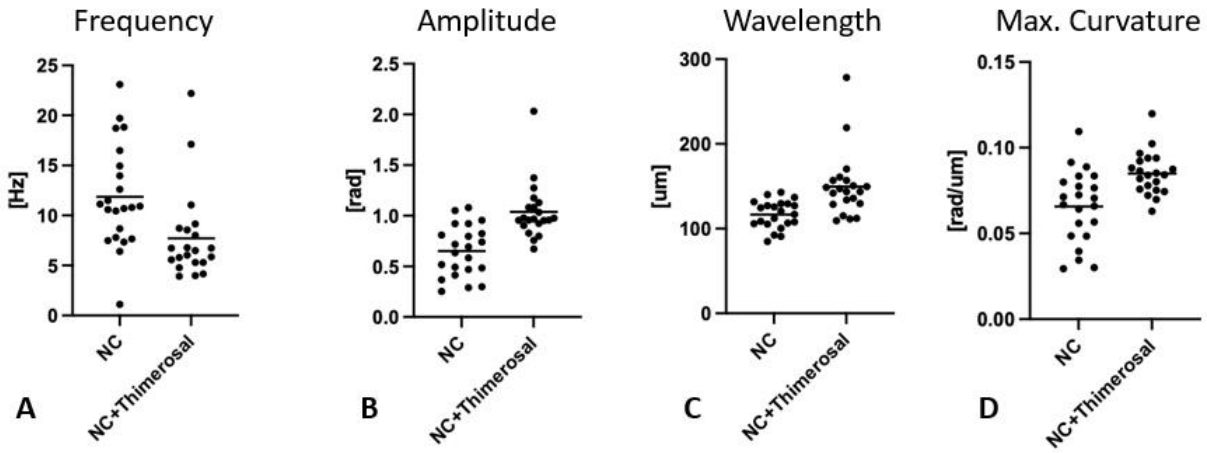

Figure 5.7: Comparison of metrics from traces of quiescent and hyperactivated sperm cells (preliminary). Analysis courtesy of Alicia Gupte. (A) Frequency of beating decreases under the presence of thimerosal. $p<0.01$ (B) Amplitude of beating increases with thimerosal. $p<0.0001$ (C) Wavelength of the flagellar beat shape increases with thimerosal. $p<0.01$ (D) Maximum curvature is increased under thimerosal. $p<0.001$.

5.4 Discussion and conclusion

The custom Autotrace algorithm has proven to be a valuable tool in the analysis of ciliary kinematics and kinetics. We have successfully applied the software to the tracing of *Chlamydomonas* cilia, pancreatic islet cilia, and sperm flagella. Undergraduate students in the Bayly Lab and the Hughes lab have successfully applied the software to research projects, providing evidence that it is user-friendly. Additionally, as this software is now publicly available and referenced in publications [39, 241], we hope that others will use the software to advance ciliary research as well.

The software algorithm is robust to difficult conditions such as noise, low contrast, and loss of focus. However, there are some conditions that will cause the algorithm to lose tracking and give spurious results. These include severe image noise, intersections of multiple cilia, and debris in the image field. Careful selection of the penalty terms has been found to help with convergence in these conditions.

5.5 Future work

Tracing live cilia and flagella through cyclic beating is an important part of research into these organelles and I expect future work to involve the application of the software presented here (or improved versions of it) to new studies.

Future versions of the Autotrace software may be improved in several ways. Selection of penalty term values has largely been done by trial and error, as once terms are found that work well on one data set, they tend to work well on similar data sets. We have created automated optimization routines that run the tracing algorithm multiple times on a sample data set, optimizing penalty terms to minimize mismatch between the trace and the cilium path, but more

work needs to be done here to make it an efficient and user-friendly process. Finally, at the end of the tracing process, the user is presented with statistics such as the total cost associated with each frame. Large jumps in these values are an indication that there may have been issues with the tracing process at a given frame. Undergraduate researcher Joey Guan is currently working on adding functionality to the software that would allow convenient manual user intervention to correct traces in cases where the algorithm fails.

The Autotrack cell body-tracking software shows potential for use in several areas. Firstly, cell body tracking may be incorporated into future Autotrace software to reduce the two-step process (cell body stabilization first, then cilium tracing) into a single tracing process, which would also simplify calculation of kinetic terms by allowing us to conduct all analysis in a single reference frame. Secondly, early results studying hydrodynamic coupling between *Chlamydomonas* cells trapped in an acoustic trap are promising and may lead to a future publication (Fig. 5.2). Multiple cells may be tracked (one at a time) to study their interactions and the relative phase of their beating, translation, and rotation both about an axis normal to the imaging plane and about their anterior-posterior axes.

Chapter 6: Dynamic analysis of ciliary and flagellar beating[1]

Abstract[2]

Hydrodynamic flow produced by multi-ciliated cells is critical for fluid circulation and cell motility. Hundreds of cilia beat with metachronal synchrony for fluid flow. Cilia-driven fluid flow produces extracellular hydrodynamic forces that cause neighboring cilia to beat in a synchronized manner. However, hydrodynamic coupling between neighboring cilia is not the sole mechanism that drives cilia synchrony. Cilia are nucleated by basal bodies (BBs) that link to each other and to the cell's cortex via BB-associated appendages. The intracellular BB and cortical network is hypothesized to synchronize ciliary beating by transmitting cilia coordination cues. The extent of intracellular ciliary connections and the nature of these stimuli remain unclear. Moreover, how BB connections influence the dynamics of individual cilia has not been established. We show by FIB-SEM imaging that cilia are coupled both longitudinally and laterally in the ciliate Tetrahymena thermophila by the underlying BB and cortical cytoskeletal network. To visualize the behavior of individual cilia in live, immobilized Tetrahymena cells, we developed Delivered Iron Particle Ubiety Live Light- (DIPULL) microscopy. Quantitative and computer analyses of ciliary dynamics reveal that BB connections control ciliary waveform and coordinate ciliary beating. Loss of BB connections reduces cilia-dependent fluid flow forces.

[1] This section reproduces sections of material from and summarizes my contributions to [36] A. W. J. Soh *et al.*, "Intracellular connections between basal bodies promote the coordinated behavior of motile cilia," *Mol Biol Cell*, Jun 29 2022, Art no. mbcE22050150, doi: https://doi.org/10.1091/mbc.e22-05-0150.. See section 1.5 *Statement of contributions*.

[2] This abstract is reproduced from the original paper for the purpose of giving the reader context for the material covered in this chapter. It contains references to material not covered in this dissertation chapter.

6.1 Introduction

Cilia driven hydrodynamic flow in the human body is essential to clearing mucus from airways, circulating cerebrospinal fluid in brain ventricles, and transporting the egg along the oviduct [1-4]. Hundreds or thousands of cilia must beat in a coordinated motion to effectively create these flows. Beating in arrays of cilia typically occurs in a 'metachronal wave' [42]. This is an activation pattern where a wave front of beat initiation propagates spatially, and cilia complete their cycles in its wake. As an analogy, the phenomenon resembles 'the wave' that spectators propagate around sports arenas (though in cilia one cycle tends to follow closely after the last). There are several possible reasons for metachronous beating patterns: (i) they are efficient for creating hydrodynamic flows and moving cargo [249], and (ii) this coordination allows cilia to complete their strokes without interfering with each other ('ciliary tangles' – see movie 4 in *Supplemental Material* for [36])[250]. However, the mechanism by which cilia coordinate these metachronal waves is not understood [205, 251]. In the current work, we investigate the role of basal body (BB) associated structures that act as mechanical couplings between adjacent BBs in coordinating ciliary beating and determining ciliary beat shape, force, and duration.

The ciliated protozoan *Tetrahymena thermophila* is a single-celled organism that swims using approximately 400 cilia distributed over its body [7]. This organism, and mutants of this organism which disrupt BB structures such as the striated fiber (SF)[191, 201], serve as a model for studying ciliary beating in this study.

Though there are many interesting experiments and findings in this paper, I will focus here on my contributions, which were waveform analysis, estimation of forces on the cilia and body of *Tetrahymena* cells, and the statistical analysis of how the *disA-1* mutation and resulting disruption of Striated Fiber (SF) development impacts ciliary beating.

6.2 Methods

Note: this chapter does not use the autotrace software from the previous chapter. Though automatic methods may be applied to tracing single cilia, tracing an individual cilium within an actively beating array is a particularly challenging problem to automate and was conducted manually by Adam Soh.

6.2.1 Ciliary force estimation

Calculation of forces based on ciliary waveform analysis using resistive force theory

Forces on *Tetrahymena* cilia were calculated using resistive force theory [107]. Estimates for the value of the resistive force coefficient vary from approximately 1 to 3.5-fold the viscosity of the fluid [8, 31, 252]. We used the values obtained for wild-type *Chlamydomonas reinhardtii* cilia as previously described ([8]; $C_N=1.53\times10^{-3}pN\cdot s/\mu m^2$, $C_T=0.64\times10^{-3}pN\cdot s/\mu m^2$). These values were adjusted to account for changes in the viscosity of the surrounding fluid due to temperature differences.

The ciliary waveform was traced using a previously published protocol [78]. To ensure equal weightage, each cilium was followed for six consecutive beat cycles. Nine cilia (each from a different cell) were analyzed. Briefly, consecutive frames of *Tetrahymena* cilia undergoing a power stroke (in the xy plane) and a recovery stroke (in the yz plane) were manually traced (Fig. 6.1). For the power stroke, each cilium was aligned along the cell's anterior-posterior axis using the base of the anterior cilium as a reference point. For the recovery stroke, each cilium was aligned relative to the power stroke axis of the same cilium and the cell's anterior-posterior axis. Next, each trace was fitted with a polynomial function. Two-dimensional average ciliary waveforms of the power stroke and recovery stroke were generated by averaging across individual ciliary traces (9 cilia, 6 ciliary beat cycles each, 9 cells). The cilium position is defined

by its orientation from the cilium's distal end (4.5 µm up from the cilium base) relative to the cilium's base and cell's anterior pole. Cilium positions are categorized into 15° bins for both the power and recovery strokes. The start and end positions of each cilium along the power stroke and recovery stroke were defined by the orientation of the first and last ciliary trace that appear along the imaging focal plane. The reference point for angle measurement is 4.5 µm up from the cilium base relative to the cell's anterior-posterior axis. The average start and stop positions for each cilium were calculated by averaging the start and end positions across 6 ciliary beat cycles. The angular trajectory for both the power and recovery strokes were quantified by measuring the angle between the average start and end positions of each cilium. Analyses were focused on ciliary traces that fell within the average angular trajectories (Fig. 5B and G).

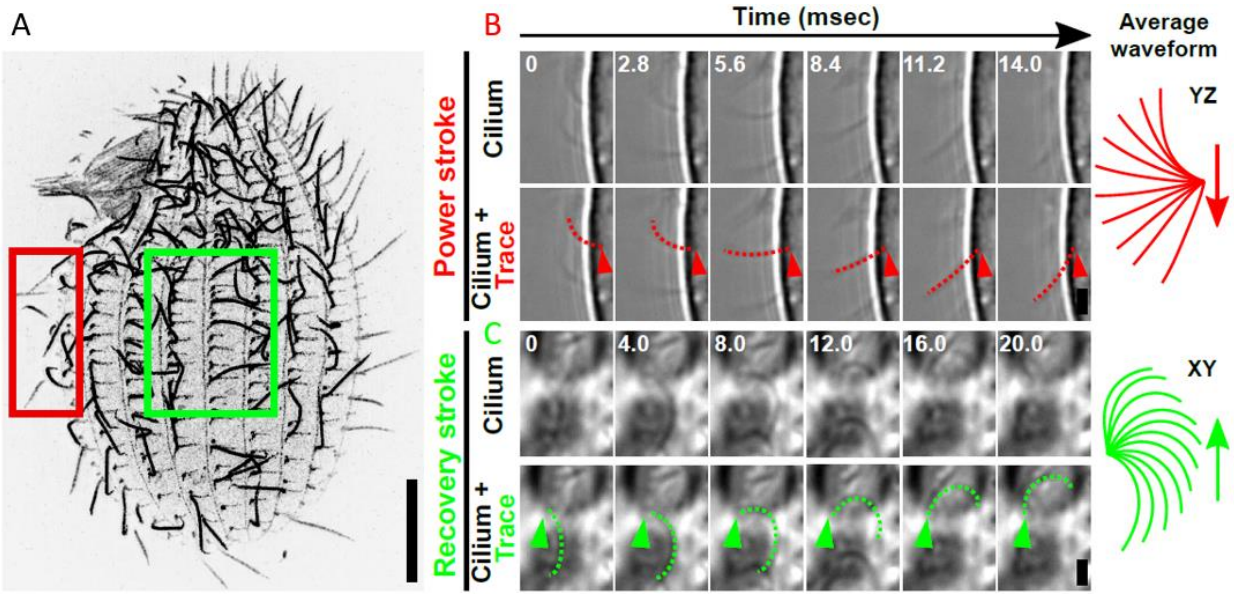

Figure 6.1: Tracing immobilized live Tetrahymena cilia during beating. Reproduced from [36]. (A) Tetrahymena ciliary array. Bar, 10 µm. (B,C) Timelapse images of power (B) and recovery (C) strokes. Time intervals (msec) are indicated. Dotted lines mark manual cilia traces. Average power stroke, red. Average recovery stroke, green. Scale bars, 2 µm.

Cilium velocity, $\boldsymbol{v_c}(s,t)$, as a function of arclength coordinate, s, and time, t, was calculated by numerically differentiating the coordinates of the cilium traces with respect to t. Velocities are projected onto the tangent and normal vectors along the cilium for calculation of the distributed resistive forces [8]. Power per unit length (fW/μm) along the cilium is calculated as the dot product of the distributed force and velocity, $P(s,t) = \boldsymbol{F}(s,t) \cdot \boldsymbol{v}_c(s,t)$. Total power produced by the cilium at a given time is obtained by numerically integrating the power over the length of the cilium. Moment at the cilium basal attachment (pNμm) is calculated as the integral along the length of the cilium of the cross product of the position relative to the basal attachment and the distributed force, $M_0(t) = \int_0^L \boldsymbol{x}(s,t) \times \boldsymbol{F}(s,t)ds$.

Calculation of forces on the cell body

Forces on the cell body were calculated for comparison against ciliary forces estimated from RFT. Average swimming velocities for WT and *disA-1* cells used in calculations were based on previously reported study [201]. The cell body was modeled as an ellipsoid moving along its major axis [8, 253]. If the length of the major and minor axes of the cell body are given as a and b, respectively, then the eccentricity is given by the equation, $e = \sqrt{1 - b^2/a^2}$. The force along the major axis (denoted F_x) is given by Eq. 6.1.

$$F_x = 6\pi\mu a v_x \times C_{F1} \tag{6.1}$$

Here μ is the dynamic viscosity of the medium, v_x is the component of the cell velocity along the major axis, and $C_{F1}$is a dimensionless correction factor to account for the eccentricity. $C_{F1}$is given in Eq. 6.2.

$$C_{F1} = \frac{8}{3}e^3\left[-2e + (1+e^2)\ln\frac{1+e}{1-e}\right]^{-1} \tag{6.2}$$

To estimate the average force for each cilium, the body drag force along the cell's anterior-posterior axis (Eq. 6.1) was divided by the estimated number of cilia, 400 (assuming all BBs are ciliated; [254]).

6.2.2 Statistical analysis

All datasets were assessed for normal distribution using the Shapiro-Wilk or Kolmogorov-Smirnov test. A student's t-test was performed on normally distributed datasets. A Mann-Whitney test was performed on datasets that do not conform to a normal distribution. An F-test was performed to compare variance between conditions. Tests for significance were unpaired and two-tailed. All error bars indicate SD. P value is indicated for all statistical analyses. All analyses were performed on samples obtained from 3 independent experiments.

6.3 Results

6.3.1 Loss of BB connections reduces ciliary power stroke durations

To test whether BB connections specifically impact ciliary forces, we focused on individual cilia with BBs that are disconnected but still oriented. Oriented cilia were identified as those in which the power stroke occurs along the cell's anterior-posterior axis and remain in-focus during the entire power stroke before transiting into the recovery stroke where they exit the imaging focal plane (Fig. 6.1B). We also imposed the requirement that the anterior and posterior neighboring cilia are similarly oriented. Ciliary parameters that affect fluid flow are defined at minimum by ciliary length, ciliary beat frequency or speed, ciliary sweep trajectory, and ciliary curvature. Ciliary length is not changed in *disA-1* mutants (WT: 5.0±0.7 μm; *disA-1*: 5.2±0.6 μm; Student's t-test; P = 0.35), and we therefore focused on the remaining three parameters to determine if they were impacted when BBs are disconnected.

To quantify the ciliary generated forces, the entire cilium must be within the imaging focal plane. The relative start and end positions of the power stroke were defined as when cilia first appear and exit the side view imaging focal plane, respectively (Fig. 6.1A; red box). The same method was applied to define the average start and stop positions of the recovery stroke when cilia were imaged from the top of the cell (Fig. 6.1A; green box). Importantly, this method only captures a portion of the complete power and recovery strokes when cilia are in focus. The WT power stroke duration was 18.0±9.3 msec while that of *disA-1* cilia was 11.0±1.8 msec (Mann-Whitney test; P value = 0.018). While the WT power stroke duration is similar to that obtained by kymograph analysis (see published article for details), the *disA-1* power stroke is much shorter and likely represents a shorter duration in the imaging plane. The WT and *disA-1* recovery stroke durations were similar to each other but significantly reduced compared to kymograph analysis (WT = 10.0±4.3 msec and *disA-1* = 10.0±3.1 msec; Mann-Whitney test; P value = 0.73). Like the power stroke, this shorter measured duration likely results from the recovery stroke moving out of the imaging focal plane. These limited segments of the ciliary beat cycle were next used to quantify the ciliary waveforms and predicted force outputs.

6.3.2 BB connections support normal ciliary waveforms

The sweep trajectory of *disA-1* cilia is not always consistent between beat strokes (see full article for details), suggesting that the ciliary waveform is disrupted when BBs are disconnected. Quantitative comparisons between the ciliary waveforms of oriented cilia suggest that *disA-1* cilia display a shorter sweep angle along the power stroke compared to WT cilia (Fig. 6.2A,B; WT cilia: 88.0±20.0°; *disA-1* cilia: 51.0±27.0°; Mann-Whitney test; P = 0.008). These average representative waveforms are generated from many individual ciliary traces that are standardized by using the average start and stop positions of all analyzed cilia (Fig. 6.2A (red highlights) and B; n = 9 cilia, 6 ciliary beat cycles each, 9 cells). *disA-1* cilia initiate the power stroke at 66.0±26.0° compared to WT cilia at 42.0±10°; and then transition into the recovery stroke at 120.0±18.0° compared to 130.0±19.0° for WT cilia (Fig. 6.2B,G). Subtle increases in variance were observed in *disA-1* cilia and may be explained by the subpopulation (49%) of oriented cilia with connected BBs that we expect to behave like WT cilia. The *disA-1* power stoke is shorter, suggesting that BB connections promote a long ciliary power stroke trajectory (Fig. 6.2A,B).

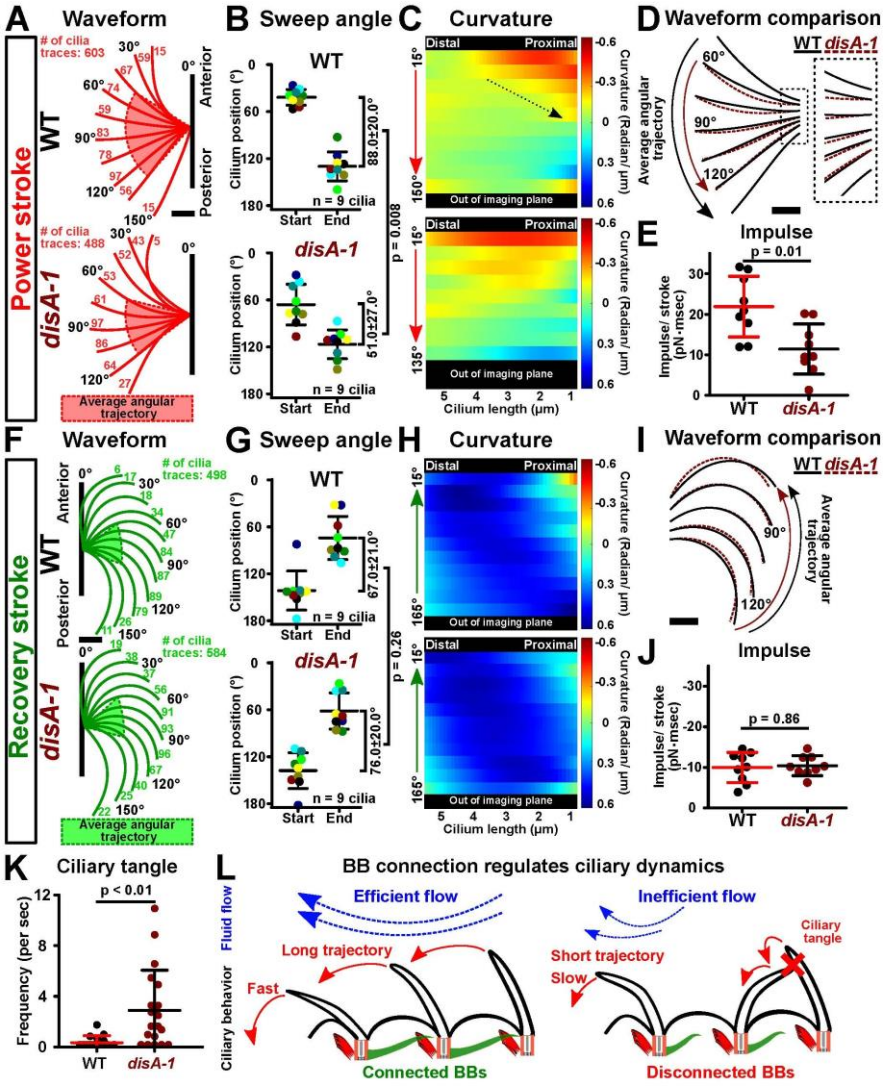

Figure 6.2: **BB connections support ciliary waveform and coordination**. Reproduced from [36]. (A) Tetrahymena power stroke waveform. Top panel: Average WT power stroke waveform. Bottom panel: Average disA-1 power stroke waveform. Red highlight indicates the average angular trajectory (n = 9 cilia). Cilium position is defined by the angle from the cilium distal end (4.5 μm up the cilium base) relative to the cell's anterior-posterior axis. Angles are categorized into 15° bins. Each angular bin contains at least 1% of all ciliary traces per condition. The number of cilia traces for each bin is indicated. (B) Angular trajectories of WT and disA-1 cilia during the power stroke. disA-1 cilia undergo shorter trajectories than WT cilia. Each cilium in the analysis is color coded. (C) Curvature heatmaps of WT and disA-1 cilia through the power stroke (blue: cilium bends towards the cell anterior pole; red: cilium bends away from the cell anterior pole; green: straight cilium). Y-axis marks the cilium position through the power stroke. Dotted arrow indicates the change in WT cilium curvature at the start to middle of the power stroke. WT power stroke: n = 603 cilia traces (9 cilia, 6 ciliary beat cycles each, 9 cells). disA-1 power stroke: n = 488 cilia traces (9 cilia, 6 ciliary beat cycles each, 9 cells). (D) Superimposed WT (black lines) and disA-1 (brown dashed lines) average power stroke waveform. Curvature differences are depicted only for stages of the power stroke that fall within the average angular trajectories of WT and disA-1 cilia. (E) Ciliary power stroke impulses were estimated using resistive force theory. WT cilia exert greater impulse (area under the force-time curve) than disA-1 cilia along the anterior-posterior axis per power stroke (n = 9 cilia). (F) Tetrahymena recovery stroke waveform. Top panel: Average WT recovery stroke waveform. Bottom panel: Average disA-1 recovery stroke waveform. Green highlight indicates the average angular trajectory (n = 9 cilia). Cilium position is defined by the angle from the cilium distal end (4.5 μm up the cilium base) relative to the cilium's power stroke axis. Angles are categorized into 15° bins. Each angular bin is at least 1% of all ciliary traces per condition. Number of cilia traces for each bin is indicated. (G)

Angular trajectories of WT and disA-1 cilia. Each cilium in the analysis is color coded. disA-1 cilia undergo comparable trajectories as WT cilia during the recovery stroke. (H) Curvature heatmaps of WT and disA-1 cilia through the recovery stroke (blue: cilium bends towards the cell anterior pole; red: cilium bends away from the cell anterior pole; green: straight cilium). Y-axis marks the cilium position through the recovery stroke. WT recovery stroke: n = 498 cilia traces (9 cilia, 6 ciliary beat cycles each, 9 cells). disA-1 recovery stroke: n = 584 cilia traces (9 cilia, 6 ciliary beat cycles each, 9 cells). (I) Superimposed WT (black lines) and disA-1 (brown dashed lines) average recovery stroke waveform. Curvature differences are depicted only for stages of the recovery stroke that fall within the average angular trajectories of WT and disA-1 cilia. (J) Ciliary recovery stroke impulses were estimated using resistive force theory. WT and disA-1 cilia exert comparable impulse (area under the force-time curve along the anterior-posterior axis per recovery stroke (n = 9 cilia). (K) Frequency of ciliary tangles. WT: n = 11 cells (14 cilia pair); disA-1: n = 13 cells (19 cilia pairs). (L) Schematic illustrates the model that BB connections promote fast and long power stroke trajectories for coordinated ciliary beating and effective fluid flow propulsion. Scale bars, 1 μm.

Changes to ciliary curvature alter the efficiency of fluid flow as straight cilia promote greater fluid propulsion than bent cilia [107, 255, 256]. We assessed the impact of BB connections on cilia curvature. A curvature value of zero indicates a straight cilium, a negative curvature value indicates a concave cilium profile that bends away from the cell anterior, and a positive curvature value indicates a convex cilium profile that bends towards the cell anterior. The greatest differences between WT and *disA-1* ciliary curvature occur primarily at the start to the middle of the power stroke (Fig. 6.2D). WT cilia are approximately 12-fold more curved than *disA-1* cilia at the proximal end of the cilium (Fig. 6.2D (inset); WT: -0.17±0.05 radians/ μm; *disA-1*: 0.01±0.11 radians/ μm; Mann-Whitney test; $P < 0.0001$). Importantly, the most proximal region of cilia (1.5 μm) could not be detected in our imaging. There may be unobservable differences between WT and *disA-1* in this proximal region. At the medial region of the cilium, *disA-1* are 2-fold more bent than WT cilia (Fig. 6.2D; WT: -0.08±0.02 radians/ μm; *disA-1*: -0.14±0.04 radians/ μm; Mann-Whitney test; $P < 0.0001$). Together, this suggests that BB connections influence ciliary curvature during the power stroke.

The recovery stroke returns cilia back to the start of the power stroke. Unlike the power stroke, SF connections do not appear to impact the angular trajectory of the recovery stroke (Fig. 6.2G; WT

cilia: 67.0±21.0°; *disA-1* cilia: 76.0±20.0°; Mann-Whitney test. P = 0.26). We were unable to visualize the transition from the power to the recovery stroke and vice-versa because cilia move out of the focal plane during the 3-dimensional ciliary beat stroke. Seemingly contradictory, the recovery stroke trajectory of WT and *disA-1* cilia appear to be similar despite the shorter average sweep trajectory of the *disA-1* power stroke (Fig. 6.2B,G). One explanation is that the recovery stroke imaging plane of WT and *disA-1* cilia is different whereby WT cilia move closer to the cell cortex. This would result in comparable recovery stroke trajectory angles between WT and *disA-1* cilia, but the total distance traveled would be reduced for *disA-1* cilia. Alternatively, *disA-1* cilia may change their trajectory during transitions between power and recovery strokes outside the imaging focal plane. We next measured the difference in curvature in *disA-1* cilia and found they are slightly more bent during the recovery stroke than WT (Fig. 6.2I; WT: 0.46±0.11 radians/ µm; *disA-1*: 0.51±0.10 radians/ µm; Mann-Whitney test; P < 0.0001). Thus, our results suggest that BB connections are not required for normal recovery stroke angular sweep trajectories but do reduce ciliary curvature.

6.3.3 Ciliary changes resulting from BB disconnections reduce ciliary force

To test whether the shorter sweep angle and abnormal curvature exhibited by *disA-1* cilia during the power stroke reduce ciliary effectiveness, the magnitude of force along the anterior-posterior axis was estimated using resistive force theory (RFT). RFT uses resistive force coefficients to determine the distributed viscous drag applied to the cilium by the surrounding fluid based on the orientation and velocity of the cilium as a function of arc length and time [107]. Overall force produced by a cilium during its beat stroke will be affected by the cilium length, angular sweep rate, beat shape, and viscosity of the medium. WT cilia exerted an average force of 1.41±0.60 pN during the observed power stroke (Fig. 6.3A and Table 6.1; maximum power stroke force by WT cilia: 2.70±0.88 pN). The average force exerted during the observed power stroke by *disA-1* cilia is reduced by 18% (Fig. 6.3A and Table 6.1; *disA-1*; average power stroke force: 1.16±0.79 pN; maximum power stroke force: 2.11±1.19 pN). As shown in Fig. 6.2D, differences in curvature of WT and *disA-1* cilia are concentrated at the beginning of the power stroke, whereas differences in force output are greater toward the middle and end of the power stroke. This suggests that the reduced force of *disA-1* cilia is not due to the change in curvature but rather to the reduced angular sweep rate (Table 6.1; WT: 6.62±2.72°/ msec; *disA-1*: 5.20±2.88°/ msec). The magnitude of force production in the opposite direction during the recovery stroke was similar between WT and *disA-1* cilia (Fig. 6.3B and Table 6.1; average recovery stroke force; WT: -1.05±0.34 pN; *disA-1*: -1.13±0.40 pN; Mann-Whitney test; P value = 0.68).

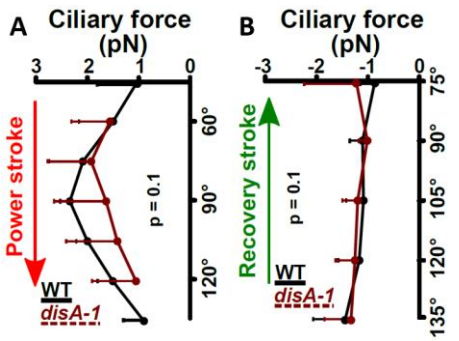

Figure 6.3: Ciliary power and recovery stroke forces for wild-type and disA-1 cells throughout the beat cycle. Reproduced from [36]. (A) Ciliary power stroke forces were estimated using resistive force theory. WT cilia exert more power stroke force per stroke than disA-1 cilia (9 cilia, 6 ciliary beat cycles each, 9 cells). Data bin size is 15°. (B) Ciliary recovery stroke forces were estimated using resistive force theory. WT cilia exert comparable recovery stroke force per stroke relative to disA-1 cilia (9 cilia, 6 ciliary beat cycles each, 9 cells). Data bin size is 15°.

Table 6.1: Tabulation of results of ciliary force estimation. Ciliary forces were estimated from manual traces using previously described resistive force coefficients (C_N=1.53μ, C_T=0.64μ; [8]). Viscosity of water, μ, applied in analysis was 0.889cP at 25°C. All average values for ciliary quantities were calculated by averaging values within the mean sweep angle range for each traced ciliary beat stroke (54 total beat strokes each in 4 data sets), then calculating the average and standard deviation of the average quantities. Maximum values were calculated by taking the maximum value for each stroke within the mean sweep angle range, then calculating the average and standard deviation for the maximum quantities. All force values integrate forces in the anterior-posterior axis direction over the length of the cilium trace. Sweep rates are calculated by numerically differentiating the angle from the base of the cilium trace to 4.5 mm up the cilium with respect to time. WT and disA-1 swim speeds [201] were used to estimate viscous drag forces on the Tetrahymena cell body using previously described methods [8, 253].

Parameter	WT	*disA-1*	P value
Average power stroke force [pN]	1.41 ± 0.60	1.16 ± 0.79	0.07
Maximum power stroke force [pN]	2.70 ± 0.88	2.11 ± 1.19	0.001
Average recovery stroke force [pN]	-1.05 ± 0.34	-1.13 ± 0.40	0.73
Maximum recovery stroke force [pN]	-1.51 ± 0.51	-1.68 ± 0.56	0.15
Average power stroke sweep rate [deg/ msec]	6.62 ± 2.72	5.20 ± 2.88	0.04
Maximum power stroke sweep rate [deg/ msec]	10.69 ± 4.18	7.74 ± 4.00	0.002
Average recovery stroke sweep rate [deg/ msec]	5.83 ± 1.94	6.37 ± 2.28	0.31
Maximum recovery stroke sweep rate [deg/ msec]	7.60 ± 2.02	9.13 ± 3.11	0.008
Average power stroke basal moment [pN·μm]	2.86 ± 0.87	1.93 ± 1.44	0.00003
Maximum power stroke basal moment [pN·μm]	10.58 ± 3.16	8.37 ± 5.05	0.0005
Average recovery stroke basal moment [pN·μm]	1.13 ± 0.59	1.36 ± 0.72	0.16
Maximum recovery stroke basal moment [pN·μm]	4.90 ± 1.98	5.10 ± 1.93	0.44
Average power stroke power [aW]	870 ± 600	690 ± 640	0.02
Average recovery stroke power [aW]	420 ± 220	500 ± 310	0.27
Swimming Speed [μm/ sec]	272	123	-
Body force / cilium [pN]	-0.26	-0.12	-

Not only do *disA-1* cilia produce lower power stroke forces on average, but they also spend a shorter duration of time producing that force due to the shorter sweep angle in our segmented analysis using only cilia in focus (Fig. 6.2A,B). This leads to a lower *impulse*, the measure of the area under the force-time curve. The mean axial impulse of WT cilia was 21.9±7.5 pN·ms, and that of *disA-1* cilia was 11.4±6.2 pN·ms (Fig. 6.2E, Mann-Whitney test; P = 0.01). During the recovery stroke, WT cilia produce an impulse of -10.0±3.7 pN·ms and *disA-1* cilia produce an impulse of -10.4±2.5 pN·ms (Fig. 6.2J, Mann-Whitney test; P = 0.86). Though the power stroke of *disA-1* cilia is significantly less productive, the recovery stroke produces a similar amount of drag impulse. The average measured impulses sum to 11.9±8.4 pN·ms per beat for WT cilia, and 1.0±6.7 pN·ms per beat for *disA-1* cilia, providing an estimate of the overall effectiveness of each beat. It should be noted that it was not possible to measure power and recovery strokes on the same cilia, and that the standard deviations on the power and recovery stroke impulses for *disA-1* cilia are larger than the difference in their magnitudes. For WT cilia, multiplying the net average impulse of 11.9 pN·ms per beat by the average frequency of 24 Hz gives an average total force per cilium of 0.29 pN, which compares well to the body drag force per cilium of -0.26 pN (Table 6.1). In summary, *disA-1* cilia are less effective in part due to their lower average force output during their beat stroke, but more significantly due to the shorter time duration spent sweeping a shorter trajectory.

6.4 Discussion

The *disA-1* mutation, and its impairment of SF formation and thus BB interconnection has been known to reduce ciliary effectiveness as measured by swimming speed in *Tetrahymena* cells [201]. Here we investigated the reasons for that reduction and found that while average and maximum powerstroke forces are reduced in *disA-1* mutants, those reductions alone are not

sufficient to account for the overall reduction in output. In addition, *disA-1* cilia sweep a shorter trajectory and spend a smaller fraction of the beat cycle in the power stroke phase. This combination of reduced force and reduced power stroke duration greatly diminishes the impulse created during the *disA-1* power stroke. Because force is proportional to velocity in RFT, the impulse produced during each ciliary beat cycle is proportional to the distance the cell is pushed forward (in this linear model). By multiplying this distance by the beat frequency and the total number of cilia we get an estimate of the swimming speed.

A possible explanation for both the reduced propulsive force and shorter angular trajectory of *disA-1* cilia is greater rotational compliance of the BB within the power stroke plane due to the lack of SF support, which is consistent with the modeling results shown in Chapter 4 [34]. The estimated average bending moment at *disA-1* BBs during the ciliary power stroke is reduced by 33% compared to WT (Table 6.1; WT: 2.86±0.87 pN·μm; *disA-1*: 1.93±1.44 pN·μm; $P < 0.0001$). If the BB has rotational compliance, the moment due to viscous forces on the cilium will tend to rotate it in the opposite direction of the cilium during the power stroke. We expect that the BB rotation predicted for WT cells would increase in *disA-1* cells where BBs are no longer connected. BB rotation will have the effect of reducing the sweep angle for a given ciliary deformation cycle. Reducing the sweep angle alone would reduce the sweep rate for a given ciliary deformation thereby reducing the applied forces. This complex interaction requires further experimental and modeling work. Recovery stroke parameters are largely unaffected in *disA-1* cells, perhaps because the recovery stroke occurs in a plane orthogonal to the BB axis and structural connections other than the SF, such as the post-ciliary microtubules (pcMTs), transverse microtubules (tMTs), and the cellular cortex, are sufficient to stabilize it against moments about its axis.

6.5 Conclusion

While forces produced by disA-1 cilia are reduced, the shortened powerstroke sweep duration is responsible for the majority of the reduction in impulse. Loss of SF stabilization may lower the ability of *disA-1* basal bodies to resist bending moments, shortening the power stroke angle and duration. Other structures such as the pcMTs, tMTs, and the cortical attachments may stabilize BB to rotations about its axis, hence the recovery stroke remains unaffected.

Chapter 7: Conclusions and Future Work

While the study of ciliary beating is a long standing endeavor dating back to the 1950s [21, 107], there is still much to be learned about how cilia beat, how internal ciliary structures deform and resist deformation, and how cilia interact within arrays to produce metachronal waves and steer multiciliated microswimmers.

The idea of mechanical-instability-driven ciliary beating is a novel one in terms of the history of ciliary research [32]. The idea has gained traction since it was first proposed, but there is still much investigation to be done both experimentally and computationally. Previous modeling studies have applied linear stability analysis to two-filament PDE models and time-stepping simulation of simple multi-filament models [32]. Hu advanced the multi-filament model by adding a sliding nonlinearity in the radial spokes [33]. Many other models of instability driven oscillations are simple single-filament models [46, 47, 257]. In Chapter 3, I confirm previous results that oscillations arise under steady dynein force in models of the axoneme that are consistent with physical laws. I also advance previous work through a custom finite-element code that enforces exact balance of internal forces and moments and allows efficient stability analysis of multi-filament models. The current work includes a "6+1" model of the axoneme but extending the software to a "9+2" model would be straightforward, as the code was designed to be versatile in this way.

There is still progress to be made in advancing the sophistication of geometrically nonlinear multifilament models to better represent our understanding of the underlying structure of the axoneme. An intended application for the efficient stability analysis model created in Chapter 3

is the prediction of the behavior of large deformation multi-filament models. Through the creation of a 9-outer-filament computer model of the axoneme and BB in Chapter 4, I have learned a lot about modeling these structures and hope to apply these techniques to advance the study of instability driven beating. Combining newly learned techniques such as the use of mapping functions to model nonlinear sliding and dynein force interactions between filaments would allow us to represent the axoneme and model large deformations in ways that are not possible without the use of these tools. These modeling advances informed by the predictions of multi-filament stability analysis would allow us to break new ground in the simulation study of ciliary beating.

To further establish the plausibity of the steady dynein force model, a future goal is to create a physical model of the axoneme, informed by computational models, that beats under steady "dynein" force. This is a challenging and ongoing project.

In Chapter 4, I recapitulate important aspects of observed BB bending in an elaborate finite-element model of the BB and axoneme. This work predicts that temperature-dependent deformations observed in the BB are related to forces transmitted between adjacent BBs by the SF, which is known to develop differently at different temperatures. The role of BB accessory structures (SF, tMT, and pcMT) are predicted by perturbing those structures in the model. The prediction that the SF plays a large role in stabilizing the BB against rocking during the powerstroke informs and agrees with dynamic analysis of WT and *disA-1* beating performed in Chapter 6, where it was found that *disA-1* cilia have slower, shorter-in-angle power strokes that produce lower impulse per beat. I hypothesize that this is due to the inability of *disA-1* cilia to resist high bending moments (for which maximum and average values were calculated to be significantly lower over the course of the power stroke).

The model used in Chapter 4 is a step forward, but it is not perfect. Deformation sizes are limited, and internal forces are not completely balanced due to necessary simplifications used in the model. A possible future project would be the improvement of the model to allow for larger deformations and the incorporation of established models of ciliary beating. This would allow us to study ciliary beating and BB deformation in tandem and would drop the necessity for commonly applied assumptions in modeling of beating such as the fixing of MTDs at their base.

Future work should also include experiments to test the predictions of computational models. In Chapter 3, I made predictions about axonemal twist and torsion by analyzing the displacements of the individual filaments in the model. In Chapter 4, collaborators in the Pearson lab used electron tomograms of rapidly frozen *Tetrahymena* cells to determine deformations of BBs and cilia at various stages of the beat stroke. A combination of these types of approaches would allow us to make predictions about the filament level deformations in beating cilia and investigate them experimentally.

Current ongoing work includes a collaboration with members of the Santi Lab – Celia Santi and Juan Ferreira – to apply dynamic analysis of sperm imaging to quantify the relevant changes in beat shape that would allow us to determine capacitation of sperm cells and possibly help clinicians to diagnose fertility issues.

Other ongoing work involves a collaboration with members of the Meacham Lab – Mark Meacham and Advaith Narayan – to track beating *Chlamydomonas* cells as they interact in an acoustic trap to uncover mechanisms of cell-cell interactions and hydrodynamic coupling of ciliary beating. We plan to extend this analysis to *Tetrahymena* cells with the help of the Pearson lab. Future projects may study the interactions of many microswimmers, emergent behavior in

swarms of these organisms, and control of these swarms through the manipulation of the phototaxis, gravitaxis, and chemotaxis of the individual microswimmers.

References

[1] L. E. Kuek and R. J. Lee, "First contact: the role of respiratory cilia in host-pathogen interactions in the airways," (in English), *Am J Physiol-Lung C,* vol. 319, no. 4, pp. L603-L619, Oct 2020, doi: 10.1152/ajplung.00283.2020.

[2] A. J. Jimenez, M. D. Dominguez-Pinos, M. M. Guerra, P. Fernandez-Llebrez, and J. M. Perez-Figares, "Structure and function of the ependymal barrier and diseases associated with ependyma disruption," *Tissue Barriers,* vol. 2, p. e28426, 2014, doi: 10.4161/tisb.28426.

[3] A. Mahuzier *et al.*, "Ependymal cilia beating induces an actin network to protect centrioles against shear stress," (in eng), *Nat Commun,* vol. 9, no. 1, p. 2279, Jun 11 2018, doi: 10.1038/s41467-018-04676-w.

[4] M. Ezzati, O. Djahanbakhch, S. Arian, and B. R. Carr, "Tubal transport of gametes and embryos: a review of physiology and pathophysiology," *J Assist Reprod Genet,* vol. 31, no. 10, pp. 1337-47, Oct 2014, doi: 10.1007/s10815-014-0309-x.

[5] C. B. Lindemann and K. A. Lesich, "Functional anatomy of the mammalian sperm flagellum," *Cytoskeleton (Hoboken),* vol. 73, no. 11, pp. 652-669, Nov 2016, doi: 10.1002/cm.21338.

[6] J. Lin and D. Nicastro, "Asymmetric distribution and spatial switching of dynein activity generates ciliary motility," *Science,* vol. 360, no. 6387, 2018/4/27 2018, doi: 10.1126/science.aar1968.

[7] B. A. Bayless, D. F. Galati, and C. G. Pearson, "Tetrahymena basal bodies," *Cilia,* vol. 5, p. 1, 2015, doi: 10.1186/s13630-016-0022-8.

[8] P. V. Bayly, B. L. Lewis, E. C. Ranz, R. J. Okamoto, R. B. Pless, and S. K. Dutcher, "Propulsive forces on the flagellum during locomotion of Chlamydomonas reinhardtii," *Biophys. J.,* vol. 100, no. 11, pp. 2716-2725, 2011/6/8 2011, doi: 10.1016/j.bpj.2011.05.001.

[9] R. A. Segal, B. Huang, Z. Ramanis, and D. J. Luck, "Mutant strains of Chlamydomonas reinhardtii that move backwards only," *J. Cell Biol.,* vol. 98, no. 6, pp. 2026-2034, 1984/6 1984, doi: 10.1083/jcb.98.6.2026.

[10] D. R. Mitchell, "Evolution of Cilia," *Cold Spring Harbor perspectives in biology,* vol. 9, no. 1, Jan 3 2017, doi: 10.1101/cshperspect.a028290.

[11] M. Fliegauf, T. Benzing, and H. Omran, "Mechanisms of disease - When cilia go bad: cilia defects and ciliopathies," (in English), *Nat Rev Mol Cell Bio,* vol. 8, no. 11, pp. 880-893, Nov 2007, doi: 10.1038/nrm2278.

[12] T. W. Ferkol and M. W. Leigh, "Ciliopathies: The Central Role of Cilia in a Spectrum of Pediatric Disorders," (in English), *J Pediatr-Us,* vol. 160, no. 3, pp. 366-371, Mar 2012, doi: 10.1016/j.jpeds.2011.11.024.

[13] Y. Okada, S. Nonaka, Y. Tanaka, Y. Saijoh, H. Hamada, and N. Hirokawa, "Abnormal nodal flow precedes situs inversus in iv and inv mice," *Mol Cell,* vol. 4, no. 4, pp. 459-68, Oct 1999, doi: 10.1016/s1097-2765(00)80197-5.

[14] C. Guichard *et al.*, "Axonemal dynein intermediate-chain gene (DNAI1) mutations result in situs inversus and primary ciliary dyskinesia (Kartagener syndrome)," *Am J Hum Genet,* vol. 68, no. 4, pp. 1030-5, Apr 2001.

[15] N. Derichs, B. J. Jin, Y. L. Song, W. E. Finkbeiner, and A. S. Verkman, "Hyperviscous airway periciliary and mucous liquid layers in cystic fibrosis measured by confocal fluorescence photobleaching," (in English), *Faseb Journal,* vol. 25, no. 7, pp. 2325-2332, Jul 2011, doi: 10.1096/fj.10-179549.

[16] M. A. Jakus and C. E. Hall, "Electron Microscope Observations of the Trichocysts and Cilia of Paramecium," (in English), *Biol Bull,* vol. 91, no. 2, pp. 141-144, 1946, doi: Doi 10.2307/1538256.

[17] B. Afzelius, "Electron microscopy of the sperm tail; results obtained with a new fixative," *J Biophys Biochem Cytol,* vol. 5, no. 2, pp. 269-78, Mar 25 1959, doi: 10.1083/jcb.5.2.269.

[18] H. J. Hoops and G. B. Witman, "Outer doublet heterogeneity reveals structural polarity related to beat direction in Chlamydomonas flagella," *J. Cell Biol.,* vol. 97, no. 3, pp. 902-908, 1983/9 1983, doi: 10.1083/jcb.97.3.902.

[19] K. Song, Z. Shang, X. Fu, X. Lou, N. Grigorieff, and D. Nicastro, "In situ structure determination at nanometer resolution using TYGRESS," *Nature Methods,* vol. 17, no. 2, pp. 201-208, 2020, doi: 10.1038/s41592-019-0651-0.

[20] I. R. Gibbons, "Studies on Protein Components of Cilia from Tetrahymena Pyriformis," (in English), *P Natl Acad Sci USA,* vol. 50, no. 5, pp. 1002-&, 1963, doi: DOI 10.1073/pnas.50.5.1002.

[21] K. E. Machin, "Wave propagation along flagella," *J. Exp. Biol.,* vol. 35, no. 4, pp. 796-806, 1958 1958.

[22] J. Howard, "Quantitative cell biology: the essential role of theory," *Mol Biol Cell,* vol. 25, no. 22, pp. 3438-40, Nov 5 2014, doi: 10.1091/mbc.E14-02-0715.

[23] P. Satir, "STUDIES ON CILIA : II. Examination of the Distal Region of the Ciliary Shaft and the Role of the Filaments in Motility," *J Cell Biol,* vol. 26, no. 3, pp. 805-34, Sep 1 1965, doi: 10.1083/jcb.26.3.805.

[24] B. A. Szabo and I. Babuška, *Introduction to finite element analysis : formulation, verification, and validation*. Hoboken, N.J.: Wiley, 2011, pp. xviii, 364 p.

[25] G. E. P. Box, "Science and Statistics," (in English), *J Am Stat Assoc,* vol. 71, no. 356, pp. 791-799, 1976, doi: Doi 10.2307/2286841.

[26] C. J. Brokaw and D. J. Luck, "Bending patterns of chlamydomonas flagella I. Wild-type bending patterns," *Cell Motil.,* vol. 3, no. 2, pp. 131-150, 1983 1983, doi: 10.1002/cm.970030204.

[27] C. J. Brokaw, "Effects of increased viscosity on the movements of some invertebrate spermatozoa," *J. Exp. Biol.,* vol. 45, no. 1, pp. 113-139, 1966/8 1966.

[28] K. S. Wilson, O. Gonzalez, S. K. Dutcher, and P. V. Bayly, "Dynein-deficient flagella respond to increased viscosity with contrasting changes in power and recovery strokes," *Cytoskeleton,* vol. 72, no. 9, pp. 477-490, 2015/9 2015, doi: 10.1002/cm.21252.

[29] C. J. Brokaw and R. Kamiya, "Bending patterns of Chlamydomonas flagella: IV. Mutants with defects in inner and outer dynein arms indicate differences in dynein arm function," *Cell Motil. Cytoskeleton,* vol. 8, no. 1, pp. 68-75, 1987 1987, doi: 10.1002/cm.970080110.

[30] C. J. Brokaw, "Bend propagation by a sliding filament model for flagella," *J. Exp. Biol.,* vol. 55, no. 2, pp. 289-304, 1971/10 1971.

[31] I. H. Riedel-Kruse, A. Hilfinger, J. Howard, and F. Julicher, "How molecular motors shape the flagellar beat," *HFSP J,* vol. 1, no. 3, pp. 192-208, Sep 2007.

[32] P. Bayly and S. Dutcher, "Steady dynein forces induce flutter instability and propagating waves in mathematical models of flagella," *J Roy Soc Interface,* vol. 13, no. 123, p. 20160523, 2016.

[33] T. Hu and P. V. Bayly, "Finite element models of flagella with sliding radial spokes and interdoublet links exhibit propagating waves under steady dynein loading," *Cytoskeleton,* vol. 75, no. 5, pp. 185-200, 2018, doi: 10.1002/cm.21432.

[34] A. D. Junker, L. G. Woodhams, A. W. J. Soh, E. T. O'Tool, P. V. Bayly, and C. G. Pearson, "Basal bodies bend in response to ciliary forces," *Current Biology,* 2022 (in review).

[35] P. V. Bayly, B. L. Lewis, P. S. Kemp, R. B. Pless, and S. K. Dutcher, "Efficient spatiotemporal analysis of the flagellar waveform of Chlamydomonas reinhardtii," *Cytoskeleton,* vol. 67, no. 1, pp. 56-69, 2010/1 2010, doi: 10.1002/cm.20424.

[36] A. W. J. Soh *et al.*, "Intracellular connections between basal bodies promote the coordinated behavior of motile cilia," *Mol Biol Cell,* Jun 29 2022, Art no. mbcE22050150, doi: https://doi.org/10.1091/mbc.e22-05-0150.

[37] L. G. Woodhams, D. Cortese, P. V. Bayly, and K. Y. Wan, "Chapter 12: Physics and mechanics of ciliary beating," in *The Chlamydomonas Sourcebook*, vol. 3, S. Dutcher Ed., Third ed.: Elsevier, 2022 (in press).

[38] L. G. Woodhams, Y. Shen, and P. V. Bayly, "Generation of ciliary beating by steady dynein activity: the effects of inter-filament coupling in multi-filament models," *J. R. Soc. Interface*, no. 19, 06/07//2022 2022, Art no. 20220264, doi: https://doi.org/10.1098/rsif.2022.0264.

[39] J. H. L. Cho, Z.A.; Zhu, L; Muegge, B.D.; Roseman, H.F.; Lee, E.Y.; Utterback, T.; Woodhams, L.G., Bayly, P.V.; Hughes, J.W., "Islet primary cilia motility controls insulin secretion," *Science Advances*, 2022 (in press).

[40] J. Lubliner and J. J. Blum, "Model for bend propagation in flagella," *Journal of Theoretical Biology*, vol. 31, no. 1, pp. 1-24, 1971 1971, doi: 10.1016/0022-5193(71)90117-2.

[41] M. Hines and J. J. Blum, "Bend propagation in flagella. I. Derivation of equations of motion and their simulation," *Biophys. J.*, vol. 23, no. 1, pp. 41-57, 1978/7 1978, doi: 10.1016/S0006-3495(78)85431-9.

[42] P. Satir, "Studies on Cilia. The Fixation of the Metachronal Wave," *J Cell Biol*, vol. 18, pp. 345-65, Aug 1963, doi: 10.1083/jcb.18.2.345.

[43] C. B. Lindemann, "A "geometric clutch" hypothesis to explain oscillations of the axoneme of cilia and flagella," *J. Theor. Biol.*, vol. 168, no. 2, pp. 175-189, 1994/5/21 1994, doi: 10.1006/jtbi.1994.1097.

[44] P. Sartori, V. F. Geyer, J. Howard, and F. Julicher, "Curvature regulation of the ciliary beat through axonemal twist," (in eng), *Phys Rev E*, vol. 94, no. 4-1, p. 042426, Oct 2016, doi: 10.1103/PhysRevE.94.042426.

[45] P. Sartori, V. F. Geyer, A. Scholich, F. Julicher, and J. Howard, "Dynamic curvature regulation accounts for the symmetric and asymmetric beats of Chlamydomonas flagella," *eLife*, vol. 5, May 11 2016, doi: 10.7554/eLife.13258.

[46] G. De Canio, E. Lauga, and R. E. Goldstein, "Spontaneous oscillations of elastic filaments induced by molecular motors," *Journal of The Royal Society Interface*, vol. 14, no. 136, p. 20170491, 2017, doi: 10.1098/rsif.2017.0491.

[47] F. Ling, H. Guo, and E. Kanso, "Instability-driven oscillations of elastic microfilaments," *Journal of the Royal Society, Interface / the Royal Society*, vol. 15, no. 149, p. 20180594, Dec 21 2018, doi: 10.1098/rsif.2018.0594.

[48] J. Howard, *Mechanics of Motor Proteins and the Cytoskeleton*. Sinauer, 2001, p. 384.

[49] D. H. Boal, *Mechanics of the cell*, 2nd ed. Cambridge ; New York: Cambridge University Press, 2012, pp. xiv, 608 p.

[50] C. R. Jacobs, H. Huang, and R. Y. Kwon, *Introduction to cell mechanics and mechanobiology*. New York: Garland Science, 2013, pp. xvi, 351 p.

[51] F. Gittes, B. Mickey, J. Nettleton, and J. Howard, "Flexural rigidity of microtubules and actin filaments measured from thermal fluctuations in shape," *J. Cell Biol.*, vol. 120, no. 4, pp. 923-934, 1993/2 1993, doi: 10.1083/jcb.120.4.923.

[52] G. Bhabha, G. T. Johnson, C. M. Schroeder, and R. D. Vale, "How Dynein Moves Along Microtubules," *Trends Biochem. Sci.*, vol. 41, no. 1, pp. 94-105, 2016/1 2016, doi: 10.1016/j.tibs.2015.11.004.

[53] K. Ishibashi, H. Sakakibara, and K. Oiwa, "Force-Generating Mechanism of Axonemal Dynein in Solo and Ensemble," *Int. J. Mol. Sci.*, vol. 21, no. 8, 2020/4/18 2020, doi: 10.3390/ijms21082843.

[54] E. F. Smith and W. S. Sale, "Structural and functional reconstitution of inner dynein arms in Chlamydomonas flagellar axonemes," *J. Cell Biol.*, vol. 117, no. 3, pp. 573-581, 1992/5 1992, doi: 10.1083/jcb.117.3.573.

[55] C. J. Brokaw, "Computer simulation of flagellar movement: VII. Conventional but functionally different cross-bridge models for inner and outer arm dyneins can explain the effects of outer arm dynein removal," *Cell Motil. Cytoskeleton*, vol. 42, no. 2, pp. 134-148, 1999 1999.

[56] C. B. Lindemann, "Geometric Clutch model version 3: the role of the inner and outer arm dyneins in the ciliary beat," *Cell Motil. Cytoskeleton*, vol. 52, no. 4, pp. 242-254, 2002/8 2002, doi: 10.1002/cm.10049.

[57] T. Yagi *et al.*, "An axonemal dynein particularly important for flagellar movement at high viscosity. Implications from a new Chlamydomonas mutant deficient in the dynein heavy chain gene DHC9," *J. Biol. Chem.*, vol. 280, no. 50, pp. 41412-41420, 2005/12/16 2005, doi: 10.1074/jbc.M509072200.

[58] T. Walton, H. Wu, and A. Brown, "Structure of a microtubule-bound axonemal dynein," *Nat Commun*, vol. 12, no. 1, p. 477, Jan 20 2021, doi: 10.1038/s41467-020-20735-7.

[59] M. Kikkawa, "Big steps toward understanding dynein," *J. Cell Biol.*, vol. 202, no. 1, pp. 15-23, 2013/7/8 2013, doi: 10.1083/jcb.201304099.

[60] A. Gennerich, A. P. Carter, S. L. Reck-Peterson, and R. D. Vale, "Force-induced bidirectional stepping of cytoplasmic dynein," *Cell*, vol. 131, no. 5, pp. 952-965, 2007/11/30 2007, doi: 10.1016/j.cell.2007.10.016.

[61] C. B. Lindemann, "A model of flagellar and ciliary functioning which uses the forces transverse to the axoneme as the regulator of dynein activation," *Cell Motil Cytoskeleton*, vol. 29, no. 2, pp. 141-54, 1994.

[62] S. Timoshenko, *Strength of materials*, 3d ed. New York,: Van Nostrand, 1955.

[63] L. D. Landau, E. M. Lifshi͡ts, A. M. Kosevich, and L. P. Pitaevskiĭ, *Theory of elasticity*, 3rd English ed. (Course of theoretical physics, no. 7). Oxford Oxfordshire ; New York: Pergamon Press, 1986, pp. viii, 187 p.

[64] D. W. Pelle, C. J. Brokaw, K. A. Lesich, and C. B. Lindemann, "Mechanical properties of the passive sea urchin sperm flagellum," *Cell Motil Cytoskel*, vol. 66, no. 9, pp. 721-735, 2009 2009, doi: 10.1002/cm.20401.

[65] H. Gadelha, E. A. Gaffney, and A. Goriely, "The counterbend phenomenon in flagellar axonemes and cross-linked filament bundles," *Proc Natl Acad Sci U S A*, vol. 110, no. 30, pp. 12180-5, Jul 23 2013, doi: 10.1073/pnas.1302113110.

[66] G. Xu, K. S. Wilson, R. J. Okamoto, J. Y. Shao, S. K. Dutcher, and P. V. Bayly, "Flexural rigidity and shear stiffness of flagella estimated from induced bends and counterbends," *Biophysical Journal*, vol. 110, no. 12, pp. 2759-68, 2016.

[67] C. J. Brokaw, "Thinking about flagellar oscillation," *Cell Motil. Cytoskeleton*, vol. 66, no. 8, pp. 425-436, 2009/8 2009, doi: 10.1002/cm.20313.

[68] R. H. Plaut and E. F. Infante, "The effect of external damping on the stability of Beck's column," *Int. J. Solids Struct.*, vol. 6, no. 5, pp. 491-496, 1970/5/1 1970, doi: 10.1016/0020-7683(70)90026-0.

[69] H. Leipholz, *Stability of elastic systems*. Sijthoff & Noordhoff, 1980.

[70] H. Gadelha, E. A. Gaffney, D. J. Smith, and J. C. Kirkman-Brown, "Nonlinear instability in flagellar dynamics: a novel modulation mechanism in sperm migration?," *Journal of the Royal Society, Interface / the Royal Society*, vol. 7, no. 53, pp. 1689-97, Dec 6 2010, doi: 10.1098/rsif.2010.0136.

[71] J. S. Guasto, K. A. Johnson, and J. P. Gollub, "Oscillatory flows induced by microorganisms swimming in two dimensions," *Phys. Rev. Lett.*, vol. 105, no. 16, p. 168102, 2010/10/15 2010, doi: 10.1103/PhysRevLett.105.168102.

[72] V. A. Martinez *et al.*, "Differential dynamic microscopy: a high-throughput method for characterizing the motility of microorganisms," *Biophys J*, vol. 103, no. 8, pp. 1637-47, Oct 17 2012, doi: 10.1016/j.bpj.2012.08.045.

[73] S. Fujita, T. Matsuo, M. Ishiura, and M. Kikkawa, "High-throughput phenotyping of chlamydomonas swimming mutants based on nanoscale video analysis," *Biophys. J.*, vol. 107, no. 2, pp. 336-345, 2014/7/15 2014, doi: 10.1016/j.bpj.2014.05.033.

[74] M. Kim, E. Huff, M. Bottier, S. K. Dutcher, P. V. Bayly, and J. M. Meacham, "Acoustic trap-and-release for rapid assessment of cell motility," *Soft Matter*, vol. 15, no. 21, pp. 4266-4275, 2019/5/29 2019, doi: 10.1039/c9sm00184k.

[75] K. Y. Wan and R. E. Goldstein, "Rhythmicity, recurrence, and recovery of flagellar beating," *Phys. Rev. Lett.*, vol. 113, no. 23, p. 238103, 2014/12/5 2014, doi: 10.1103/PhysRevLett.113.238103.

[76] U. Ruffer and W. Nultsch, "High-Speed Cinematographic Analysis of the Movement of Chlamydomonas," (in English), *Cell Motil Cytoskel*, vol. 5, no. 3, pp. 251-263, 1985, doi: DOI 10.1002/cm.970050307.

[77] R. P. McCord, J. N. Yukich, and K. K. Bernd, "Analysis of force generation during flagellar assembly through optical trapping of free-swimming Chlamydomonas reinhardtii," *Cell Motil. Cytoskeleton*, vol. 61, no. 3, pp. 137-144, 2005/7 2005, doi: 10.1002/cm.20071.

[78] M. Bottier, K. A. Thomas, S. K. Dutcher, and P. V. Bayly, "How Does Cilium Length Affect Beating?," *Biophys. J.*, vol. 116, no. 7, pp. 1292-1304, 2019/4/2 2019, doi: 10.1016/j.bpj.2019.02.012.

[79] T. J. Boddeker, S. Karpitschka, C. T. Kreis, Q. Magdelaine, and O. Baumchen, "Dynamic force measurements on swimming Chlamydomonas cells using micropipette force sensors," *Journal of the Royal Society, Interface / the Royal Society*, vol. 17, no. 162, p. 20190580, Jan 2020, doi: 10.1098/rsif.2019.0580.

[80] C. J. Brokaw, D. J. Luck, and B. Huang, "Analysis of the movement of Chlamydomonas flagella:" the function of the radial-spoke system is revealed by comparison of wild-type and mutant flagella," *J. Cell Biol.*, vol. 92, no. 3, pp. 722-732, 1982/3 1982, doi: 10.1083/jcb.92.3.722.

[81] B. Huang, Z. Ramanis, S. K. Dutcher, and D. J. Luck, "Uniflagellar mutants of Chlamydomonas: evidence for the role of basal bodies in transmission of positional information," *Cell*, vol. 29, no. 3, pp. 745-753, 1982/7 1982, doi: 10.1016/0092-8674(82)90436-6.

[82] S. K. Dutcher and E. C. Trabuco, "The UNI3 gene is required for assembly of basal bodies of Chlamydomonas and encodes delta-tubulin, a new member of the tubulin superfamily," (in English), *Molecular Biology of the Cell*, vol. 9, no. 6, pp. 1293-1308, Jun 1998, doi: DOI 10.1091/mbc.9.6.1293.

[83] B. P. Piasecki, M. LaVoie, L. W. Tam, P. A. Lefebvre, and C. D. Silflow, "The Uni2 phosphoprotein is a cell cycle-regulated component of the basal body maturation pathway in Chlamydomonas reinhardtii," (in English), *Molecular Biology of the Cell*, vol. 19, no. 1, pp. 262-273, Jan 2008, doi: 10.1091/mbc.E07-08-0798.

[84] I. Minoura and R. Kamiya, "Strikingly different propulsive forces generated by different dynein-deficient mutants in viscous media," *Cell Motil. Cytoskeleton*, vol. 31, no. 2, pp. 130-139, 1995 1995, doi: 10.1002/cm.970310205.

[85] R. Kamiya, "Exploring the function of inner and outer dynein arms with Chlamydomonas mutants," *Cell Motil. Cytoskeleton,* vol. 32, no. 2, pp. 98-102, 1995 1995, doi: 10.1002/cm.970320205.

[86] M. LeDizet and G. Piperno, "ida4-1, ida4-2, and ida4-3 are intron splicing mutations affecting the locus encoding p28, a light chain of Chlamydomonas axonemal inner dynein arms," *Mol Biol Cell,* vol. 6, no. 6, pp. 713-23, Jun 1995, doi: 10.1091/mbc.6.6.713.

[87] L. W. Tam and P. A. Lefebvre, "The Chlamydomonas MBO2 locus encodes a conserved coiled-coil protein important for flagellar waveform conversion," *Cell Motil Cytoskeleton,* vol. 51, no. 4, pp. 197-212, Apr 2002, doi: 10.1002/cm.10023.

[88] D. Luck, G. Piperno, Z. Ramanis, and B. Huang, "Flagellar Mutants of Chlamydomonas - Studies of Radial Spoke-Defective Strains by Dikaryon and Revertant Analysis," (in English), *P Natl Acad Sci USA,* vol. 74, no. 8, pp. 3456-3460, 1977, doi: DOI 10.1073/pnas.74.8.3456.

[89] E. F. Smith and W. S. Sale, "Regulation of dynein-driven microtubule sliding by the radial spokes in flagella," *Science,* vol. 257, no. 5076, pp. 1557-1559, 1992/9/11 1992, doi: 10.1126/science.1387971.

[90] T. Yagi and R. Kamiya, "Novel mode of hyper-oscillation in the paralyzed axoneme of achlamydomonas mutant lacking the central-pair microtubules," *Cell Motil Cytoskel,* vol. 31, no. 3, pp. 207-214, 1995 1995, doi: 10.1002/cm.970310304.

[91] A. M. Curry and J. L. Rosenbaum, "Flagellar Radial Spoke - a Model Molecular Genetic System for Studying Organelle Assembly," (in English), *Cell Motil Cytoskel,* vol. 24, no. 4, pp. 224-232, 1993, doi: DOI 10.1002/cm.970240403.

[92] B. D. Williams, M. A. Velleca, A. M. Curry, and J. L. Rosenbaum, "Molecular-Cloning and Sequence-Analysis of the Chlamydomonas Gene Coding for Radial Spoke Protein-3 - Flagellar Mutation Pf-14 Is an Ochre Allele," (in English), *Journal of Cell Biology,* vol. 109, no. 1, pp. 235-245, Jul 1989, doi: DOI 10.1083/jcb.109.1.235.

[93] G. M. W. Adams, B. Huang, G. Piperno, and D. J. L. Luck, "Central-Pair Microtubular Complex of Chlamydomonas Flagella - Polypeptide Composition as Revealed by Analysis of Mutants," (in English), *Journal of Cell Biology,* vol. 91, no. 1, pp. 69-76, 1981, doi: DOI 10.1083/jcb.91.1.69.

[94] R. D. Smyth and W. T. Ebersold, "Genetic Investigation of a Negatively Phototactic Strain of Chlamydomonas-Reinhardtii," (in English), *Genet Res,* vol. 46, no. 2, pp. 133-&, Oct 1985, doi: Doi 10.1017/S001667230002262x.

[95] T. Ide *et al.,* "Identification of the agg1 mutation responsible for negative phototaxis in a "wild-type" strain of Chlamydomonas reinhardtii," *Biochem Biophys Rep,* vol. 7, pp. 379-385, Sep 2016, doi: 10.1016/j.bbrep.2016.07.016.

[96] C. J. Horst and G. B. Witman, "ptx1, a nonphototactic mutant of Chlamydomonas, lacks control of flagellar dominance," *J Cell Biol,* vol. 120, no. 3, pp. 733-41, Feb 1993, doi: 10.1083/jcb.120.3.733.

[97] G. J. Pazour, O. A. Sineshchekov, and G. B. Witman, "Mutational analysis of the phototransduction pathway of Chlamydomonas reinhardtii," *J Cell Biol,* vol. 131, no. 2, pp. 427-40, Oct 1995, doi: 10.1083/jcb.131.2.427.

[98] U. Ruffer and W. Nultsch, "Flagellar photoresponses of ptx1, a nonphototactic mutant of Chlamydomonas," *Cell Motil Cytoskeleton,* vol. 37, no. 2, pp. 111-9, 1997, doi: 10.1002/(SICI)1097-0169(1997)37:2<111::AID-CM3>3.0.CO;2-B.

[99] K. C. Leptos, K. Y. Wan, M. Polin, I. Tuval, A. I. Pesci, and R. E. Goldstein, "Antiphase synchronization in a flagellar-dominance mutant of Chlamydomonas," *Phys. Rev. Lett.,* vol. 111, no. 15, p. 158101, 2013/10/11 2013, doi: 10.1103/PhysRevLett.111.158101.

[100] G. M. Adams, R. L. Wright, and J. W. Jarvik, "Defective temporal and spatial control of flagellar assembly in a mutant of Chlamydomonas reinhardtii with variable flagellar number," (in eng), *J Cell Biol,* vol. 100, no. 3, pp. 955-64, Mar 1985.

[101] R. L. Wright, S. A. Adler, J. G. Spanier, and J. W. Jarvik, "Nucleus-basal body connector in Chlamydomonas: evidence for a role in basal body segregation and against essential roles in mitosis or in determining cell polarity," (in eng), *Cell Motil Cytoskeleton,* vol. 14, no. 4, pp. 516-26, 1989, doi: 10.1002/cm.970140409.

[102] C. D. Silflow *et al.*, "The Vfl1 Protein in *Chlamydomonas* localizes in a rotationally asymmetric pattern at the distal ends of the basal bodies," *J Cell Biol,* vol. 153, no. 1, pp. 63-74, Apr 2 2001.

[103] T. Ochi *et al.*, "CCDC61/VFL3 Is a Paralog of SAS6 and Promotes Ciliary Functions," *Structure,* vol. 28, no. 6, pp. 674-689 e11, Jun 2 2020, doi: 10.1016/j.str.2020.04.010.

[104] D. Bray, *Cell movements : from molecules to motility*. New York: Garland Publishing, 2001.

[105] E. M. Purcell, "Life at Low Reynolds-Number," (in English), *Am J Phys,* vol. 45, no. 1, pp. 3-11, 1977, doi: Doi 10.1119/1.10903.

[106] S. Vogel, *Life in moving fluids : the physical biology of flow*, 2nd ed. Princeton, N.J.: Princeton University Press, 1994, pp. 1 online resource (xiii, 467 p.).

[107] J. Gray and G. J. Hancock, "The Propulsion of Sea-Urchin Spermatozoa," *J. Exp. Biol.,* vol. 32, no. 4, pp. 802-814, 1955/12/1 1955.

[108] R. E. Johnson and C. J. Brokaw, "Flagellar hydrodynamics. A comparison between resistive-force theory and slender-body theory," *Biophys. J.,* vol. 25, no. 1, pp. 113-127, 1979/1 1979, doi: 10.1016/S0006-3495(79)85281-9.

[109] B. Qin, A. Gopinath, J. Yang, J. P. Gollub, and P. E. Arratia, "Flagellar kinematics and swimming of algal cells in viscoelastic fluids," *Sci. Rep.*, vol. 5, p. 9190, 2015/3/17 2015, doi: 10.1038/srep09190.

[110] C. Li, B. Qin, A. Gopinath, P. E. Arratia, B. Thomases, and R. D. Guy, "Flagellar swimming in viscoelastic fluids: role of fluid elastic stress revealed by simulations based on experimental data," *J. R. Soc. Interface*, vol. 14, no. 135, 2017/10 2017, doi: 10.1098/rsif.2017.0289.

[111] C. H. Wiggins, D. Riveline, A. Ott, and R. E. Goldstein, "Trapping and wiggling: elastohydrodynamics of driven microfilaments," *Biophys. J.*, vol. 74, no. 2 Pt 1, pp. 1043-1060, 1998/2 1998, doi: 10.1016/S0006-3495(98)74029-9.

[112] B. Chakrabarti and D. Saintillan, "Hydrodynamic Synchronization of Spontaneously Beating Filaments," *Phys Rev Lett*, vol. 123, no. 20, p. 208101, Nov 15 2019, doi: 10.1103/PhysRevLett.123.208101.

[113] Y. Man, F. Ling, and E. Kanso, "Cilia oscillations," *Philos. Trans. R. Soc. Lond. B Biol. Sci.*, vol. 375, no. 1792, p. 20190157, 2020/2/17 2020, doi: 10.1098/rstb.2019.0157.

[114] I. R. Gibbons and A. V. Grimstone, "On flagellar structure in certain flagellates," *J. Biophys. Biochem. Cytol.*, vol. 7, pp. 697-716, 1960/7 1960, doi: 10.1083/jcb.7.4.697.

[115] D. Nicastro, C. Schwartz, J. Pierson, R. Gaudette, M. E. Porter, and J. R. McIntosh, "The molecular architecture of axonemes revealed by cryoelectron tomography," *Science*, vol. 313, no. 5789, pp. 944-948, 2006/8/18 2006, doi: 10.1126/science.1128618.

[116] S. K. Dutcher, Ed. *The Chlamydomonas Sourcebook*. Elsevier, 2022.

[117] D. Cortese and K. Y. Wan, "Control of helical navigation by three-dimensional flagellar beating," *Physical Review Letters*, 2021 2021, doi: 10.1101/2020.09.27.315606.

[118] R. Rikmenspoel, "Elastic properties of the sea urchin sperm flagellum," *Biophys. J.*, vol. 6, no. 4, pp. 471-479, 1966/7 1966, doi: 10.1016/S0006-3495(66)86670-5.

[119] S. A. Baba, "Flexural rigidity and elastic constant of cilia," *J. Exp. Biol.*, vol. 56, no. 2, pp. 459-467, 1972/4 1972.

[120] C. B. Lindemann, W. G. Rudd, and R. Rikmenspoel, "The stiffness of the flagella of impaled bull sperm," *Biophys. J.*, vol. 13, no. 5, pp. 437-448, 1973/5 1973, doi: 10.1016/S0006-3495(73)85997-1.

[121] M. Okuno and Y. Hiramoto, "Direct measurements of the stiffness of echinoderm sperm flagella," *J. Exp. Biol.*, vol. 79, no. 1, pp. 235-243, 1979 1979.

[122] I. Minoura, T. Yagi, and R. Kamiya, "Direct measurement of inter-doublet elasticity in flagellar axonemes," *Cell Struct. Funct.*, vol. 24, no. 1, pp. 27-33, 1999/2 1999, doi: 10.1247/csf.24.27.

[123] C. Shingyoji, H. Higuchi, M. Yoshimura, E. Katayama, and T. Yanagida, "Dynein arms are oscillating force generators," *Nature,* vol. 393, no. 6686, pp. 711-714, 1998/6/18 1998, doi: 10.1038/31520.

[124] C. B. Lindemann and D. R. Mitchell, "Evidence for axonemal distortion during the flagellar beat of Chlamydomonas," *Cell Motil. Cytoskeleton,* vol. 64, no. 8, pp. 580-589, 2007/8 2007, doi: 10.1002/cm.20205.

[125] C. J. Brokaw, "Stochastic simulation of processive and oscillatory sliding using a two-headed model for axonemal dynein," *Cell Motil. Cytoskeleton,* vol. 47, no. 2, pp. 108-119, 2000/10 2000, doi: 10.1002/1097-0169(200010)47:2<108::AID-CM2>3.0.CO;2-7.

[126] P. Satir and W. S. Sale, "Tails of Tetrahymena," *J Protozool,* vol. 24, no. 4, pp. 498-501, Nov 1977, doi: 10.1111/j.1550-7408.1977.tb00999.x.

[127] C. Cibert, "Are the local adjustments of the relative spatial frequencies of the dynein arms and the beta-tubulin monomers involved in the regulation of the "9+2" axoneme?," (in eng), *J Theor Biol,* vol. 253, no. 1, pp. 74-89, Jul 7 2008, doi: S0022-5193(08)00036-2 [pii]

[128] C. B. Lindemann and K. A. Lesich, "Flagellar and ciliary beating: the proven and the possible," *J. Cell Sci.,* vol. 123, no. Pt 4, pp. 519-528, 2010/2/15 2010, doi: 10.1242/jcs.051326.

[129] C. K. Omoto and C. Kung, "Rotation and twist of the central-pair microtubules in the cilia of Paramecium," *J. Cell Biol.,* vol. 87, no. 1, pp. 33-46, 1980/10 1980, doi: 10.1083/jcb.87.1.33.

[130] R. Kamiya, R. Nagai, and S. Nakamura, "ROTATION OF THE CENTRAL-PAIR MICROTUBULES IN CHLAMYDOMONAS FLAGELLA," *Biological Functions of Microtubules and Related Structures,* pp. 189-198, 1982 1982, doi: 10.1016/b978-0-12-615080-3.50025-2.

[131] D. R. Mitchell, "Orientation of the central pair complex during flagellar bend formation in Chlamydomonas," *Cell Motil. Cytoskeleton,* vol. 56, no. 2, pp. 120-129, 2003/10 2003, doi: 10.1002/cm.10142.

[132] D. R. Mitchell and M. Nakatsugawa, "Bend propagation drives central pair rotation in Chlamydomonas reinhardtii flagella," *J. Cell Biol.,* vol. 166, no. 5, pp. 709-715, 2004/8/30 2004, doi: 10.1083/jcb.200406148.

[133] C. K. Omoto, I. R. Gibbons, R. Kamiya, C. Shingyoji, K. Takahashi, and G. B. Witman, "Rotation of the central pair microtubules in eukaryotic flagella," *Mol. Biol. Cell,* vol. 10, no. 1, pp. 1-4, 1999/1 1999, doi: 10.1091/mbc.10.1.1.

[134] E. F. Smith and P. Yang, "The radial spokes and central apparatus: mechano-chemical transducers that regulate flagellar motility," *Cell Motil. Cytoskeleton,* vol. 57, no. 1, pp. 8-17, 2004/1 2004, doi: 10.1002/cm.10155.

[135] B. H. Gibbons and I. R. Gibbons, "Flagellar movement and adenosine triphosphatase activity in sea urchin sperm extracted with triton X-100," *J. Cell Biol.*, vol. 54, no. 1, pp. 75-97, 1972/7 1972, doi: 10.1083/jcb.54.1.75.

[136] M. Murase, "Excitable dynein model with multiple active sites for large-amplitude oscillations and bend propagation in flagella," *J. Theor. Biol.*, vol. 149, no. 2, pp. 181-202, 1991/3/21 1991, doi: 10.1016/s0022-5193(05)80276-0.

[137] C. J. Brokaw, "Computer Simulation of Flagellar Movement," *Biophysical Journal*, vol. 12, no. 5, pp. 564-586, 1972 1972, doi: 10.1016/s0006-3495(72)86104-6.

[138] P. Sartori, V. F. Geyer, J. Howard, and F. Jülicher, "Curvature regulation of the ciliary beat through axonemal twist," *Phys Rev E*, vol. 94, no. 4-1, p. 042426, 2016/10 2016, doi: 10.1103/PhysRevE.94.042426.

[139] P. Sartori, V. F. Geyer, A. Scholich, F. Jülicher, and J. Howard, "Dynamic curvature regulation accounts for the symmetric and asymmetric beats of Chlamydomonas flagella," *eLife*, vol. 5, 2016/5/11 2016, doi: 10.7554/eLife.13258.

[140] P. V. Bayly and K. S. Wilson, "Equations of interdoublet separation during flagella motion reveal mechanisms of wave propagation and instability," *Biophys. J.*, vol. 107, no. 7, pp. 1756-1772, 2014/10/7 2014, doi: 10.1016/j.bpj.2014.07.064.

[141] M. Ma, M. Stoyanova, G. Rademacher, S. K. Dutcher, A. Brown, and R. Zhang, "Structure of the Decorated Ciliary Doublet Microtubule," (in eng), *Cell*, vol. 179, no. 4, pp. 909-922.e12, Oct 31 2019, doi: 10.1016/j.cell.2019.09.030.

[142] M. Gui *et al.*, "Structures of radial spokes and associated complexes important for ciliary motility," *Nat Struct Mol Biol*, vol. 28, no. 1, pp. 29-37, Jan 2021, doi: 10.1038/s41594-020-00530-0.

[143] J. Lin, K. Okada, M. Raytchev, M. C. Smith, and D. Nicastro, "Structural mechanism of the dynein power stroke," *Nat Cell Biol*, vol. 16, no. 5, pp. 479-85, May 2014, doi: 10.1038/ncb2939.

[144] J. Lin *et al.*, "Cryo-electron tomography reveals ciliary defects underlying human RSPH1 primary ciliary dyskinesia," *Nat Commun*, vol. 5, p. 5727, Dec 04 2014, doi: 10.1038/ncomms6727.

[145] K. Oiwa and K. Takahashi, "The force-velocity relationship for microtubule sliding in demembranated sperm flagella of the sea urchin," *Cell Struct Funct*, vol. 13, no. 3, pp. 193-205, Jun 1988, doi: 10.1247/csf.13.193.

[146] K. E. Summers and I. R. Gibbons, "Adenosine triphosphate-induced sliding of tubules in trypsin-treated flagella of sea-urchin sperm," *Proc Natl Acad Sci U S A*, vol. 68, no. 12, pp. 3092-6, Dec 1971.

[147] W. S. Sale and P. Satir, "Direction of active sliding of microtubules in Tetrahymena cilia," *Proc Natl Acad Sci U S A,* vol. 74, no. 5, pp. 2045-9, May 1977, doi: 10.1073/pnas.74.5.2045.

[148] S. Brenner, F. Berger, L. Rao, M. P. Nicholas, and A. Gennerich, "Force production of human cytoplasmic dynein is limited by its processivity," (in English), *Science Advances,* vol. 6, no. 15, Apr 2020, doi: ARTN eaaz4295

[149] E. H. Dowell, "FLUTTER OF A BUCKLED PLATE AS AN EXAMPLE OF CHAOTIC MOTION OF A DETERMINISTIC AUTONOMOUS SYSTEM," *J Sound Vib,* vol. 85, no. 3, pp. 333-344, 1982, doi: 10.1016/0022-460x(82)90259-0.

[150] S. H. Strogatz, *Nonlinear dynamics and Chaos : with applications to physics, biology, chemistry, and engineering* (Studies in nonlinearity). Reading, Mass.: Addison-Wesley Pub., 1994, pp. xi, 498 p.

[151] G. E. Olson and R. W. Linck, "Observations of the structural components of flagellar axonemes and central pair microtubules from rat sperm," *J Ultrastruct Res,* vol. 61, no. 1, pp. 21-43, Oct 1977, doi: 10.1016/s0022-5320(77)90004-1.

[152] C. B. Lindemann, A. Orlando, and K. S. Kanous, "The Flagellar Beat of Rat Sperm Is Organized by the Interaction of 2 Functionally Distinct Populations of Dynein Bridges with a Stable Central Axonemal Partition," (in English), *Journal of Cell Science,* vol. 102, pp. 249-260, Jun 1992.

[153] S. A. Burgess and P. J. Knight, "Is the dynein motor a winch?," (in English), *Curr Opin Struc Biol,* vol. 14, no. 2, pp. 138-146, Apr 2004, doi: 10.1016/j.sbi.2004.03.013.

[154] S. M. King, "Axonemal dyneins winch the cilium," (in English), *Nature Structural & Molecular Biology,* vol. 17, no. 6, pp. 673-674, Jun 2010, doi: DOI 10.1038/nsmb0610-673.

[155] *Matlab 2021b, The Mathworks Inc., Natick, Massachusetts, USA.*

[156] T. Heuser, M. Raytchev, J. Krell, M. E. Porter, and D. Nicastro, "The dynein regulatory complex is the nexin link and a major regulatory node in cilia and flagella," *J Cell Biol,* vol. 187, no. 6, pp. 921-33, Dec 14 2009, doi: 10.1083/jcb.200908067.

[157] V. F. Geyer, P. Sartori, B. M. Friedrich, F. Julicher, and J. Howard, "Independent Control of the Static and Dynamic Components of the Chlamydomonas Flagellar Beat," *Curr Biol,* vol. 26, no. 8, pp. 1098-103, Apr 25 2016, doi: 10.1016/j.cub.2016.02.053.

[158] C. J. Brokaw, "Non-sinusoidal bending waves of sperm flagella," *J Exp Biol,* vol. 43, no. 1, pp. 155-69, Aug 1965, doi: 10.1242/jeb.43.1.155.

[159] C. J. Brokaw, "Computer simulation of flagellar movement VIII: Coordination of dynein by local curvature control can generate helical bending waves," (in English), *Cell Motil Cytoskel,* vol. 53, no. 2, pp. 103-124, Oct 2002, doi: 10.1002/cm.10067.

[160] S. Mojiri *et al.*, "Rapid multi-plane phase-contrast microscopy reveals torsional dynamics in flagellar motion," *Biomed Opt Express,* vol. 12, no. 6, pp. 3169-3180, Jun 1 2021, doi: 10.1364/BOE.419099.

[161] J. A. Schmidt and R. Eckert, "Calcium couples flagellar reversal to photostimulation in Chlamydomonas reinhardtii," *Nature,* vol. 262, no. 5570, pp. 713-5, Aug 19 1976, doi: 10.1038/262713a0.

[162] M. E. Porter, J. A. Knott, L. C. Gardner, D. R. Mitchell, and S. K. Dutcher, "Mutations in the SUP-PF-1 locus of Chlamydomonas reinhardtii identify a regulatory domain in the beta-dynein heavy chain," *J Cell Biol,* vol. 126, no. 6, pp. 1495-507, Sep 1994, doi: 10.1083/jcb.126.6.1495.

[163] P. V. Bayly and K. S. Wilson, "Analysis of unstable modes distinguishes mathematical models of flagellar motion," *Journal of the Royal Society, Interface / the Royal Society,* vol. 12, no. 106, May 6 2015, doi: 10.1098/rsif.2015.0124.

[164] E. Kreyszig, H. Kreyszig, and E. J. Norminton, *Advanced engineering mathematics,* 10th ed. Hoboken, NJ: John Wiley, 2011.

[165] X. M. Bustamante-Marin and L. E. Ostrowski, "Cilia and Mucociliary Clearance," (in eng), *Cold Spring Harbor perspectives in biology,* vol. 9, no. 4, Apr 3 2017, doi: 10.1101/cshperspect.a028241.

[166] B. A. Bayless, F. M. Navarro, and M. Winey, "Motile Cilia: Innovation and Insight From Ciliate Model Organisms," (in English), *Frontiers in Cell and Developmental Biology,* Mini Review vol. 7, no. 265, 2019-November-01 2019, doi: 10.3389/fcell.2019.00265.

[167] R. Viswanadha, W. S. Sale, and M. E. Porter, "Ciliary Motility: Regulation of Axonemal Dynein Motors," (in eng), *Cold Spring Harbor perspectives in biology,* vol. 9, no. 8, Aug 1 2017, doi: 10.1101/cshperspect.a018325.

[168] C. J. Brokaw, "Computer simulation of flagellar movement. VI. Simple curvature-controlled models are incompletely specified," *Biophys J,* vol. 48, no. 4, pp. 633-42, Oct 1985.

[169] C. J. Brokaw, "Simulation of cyclic dynein-driven sliding, splitting, and reassociation in an outer doublet pair," *Biophys J,* vol. 97, no. 11, pp. 2939-47, Dec 2 2009, doi: 10.1016/j.bpj.2009.09.022.

[170] P. Satir, "Morphological aspects of ciliary motility," (in eng), *J Gen Physiol,* vol. 50, no. 6, pp. Suppl:241-58, Jul 1967, doi: 10.1085/jgp.50.6.241.

[171] K. A. Lesich, T. G. dePinho, D. W. Pelle, and C. B. Lindemann, "Mechanics of the eukaryotic flagellar axoneme: Evidence for structural distortion during bending," (in eng), *Cytoskeleton (Hoboken),* vol. 73, no. 5, pp. 233-45, May 2016, doi: 10.1002/cm.21296.

[172] P. Satir, T. Heuser, and W. S. Sale, "A Structural Basis for How Motile Cilia Beat," (in Eng), *Bioscience,* vol. 64, no. 12, pp. 1073-1083, Dec 1 2014, doi: 10.1093/biosci/biu180.

[173] G. G. Vernon and D. M. Woolley, "Basal sliding and the mechanics of oscillation in a mammalian sperm flagellum," (in eng), *Biophys J,* Research Support, Non-U.S. Gov't vol. 87, no. 6, pp. 3934-44, Dec 2004, doi: 10.1529/biophysj.104.042648.

[174] D. M. Woolley and H. H. Bozkurt, "The distal sperm flagellum: its potential for motility after separation from the basal structures," *J Exp Biol,* vol. 198, no. Pt 7, pp. 1469-81, Jul 1995, doi: 10.1242/jeb.198.7.1469.

[175] G. G. Vernon and D. M. Woolley, "Microtubule displacements at the tips of living flagella," *Cell Motil Cytoskeleton,* vol. 52, no. 3, pp. 151-60, Jul 2002, doi: 10.1002/cm.10041.

[176] S. F. Goldstein, "Motility of basal fragments of sea urchin sperm flagella," *J Cell Sci,* vol. 50, pp. 65-77, Aug 1981, doi: 10.1242/jcs.50.1.65.

[177] C. B. Lindemann, "The geometric clutch as a working hypothesis for future research on cilia and flagella," *Ann N Y Acad Sci,* vol. 1101, pp. 477-93, Apr 2007.

[178] F. D. Warner and P. Satir, "The structural basis of ciliary bend formation. Radial spoke positional changes accompanying microtubule sliding," *J Cell Biol,* vol. 63, no. 1, pp. 35-63, Oct 1974, doi: 10.1083/jcb.63.1.35.

[179] B. A. Bayless, T. H. Giddings, Jr., M. Winey, and C. G. Pearson, "Bld10/Cep135 stabilizes basal bodies to resist cilia-generated forces," (in eng), *Mol Biol Cell,* vol. 23, no. 24, pp. 4820-32, Dec 2012, doi: 10.1091/mbc.E12-08-0577.

[180] B. A. Bayless, D. F. Galati, A. D. Junker, C. B. Backer, J. Gaertig, and C. G. Pearson, "Asymmetrically localized proteins stabilize basal bodies against ciliary beating forces," *J Cell Biol,* vol. 215, no. 4, pp. 457-466, Nov 21 2016, doi: 10.1083/jcb.201604135.

[181] J. B. Meehl, B. A. Bayless, T. H. Giddings, Jr., C. G. Pearson, and M. Winey, "Tetrahymena Poc1 ensures proper intertriplet microtubule linkages to maintain basal body integrity," *Mol Biol Cell,* vol. 27, no. 15, pp. 2394-403, Aug 1 2016, doi: 10.1091/mbc.E16-03-0165.

[182] S. Li, J. J. Fernandez, W. F. Marshall, and D. A. Agard, "Electron cryo-tomography provides insight into procentriole architecture and assembly mechanism," (in eng), *eLife,* vol. 8, Feb 11 2019, doi: 10.7554/eLife.43434.

[183] M. Le Guennec *et al.*, "A helical inner scaffold provides a structural basis for centriole cohesion," *Science Advances,* vol. 6, no. 7, p. eaaz4137, 2020, doi: 10.1126/sciadv.aaz4137.

[184] C. G. Pearson, D. P. Osborn, T. H. Giddings, Jr., P. L. Beales, and M. Winey, "Basal body stability and ciliogenesis requires the conserved component Poc1," (in eng), *J Cell Biol,* vol. 187, no. 6, pp. 905-20, Dec 14 2009, doi: 10.1083/jcb.200908019.

[185] C. Basquin *et al.*, "Emergence of a Bilaterally Symmetric Pattern from Chiral Components in the Planarian Epidermis," (in eng), *Developmental cell,* vol. 51, no. 4, pp. 516-525.e5, Nov 18 2019, doi: 10.1016/j.devcel.2019.10.021.

[186] Y. Bobinnec, M. Moudjou, J. P. Fouquet, E. Desbruyeres, B. Edde, and M. Bornens, "Glutamylation of centriole and cytoplasmic tubulin in proliferating non-neuronal cells," (in eng), *Cell Motil Cytoskeleton,* Research Support, Non-U.S. Gov't vol. 39, no. 3, pp. 223-32, 1998, doi: 10.1002/(SICI)1097-0169(1998)39:3<223::AID-CM5>3.0.CO;2-5.

[187] A. M. Tassin, M. Lemullois, and A. Aubusson-Fleury, "Paramecium tetraurelia basal body structure," (in eng), *Cilia,* vol. 5, p. 6, 2015, doi: 10.1186/s13630-016-0026-4.

[188] S. Khanal *et al.*, "A dynamic basal complex modulates mammalian sperm movement," (in eng), *Nat Commun,* vol. 12, no. 1, p. 3808, Jun 21 2021, doi: 10.1038/s41467-021-24011-0.

[189] E. L. Fishman *et al.*, "A novel atypical sperm centriole is functional during human fertilization," *Nature communications,* vol. 9, no. 1, pp. 1-12, 2018.

[190] A. D. Junker *et al.*, "Microtubule glycylation promotes attachment of basal bodies to the cell cortex," *J Cell Sci,* vol. 132, no. 15, Aug 7 2019, doi: 10.1242/jcs.233726.

[191] A. W. J. Soh *et al.*, "Ciliary force-responsive striated fibers promote basal body connections and cortical interactions," *J. Cell Biol.,* vol. 219, no. 1, 2020/1/6 2020, doi: 10.1083/jcb.201904091.

[192] K. Kunimoto *et al.*, "Coordinated ciliary beating requires Odf2-mediated polarization of basal bodies via basal feet," (in eng), *Cell,* vol. 148, no. 1-2, pp. 189-200, Jan 20 2012, doi: 10.1016/j.cell.2011.10.052.

[193] E. Herawati, D. Taniguchi, H. Kanoh, K. Tateishi, S. Ishihara, and S. Tsukita, "Multiciliated cell basal bodies align in stereotypical patterns coordinated by the apical cytoskeleton," (in eng), *J Cell Biol,* vol. 214, no. 5, pp. 571-86, Aug 29 2016, doi: 10.1083/jcb.201601023.

[194] M. E. Werner, P. Hwang, F. Huisman, P. Taborek, C. C. Yu, and B. J. Mitchell, "Actin and microtubules drive differential aspects of planar cell polarity in multiciliated cells," *J. Cell Biol.,* vol. 195, no. 1, pp. 19-26, 2011/10/3 2011, doi: 10.1083/jcb.201106110.

[195] Y. H. Chien *et al.*, "Bbof1 is required to maintain cilia orientation," (in eng), *Development (Cambridge, England),* vol. 140, no. 16, pp. 3468-77, Aug 2013, doi: 10.1242/dev.096727.

[196] A. Nabi, J. Yano, M. S. Valentine, T. Picariello, and J. L. Van Houten, "SF-Assemblin genes in Paramecium: phylogeny and phenotypes of RNAi silencing on the ciliary-striated rootlets and surface organization," (in eng), *Cilia,* vol. 8, p. 2, 2019, doi: 10.1186/s13630-019-0062-y.

[197] E. Turk, A. A. Wills, T. Kwon, J. Sedzinski, J. B. Wallingford, and T. Stearns, "Zeta-Tubulin Is a Member of a Conserved Tubulin Module and Is a Component of the Centriolar Basal Foot in Multiciliated Cells," (in eng), *Curr Biol,* vol. 25, no. 16, pp. 2177-83, Aug 17 2015, doi: 10.1016/j.cub.2015.06.063.

[198] B. Mitchell, R. Jacobs, J. Li, S. Chien, and C. Kintner, "A positive feedback mechanism governs the polarity and motion of motile cilia," (in eng), *Nature,* Research Support, N.I.H., Extramural vol. 447, no. 7140, pp. 97-101, May 3 2007, doi: 10.1038/nature05771.

[199] W. F. Marshall and C. Kintner, "Cilia orientation and the fluid mechanics of development," (in eng), *Current opinion in cell biology,* Research Support, N.I.H., Extramural

[200] R. D. Allen, "Fine structure, reconstruction and possible functions of components of the cortex of Tetrahymena pyriformis," *J Protozool,* vol. 14, no. 4, pp. 553-65, Nov 1967.

[201] D. F. Galati *et al.*, "DisAp-dependent striated fiber elongation is required to organize ciliary arrays," (in eng), *J Cell Biol,* vol. 207, no. 6, pp. 705-15, Dec 22 2014, doi: 10.1083/jcb.201409123.

[202] J. Yang *et al.*, "The ciliary rootlet maintains long-term stability of sensory cilia," *Mol Cell Biol,* vol. 25, no. 10, pp. 4129-37, May 2005, doi: 10.1128/MCB.25.10.4129-4137.2005.

[203] S. Mohan, T. A. Timbers, J. Kennedy, O. E. Blacque, and M. R. Leroux, "Striated rootlet and nonfilamentous forms of rootletin maintain ciliary function," (in eng), *Curr Biol,* Research Support, Non-U.S. Gov't vol. 23, no. 20, pp. 2016-22, Oct 21 2013, doi: 10.1016/j.cub.2013.08.033.

[204] M. Jerka-Dziadosz, L. M. Jenkins, E. M. Nelsen, N. E. Williams, R. Jaeckel-Williams, and J. Frankel, "Cellular polarity in ciliates: persistence of global polarity in a disorganized mutant of Tetrahymena thermophila that disrupts cytoskeletal organization," (in eng), *Dev Biol,* vol. 169, no. 2, pp. 644-61, Jun 1995, doi: 10.1006/dbio.1995.1176.

[205] K. Y. Wan and R. E. Goldstein, "Coordinated beating of algal flagella is mediated by basal coupling," *Proc. Natl. Acad. Sci. U. S. A.,* vol. 113, no. 20, pp. E2784-93, 2016/5/17 2016, doi: 10.1073/pnas.1518527113.

[206] R. D. Allen, "The morphogenesis of basal bodies and accessory structures of the cortex of the ciliated protozoan Tetrahymena pyriformis," *J Cell Biol,* vol. 40, no. 3, pp. 716-33, Mar 1969, doi: 10.1083/jcb.40.3.716.

[207] C. R. Wood, R. Hard, and T. M. Hennessey, "Targeted gene disruption of dynein heavy chain 7 of Tetrahymena thermophila results in altered ciliary waveform and reduced swim speed," (in eng), *J Cell Sci,* Research Support, U.S. Gov't, Non-P.H.S. vol. 120, no. Pt 17, pp. 3075-85, Sep 1 2007, doi: 10.1242/jcs.007369.

[208] M. Goto, K. Ohki, and Y. Nozawa, "Evidence for a correlation between swimming velocity and membrane fluidity of Tetrahymena cells," (in eng), *Biochim Biophys Acta,* vol. 693, no. 2, pp. 335-40, Dec 22 1982.

[209] M. Le Guennec *et al.*, "A helical inner scaffold provides a structural basis for centriole cohesion," *Sci Adv,* vol. 6, no. 7, p. eaaz4137, Feb 2020, doi: 10.1126/sciadv.aaz4137.

[210] G. Quaranta, M. E. Aubin-Tam, and D. Tam, "Hydrodynamics Versus Intracellular Coupling in the Synchronization of Eukaryotic Flagella," *Phys Rev Lett,* vol. 115, no. 23, p. 238101, Dec 4 2015, doi: 10.1103/PhysRevLett.115.238101.

[211] S. Li, J. J. Fernandez, W. F. Marshall, and D. A. Agard, "Three-dimensional structure of basal body triplet revealed by electron cryo-tomography," (in eng), *The EMBO journal,* Research Support, Non-U.S. Gov't vol. 31, no. 3, pp. 552-62, Feb 1 2012, doi: 10.1038/emboj.2011.460.

[212] M. E. Hodges, B. Wickstead, K. Gull, and J. A. Langdale, "The evolution of land plant cilia," (in eng), *The New phytologist,* vol. 195, no. 3, pp. 526-540, Aug 2012, doi: 10.1111/j.1469-8137.2012.04197.x.

[213] T. Cavalier-Smith, "The phagotrophic origin of eukaryotes and phylogenetic classification of Protozoa," *International journal of systematic and evolutionary microbiology,* vol. 52, no. 2, pp. 297-354, 2002.

[214] Z. Carvalho-Santos, J. Azimzadeh, J. B. Pereira-Leal, and M. Bettencourt-Dias, "Evolution: Tracing the origins of centrioles, cilia, and flagella," (in eng), *J Cell Biol,* vol. 194, no. 2, pp. 165-75, Jul 25 2011, doi: 10.1083/jcb.201011152.

[215] R. Allen, "Paramecium and Other Ciliates: Richard Allen's Image Collection," *Pacific Biosciences Research Center, University of Hawaii at Manoa,* 2007.

[216] D. Gogendeau *et al.*, "MKS-NPHP module proteins control ciliary shedding at the transition zone," (in eng), *PLoS biology,* vol. 18, no. 3, p. e3000640, Mar 2020, doi: 10.1371/journal.pbio.3000640.

[217] R. D. Sloboda and J. L. Rosenbaum, "Making sense of cilia and flagella," (in eng), *J Cell Biol,* vol. 179, no. 4, pp. 575-82, Nov 19 2007, doi: 10.1083/jcb.200709039.

[218] R. G. Anderson, "The three-dimensional structure of the basal body from the rhesus monkey oviduct," (in eng), *J Cell Biol,* vol. 54, no. 2, pp. 246-65, Aug 1972.

[219] T. Avidor-Reiss and K. Turner, "The Evolution of Centriole Structure: Heterochrony, Neoteny, and Hypermorphosis," (in eng), *Results and problems in cell differentiation,* vol. 67, pp. 3-15, 2019, doi: 10.1007/978-3-030-23173-6_1.

[220] C. B. Lindemann and K. A. Lesich, "The many modes of flagellar and ciliary beating: Insights from a physical analysis," *Cytoskeleton (Hoboken),* vol. 78, no. 2, pp. 36-51, Feb 2021, doi: 10.1002/cm.21656.

[221] V. F. Geyer, J. Howard, and P. Sartori, "Ciliary beating patterns map onto a low-dimensional behavioural space," *Nature Physics,* 2022/01/10 2022, doi: 10.1038/s41567-021-01446-2.

[222] R. Rikmenspoel, "Movements and active moments of bull sperm flagella as a function of temperature and viscosity," *J Exp Biol,* vol. 108, pp. 205-30, Jan 1984, doi: 10.1242/jeb.108.1.205.

[223] Z. Teff, Z. Priel, and L. A. Gheber, "The forces applied by cilia depend linearly on their frequency due to constant geometry of the effective stroke," *Biophys J,* vol. 94, no. 1, pp. 298-305, Jan 1 2008, doi: 10.1529/biophysj.107.111724.

[224] C. F. Clary-Meinesz, J. Cosson, P. Huitorel, and B. Blaive, "Temperature effect on the ciliary beat frequency of human nasal and tracheal ciliated cells," (in eng), *Biol Cell,* vol. 76, no. 3, pp. 335-8, 1992, doi: 10.1016/0248-4900(92)90436-5.

[225] C. O'Callaghan, M. Achaval, I. Forsythe, and P. W. Barry, "Brain and respiratory cilia: the effect of temperature," *Neonatology,* vol. 68, no. 6, pp. 394-397, 1995.

[226] H. Guo, Y. Man, K. Y. Wan, and E. Kanso, "Intracellular coupling modulates biflagellar synchrony," (in eng), *Journal of the Royal Society, Interface / the Royal Society,* vol. 18, no. 174, p. 20200660, Jan 2021, doi: 10.1098/rsif.2020.0660.

[227] M. Arslanyolu and F. P. Doerder, "Genetic and environmental factors affecting mating type frequency in natural isolates of Tetrahymena thermophila," (in eng), *The Journal of eukaryotic microbiology,* vol. 47, no. 4, pp. 412-8, Jul-Aug 2000, doi: 10.1111/j.1550-7408.2000.tb00068.x.

[228] T. H. Giddings, Jr., J. B. Meehl, C. G. Pearson, and M. Winey, "Electron tomography and immuno-labeling of Tetrahymena thermophila basal bodies," *Methods Cell Biol,* vol. 96, pp. 117-41, 2010, doi: 10.1016/S0091-679X(10)96006-8.

[229] D. N. Mastronarde, "Automated electron microscope tomography using robust prediction of specimen movements," (in eng), *Journal of structural biology,* vol. 152, no. 1, pp. 36-51, Oct 2005, doi: 10.1016/j.jsb.2005.07.007.

[230] D. N. Mastronarde, "Dual-axis tomography: an approach with alignment methods that preserve resolution," (in eng), *Journal of structural biology,* vol. 120, no. 3, pp. 343-52, Dec 1997, doi: 10.1006/jsbi.1997.3919.

[231] J. R. Kremer, D. N. Mastronarde, and J. R. McIntosh, "Computer visualization of three-dimensional image data using IMOD," (in eng), *Journal of structural biology,* vol. 116, no. 1, pp. 71-6, Jan-Feb 1996, doi: 10.1006/jsbi.1996.0013.

[232] M. Hines and J. J. Blum, "Three-dimensional mechanics of eukaryotic flagella," (in eng), *Biophys J,* vol. 41, no. 1, pp. 67-79, Jan 1983, doi: 10.1016/s0006-3495(83)84406-3.

[233] P. Satir and T. Matsuoka, "Splitting the ciliary axoneme: implications for a "switch-point" model of dynein arm activity in ciliary motion," *Cell Motil Cytoskeleton,* vol. 14, no. 3, pp. 345-58, 1989.

[234] J. N. Hansen, S. Rassmann, J. E. Jikeli, and D. Wachten, "SpermQ-A Simple Analysis Software to Comprehensively Study Flagellar Beating and Sperm Steering," (in English), *Cells-Basel,* vol. 8, no. 1, Jan 2019, doi: ARTN 10

[235] M. T. Gallagher, G. Cupples, E. H. Ooi, J. C. Kirkman-Brown, and D. J. Smith, "Rapid sperm capture: high-throughput flagellar waveform analysis," *Hum Reprod,* vol. 34, no. 7, pp. 1173-1185, Jul 8 2019, doi: 10.1093/humrep/dez056.

[236] A. M. Folcik *et al.*, "Computer-Assisted Tracking of Chlamydomonas Species," *Front Plant Sci,* vol. 10, p. 1616, 2019, doi: 10.3389/fpls.2019.01616.

[237] T. J. Racey, R. Hallett, and B. Nickel, "A quasi-elastic light scattering and cinematographic investigation of motile Chlamydomonas reinhardtii," *Biophys J,* vol. 35, no. 3, pp. 557-71, Sep 1981, doi: 10.1016/S0006-3495(81)84812-6.

[238] U. Rüffer and W. Nultsch, "High-speed cinematographic analysis of the movement of Chlamydomonas," *Cell Motility,* vol. 5, no. 3, pp. 251-263, 1985 1985, doi: 10.1002/cm.970050307.

[239] M. Kim, P. V. Bayly, and J. M. Meacham, "Motile cells as probes for characterizing acoustofluidic devices," *Lab Chip,* vol. 21, no. 3, pp. 521-533, Feb 9 2021, doi: 10.1039/d0lc01025a.

[240] S. Baker and I. Matthews, "Lucas-Kanade 20 years on: A unifying framework," (in English), *International Journal of Computer Vision,* vol. 56, no. 3, pp. 221-255, Feb-Mar 2004, doi: DOI 10.1023/B:VISI.0000011205.11775.fd.

[241] Z. Li, J. Cho, W. LG, and H. JW, "Fluorescence imaging of beta cell primary cilia," *Frontiers in Endocrinology,* 2022 (in review).

[242] M. Yamamoto and K. Kataoka, "Electron microscopic observation of the primary cilium in the pancreatic islets," *Arch Histol Jpn,* vol. 49, no. 4, pp. 449-57, Oct 1986, doi: 10.1679/aohc.49.449.

[243] J. M. Gerdes *et al.*, "Ciliary dysfunction impairs beta-cell insulin secretion and promotes development of type 2 diabetes in rodents," *Nat Commun,* vol. 5, p. 5308, Nov 6 2014, doi: 10.1038/ncomms6308.

[244] J. W. Hughes *et al.*, "Primary cilia control glucose homeostasis via islet paracrine interactions," *Proc Natl Acad Sci U S A*, vol. 117, no. 16, pp. 8912-8923, Apr 21 2020, doi: 10.1073/pnas.2001936117.

[245] I. Lopez-Gonzalez *et al.*, "Membrane hyperpolarization during human sperm capacitation," *Mol Hum Reprod*, vol. 20, no. 7, pp. 619-29, Jul 2014, doi: 10.1093/molehr/gau029.

[246] Y. Zeng, E. N. Clark, and H. M. Florman, "Sperm membrane potential: hyperpolarization during capacitation regulates zona pellucida-dependent acrosomal secretion," *Dev Biol*, vol. 171, no. 2, pp. 554-63, Oct 1995, doi: 10.1006/dbio.1995.1304.

[247] J. B. Tenenbaum, V. de Silva, and J. C. Langford, "A global geometric framework for nonlinear dimensionality reduction," *Science*, vol. 290, no. 5500, pp. 2319-23, Dec 22 2000.

[248] B. Marquez and S. S. Suarez, "Different signaling pathways in bovine sperm regulate capacitation and hyperactivation," *Biology of reproduction*, vol. 70, no. 6, pp. 1626-33, Jun 2004, doi: 10.1095/biolreprod.103.026476.

[249] J. Elgeti and G. Gompper, "Emergence of metachronal waves in cilia arrays," (in eng), *Proc Natl Acad Sci U S A*, vol. 110, no. 12, pp. 4470-5, Mar 19 2013, doi: 10.1073/pnas.1218869110.

[250] W. Gilpin, V. N. Prakash, and M. Prakash, "Vortex arrays and ciliary tangles underlie the feeding–swimming trade-off in starfish larvae," *Nature Physics*, vol. 13, no. 4, pp. 380-386, 2017/04/01 2017, doi: 10.1038/nphys3981.

[251] D. R. Brumley, M. Polin, T. J. Pedley, and R. E. Goldstein, "Hydrodynamic synchronization and metachronal waves on the surface of the colonial alga Volvox carteri," *Phys. Rev. Lett.*, vol. 109, no. 26, p. 268102, 2012/12/28 2012, doi: 10.1103/PhysRevLett.109.268102.

[252] J. Lighthill, "Flagellar Hydrodynamics: The John von Neumann Lecture, 1975," *SIAM Review*, vol. 18, no. 2, pp. 161-230, 1976.

[253] A. T. Chwang and T. Y.-T. Wu, "Hydromechanics of low-Reynolds-number flow. Part 2. Singularity method for Stokes flows," *J Fluid Mech*, vol. 67, no. 4, pp. 787-815, 1975, doi: 10.1017/S0022112075000614.

[254] D. F. Galati, D. S. Abuin, G. A. Tauber, A. T. Pham, and C. G. Pearson, "Automated image analysis reveals the dynamic 3-dimensional organization of multi-ciliary arrays," (in eng), *Biol Open*, vol. 5, no. 1, pp. 20-31, Dec 23 2015, doi: 10.1242/bio.014951.

[255] Y. Naitoh and K. Sugino, "Ciliary Movement and Its Control in Paramecium1," *The Journal of Protozoology*, vol. 31, no. 1, pp. 31-40, 1984, doi: https://doi.org/10.1111/j.1550-7408.1984.tb04285.x.

[256] C. J. Brokaw, "Computer simulation of flagellar movement. I. Demonstration of stable bend propagation and bend initiation by the sliding filament model," *Biophys J*, vol. 12, no. 5, pp. 564-86, May 1972.

[257] D. B. Stein, G. De Canio, E. Lauga, M. J. Shelley, and R. E. Goldstein, "Swirling Instability of the Microtubule Cytoskeleton," *Phys Rev Lett*, vol. 126, no. 2, p. 028103, Jan 15 2021, doi: 10.1103/PhysRevLett.126.028103.

[258] L. N. Virgin, *Vibration of axially loaded structures*. New York, NY: Cambridge University Press, 2007, pp. xvi, 351 p.

[259] D. J. Inman, *Engineering vibration*, Fourth edition. ed. Boston: Pearson, 2014, pp. xii, 707 pages.

[260] J. S. Przemieniecki, *Theory of Matrix Structural Analysis*. New York: Dover, 1968.

[261] A. D. Junker, S. Jacob, H. Philippe, D. Legrand, and C. G. Pearson, "Plastic cell morphology changes during dispersal," *iScience*, vol. 24, no. 8, p. 102915, Aug 20 2021, doi: 10.1016/j.isci.2021.102915.

Appendix A: Derivation of Finite Element Matrices

Work and Energy in the Finite Element Model

Finite Element Representation

In the finite element formulation, transverse displacements of a doublet are represented as a sum of the products of spatially dependent shape functions and temporally-dependent generalized (modal) coordinates. Here ϕ_i is the i^{th} shape function, expressed in terms of the local axial coordinate, x, and q_i is the i^{th} generalized (modal) displacement, which depends only on time, t. Using the Einstein summation convention for repeated indices, the displacement can be represented as

$$y(x,t) = \phi_i(x) q_i(t). \tag{A1}$$

Cubic Hermite polynomials were used for element-level shape functions. Element-level shape functions were combined into filament-level shape functions by assuming that elements are continuous in displacement and slope at the nodes. Results were compared with different numbers of elements to check convergence; 10 elements per filament were found to be sufficient to capture system behavior.

To derive the finite element matrices, kinetic energy, potential energy, and non-conservative work terms were derived for the physical forces and phenomena to be represented in the system. Lagrange's equations were used to find element-level matrices, which were then combined into filament-level matrices. Filament-level matrices are then combined in block matrices to represent the deflections of multiple filaments in two transverse directions.

Potential Energy

The potential energy due to elastic bending in a differential element of length dx of an Euler-Bernoulli beam is:

$$dV_E = \frac{1}{2} EI \left(\frac{\partial^2 y}{\partial x^2}\right)^2 dx. \quad \text{(A2)}$$

In addition, the potential energy arising from the work done by axial tension during rotation of that differential element is [258]:

$$dV_T = \frac{1}{2} N \left(\frac{\partial y}{\partial x}\right)^2 dx, \quad \text{(A3)}$$

where N is the internal axial tension in the beam (positive in tension, negative in compression).

Kinetic Energy

The kinetic energy of a differential element of an Euler-Bernoulli beam is:

$$dT = \frac{1}{2} \rho A dx \left(\frac{\partial y}{\partial t}\right)^2 = \frac{1}{2} \overline{m} \left(\frac{\partial y}{\partial t}\right)^2 dx, \quad \text{(A4)}$$

where ρ is the density, A is the cross-sectional area, $\overline{m}$ is the mass per unit length.

Total potential and kinetic energy in a finite element of length L are obtained by integrating over the length of the element:

$$V = \int_0^L dV\,,\ T = \int_0^L dT \quad \text{(A5)}$$

Virtual Work of Non-Conservative Forces

The virtual work done by non-conservative forces external to the finite element is:

$$\delta W_{nc} = \int_0^L F(x)\delta y\, dx = \int_0^L F(x) \left(\frac{\partial y}{\partial q_i}\delta q_i\right) dx = \left(\int_0^L F(x) \frac{\partial y}{\partial q_i} dx\right) \delta q_i = Q_i \delta q_i. \quad \text{(A6)}$$

Here $F(x)$ is the transverse (y-directed) component of externally applied loads acting on the element. If the externally applied load is a follower load, the y-component is proportional to the sine of the tangent angle of the beam, which for small angles may be approximated by the slope:

$$F(x) = -p(x)\frac{\partial y(x,t)}{\partial x} = -p(x)\frac{\partial \phi_i(x)}{\partial x}q_i(t). \quad \text{(A7)}$$

Here $p(x)$ is a baseward-oriented follower load applied to the element. The corresponding generalized force, Q_i, is

$$Q_i = \int_0^L F(x)\frac{\partial y(x,t)}{\partial q_i}dx = \int_0^L \left(-p\frac{\partial \phi_j(x)}{\partial x}q_j(t)\right)\phi_i(x)\,dx = q_j(t)\int_0^L -p\phi_i(x)\phi_j'(x)\,dx \quad \text{(A8)}$$

Lagrange's Equations

Using Lagrange's equations [258, 259], we may derive a system of equations from the potential and kinetic energies as well as the work done by non-conservative forces on the system.

$$\frac{d}{dt}\left(\frac{\partial T}{\partial \dot{q}_i}\right) - \frac{\partial T}{\partial q_i} + \frac{\partial V}{\partial q_i} = Q_i^{nc} \quad \text{(A9)}$$

Terms from Kinetic Energy

$$T = \frac{1}{2}\int_0^L \bar{m}\dot{y}^2 dx = \frac{1}{2}\int_0^L \bar{m}(\phi_i\dot{q}_i)^2 dx \quad \text{(A10)}$$

Eq. A9 term 1:

$$\left(\frac{\partial T}{\partial \dot{q}_i}\right) = \int_0^L \bar{m}(\phi_j\dot{q}_j)\phi_i dx \quad \text{(A11)}$$

$$\frac{d}{dt}\left(\frac{\partial T}{\partial \dot{q}_i}\right) = \int_0^L \bar{m}(\phi_j\ddot{q}_j)\phi_i dx = \ddot{q}_j\int_0^L \bar{m}\phi_i\phi_j dx \quad \text{(A12)}$$

Eq. A9 term 2:

$$\frac{\partial T}{\partial q_i} = 0 \quad \text{(A13)}$$

Terms from Potential Energy

$$V = \frac{1}{2}\int_0^L EI(y'')^2 dx + \frac{1}{2}\int_0^L N(y')^2 dx = \frac{1}{2}\int_0^L EI(\phi_i'' q_i)^2 dx + \frac{1}{2}\int_0^L N(\phi_i' q_i)^2 dx \quad \text{(A14)}$$

Eq. A9 term 3:

$$\frac{\partial V}{\partial q_i} = \int_0^L EI(\phi_j'' q_j)\phi_i'' dx + \int_0^L N(\phi_j' q_j)\phi_i' dx = q_j\int_0^L EI\phi_i''\phi_j'' dx + q_j\int_0^L N\phi_i'\phi_j' dx \quad \text{(A15)}$$

Terms from Non-Conservative Forces

Non-conservative work due to generalized displacements:

$$Q_i = \int_0^L -py'\phi_i \, dx \tag{A16}$$

$$Q_i = \int_0^L -p\phi_j' q_j \phi_i \, dx = q_j \int_0^L -p\phi_i \phi_j' \, dx \tag{A17}$$

Local Equations of Motion in Matrix Form

Combining the terms above in Lagrange's equations leads to a set of equations for each finite element.

$$\frac{d}{dt}\left(\frac{\partial T}{\partial \dot{q}_i}\right) - \frac{\partial T}{\partial q_i} + \frac{\partial V}{\partial q_i} = Q_i^{nc} \tag{A18}$$

$$\ddot{q}_j \int_0^L \bar{m}\phi_i\phi_j dx + q_j \int_0^L EI\phi_i''\phi_j'' dx + q_j \int_0^L N\phi_i'\phi_j' dx = q_j \int_0^L -p\phi_i\phi_j' \, dx \tag{A19}$$

$$\ddot{q}_j \int_0^L \bar{m}\phi_i\phi_j dx + q_j \left[\int_0^L EI\phi_i''\phi_j'' dx + \int_0^L N\phi_i'\phi_j' dx - \int_0^L -p\phi_i\phi_j' \, dx\right] = 0 \tag{A20}$$

The individual terms of the equation above can be written using local system matrices.

Mass matrix:

$$M_{ij} = \int_0^L \bar{m}\phi_i\phi_j dx \tag{A21}$$

Stiffness matrix:

$$K_{ij} = \int_0^L EI\phi_i''\phi_j'' dx \tag{A22}$$

"Geometric stiffness" matrix:

$$K_{Gij} = \int_0^L N\phi_i'\phi_j' dx \tag{A23}$$

"Geometric loading" matrix:

$$P_{ij} = \int_0^L -p\phi_i\phi_j' \, dx \tag{A24}$$

The term "geometric stiffness" follows the nomenclature of [258, 260]. The term "geometric loading" is introduced here (we are not aware of another name for this matrix).

The set of local equations governing each finite element (in generalized coordinates) is then given by:

$$M_{ij}\ddot{q}_j + \left(K_{ij} + K_{Gij} - P_{ij}\right)q_j = 0 \tag{A25}$$

Non-conservative transverse forces from external viscous loading are modeled by resistive force theory [107]:

$$\delta W_v^{NC} = \int_0^L -c_N \dot{y}\delta y dx = \int_0^L -c_N\left(\phi_j \dot{q}_j\right)\left(\frac{\partial y}{\partial q_i}\delta q_i\right)dx =$$

$$-\left(\dot{q}_j \int_0^L c_N \phi_i \phi_j dx\right)\delta q_i = Q_v^{NC}\delta q_i \tag{A26}$$

where $Q_v^{NC} = C_{ij}\dot{q}_j$ (note the damping matrix differs from the mass matrix only by a constant factor):

$$C_{ij} = \int_0^L c_N \phi_i \phi_j dx = \alpha M_{ij} \tag{A27}$$

The final form of the equation is then:

$$M_{ij}\ddot{q}_j + C_{ij}\dot{q}_j + \left(K_{ij} + K_{Gij} - P_{ij}\right)q_j = 0 \tag{A28}$$

Or in matrix notation:

$$\mathbf{M}\ddot{\boldsymbol{q}} + \mathbf{C}\dot{\boldsymbol{q}} + [\mathbf{K} + \mathbf{K_G} - \mathbf{P}]\boldsymbol{q} = \mathbf{0} \tag{A29}$$

Shear Stiffness

Shear stiffness may be modeled as a distributed spring stiffness that resists rotation. Let k_T be a distributed elastic resistance to tangential displacement between two filaments spaced a distance d apart. If the filaments remain approximately parallel under deformation, then the shear stiffness, k_τ, provides a distributed moment in response to rotation [30]:

$$k_\tau = k_T d^2 \tag{A30}$$

$$m(x) = -k_\tau \theta(x) = -k_\tau \frac{\partial y}{\partial x}(x) \tag{A31}$$

To derive the FE matrix:

$$dV = \frac{1}{2} k_\tau \theta^2 dx \tag{A32}$$

$$V = \frac{1}{2}\int_0^L k_\tau \theta^2 dx = \frac{1}{2}\int_0^L k_\tau (y')^2 dx = \frac{1}{2}\int_0^L k_\tau \left(\phi_j' q_j\right)^2 dx \tag{A33}$$

$$\frac{\partial V}{\partial q_i} = \int_0^L k_\tau \left(\phi_j' q_j\right)\phi_i' dx = q_j \int_0^L k_\tau \phi_i' \phi_j' dx \tag{A34}$$

Coupling between doublets

In actively coupled pairs, the first beam has a baseward applied load ($-p$) and the second beam has a tipward applied load (p). The applied moment (m) is proportional to the distance between the beams (Fig. A1A). In both actively coupled and passively coupled pairs, there is a distributed viscoelastic coupling (Fig. A1B).

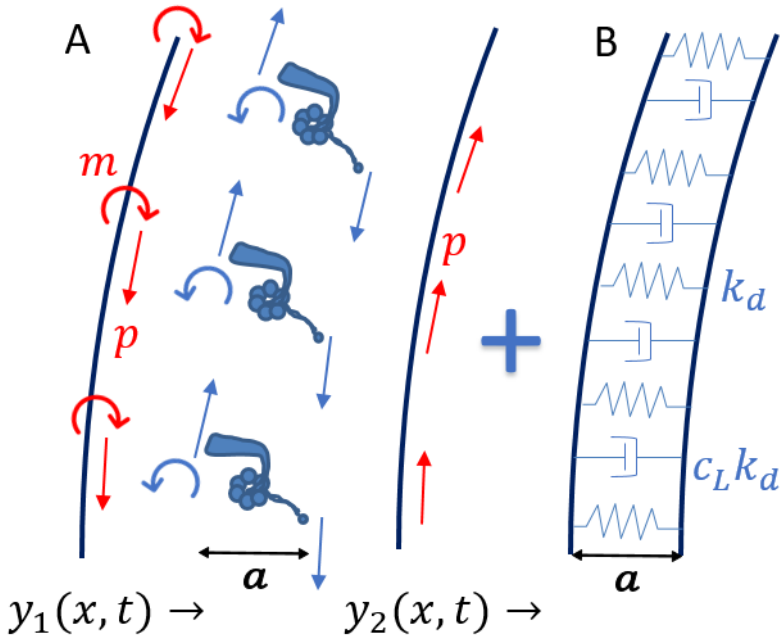

Figure A1: Two coupled filaments with active and passive coupling. (A) Dynein forces and moments are applied to filament 1. Reaction forces on dynein motors are shown for illustration. Dynein forces on filament 2 are equal and opposite to those applied to filament 1. (B) Filaments are coupled by a distributed spring with constant k_d $[pN\mu m^{-2}]$ and stiffness proportional damping with constant $C_L k_d [pNs\mu m^{-2}]$. The active coupling in (A) applies only to the active pairs of doublets, but the passive coupling in (B) represents doublet couples with NDRC stiffness k_L or CPC-MTD couples with stiffness k_S.

The transverse displacements of the two filaments are, as usual, represented by summation of filament-level shape functions, but now the first n coefficients correspond to filament 1, and coefficients $n+1$ to $2n$ correspond to filament 2. Here n is the number of shape functions (degrees of freedom) per filament, which in the case of fixed-free filaments with cubic shape

functions is simply twice the number of elements used per filament. This can then be generalized to create block matrix coupling between any number of filaments.

$$y_1(x,t) = \sum_{i=1}^{n} q_i \phi_i \,,\; y_2(x,t) = \sum_{i=1}^{n} q_{n+i} \phi_{n+i} \tag{A35}$$

Distributed elastic coupling:

Potential energy stored in a distributed elastic coupling is given in the following equation where k_d is a distributed elastic coupling stiffness with units $\frac{\text{pN}}{\mu\text{m}^2}$.

$$dV_e = \frac{1}{2} k_d \big(y_2(x) - y_1(x)\big)^2 dx \tag{A36}$$

$$V_e = \frac{1}{2}\int_0^L k_d \big(y_2(x) - y_1(x)\big)^2 dx = \frac{1}{2}\int_0^L k_d (\phi_{n+i} q_{n+i} - \phi_i q_i)^2 dx \tag{A37}$$

$$\frac{\partial V_e}{\partial q_i} = \int_0^L k_d \big(\phi_{n+j} q_{n+j} - \phi_j q_j\big)(\phi_{n+i} - \phi_i) dx \tag{A38}$$

$$= k_d \left[q_j \int_0^L \big(\phi_i \phi_j - \phi_{n+i} \phi_j\big) dx + q_{n+j} \int_0^L \big(\phi_{n+i} \phi_{n+j} - \phi_i \phi_{n+j}\big) dx \right] \tag{A39}$$

Here we have used the subscripts $n + i$, and $n + j$ to indicate the degrees of freedom of the second of two coupled beams (where n is the number of degrees of freedom per filament). This yields a 2 x 2 block matrix of $n\ x\ n$ matrices with the same form as the consistent mass matrix.

$$= \frac{k_d}{\bar{m}} \begin{bmatrix} M & -M \\ -M & M \end{bmatrix} \tag{A40}$$

Distributed rotational coupling

This coupling mechanism maintains spacing between a pair of filaments by creating resistance to the difference between their tangent angles.

$$m_1(x) = k_\theta \big(\theta_2(x) - \theta_1(x)\big) \tag{A41}$$

$$m_2(x) = -k_\theta \big(\theta_2(x) - \theta_1(x)\big) \tag{A42}$$

$$dV_\theta = \frac{1}{2} k_\theta \big(y_2'(x) - y_1'(x)\big)^2 dx \tag{A43}$$

$$V_\theta = \frac{1}{2}\int_0^L k_\theta \left(y_2'(x) - y_1'(x)\right)^2 dx = \frac{1}{2}\int_0^L k_\theta (\phi_{n+i}' q_{n+i} - \phi_i' q_i)^2 dx \tag{A44}$$

$$\frac{\partial V_\theta}{\partial q_i} = \int_0^L k_\theta \left(\phi_{n+j}' q_{n+j} - \phi_j' q_j\right)(\phi_{n+i}' - \phi_i') dx \tag{A45}$$

$$= k_d \left[q_j \int_0^L \left(\phi_i' \phi_j' - \phi_{n+i}' \phi_j'\right) dx + q_{n+j} \int_0^L \left(\phi_{n+i}' \phi_{n+j}' - \phi_i' \phi_{n+j}'\right) dx\right] \tag{A46}$$

This has the same form as a block matrix of $n\ x\ n$ geometric stiffness matrices without the internal axial force (denoted $K_{\tilde{G}}$):

$$= k_d \begin{bmatrix} K_{\tilde{G}} & -K_{\tilde{G}} \\ -K_{\tilde{G}} & K_{\tilde{G}} \end{bmatrix} \tag{A47}$$

Alignment of Non-Conservative Forces to Ensure Internal Equilibrium

The non-conservative work due to a distributed follower load was given above as:

$$Q_i = \int_0^L -p y' \phi_i \, dx \tag{A48}$$

To ensure that the vector sum of all non-conservative applied loads acting on the two-doublet system is zero, the average of the tangent angles of the two doublets is used to obtain the angle of the internal load, and the load applied to one of the doublets is simply opposite in direction to the other.

$$y_{avg}' = \frac{y_1' + y_2'}{2} \approx \psi_{avg} = \frac{\psi_1 + \psi_2}{2} \tag{A49}$$

$$p_2 = -p_1 \tag{A50}$$

$$Q_i^{avg} = \int_0^L -p \frac{\phi_j' q_j + \phi_{j+n}' q_{j+n}}{2} \phi_i \, dx \tag{A51}$$

$$Q_i^{avg} = \frac{1}{2} q_j \int_0^L -p \phi_i \phi_j' \, dx + \frac{1}{2} q_{j+n} \int_0^L -p \phi_i \phi_{j+n}' \, dx \tag{A52}$$

Negating the sign for the non-conservative work done on the second doublet, we have:

$$Q_{i+n}^{avg} = -\frac{1}{2} q_j \int_0^L -p \phi_i \phi_j' \, dx - \frac{1}{2} q_{j+n} \int_0^L -p \phi_i \phi_{j+n}' \, dx \tag{A53}$$

This gives a two-doublet system coupling matrix of the following form:

$$= \frac{1}{2}\begin{bmatrix} P_g & P_g \\ -P_g & -P_g \end{bmatrix} \quad \text{(A54)}$$

Virtual work of applied moments

The applied distributed moment can be treated as a nonconservative external load on the filament. The work done by this load under deformation of the filament is given by:

$$\delta W = \int_0^L m(x,t)\delta\theta dx = \int_0^L m(x,t)\frac{\partial y'}{\partial q_i}\delta q_i dx = \delta q_i \int_0^L m(x,t)\phi_i' dx = Q_i \delta q_i \quad \text{(A55)}$$

$$Q_i = \int_0^L m(x,t)\phi_i' dx \quad \text{(A56)}$$

If the moment, $m(x,t)$, in this term is not a function of the displacement of the filament, it can be represented by a 'load vector' on the right-hand side of our matrix equations. This term may be included in time-domain simulations, but it does not play a role in the eigenvalue-based stability analysis of the system about an undeformed configuration.

Variation of the moment with interdoublet spacing

If the distributed moment is a function of the interdoublet spacing (for example, if the tangential component of force remains constant), the variation of the moment with transverse displacement leads to a matrix term in the equation of motion. In the case where the moment is directly proportional to interdoublet spacing, the moment gain is equal to 1:

$$m(x,t) = -p\big(a + y_2(x,t) - y_1(x,t)\big) \tag{A57}$$

$$\delta W_i = \int_0^L -p\big(a - q_j\phi_j + q_{n+j}\phi_{n+j}\big)\delta(-q_i\phi_i')dx \tag{A58}$$

$$\delta W_i = \int_0^L p\big(a - q_j\phi_j + q_{n+j}\phi_{n+j}\big)\frac{\partial}{\partial q_i}(q_i\phi_i')\delta q_i dx = Q_i\delta q_i \tag{A59}$$

$$Q_i = \int_0^L pa\phi_i' dx + q_j\int_0^L -p\phi_i'\phi_j dx + q_{n+j}\int_0^L p\phi_i'\phi_{n+j}dx \tag{A60}$$

The term with only one index is the load vector term described in the previous section 4.4. The other two terms form a coupling matrix that is a block matrix of $n\ x\ n$ matrices with the form of the transpose of the geometric loading matrix. This geometric coupling may be applied to a single filament with the following matrix:

$$= \begin{bmatrix} P_G^T & -P_G^T \\ 0 & 0 \end{bmatrix} \tag{A61}$$

or it may be distributed between the two filaments to represent a model where the moment is equally applied at the dynein MTBD.

$$= \frac{1}{2}\begin{bmatrix} P_G^T & -P_G^T \\ P_G^T & -P_G^T \end{bmatrix} \tag{A62}$$

In either case, the matrix is multiplied by a ‘moment gain’ coefficient that represents the variation of the moment with interdoublet spacing. This concept is discussed further below.

Nondimensionalization of system

When the system is nondimensionalized by a characteristic length L_c and characteristic time τ, the following set of equations is obtained in terms of the dimensionless shape functions $\tilde{\phi}_i$:

$$\ddot{q}_j \frac{\bar{m}L_c^3}{\tau^2}\int_0^1 \tilde{\phi}_i\tilde{\phi}_j d\tilde{x} + \dot{q}_j \frac{c_N L_c^3}{\tau}\int_0^1 \tilde{\phi}_i\tilde{\phi}_j d\tilde{x} + q_j \frac{EI}{L_c}\int_0^1 \tilde{\phi}_i{}''\tilde{\phi}_j{}'' d\tilde{x} + q_j F_c L_c \int_0^1 \tilde{N}(L_c\tilde{x})\tilde{\phi}_i{}'\tilde{\phi}_j{}' d\tilde{x} =$$

$$q_j \frac{EI}{L_c}\int_0^1 -\bar{p}(L_c\tilde{x})\tilde{\phi}_i\tilde{\phi}_j' \, d\tilde{x} \tag{A63}$$

Defining the characteristic time, $\tau = \frac{c_N L_c^4}{EI}$, and letting $F_c = \frac{EI}{L_c^2}$, the coefficient of the second term (the damping matrix) reduces to unity and first term (the mass matrix) becomes negligibly small for physical parameters of cilia. The matrix representation of this system is then given as:

$$\widetilde{\boldsymbol{C}}\dot{\boldsymbol{q}} + \left(\widetilde{\boldsymbol{K}} + \widetilde{\boldsymbol{K}}_{\boldsymbol{G}} - \widetilde{\boldsymbol{P}}\right)\boldsymbol{q} = \boldsymbol{0} \tag{A64}$$

where the tildes indicate that the matrices are now dimensionless.

Dynein Kinematics and Moment Gain

In Eq. 3.2 of the manuscript, we show that the variation in the applied moment with interdoublet spacing (the moment gain) for the constant-force winch model shown in Fig. 3.4 is given by the nondimensional term $\left(1 - \frac{a_0(a_0-d)}{b^2}\right)$. Here a_0 is the interdoublet spacing, d is the length of the stem, and b is the distance along the filaments from the stem attachment to the binding domain. All values are given in the undeformed configuration. If the length of the stem, d, equals the full distance between the doublets, a_0, the moment gain is 1. However, many plausible values for the dynein dimensions lead to moment gains that are less than 1 including negative values. For instance, if $a_0 = 33\text{nm}, d = 10\text{nm}, b = 16\text{nm}$ (reasonable values given imaging from [143]), the moment gain is -2.

Appendix B: Finite Element Code

Some sample code for Chapter 3 is given here. Full code may be downloaded on Zenodo: https://doi.org/10.5281/zenodo.6762934

Set system parameters

```
% Parameters
Par.n = 10;             % number of elements per beam
Par.fix_vec = [1 2];    % vector of fixed nodes ([1,2] means cantilever)

% apply follower load according to 'indep' or 'avg' tan angle
Par.tangentAngle = 'avg';
Par.L_total = 12e-6;         % [m] Length of beam
Par.d = 200e-9;              % [m] axoneme diameter
Par.EI = (800e-24)/nBeams;   % [N*m^2] flexural rigidity / filament
Par.m_bar = 1;               % [Kg/M] mass per unit length (leave 1 for viscous only)
Par.kLinks =  1e4;           % [N/m/m] distributed coupling links
Par.kSpokes =  1e4;          % [N/m/m] distributed coupling spokes
Par.k_Sg = 0;                % [N/rad] shear stiff = k_T * d^2 (consistent ver)
Par.k_th = 1e-9;             % [N/rad] theta coupling
Par.massDamp = 0.003;        % [1/s] mass damping (c_N) (alpha)
Par.stiffDamp = 0;           % [s] stiffness damping    (beta)

Par.tc = Par.massDamp*Par.L_total^4/Par.EI; % Characteristic time of system
Par.linkDamp = Par.tc/200;   % [s] link damping
Par.F_tip = 0;               % [N] tip load
Par.P_dist = 200e-6;         % [N/m] distributed load
Par.distMoment = Par.P_dist*Par.d; % distributed moment on baseward force beams

% 3D only
Par.geoMom = 0;              % geometric moment
Par.yStiffnessRatio = 2;     % ratio of y beam stiffness to default
Par.DNL_ratio = 0.1;         % ratio of NL stiffness at dynein pairs

% Time domain only:
Par.structNonLin = 0;        % coefficient of structural nonlinearity
Par.linkNonLin = 0.1;        % coefficient of linking nonlinearity
```

Create single filament matrices

Consistent mass matrix

```
function M = matConsistentMass(Par)
n = Par.n;
m_bar = Par.m_bar;
L_total = Par.L_total;
fix_vec = Par.fix_vec;

% Calculated values
L = L_total/n;           % length per element

Mi = m_bar*L/420*[ ...
      156,    22*L,    54,    -13*L;...
     22*L,   4*L^2,  13*L,   -3*L^2;...
       54,    13*L,   156,    -22*L;...
    -13*L,  -3*L^2, -22*L,    4*L^2];

% Combine into System Mass matrix
M = zeros(2+2*n);
for i = 1:n         % for all elements
    ul = 2*i-1;     % this is the diagonal coordinate of upper left corner
    M(ul:ul+3,ul:ul+3) = M(ul:ul+3,ul:ul+3) + Mi;
end

% eliminate first two dof
M(:,fix_vec)=[];    % eliminate dof fixed columns
M(fix_vec,:)=[];    % eliminate dof fixed rows
```

Create stiffness matrix

```
% Per element stiffness matrix
Ki = 2*EI/L^3*[ ...
      6,      3*L,      -6,       3*L;  ...
    3*L,    2*L^2,    -3*L,       L^2;  ...
     -6,     -3*L,       6,      -3*L;  ...
    3*L,      L^2,    -3*L,     2*L^2];
```

Create geometric stiffness and load matrices

```
% geometric stiffness due to a constant internal force
Kgc = -P_dist*L/(30*L)*[...
         36,      3*L,    -36,    3*L;
        3*L,    4*L^2,   -3*L,   -L^2;
        -36,     -3*L,     36,   -3*L;
        3*L,     -L^2,   -3*L,  4*L^2];
```

```
% geometric stiffness due to a sloped internal force (1-x/L)
Kgs = -P_dist*L*[ ...
       3/(5*L),      0,  -3/(5*L),    1/10;...
             0,   L/10,         0,   -L/60;...
      -3/(5*L),      0,   3/(5*L),   -1/10;...
          1/10,  -L/60,     -1/10,    L/30];

    KgD = zeros(2+2*n);

for i = 1:n         % for all elements
    ul = 2*i-1;     % this is the diagonal coordinate of upper left corner
    KgD(ul:ul+3,ul:ul+3) = KgD(ul:ul+3,ul:ul+3) + Kgc*(n-i)+Kgs;
end

%% Geometric Load Matrix - Distributed load
Pgi = -P_dist*[...
         -1/2,    L/10,     1/2,    -L/10;  ...
        -L/10,       0,    L/10,  -L^2/60;...
         -1/2,   -L/10,     1/2,     L/10;  ...
         L/10,  L^2/60,   -L/10,        0];

PgD = zeros(2+2*n);
for i = 1:n         % for all elements
    ul = 2*i-1;     % this is the diagonal coordinate of upper left corner
    PgD(ul:ul+3,ul:ul+3) = PgD(ul:ul+3,ul:ul+3) + Pgi;
end

%% Geometric Stiffness Matrix - tip load
Kgi = -F_tip/(30*L)*[...
         36,      3*L,    -36,     3*L;
        3*L,    4*L^2,   -3*L,    -L^2;
        -36,     -3*L,     36,    -3*L;
        3*L,     -L^2,   -3*L,   4*L^2];

KgT = zeros(2+2*n);
for i = 1:n         % for all elements
    ul = 2*i-1;     % this is the diagonal coordinate of upper left corner
    KgT(ul:ul+3,ul:ul+3) = KgT(ul:ul+3,ul:ul+3) + Kgi;
end

%% Geometric Load matrix - follower tip load
PgT = zeros(2+2*n);
PgT(end-1, end) = -F_tip;

% combine distributed and tip load matrices
Kg = KgD + KgT;
Pg = PgD + PgT;
% eliminate first two dof
Kg(:,fix_vec)=[];    % eliminate dof 1 and 2 columns
Kg(fix_vec,:)=[];    % eliminate dof 1 and 2 rows
Pg(:,fix_vec)=[];    % eliminate dof 1 and 2 columns
Pg(fix_vec,:)=[];    % eliminate dof 1 and 2 rows
```

Create ‘6+1’ filament coupling matrices

```
function [Geo] = setGeometry6p1(Par)
% set geometry parameters of model
% input parameters
kLinks  = Par.kLinks;   % nexin links stiffness
kSpokes = Par.kSpokes;  % radial spoke stiffness
r = Par.d/2;            % axoneme radius

% initial position of x,y points
%     1   2
%   6   7   3
%     5   4
s30 = sind(30); c30 = cosd(30);
x0 = r*[-s30, s30,  1,  s30, -s30, -1, 0];
y0 = r*[ c30, c30,  0, -c30, -c30,  0, 0];

% axial load application vector: 1 is tipward, -1 is baseward
%    -1  +2
%   6   7   3
%    +5  -4
axLoadVec = [-1 1 0 -1 1 0 0];

% doublet coupling for tangent angle averaging in geometric load
%     1---2
%   6   7   3
%     5---4
dynCouples = [1 2; 5 4];

% connections between nodes
links  = [1 2; 2 3; 3 4; 4 5; 5 6; 6 1];
spokes = [7 1; 7 2; 7 3; 7 4; 7 5; 7 6];

% theta coupling between central and outer filaments
%     1   2
%   6   7   3
%     5   4
% use spokes and links

numLinks = length(links);
numSpokes = length(spokes);
linksSpokes = [links; spokes];
xydof = numel(x0)+numel(y0);
if numel(x0) ~= numel(y0), error('x,y vectors not same length'), end

% For each link, generate element stiffness matrix in global coordinates
% using the direction cosines. This is following from Chapter 2 of
% 'Finite Element Analysis Using SOLIDWORKS Simulation 2020' by Shih
% The matrix is then broken up and added to appropriate blocks of the
% global stiffness matrix.
KNL = zeros(2*length(x0)); % just the nexin links
KRS = zeros(2*length(x0)); % just the radial spokes
KSNL = KNL; % simple coupling
KSRS = KRS;
```

```
for n = 1:(numLinks + numSpokes)
    n1 = linksSpokes(n,1); n2 = linksSpokes(n,2);
    x1 = x0(n1); x2 = x0(n2);
    y1 = y0(n1); y2 = y0(n2);
    dx = x2 - x1; dy = y2 - y1;
    L = sqrt(dx^2 + dy^2);
    c = dx/L; s = dy/L;

    % Truss element matrix in x1y1x2y2
    Kn = [c^2   c*s  -c^2  -c*s
          c*s   s^2  -c*s  -s^2
         -c^2  -c*s   c^2   c*s
         -c*s  -s^2   c*s   s^2];

    % simple coupling in x1y1x2y2
    Ksimple = [1  0 -1  0
               0  1  0 -1
              -1  0  1  0
               0 -1  0  1];

    idx = [2*n1-1, 2*n1, 2*n2-1, 2*n2];

    if n <= numLinks
        % k = kLinks;
        % ****LINKS AT DYNEIN PAIR LESS STIFF*********
        if (n==1 || n==4)
            Kn = Kn*Par.DNL_ratio;
        end
        KNL(idx,idx) = KNL(idx, idx) + Kn;
        KSNL(idx,idx) = KSNL(idx, idx) + Ksimple;
    else
        % k = kSpokes;
        KRS(idx,idx) = KRS(idx, idx) + Kn;
        KSRS(idx,idx) = KSRS(idx, idx) + Ksimple;
    end
end

K = kLinks*KNL + kSpokes*KRS;

% the method above uses (x1,y1,x2,y2...) coordinates. Below I reorder the
% matrix into (x1,x2...y1,y2...) coordinates.
xxyyIdx = [1:2:xydof,2:2:xydof];
Kxxyy = K(xxyyIdx,xxyyIdx);
KNLxxyy = KNL(xxyyIdx,xxyyIdx);
KRSxxyy = KRS(xxyyIdx,xxyyIdx);
KSNLxxyy = KSNL(xxyyIdx,xxyyIdx);
KSRSxxyy = KSRS(xxyyIdx,xxyyIdx);
```

Combine filament-level matrices into global matrices

```
function [MatND] = makeNBeamMatrices(Mat1,Par,Geo)

% beam coupling matrix (links and spokes)
Kc = kron(Geo.KTruss, Mat1.M/Par.m_bar);

% system mass matrix
M = kron(eye(Geo.numBeams*2),Mat1.M);

% system beam stiffness matrix: y-stiffness is modified here
coeffK = blkdiag(eye(Geo.numBeams), eye(Geo.numBeams)*Par.yStiffnessRatio);
K = kron(coeffK, Mat1.K);

% system shear stiffness: applied to all beams, so divided by nBeams
Ks = kron(eye(Geo.numBeams*2), Mat1.Ks)/Geo.numBeams;

% geometric stiffness matrix applies to axially loaded beams
Kg = kron(-diag([Geo.axLoadVec; Geo.axLoadVec]),Mat1.Kg);

C = Par.massDamp*M + Par.stiffDamp*K + Par.linkDamp*Kc;

% System geometric load matrix
if strcmp(Par.tangentAngle,'avg')
    Pg2 = [Mat1.Pg, Mat1.Pg; -Mat1.Pg, -Mat1.Pg]/2;
elseif strcmp(Par.tangentAngle,'indep')
    Pg2 = blkdiag(Mat1.Pg, -Mat1.Pg);
else
    error('must set tangentAngle parameter')
end

% geometric load matrix for changing moment due to changing
% doublet spacing
Pm2 = [Mat1.Pg', -Mat1.Pg'; Mat1.Pg', -Mat1.Pg']/2;

Pg = zeros(size(M));
Pm = zeros(size(M));
for n = 1:size(Geo.dynCouples,1)
    d1 = Geo.dynCouples(n,1);
    d2 = Geo.dynCouples(n,2);
    % need to get orientation of the geometric load matrix
    % this is based on orientation of applied load
    flipBeams = sign(Geo.axLoadVec(d2)-Geo.axLoadVec(d1));
    numDofBeam = Mat1.dim(1);
    ind1 = 1:numDofBeam;
    ind2 = [(d1-1)*numDofBeam+ind1, (d2-1)*numDofBeam+ind1];
    % This is x only
    Pg(ind2, ind2) = Pg(ind2, ind2) + Pg2*flipBeams;
    Pm(ind2, ind2) = Pm(ind2, ind2) + Pm2*flipBeams;
    % This is y only
    ind2y = ind2 + size(M,1)/2;
    Pg(ind2y, ind2y) = Pg(ind2y, ind2y) + Pg2*flipBeams;
end
```

```
% Distributed torsional coupling between beams
KthetaRS = kron(Geo.KSRS_0, Mat1.Kth)*Par.k_th;
KthetaNL = kron(Geo.KSNL_0, Mat1.Kth)*Par.k_th;
Ktheta = 0*KthetaRS + 1*KthetaNL; % torsional couple in NL only

MatND.Kc = Kc + Ktheta; % stiffness coupling
MatND.C  = C;           % damping
MatND.K  = K + Ks;      % flexural and shear stiffness
MatND.M  = M;           % mass
MatND.Kg = Kg;          % geometric stiffness
% geometric loading matrix (including moment gain effects)
if Geo.numBeams == 1
    MatND.Pg = blkdiag(Mat1.Pg, Mat1.Pg);
else
    MatND.Pg = Pg + Pm * Par.geoMom;
end
```

Appendix C: Supporting information for Chapter 4

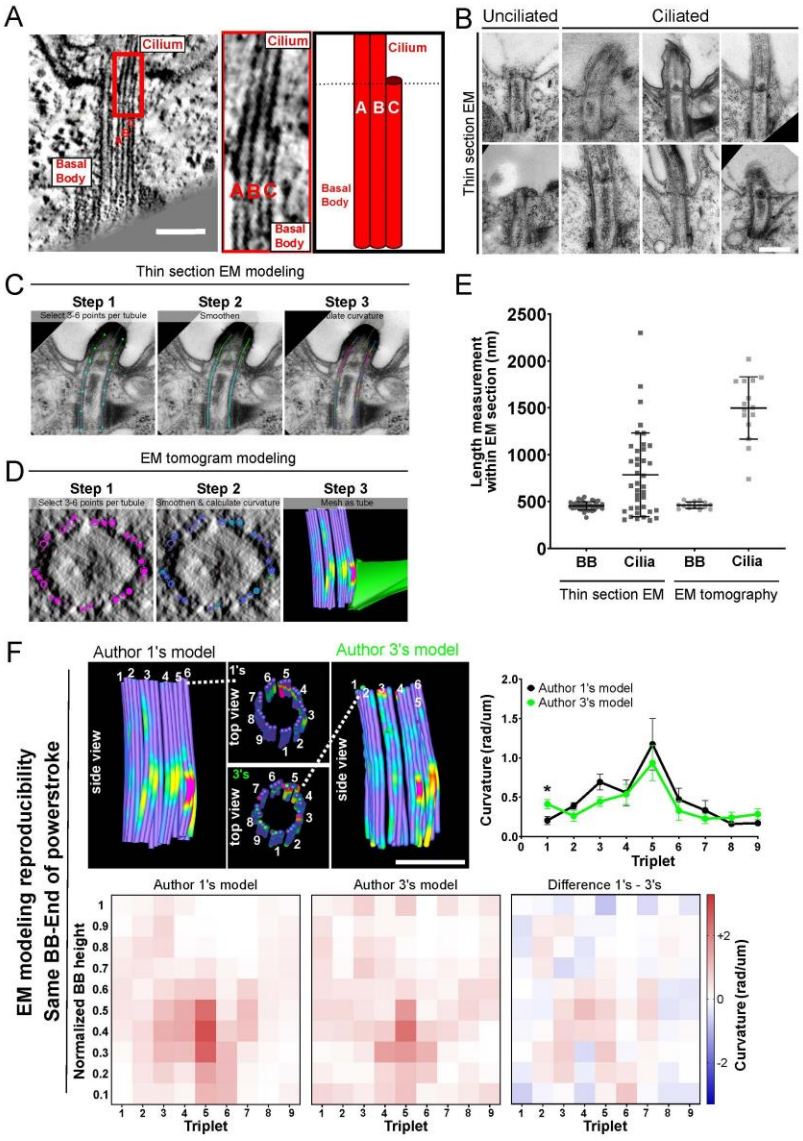

Figure C1: BB MTs display bending consistent with ciliary bending. (A) The A and B tubules of cilia are structurally continuous with the A and B tubules of the BB. The left image is a maximum-projected EM tomogram image showing BB triplet MTs continuous with its associated ciliary doublet MTs. The cortical cytoskeleton and plasma membrane flanks the cilium. Scale bar, 100 nm. Middle image is an inset from the tomogram defined by red box, the model to the right of the inset indicates the continuity of A- and B-tubules between the BB and the cilium. Schematic model on the right highlights structural continuity between ciliary doublet MTs and BB A-B tubules (B) Representative thin section EM images of unciliated and ciliated BBs and their respective bending profiles. Scale bar, 200 nm. n=37 BBs. (C) Schematized images show the process used to obtain curvature values from BBs and cilia in thin section EM images quantified in Fig. 4.1B. (D) Schematized images of the process used to obtain curvature values from BBs and cilia in 3-dimentional EM tomograms (Fig. 4.1C) quantified in Fig. 4.2. (E) The scatter plot graphs the distribution of BB and proximal cilium lengths contained within the EM thin sections (Fig. 4.1B) and EM tomogram volumes (Figs. 4.2-4.6). (F) Analysis compares MT curvature of BBs between two independent modelers Author 1 (A. Junker) and Author 3 (A. Soh). Left panels show side views and top views of the

same BB modeled independently. The graph on the right compares mean curvature values for each triplet obtained from each model, curvatures are consistently most prominent at triplets 5 and 6. Asterisk denotes p-value <0.05. Heat maps below show distribution of curvature between independent models. Curvature is consistently most prominent near the base-middle of triplets 5-6.

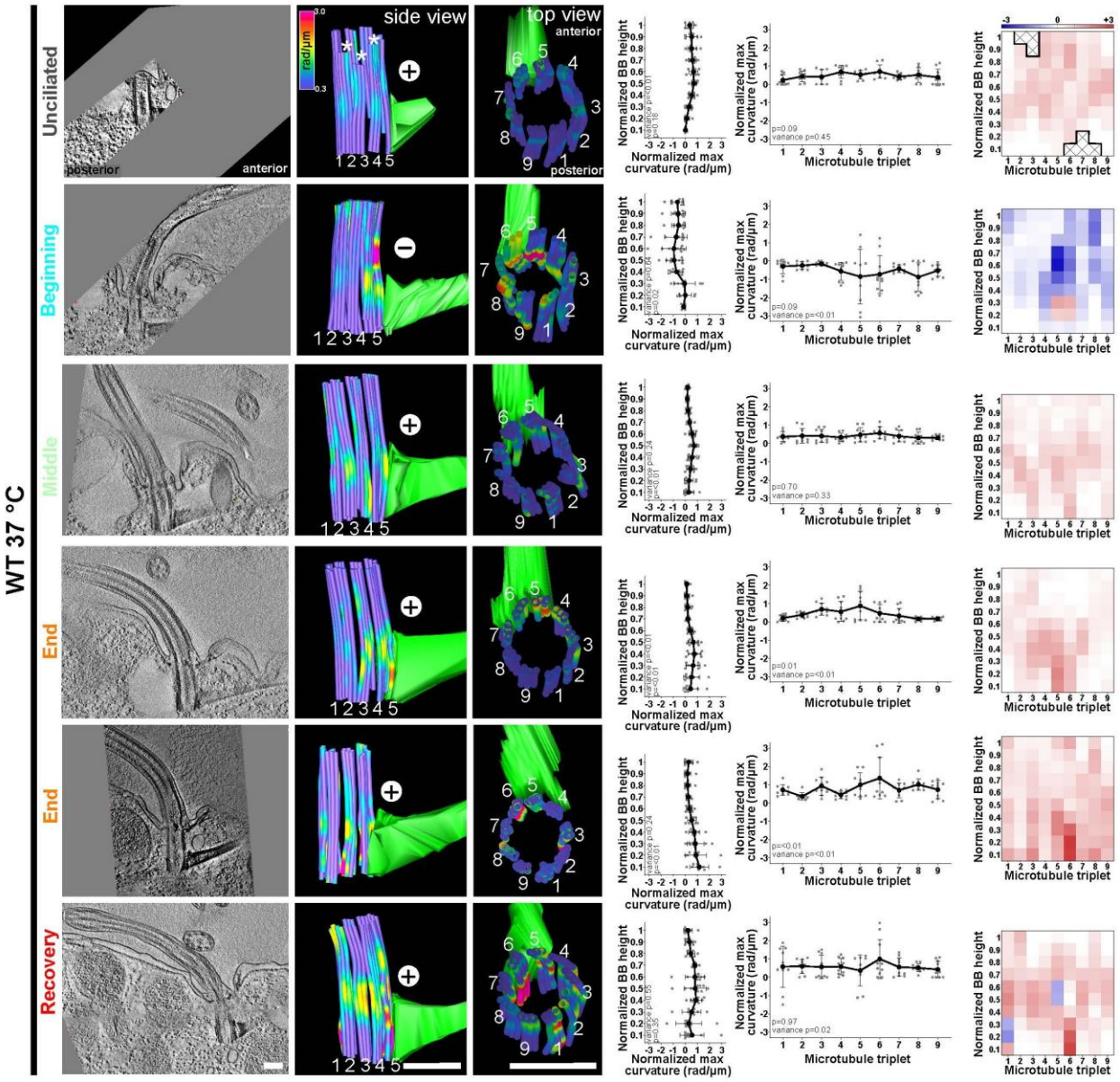

Figure C2: **BBs bend consistent with ciliary beat stroke at 37°C.** BBs display different bending patterns depending on where the cilium is in the beat stroke. Left panels are 8.6 nm max-projected images of EM tomograms. Scale bar, 200 nm. The two middle panels on the left are model views (side view and top view) of BB triplet MTs from corresponding BBs in EM tomogram. Colors indicate curvature of the modeled triplet MTs where cold colors (purple-blue) indicate low curvature and warm colors indicate high curvature (red-magenta) (range= 0.3 to 3 rad/µm). The two middle panels on the right are graphs showing BB curvature for the BB proximal to distal axis (left) or for each triplet MT (right). The maximum value for each bin (1/10th the length of the BB) along the BB proximal-distal axis is normalized by subtracting the lowest maximum value of all bins in each BB. The graph represents the means and standard deviations of these normalized maximum values for each proximal to distal bin (left) or each triplet MT (right). BBs exhibit different bending profiles depending on the cilium's position on the

beat cycle. Grey dots represent curvature values from individual bins, black lines indicate means, and error bars indicate the standard deviation. Right panels show curvature heatmaps of the positive and negative curvature for each proximal-distal bin in each triplet MT. Black "X's" indicate missing bins due to incomplete EM tomogram volumes. The blue and red colors indicate the direction of curvature relative to the cell's anterior-posterior axis (axis of the ciliary power stroke). Blue indicates negative bending which is towards the cell anterior. Red indicates positive bending which is towards the cell posterior (range= -3.3 to +3.3 rad/μm). n=8 tomograms, 5 BBs analyzed.

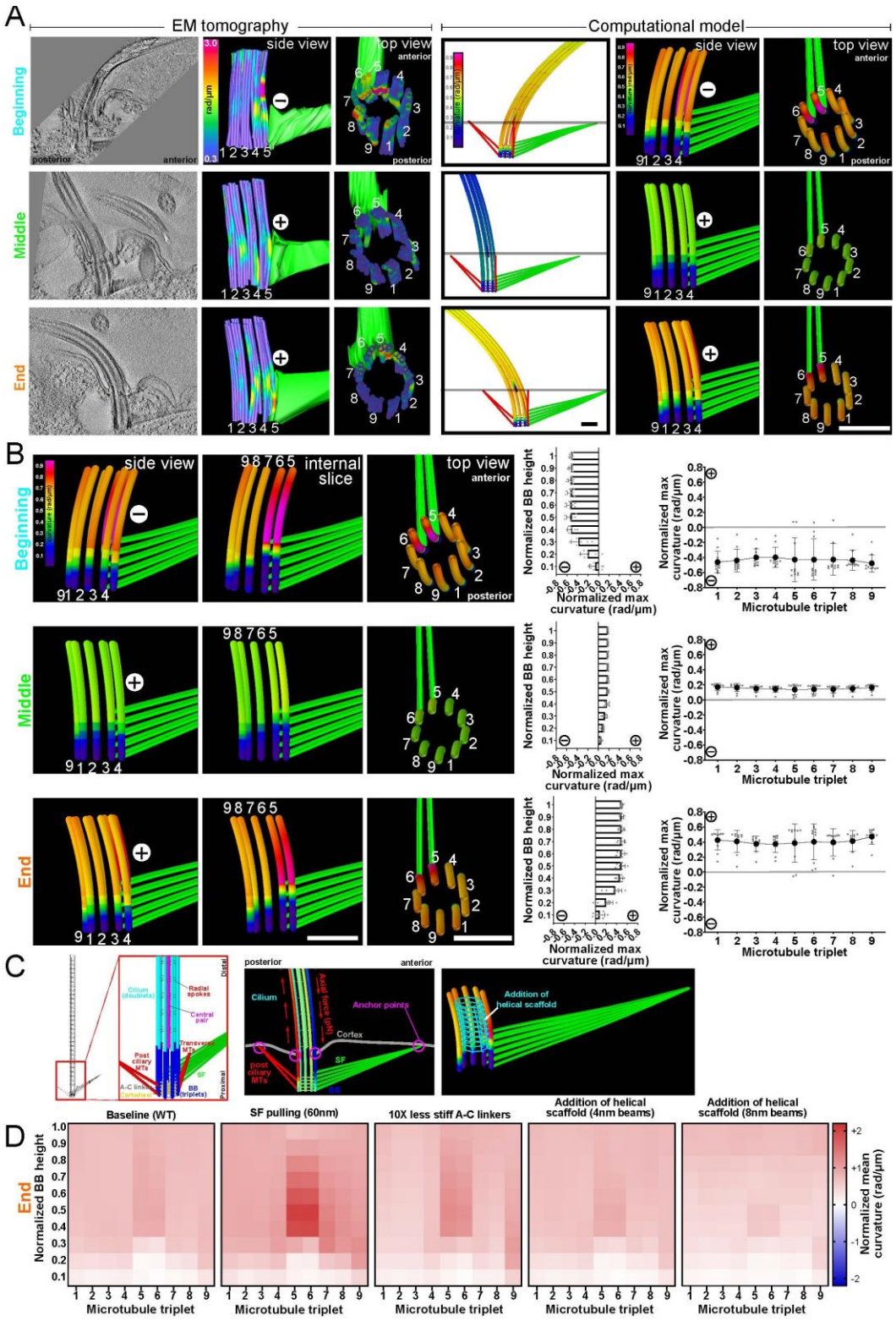

Figure C3: **Computational model of BB bending.** (A) A computational (finite-element) model of the cilium, BB, SF, BB-appendage MTs, and cell cortex was generated in COMSOL Multiphysics using the Beam interface within the Structural Mechanics module. EM tomogram BB mode (left) matched for the angle of their cilium is compared to this computational model (right) and show consistent MT bending direction and similarly increased bending at tubule 5-6. Model colors indicate curvature of the modeled triplet MTs where cold colors (purple-blue) indicate low

curvature and warm colors indicate high curvature (red-magenta) (EM tomogram range= 0.3 to 3 rad/µm, COMSOL model 0.1 to 0.9 rad/µm). (B) Representative images of computational model at the beginning, middle and end of the power stroke (left panels). The panels on the left are model views (side view and top view) of BB triplet MTs. The two panels on the right are graphs showing BB curvature for the BB proximal to distal axis (left) or for each triplet MT (right). The maximum value for each bin ($1/10^{th}$ the length of the BB) along the BB proximal-distal axis is normalized by subtracting the lowest maximum value of all bins in each BB. The graph represents the means and standard deviations of these normalized maximum values for each proximal to distal bin (left) or each triplet MT (right). (C) Computational model components are depicted by the scaffolded model (left) and red inset shows the elements which represent structures present within and around T. thermophila cilia and BBs. Modeled structures include ciliary doublet MTs (cyan), central pair MTs (magenta), radial spokes (red), BB triplet MTs (blue), cartwheel (yellow), A-C linkers (grey), and BB-appendage MTs and SF (green) (Table 2&3). Representative image in the middle shows the computational model with the axial forces within the cilium and the cortical anchor points (magenta circles) of the BB, BB-appendage MTs (post-ciliary MTs) and SF. Scale bar, 200 nm. Representative image (right) of the separately added helical inner scaffold structure is shown in cyan, this structure is not included in any other computational models and its effect on BB MT curvature is quantified in Fig. C3D with 4nm and 8nm beams. (D) Heatmaps show baseline model (left) at the end of the power stroke (Figs. 4.3, C3A-B) and several perturbations to this model. In each model curvature is consistently increased at triplets 5-6 above the SF attachment point. SF pulling (60nm) is the inverse of the manipulations made in later figures (Fig. 4.4) and A-C linker and helical inner scaffold manipulations identify potential differences in curvature when BB triplet interconnectivity is disrupted. Additional perturbations to this baseline model are shown in Table 4.4 and Movies 3-10.

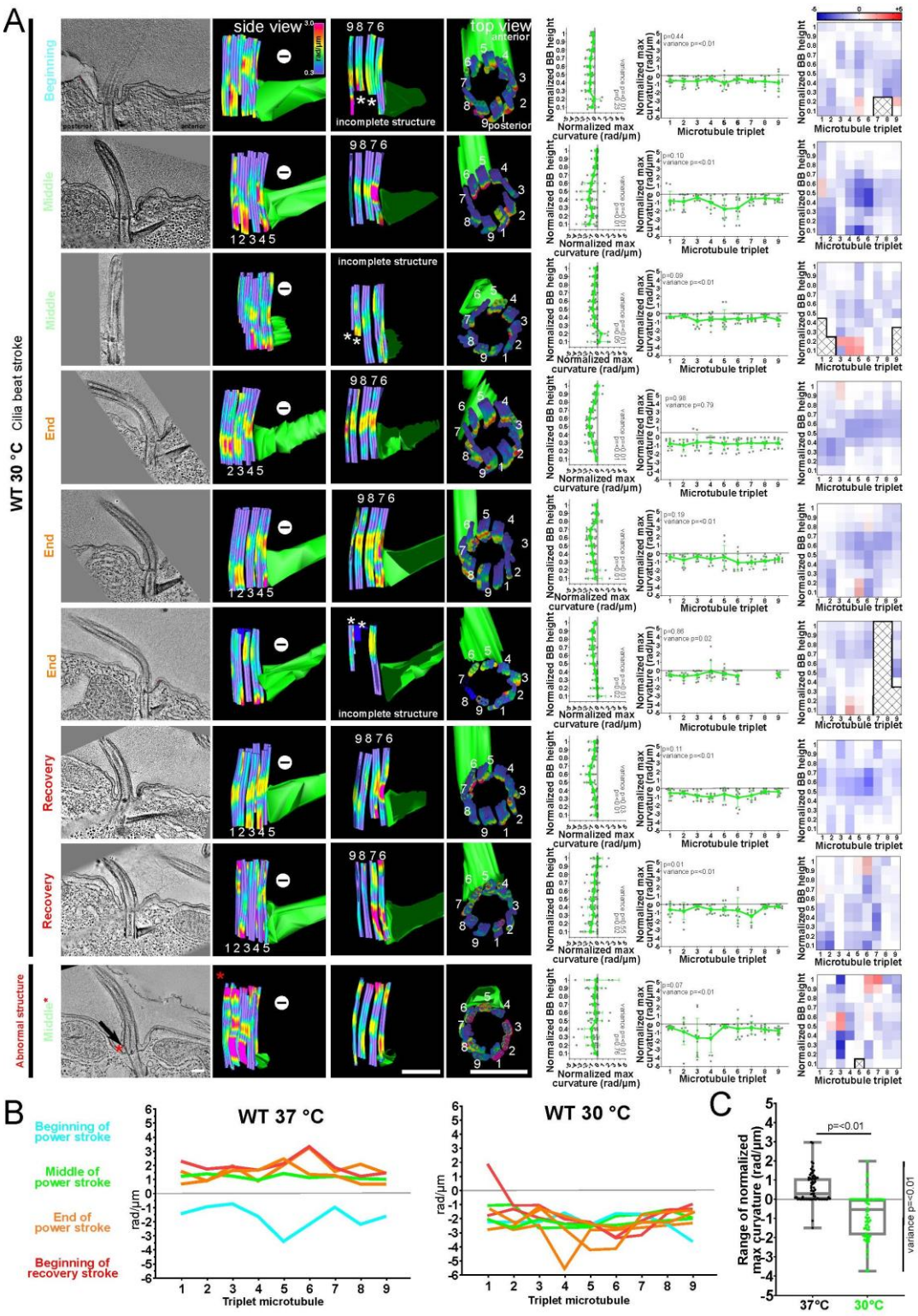

Figure C4: **BB display reversed bending patterns at 30°C.** (A) 30°C BBs display different bending patterns depending on where the cilium is in the beat stroke. Left panels are 8.6 nm max-projected images of EM tomograms. Scale bar, 200 nm. The two middle panels on the left are model views (side view and top view) of BB triplet MTs from corresponding BBs in EM tomogram. White asterisks indicate incomplete structures of triplet MTs that extended outside the imaged EM tomogram volume. Red asterisk indicates a BB with a cilium that displays

outwardly distended MTs. Colors indicate curvature of the modeled triplet MTs where cold colors (purple-blue) indicate low curvature and warm colors indicate high curvature (red-magenta) (range= 0.3 to 3 rad/μm). The two middle panels on the right are graphs showing BB curvature for the BB proximal to distal axis (left) or for each triplet MT (right). The maximum value for each bin ($1/10^{th}$ the length of the BB) along the BB proximal-distal axis is normalized by subtracting the lowest maximum value of all bins in each BB. The graph represents the means and standard deviations of these normalized maximum values for each proximal to distal bin (left) or each triplet MT (right). BBs show differences in whether they have significantly different bending between triplet MTs or along the BB proximal-distal axis (ANOVA p-values) or whether they have significantly different distribution of curvatures as indicated by variance (Bartlett's test p-values). Grey dots represent curvature values from individual bins, black lines indicate means, and error bars indicate the standard deviation. The right panels show heatmaps of the positive and negative curvature for each proximal-distal bin in each triplet MT. Black "X's" indicate missing bins from incomplete structures of triplet MTs that extended outside the imaged EM tomogram volume. The blue and red colors indicate the direction of curvature relative to the cell's anterior-posterior axis (axis of the ciliary power stroke). Blue indicates negative bending which is towards the cell anterior. Red indicates positive bending which is towards the cell posterior (range= -5 to +5 rad/μm). n= 15 tomograms, 9 BBs analyzed. (B) WT BBs predominantly bend in opposite directions between 30°C and 37°C BBs at all phases of the beat stroke. The color of lines indicates the position of each corresponding BB's cilium in the analyzed parts of the beat stroke. n= 15 tomograms, 9 BBs analyzed. (C) BB curvature is more variable at 30°C than 37°C. 30°C BBs bend more in the negative direction and display wider range in distribution of positive or negative curvature in individual BBs (Mann-Whitney test: $p=<0.01$, F-test: $p=<0.01$). Data is represented as individual maximum and minimum values from triplet MTs (dots), mean and quartiles of maximum values (boxes) and standard deviation (error bars). n= 15 tomograms, 9 BBs analyzed.

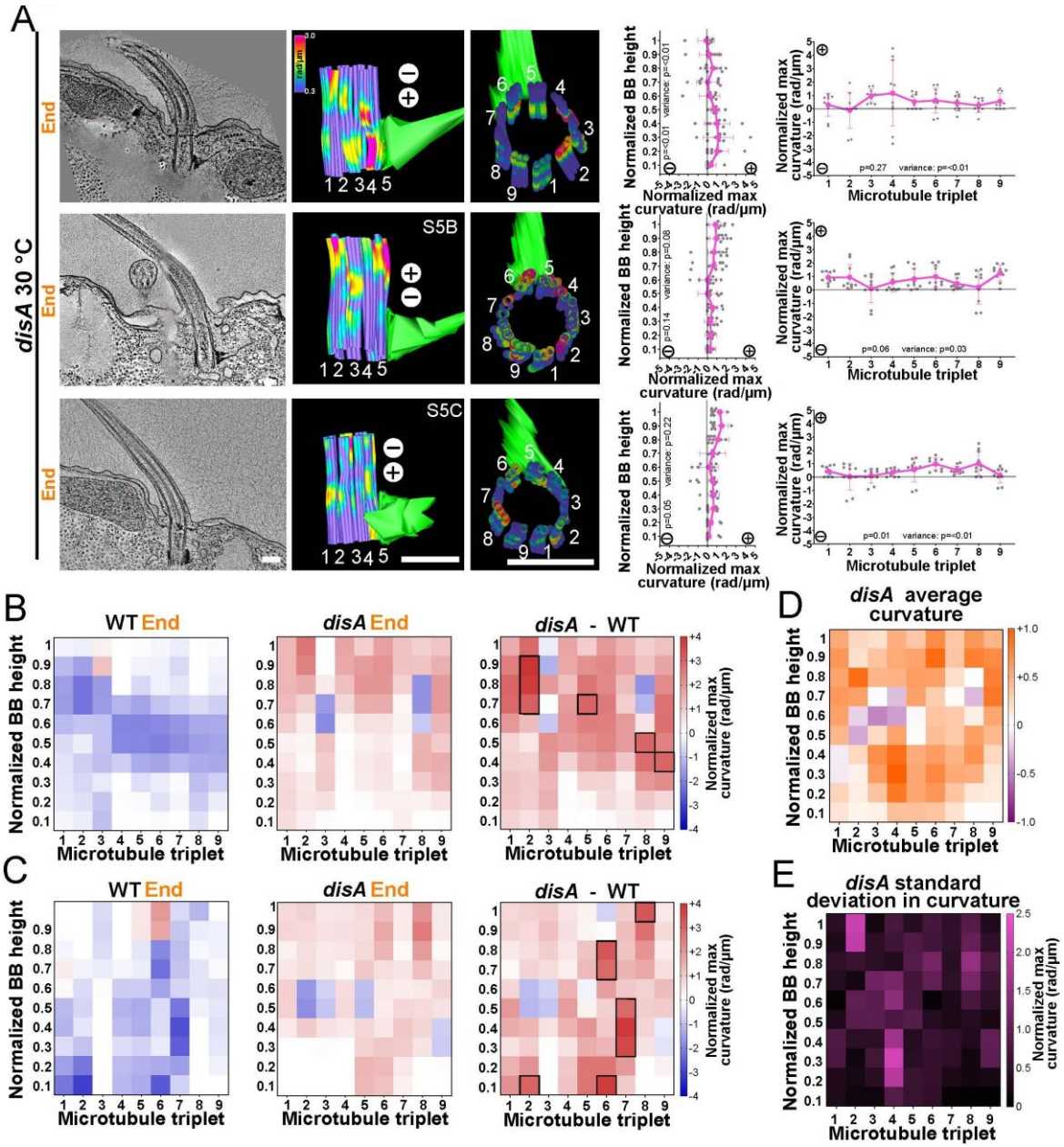

Figure C5: **The striated fiber promotes focal bending in BBs.** (A) disA-1 BBs at 30°C display inconsistent bending patterns at the end of the power stroke. Left panels are 8.6 nm max-projected images of EM tomograms. Scale bar, 200 nm. The two middle panels on the left are model views (side view and top view) of BB triplet MTs from corresponding BBs in EM tomogram. Colors indicate curvature of the modeled triplet MTs where cold colors (purple-blue) indicate low curvature and warm colors indicate high curvature (red-magenta) (range= 0.3 to 3 rad/μm). The two middle panels on the right are graphs showing BB curvature for the BB proximal to distal axis (left) or for each triplet MT (right). The maximum value for each bin (1/10th the length of the BB) along the BB proximal-distal axis is normalized by subtracting the lowest maximum value of all bins in each BB. The graph represents the means and standard deviations of these normalized maximum values for each proximal to distal bin (left) or each triplet MT (right). BBs show differences in whether they have significantly different bending between triplets or along the BB proximal-distal axis (ANOVA p-values) or whether they have significantly different distribution of curvatures as indicated by variance (Bartlett's test p-values). Grey dots represent curvature values from individual bins, black lines indicate means, and error bars indicate the standard deviation. n=7 tomograms, 3 BBs analyzed. (B) WT and disA-1 BB bending display difference at the end of the power stroke. The top panel heatmaps compare the disA-1 BB shown in the middle panel of S5A to a matched WT BB. The heatmap on the left

shows BB bending in a matched WT BB with the most similar cilia angle to the cilia of disA-1 BBs being analyzed. The heatmap in the middle shows disA-1 BB bending. The heatmap on the right quantifies the difference between the corresponding WT and disA-1 BBs. Prominent differences between WT and disA-1 BB bending are observed scattered across the BB (indicated by black boxes; p=>0.05; >75% highest difference from other bins). (C) Heatmaps compare the disA-1 BB shown at the bottom panel of S5A to a matched WT BB. The heatmap on the left shows BB bending in a matched WT BB with the most similar cilia angle to the cilia of disA-1 BBs being analyzed. The heatmap in the middle shows disA-1 BB bending. The heatmap on the right quantifies the difference between the corresponding WT and disA-1 BBs. Prominent differences between WT and disA-1 BB bending are observed scattered across the BB (indicated by black boxes; p=>0.05; >75% highest difference from other bins). The blue and red colors indicate the direction of curvature relative to the cell's anterior-posterior axis (axis of the ciliary power stroke). Blue indicates negative bending which is towards the cell anterior. Red indicates positive bending which is towards the cell posterior (range= -4 to +4 rad/μm). (D) disA-1 BBs bend inconsistently at the end of the beat stroke. The heatmap indicates that the average curvatures for the disA-1 shown above (Fig 5A and S5A). Purple indicates negative bending and orange indicates positive bending (range= -1 to +1 rad/μm). (E) disA-1 BBs exhibit variable BB curvature. Heatmap indicates the standard deviation of BB curvature in disA-1 cells. Black indicates low standard deviation and magenta indicates high standard deviation (range= 0 to 2.5 rad/μm).

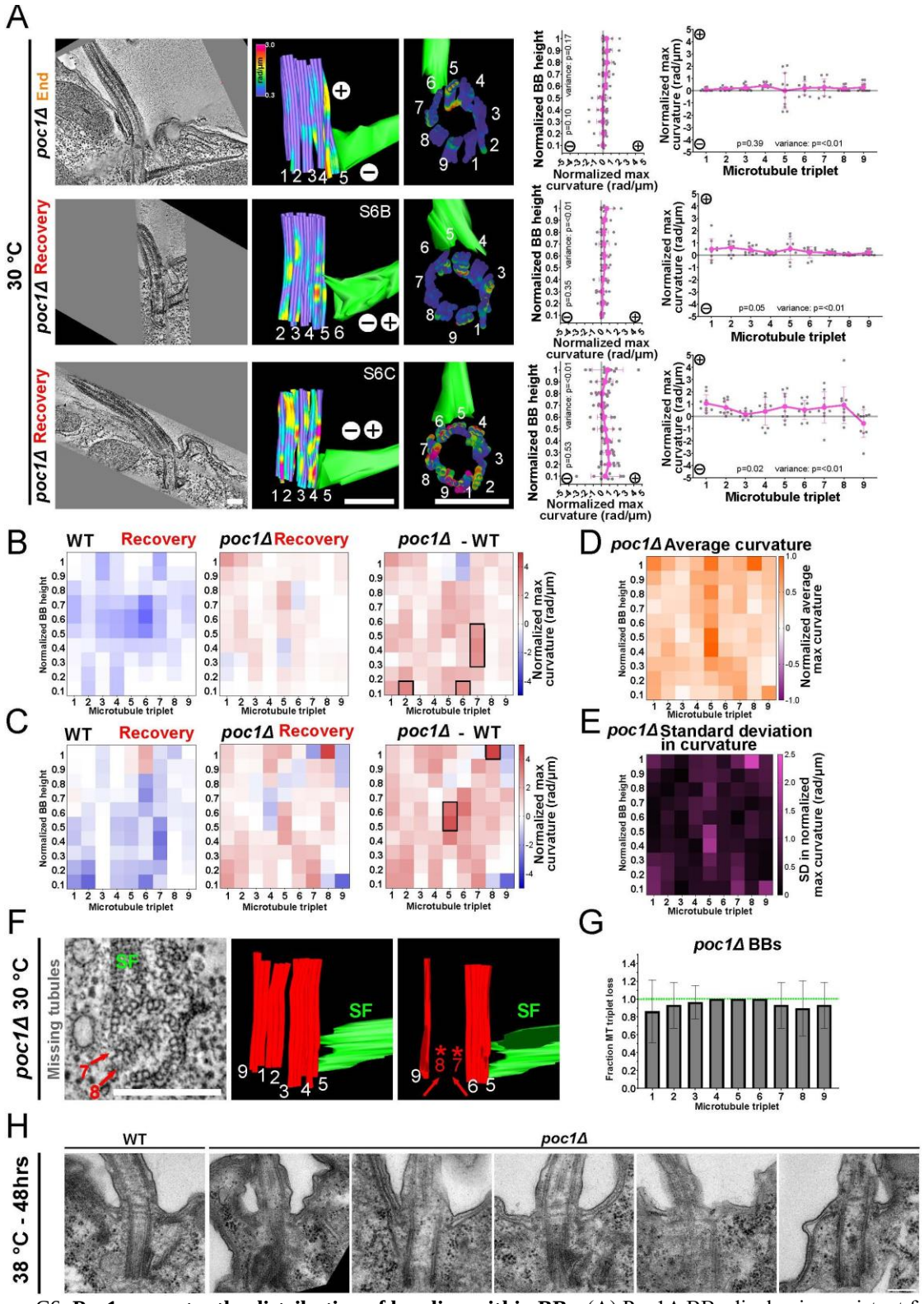

Figure C6: **Poc1 promotes the distribution of bending within BBs.** (A) Poc1Δ BBs display inconsistent focal triplet MT bending at the end of the power stroke. Left panels are 8.6 nm max-projected images of EM tomograms. Scale bar, 200 nm. The two middle panels on the left are model views (side view and top view) of BB triplet MTs from corresponding BBs in EM tomogram. Colors indicate curvature of the modeled triplet MTs where cold colors

(purple-blue) indicate low curvature and warm colors indicate high curvature (red-magenta) (range= 0.3 to 3 rad/µm). The two middle panels on the right are graphs showing BB curvature for the BB proximal to distal axis (left) or for each triplet MT (right). The maximum value for each bin ($1/10^{th}$ the length of the BB) along the BB proximal-distal axis is normalized by subtracting the lowest maximum value of all bins in each BB. The graph represents the means and standard deviations of these normalized maximum values for each proximal to distal bin (left) or each triplet MT (right). BBs show differences in whether they have significantly different bending between triplets or along the BB proximal-distal axis (ANOVA p-values) or whether they have significantly different distribution of curvatures as indicated by variance (Bartlett's test p-values). Grey dots represent curvature values from individual bins, black lines indicate means, and error bars indicate the standard deviation. n=12 tomograms, 3 BBs analyzed. (B) WT and poc1Δ BBs display difference at the beginning of the recovery stroke. Top panel heatmaps compare the poc1Δ BB shown in the middle panel of (A) to a matched WT BB. The heatmap on the left shows BB bending in a matched WT BB with the most similar cilia angle to the cilia of poc1Δ BB s being analyzed. The heatmap in the middle shows poc1Δ BB bending. The heatmap on the right quantifies the difference between the corresponding WT and poc1Δ BBs. Prominent differences between WT and poc1Δ BB bending at the bottoms of triplet MTs 2,6 and 7 (indicated by black boxes; p=>0.05; >75% highest difference from other bins). (C) Heatmaps compare the poc1Δ BB shown in the bottom panel of S6A to a matched WT BB. The heatmap on the left shows BB bending in a matched WT BB with the most similar cilia angle to the cilia of poc1Δ BB s being analyzed. The heatmap in the middle shows poc1Δ BB bending. The heatmap on the right quantifies the difference between the corresponding WT and poc1Δ BBs. Prominent differences between WT and poc1Δ BB bending at the middle of triplet 5 and top of triplet 8 (indicated by black boxes; p=>0.05; >75% highest difference from other bins). The blue and red colors indicate the direction of curvature relative to the cell's anterior-posterior axis (axis of the ciliary power stroke). Blue indicates negative bending which is towards the cell anterior. Red indicates positive bending which towards the cell posterior (range= -4.5 to +4.5 rad/µm). (D) poc1Δ BBs do not distribute bending well at the end of the power stroke and the beginning of the recovery stroke. The heatmap indicates that the average curvatures for the poc1Δ shown above in (A). Curvature is most prominent on triplet MT 5. (E) poc1Δ BBs bend have high standard deviation in curvature across the BB. The heatmap indicates the standard deviation in the poc1Δ BBs. The standard deviation is most prominent on triplet MT 5. (F) poc1Δ BBs asymmetrically lose triplet MTs [181]. A section through a tomogram of the proximal region of a poc1Δ BB show the loss of triplet MTs 7-8. This is modeled in the right two panels showing that these triplet MTs are lost from the whole BB. This is consistent with the very high and inconsistent bending in triplet MTs 7-9 of the bottom BB shown in (A). (G) Graph shows the mean and standard deviation of triplet MT loss from poc1Δ BBs re-analyzed from tomograms used in Meehl et al., 2016 [181]. Triplet MTs 1,2,7,8, and 9 are most frequently lost. These triplet MTs face the cell posterior and lack connections to the SF. (H) Selected thin section images (~450 acquired BBs) of poc1Δ BBs from cells grown at 38 °C. BBs show damage to MTs or an abnormal or wavy MT curvature. Scale bar, 200nm.

Table C1. Sample size and quality. Table contains data on sample size, type, acquisition status, genotype, and structural parameters.

Genotype	WT	WT	*disA*1-1	*poc1Δ*
Temperature	37°C	30°C	30°C	30°C
EM grids	3	2	1	1
Cells screened	150~	100~	100~	100~
Cells acquired	7	14	5	15
BBs acquired	10	15	8	15
BB modeled	4	9	3	3

Table C2. Modeled structures. Tables compares the structures present and/or modeled in EM tomograms vs computational models.

Cellular/molecular structure	EM tomography	COMSOL model
Cell geometry present	✓	✗
Cell geometry modeled	✗	✗
Plasma membrane present	✓	✓
Plasma membrane modeled	✗	✓
Cortical cytoskeleton present	✓	✓
Cortical cytoskeleton modeled	(Junker et al., 2019)	✓
Cilium present	✓	✓
Cilium modeled	✗	✓
Doublet MTs present	✓	✓
Doublet MTs modeled	✗	✓
Dynein present	✓	✓
Dynein modeled	✗	✓
Radial spokes present	✓	✓
Radial spokes modeled	✗	✓
Nexin links present	✓	✓
Nexin links modeled	✗	✓
Axosome present	✓	✗
Axosome modeled	✗	✗
Terminal plate present	✓	✗
Terminal plate modeled	✗	✗
BB present	✓	✓
BB modeled	✓	✓
Triplet MTs present	✓	✓
Triplet MTs modeled	✓	✓
A-C linkers present	✓	✓
A-C linkers modeled	✗	✓
Inner scaffold present	✓	✓
Inner scaffold modeled	✗	✓
Cartwheel present	✓	✓
Cartwheel modeled	✗	✓
Striated fiber present	✓	✓
Striated fiber modeled	(Junker et al., 2019)	✓
Post-ciliary MTs present	✓	✓
Post-ciliary MTs modeled	(Junker et al., 2019)	✓
Transverse MTs present	✓	✓
Transverse MTs modeled	(Junker et al., 2019)	✓
Interconnections present	✓	✓
Interconnections modeled	(Junker et al., 2019)	✓
Temperature changes	✓	✗
Temperature effects	✓	✓
Genotype-derived defects	✓	✓

Table C3. MT parameters and sliding in computational model. Table contains computational model parameters and data for the relative sliding between adjacent tubules in both the cilium and BB.

Parameter	Value	Description	References
EI	73 pN μm^2	Flexural rigidity per doublet	[64, 66, 121]
k_N	10^5 pN μm^{-2}	Inter-doublet normal stiffness	[66, 90, 122]
k_{NRS}	10^5 pN μm^{-2}	Radial spoke normal stiffness	Estimate found to sufficiently maintain axoneme cross-sectional shape without creating convergence issues
k_{TRS}	100 pN μm^{-2}	Radial spoke shear stiffness	Estimate found to allow sufficient range of motion
k_{NAC}	10^6 pN μm^{-2}	AC linker normal stiffness	Estimate found to give triplet separation and curvature independence consistent with data
k_{TAC}	10^5 pN μm^{-2}	AC linker shear stiffness	Estimate found to give triplet translocations consistent with data
k_{Cortex}	11 pN μm^{-1}	Cortical attachment stiffness per filament	Estimate found to allow BB bending consistent with data
L_c	5.6μm	Cilium length	[261]
L_{bb}	500nm	Basal body length	[206]
r	100nm	Axoneme radius	[115, 124]
p	500 pN μm^{-1}	Distributed dynein force	[123]
f	25 Hz	Beat frequency	[36]

	Maximum relative sliding (nm)								
MT pair:	**1-2**	**2-3**	**3-4**	**4-5**	**5-6**	**6-7**	**7-8**	**8-9**	**9-1**
Tip	136	147	106	8	109	151	137	61	62
Base	19	25	21	6	12	21	21	12	7
10x less stiff A-C linkers	23	28.5	23	8	12	25	24	12	11
% diff from Baseline	21%	14%	10%	33%	0%	19%	14%	0%	57%

Table C4. Perturbations to computational model. Table contains the quantifications of BB parameters when structural elements are perturbed in the computational model.

	Rocking (degrees)		**Maximum bending beginning/end (rad/μm)**			
Perturbation	Front-back	Lateral	Triplet MT 4	Triplet MT 5	Triplet MT 6	Triplet MT 9
none	6.9	6.0	-0.78/0.70	-1.06/0.90	-0.97/0.92	-0.76/0.73
SF detachment	43.0	66.0	-1.01/0.70	-0.74/0.74	-0.69/0.70	-1.41/1.28
pcMT detachment	22.0	32.0	-0.77/0.72	-1.14/1.03	-1.05/1.00	-0.76/0.72
tMT detachment	7.6	35.0	-0.77/0.70	-1.10/0.91	-0.92/0.92	-0.74/0.86
10x less stiff A-C linkers	14.6	8.8	-0.77/1.06	-1.42/1.23	-1.27/1.17	-0.95/1.06

Movies will be made available online upon publication of this manuscript

Movie 1 Baseline side. Side view movie of a computational model representing 37°C *T. thermophila* BB and ciliary movements (Fig. 4.3 and C3).

Movie 2 Baseline top. Top view movie of a computational model representing 37°C *T. thermophila* BB and ciliary movements (Fig. 4.3 and C3).

Movie 3 No SF connection side. Side view movie of a computational model representing 37°C *T. thermophila* BB and ciliary movements when SF connections to the anterior BB and the cell cortex are lost (Figs. 4.3 and C3).

Movie 4 No SF connection top. Top view movie of a computational model representing 37°C *T. thermophila* BB and ciliary movements when SF connections to the anterior BB and the cell cortex are lost (Figs. 4.3 and C3).

Movie 5 No pcMT side. Side view movie of a computational model representing 37°C *T. thermophila* BB and ciliary movements when pcMTs are lost (Figs. 4.3 and C3).

Movie 6 No pcMT top. Top view movie of a computational model representing 37°C *T. thermophila* BB and ciliary movements when pcMTs are lost (Figs. 4.3 and C3).

Movie 7 No tMT side. Side view movie of a computational model representing 37°C *T. thermophila* BB and ciliary movements when tMTs are lost (Figs. 4.3 and C3).

Movie 8 No tMT top. Top view movie of a computational model representing 37°C *T. thermophila* BB and ciliary movements when tMTs are lost (Figs. 4.3 and C3).

Movie 9 30°C model side. Side view of a computational model representing 30°C *T. thermophila* BB and ciliary movements when forces are produced through the SF and cell cortex (Figs. 4.3, 4.4, and C3).

Movie 10 30°C model top. Top view of a computational model representing 30°C *T. thermophila* BB and ciliary movements when forces are produced through the SF and cell cortex (Figs. 4.3, 4.4, and C3).

Appendix D: Autotrace and body tracking code

Some sample code for Chapter 5 is given here. Full autotrace code is on Zenodo: https://doi.org/10.5281/zenodo.6687921

Autotrace code

see link above for complete version

```
function [Out, FileInfo] = autotrace_fun3(FileInfo)
% Autotrace function for cilia and flagella
%
% Run this function initially with no input and it will open a dialog that
% will allow you to select a video file. Trace several points along the
% cilium (base to tip) by left-clicking with the mouse.  Double-click when
% you have traced the entire length. To run the analysis again with
% different parameters on the same video, feed the 'FileInfo' structure
% back to the function as an input.
%
% Inputs:
%   Dialog box will open to select video on first run (no input)
%   FileInfo - this struct is generated as an output after initial run
%
% Outputs:
%   Out - struct with the following fields:
%       Data: angle and position data from trace
%       Stats: cost function values of trace
%       PP: values from post-processing and polynomial fit

% Louis Woodhams 09/2020, last modified 07/2022
%
% This software is made available under the CC BY NC license:
% https://creativecommons.org/licenses/by-nc/4.0/

%****************** USER PARAMETERS ************************************
umpp = 0.194;   % [um/pixel] spatial resolution of image
fps = 2000;     % [frames/sec]

n = 12;     % number of segments along length to use
nT = 50;    % number of theta values to try
dd = 2;     % rod width in pixels
sd = 0.8;   % standard deviation of gaussian dist (normalized)

sweepWidthRatio = 5; % if this is too low, angles may be out of range
a1 = 1;        % weight of correlation value
a2 = 0.0005;   % penalty for curvature along length (dTheta/ds)
a3 = 0.0002;   % penalty for change in position from last frame (dX/dt)
a4 = 0.001;    % penalty for change in angle from last frame(dTheta/dt)
a5 = 0.001;    % penalty for change in curvature from last frame(dKappa/dt)

interpType = 'cubic'; % type of image interpolation to use

step = 0; % step through points
```

```
ndp = 5; % number of points in disk diameter (keep odd)
%******************END USER PARAMETERS***********************************
if nargin == 0
    [file,path] = uigetfile({'*.avi;*.mp4;*.mpg;*.mpeg','Videos';...
        '*.*','All Files'}, 'Select a video');
    fileName = fullfile(path,file);
else
    fileName = FileInfo.fileName;
end
dt = 1/fps;     % time step

v = VideoReader(fileName); numFrames = v.NumFrames;

% get start and end frames
if nargin == 0
    prompt = {'first frame','last frame'};
    dlgtitle = 'Input';
    dims = [1 20];
    definput = {'1',num2str(numFrames)};
    answer = inputdlg(prompt,dlgtitle,dims,definput);
    firstFrame = str2double(answer{1});
    lastFrame  = str2double(answer{2});
    numFrames = lastFrame - firstFrame +1;
else
    firstFrame = FileInfo.firstFrame;
    lastFrame  = FileInfo.lastFrame;
end
nFrame = read(v,firstFrame);
nFrame = im2double(nFrame);
if size(nFrame,3)==3, nFrame = rgb2gray(nFrame); end

% this is for visual interpolation of the image.
interpFactor = 4;
[rows,cols] = size(nFrame);
[Xint, Yint] = ndgrid(1:1/interpFactor:rows,1:1/interpFactor:cols);

costArray = zeros(numFrames,5); % compare cost terms
totalCost = zeros(numFrames,1); % see if there are any high frames here

thetaSweepVec = linspace(-pi,pi,nT)*sweepWidthRatio/n; % angles to sweep
pointArray = zeros(n+1,2,numFrames);
thetaArray = zeros(n+1, numFrames);
c3 = 0; c4 = 0; c5 = 0;

%% get an initial line trace from base to tip then double click
% this gets us length, initial position, and initial angle
if nargin == 0
    imshow(nFrame)
    roi = drawpolygon('FaceAlpha',0);
    % roi = drawassisted; % this is another possible option
    % roi.Closed = 0;

    % find arclength
    line1 = roi.Position;
```

```
    close,    delete(roi)
else
    line1 = FileInfo.line1;
end

disp = line1(2:end,:)-line1(1:end-1,:);
    dist = sqrt(disp(:,1).^2 + disp(:,2).^2);
    arcLenPix = sum(dist);
    r = arcLenPix/n;   % individual segment length
    r_um = r*umpp; r_m = 1e-6*r_um; % in umints of um
    rs = ceil(r); % rounding segment length up for sweeper

d = gaussRod(ndp,rs,sd); % this is the 'rod' we will sweep across the cilium
dSum = sum(d(:));
dVec = linspace(-dd/2,dd/2,ndp); % points around zero to evaluate for corr
Y0 = repmat(dVec',[1, rs+1]);
X0 = repmat(0:rs,[ndp, 1]);
XY0 = [X0(:), Y0(:)]';

ind = 1;
for iFrame = firstFrame:lastFrame
    nFrame = read(v,iFrame);
    nFrame = im2double(nFrame);
    if size(nFrame,3)==3, nFrame = rgb2gray(nFrame); end
    I = griddedInterpolant(nFrame,interpType,'none');
    nFrameInt = I(Xint, Yint);

    %% initial pos and angle
    x = NaN(n+1,2);
    x(1,:) = line1(1,:);
    theta = zeros(n+1,1);
    if ind == 1
        theta(1) = atan2(disp(1,2), disp(1,1));
        if ~showTrace, w1 = waitbar(1,'Finding paths'); end
    else
        theta(1) = thetaBaseLast;
    end

    for iStep = 1:n
        %initialize cost and position arrays
        c = zeros(nT,5);
        xVec = zeros(nT,2);

        for iTheta = 1:length(thetaSweepVec)
            nTheta = (thetaSweepVec(iTheta) + theta(iStep));
            iX = x(iStep,:)+[r*cos(nTheta), r*sin(nTheta)];

            % create rotation matrix with current trial angle nTheta
            ROTMAT = [cos(nTheta), -sin(nTheta);
                      sin(nTheta),  cos(nTheta)];
            % rotate and translate 'rod' of evaluation points
            XYRot = ROTMAT*XY0+x(iStep,:)';
            % evaluate intensities at these coordinates
            blockVal = I(XYRot(2,:),XYRot(1,:));
```

```
            % take weighted average using weights in 'd'

            c1 = a1*dot(d(:),blockVal(:))/dSum; % weighted average pixel vals
            if isnan(c1) % assign penalty for going out of image bounds
                c1 = a1*10;
            end
            % curvature cost ~(dTheta/ds)^2
            c2 = a2*(thetaSweepVec(iTheta)/r_um)^2;
            if ind > 1
                % c3 is cost due to (dX/dt)^2, dXdt in um/s
                dXdt = norm(iX - pointArray(iStep+1,:,ind-1))*umpp/dt;
                c3 = a3*dXdt^2*(1-iStep/(n+1))/1e6; % diminishes along length
                % c4 is cost due to dTheta/dt
                dThetadt = (nTheta - thetaArray(iStep+1,ind-1))/dt;
                c4 = a4*dThetadt^2/1e6;
                % c4 = c4*(1-iStep/(n+1))/arcLen; % diminishes along length
                % c5 is cost due to d(dTheta/ds)/dt
                c5 = a5*(thetaSweepVec(iTheta)-...
                    (thetaArray(iStep+1,ind-1)-...
                    thetaArray(iStep,ind-1)))^2/r_um^2/dt^2/1e6 ;
            end
            c(iTheta,:) = [c1, c2, c3, c4, c5];
            xVec(iTheta,:) = iX;
        end

        [minVal, minInd] = min(sum(c,2));
        totalCost(ind) = totalCost(ind) + minVal/n;
        c = c - min(c,[],1);
        costArray(ind,:) = costArray(ind,:) + c(minInd,:)/n;
        theta(iStep+1) = theta(iStep)+thetaSweepVec(minInd);
        x(iStep+1,:) = xVec(minInd,:);
        if iStep == 1
            thetaBaseLast = theta(iStep)+thetaSweepVec(minInd);
        end
    end
    pointArray(:,:,ind) = x;
    thetaArray(:,ind) = theta(:);
    ind = ind + 1;
end
thetaArray(1,:) = []; % discard first row - JUNK
```

Autotrack code

```
function Out = autotrack
% autotrack cell body motion
% Louis Woodhams 07/2022

%% ******************User parameters*************************************
% Do we want to minimize SSRs or maximize correlation
% objective = 'sumofsquares';
objective = 'correlation';

fps = 2000;  % fps of recording for kinematic analysis
umpp = 0.194; % um per pixel for kinematic analysis
drawShape = 'ellipse'; % 'ellipse' or 'circle'
framesToRead = inf;    % set to inf for all frames
plotWhileRunning = true; % show tracking as it is happening?
keepWarpedImages = true; % do you want to save these?
smearTemplate = true; % average the template image as stracking runs
numToSmear = 700; % how many template frames to smear? inf for all
trackFrameToFrame = false; % EXPERIMENTAL may lead to 'drift' of tracking
pixSize = 0.5; % make less than 1 for sub-pixel sampling [default 1]
reduceSize = true; % save stabilized images as uint8
nfpsAvg = 60; % just for showing fps while running NBD
% ********************End User Parameters*********************************

%% get a filename
[file,path] = uigetfile({'*.avi;*.mp4;*.mpg;*.mpeg','Videos';...
    '*.*','All Files'}, 'Select a video');
fileName = fullfile(path,file);

% read video and convert frame to grayscale if necessary
v = VideoReader(fileName);
numFrames = v.NumFrames;
if numFrames > framesToRead, numFrames = framesToRead; end
frame1 = read(v,1);
[numRows,numCols,numColors] = size(frame1);
frame1 = im2double(frame1);
if numColors==3, frame1 = rgb2gray(frame1); end
frame1 = flipud(frame1);

% get our region of interest
hIm = imshow(frame1);
axis xy
ttl = title('Frame 1');
switch drawShape
    case 'circle'
        roi = drawcircle;
        disp('press any key to continue')
        pause
        center0 = roi.Center;
        R0 = roi.Radius;
        delete(roi)
        [XC, YC, mask] = makeCircle(R0, pixSize);
        theta0 = 0;
```

```
        crossXC = [-R0, R0,   0,  0];
        crossYC = [  0,  0, -R0, R0];
    case 'ellipse'
        roi = drawellipse;
        disp('press any key to continue')
        pause
        center0 = roi.Center;
        ab = roi.SemiAxes;
        theta0 = 2*pi*(1 - roi.RotationAngle/360);
        delete(roi)
        % create evaluation elipse points and rotate
        [XC, YC, mask] = makeEllipse(ab(1),ab(2),pixSize);
        [XC,YC] = simpleWarp([0 0 theta0],XC,YC);
        % create crosshairs and rotate
        crossXC = [-ab(1), ab(1),      0,     0];
        crossYC = [     0,     0, -ab(2), ab(2)];
        [crossXC, crossYC] = simpleWarp([0 0 theta0],crossXC,crossYC);
end

% shift coordinates for initial interpolation
X = XC + center0(1);
Y = YC + center0(2);
% get template image
iFInterp = griddedInterpolant(frame1,'cubic');
Template = iFInterp(Y, X); %
T = Template - mean(Template(:));
T2 = T*T';
template0 = Template;

if keepWarpedImages
    IMWarp = zeros(size(Template)); % initialize for global use
    unwarped = zeros([size(mask), numFrames]);
    im_ =  zeros(size(mask));
    im_(mask) = Template;
    unwarped(:,:,1) = im_;
end

% Crosshairs for display
crossX =  crossXC + center0(1);
crossY =  crossYC + center0(2);
hold on
hCross = plot(crossX([1,2]),crossY([1,2]),'r--', ...
              crossX([3,4]),crossY([3,4]),'b--', ...
              crossX(1),    crossY(1),    'w.');
hCross(4) = plot (center0(1),center0(2),'g-');
hold off
hCross(1).LineWidth = 2; hCross(2).LineWidth = 2;
drawnow
pause(1)

if ~plotWhileRunning
    close
    hwait = waitbar(0,'Progress');
end
```

```
%%
opts = optimset('TolFun',1e-6,'TolX',1e-6);
p = zeros(3,numFrames);
resid = nan(1, numFrames);
iterations = zeros(1, numFrames);
funcCount = zeros(1, numFrames);
exitflag = zeros(1,numFrames);
im_ =  zeros(size(mask));
dtVec = nan(nfpsAvg,1);
for ii = 2:numFrames
    tic
    p0 = p(:,ii-1);
    iFrame = read(v,ii);
    iFrame = im2double(iFrame);
    if numColors==3, iFrame = rgb2gray(iFrame); end
    iFrame = flipud(iFrame);

    iFInterp = griddedInterpolant(iFrame,'cubic');
    [p_, resid_, exitflag_, fmsOut] = fminsearch(@sumSQR,p0, opts);
    p(:,ii) = p_;
    resid(ii) = resid_;
    exitflag(ii) = exitflag_;
    iterations(ii) = fmsOut.iterations;
    funcCount(ii) = fmsOut.funcCount;


    if keepWarpedImages
        im_(mask) = IMWarp;
        unwarped(:,:,ii) = im_;
    end

    if smearTemplate && (ii < numToSmear)
        % could check that correlation is above some threshhold?
        Template = (1-1/ii)*Template + (1/ii)*IMWarp;
        T = Template - mean(Template(:));
        T2 = dot(T,T);
    end

    if trackFrameToFrame
        Template = IMWarp;
        T = Template - mean(Template(:));
        T2 = dot(T,T);
    end

    prog = round(ii/numFrames * 100);
    if plotWhileRunning
        try
            hIm.CData = iFrame; % update the images
            % trace the path of the centroid
            hCross(4).XData = [hCross(4).XData, center0(1) + p_(1)];
            hCross(4).YData = [hCross(4).YData, center0(2) + p_(2)];

            % display crosshairs
```

```
            [crossWXC, crossWYC] = simpleWarp(p_,crossXC,crossYC);
            crossWX = crossWXC + center0(1);
            crossWY = crossWYC + center0(2);
            hCross(1).XData = crossWX([1,2]);
            hCross(2).XData = crossWX([3,4]);
            hCross(3).XData = crossWX(1);
            hCross(1).YData = crossWY([1,2]);
            hCross(2).YData = crossWY([3,4]);
            hCross(3).YData = crossWY(1);

            % stuff for monitoring progress during analysis
            dtVec(mod(ii,nfpsAvg)+1) = toc;
            dt = mean(dtVec,'omitnan');

            ttl.String = sprintf('Frame %d, %d%%, fps %0.1f',ii, prog, 1/dt);
            drawnow limitrate
            % pause(0.01)
        catch
            break
        end
    else
        try
            waitbar(prog/100, hwait,'Progress')
        catch
            break
        end
    end
end

Out.p = p;
Out.theta0 = theta0; % theta in radians
Out.fps = fps;
Out.umpp = umpp;
Out.Stats.resid = resid;
Out.Stats.iterations = iterations;
Out.Stats.funcCount = funcCount;
Out.Stats.totalIterations = sum(iterations);
Out.Stats.totalFuncEvals = sum(funcCount);


if smearTemplate
    im_(mask) = Template;
    Out.template = im_;
    im_(mask) = template0;
    Out.template0 = im_;
    figure
    imshow([Out.template0, Out.template])
end

if keepWarpedImages
    % normalize just in case
    unwarped = unwarped - min(unwarped(:));
    unwarped = unwarped/max(unwarped(:));
    Out.unwarped = unwarped;
```

```
    Out.mask = mask;
    try
        Out = bodyKinematics(Out);
    end
end

if reduceSize
    Out.unwarped = im2uint8(Out.unwarped);
end

%% plot
figure
subplot(3,1,1)
plot(p([1,2],:)'), grid on
ylabel('displacement (pix)')
legend('x','y','Location','best')

subplot(3,1,2)
plot(p(3,:)), grid on
ylabel('theta (rad)')

subplot(3,1,3)
plot(-resid), grid on
xlabel('frame #')
ylabel('correlation coeff to frame1')

%% objective function
    function SSr = sumSQR(p)
        [wXC, wYC] = simpleWarp(p,XC,YC);
        IMWarp = iFInterp(wYC+center0(2),wXC+center0(1));
        switch objective
            case 'sumofsquares'
                eResidual = Template - IMWarp;
                SSr = dot(eResidual,eResidual);
            case 'correlation'
                I = IMWarp - mean(IMWarp);
                correl = (T*I')/sqrt(T2*(I*I'));
                SSr = -correl;
        end
    end
end
```

Appendix E: Dynamic analysis code

Representative code for obtaining dynamic quantities from position data. In the code below, `X` is an array of x-positions where row indices represent position along the cilium length and column indices represent frame number in the time sequence (each column of `X` is a vector of positions along the cilium length at a given frame). `Y` is an array of y-positions and `dt` is the time delay between frames. `cN` and `cT` are resistive force coefficients.

```
% Get velocities [um/s]
[Vx, dxds] = gradient(X);
[Vy, dyds] = gradient(Y);
Vx = Vx/dt; Vy = Vy/dt;

% Tangent angle [rad]
Theta = atan2(dyds,dxds);
Theta = unwrap(Theta');

% segment lengths [um]
dL = sqrt(dxds.^2 + dyds.^2);
L_cilia = trapz(dL);
L = mean(L_cilia); % average length from plots

% Tangent and Normal Vectors
Tx = dxds./dL;
Ty = dyds./dL;
Nx = -Ty;
Ny =  Tx;

% Tangent velocity is dot product of velocity and tangent vector
% Normal  velocity is dot product of velocity and normal vector
Vt = Vx.*Tx + Vy.*Ty;
Vn = Vx.*Nx + Vy.*Ny;

% tangent and normal force (Positive - power applied by cilium)
Ft = Vt * cT; % [pN/um]
Fn = Vn * cN;

% x and y force
Fx = Ft.*Tx + Fn.*Nx;
Fy = Ft.*Ty + Fn.*Ny;

% Moment (Check on final sign convention!!!)
Mz = Fy.*X - Fx.*Y;

% power
P = Fx.*Vx + Fy.*Vy;

% Integrate forces and moments along length
F_total_x = trapz(Fx.*dL);      % [pN]
F_total_y = trapz(Fy.*dL);
```

```
M_total_z = trapz(Mz.*dL);      % [pN-um]
P_total   = trapz( P.*dL)/1000; % [fW]

% integrate over time:
Work = trapz(P_total)*dt*1000;          % [atto Joules]
Work_y = trapz(trapz( Fy.*Vy.*dL))*dt;  % [atto Joules]
Impulse_y = trapz(F_total_y)*dt*1000;   % [pN-ms]
```